

---

# Strongly Interacting Quantum Systems out of Equilibrium

## Ultracold Quantum Gases and Magnetic Systems

Christian Kasztelan

---



München 2010



---

**Strongly Interacting Quantum Systems out of  
Equilibrium**  
**Ultracold Quantum Gases and Magnetic Systems**

**Christian Kasztelan**

---

Dissertation  
an der Fakultät für Theoretische Physik  
der Ludwig–Maximilians–Universität  
München

vorgelegt von  
Christian Kasztelan  
aus Gdańsk (Danzig, Polen)

München, den 12.10.2010

Erstgutachter: Prof. Dr. Ulrich Schollwöck

Zweitgutachter: Prof. Dr. Matthias Christandl

Tag der mündlichen Prüfung: 8.12.2010

# Inhaltsverzeichnis

<b>Zusammenfassung</b>	<b>ix</b>
<b>Summary</b>	<b>xi</b>
<b>Publication List</b>	<b>xiii</b>
<b>1 Introduction and overview</b>	<b>1</b>
1.1 Goals of this thesis . . . . .	3
1.2 Content of the thesis and outlook . . . . .	4
<b>2 Matrix Product State, DMRG, Time evolution</b>	<b>7</b>
2.1 Matrix Product States . . . . .	8
2.2 DMRG . . . . .	16
2.3 Time dependent DMRG methods . . . . .	21
2.3.1 Trotter Algorithm . . . . .	21
2.3.2 Krylov Algorithm . . . . .	23
2.3.3 Folding Algorithm . . . . .	25
<b>3 Ultra Cold Gases</b>	<b>29</b>
3.1 Bose Einstein Condensation . . . . .	30
3.1.1 BEC of an ideal gas . . . . .	31
3.1.2 Ultracold collisions . . . . .	32
3.1.3 BEC of a weakly interacting gas . . . . .	35
3.1.4 Thomas-Fermi approximation . . . . .	36
3.1.5 Recent development . . . . .	36
3.2 BEC in optical lattices . . . . .	38
3.2.1 Dipole force . . . . .	38
3.2.2 Optical potential . . . . .	39
3.2.3 Optical lattices . . . . .	39
3.2.4 Band structure . . . . .	40
3.2.5 Bose Hubbard Hamiltonian . . . . .	41
3.2.6 Recent development . . . . .	42
3.3 Measurement in optical lattices . . . . .	45

3.3.1	Time-of-flight and adiabatic measurement . . . . .	45
3.3.2	Noise correlations . . . . .	47
3.3.3	Recent development . . . . .	48
<b>4</b>	<b>Magnetism, coherent many-particle dynamics, and relaxation with ultracold bosons in optical superlattices</b>	<b>51</b>
4.1	Setup and model . . . . .	53
4.2	Effective model . . . . .	55
4.3	Time-evolution from the Néel state . . . . .	57
4.3.1	Errors through experimental limitations in state preparation and measurement . . . . .	58
4.3.2	Symmetry between the ferromagnetic and the antiferromagnetic cases . . . . .	60
4.3.3	Numerical method and parameters . . . . .	60
4.3.4	Site magnetization . . . . .	61
4.3.5	Correlation functions . . . . .	64
4.3.6	Momentum distribution and correlators . . . . .	64
4.4	Relaxation to steady states . . . . .	67
4.4.1	General features . . . . .	67
4.4.2	Relaxation for the Heisenberg magnet in mean field approximation . . . . .	68
4.5	Validity of the effective spin model . . . . .	71
4.6	Preparation of the antiferromagnetic groundstate by adiabatic evolution . . . . .	74
4.7	Conclusion . . . . .	76
<b>5</b>	<b>Landau Zener dynamics on a ladder with ultra cold bosons</b>	<b>77</b>
5.1	Mean field description . . . . .	78
5.1.1	Landau-Zener formula . . . . .	79
5.1.2	Extensions of the Landau-Zener formula . . . . .	80
5.2	Setup and model for the time-dependent DMRG calculations . . . . .	84
5.2.1	Numerical method and parameters . . . . .	85
5.3	Forward sweep . . . . .	85
5.4	Inverse sweep . . . . .	86
5.5	Time-evolution after quenches . . . . .	90
<b>6</b>	<b>Entanglement and Decoherence of Multi-Qubit-Systems in external Baths</b>	<b>93</b>
6.1	Quantifying Entanglement and Decoherence . . . . .	95
6.2	General entanglement law for entangled qubit pairs . . . . .	99
6.3	Few qubits in a general spin bath . . . . .	101
6.3.1	The two qubit case, Bell states . . . . .	103
6.3.2	The three and more qubit case, general $W$ - and $GHZ$ -state . . . . .	108
6.3.3	Summary and outlook . . . . .	111
	<b>Acknowledgments</b>	<b>129</b>

**Contents**

---

**vii**

**Curriculum Vitae**

**131**





# Zusammenfassung

Der Hauptgegenstand dieser Arbeit ist die Untersuchung von Vielteilcheneffekten in stark korrelierten eindimensionalen oder quasi-eindimensionalen Festkörpersystemen. Das charakteristische an solchen Systemen sind ihre großen thermischen und quantenmechanischen Fluktuationen. Da aufgrund dieser Eigenschaften ein Zugang mittels Molekularfeldmethoden oder auch störungstheoretischer Methoden ausgeschlossen ist, können solche Systeme in der Regel nur numerisch untersucht werden. Die Dichtematrix-Renormierungsgruppe (DMRG) ist eine ausgereifte und gut verstandene Methode, die geeignet ist, um aussergewöhnlich große eindimensionale Systeme mit hoher Präzision zu untersuchen. Diese ist 1992 von Steven White zunächst nur für statische Probleme entwickelt worden und wurde im Laufe der Zeit zu der zeitabhängigen DMRG erweitert, mit welcher sich auch Nichtgleichgewichtsszenarien erfolgreich untersuchen lassen.

In dieser Arbeit untersuche ich drei konzeptionell unterschiedliche Probleme, wobei ich größtenteils die Krylov-Unterraum Variante der zeitabhängigen DMRG Methode benutze. Meine Ergebnisse sind für kürzlich gemachte Experimente mit ultrakalten Atomgasen unmittelbar von Bedeutung. Diese Experimente sind unter anderem auch an der LMU in der Gruppe von Immanuel Bloch durchgeführt worden.

Das erste Projekt zielt bereits auf die ultimative Anwendung ultrakalter Atome in optischen Gittern ab, nämlich der Möglichkeit diese als Quantensimulator für kompliziertere Festkörpersysteme zu benutzen. Die bei diesem Projekt zugrunde liegende Idee ist die Simulation eines magnetischen Modells mittels bosonischer Atome in zwei verschiedenen Hyperfeinzuständen, welche in einem optischen Übergitter gefangen sind. Das System wird durch das Bose-Hubbard Modell für zwei Spezies beschrieben und kann in einem bestimmten Parameterbereich näherungsweise eine Spin-1/2 Heisenbergkette simulieren, wobei die Wechselwirkung zwischen den Spins über einen Hüpfprozess zweiter Ordnung realisiert wird. Das Umschalten zwischen den schnellen Hüpfprozessen erster Ordnung und denen zweiter Ordnung lässt sich über die Abstimmung der Parameter des Übergitters steuern. Diese Untersuchung orientiert sich an zwei erst kürzlich durchgeführten Experimenten, in denen eine kohärente Zweiteilchendynamik mittels ultrakalter Bosonen in isolierten Doppelmulden realisiert worden ist. In meinen Rechnungen befasse ich mich mit der kohärenten Vielteilchendynamik nach dem Koppeln dieser isolierten Doppelmulden zu einer Kette. Dabei untersuche ich analytisch und numerisch die Zeitentwicklung von experimentell zugänglichen Größen. Das relativ einfache Umschalten zwischen dem Bose-Hubbard und dem Heisenberg Modell kann dazu genutzt werden, um experimentell die Unterschiede der Relaxation in den stationären Zustand zwischen nicht-integrablen und Bethe-Ansatz-integrablen

Modellen zu untersuchen. Es stellt sich heraus, dass die Relaxation beim Heisenberg Modell über eine Phasenmittelung geschieht, welche sich vollständig vom Thermalisierungsprozess über Stöße, welcher typisch für nicht-integrable Prozesse ist, unterscheidet.

Im zweiten Teil meiner Arbeit untersuche ich die Erweiterung der ursprünglichen Landau-Zener Formel auf ein bosonisches Vielteilchensystem. Diese Formel gibt die Tunnelwahrscheinlichkeit zwischen den zwei Zuständen eines Zwei-Niveau Systems an, wobei die Energiedifferenz zwischen diesen zwei Niveaus linear in der Zeit verändert wird. In einem kürzlich realisierten Experiment wurde diese Fragestellung auf ein Vielteilchensystem übertragen, welches aus mehreren paarweise miteinander gekoppelten eindimensionalen Bose-Einstein Kondensaten besteht. Man hat festgestellt, dass die Kopplungsstärke zwischen den Bose-Einstein Kondensaten und die Kopplung innerhalb der einzelnen Bose-Einstein Kondensate das ursprüngliche Landau-Zener Szenario stark modifizieren. Nach einer kurzen Einführung in das Zwei-Niveau und das Drei-Niveau Landau-Zener Problem zeige ich die Resultate der Quantendynamik des mikroskopischen Modells und den Vergleich mit den experimentellen Ergebnissen. Dabei berechne ich sowohl die beiden möglichen Landau-Zener Szenarien als auch die Zeitentwicklung zu einer fixen Energiedifferenz. Letzteres kann, vorausgesetzt die Anfangsteilchendichte ist ausreichend hoch, dazu benutzt werden, um einen quasi-thermalisierten Zustand mit einer beliebigen Temperatur zu erzeugen.

Das dritte Projekt ist mathematischer Natur und verbindet die beiden Forschungsbereiche des Quantencomputings und der Quanteninformation. Die Aufgabe besteht darin, systematisch die Auswirkungen der Dekohärenz auf maximal verschränkte multipartite Zustände zu untersuchen, welche typischerweise beim Durchlaufen eines Quantenalgorithmus generiert werden. Dabei gilt, je höher die Anzahl der verschränkten Qubits desto fragiler ist die kostbare Gesamtverschränkung unter dem Einfluß von Dekohärenz. Ich untersuche zunächst nur zwei verschränkte Qubits, wobei eines an eine beliebige Umgebung gekoppelt ist. Für diesen besonderen Fall kann ich eine einfache Formel für den Verschränkungsabbau herleiten. Als nächstes untersuche ich die Verschränkungsabnahme von zwei, drei und vier verschränkten Qubits, welche mit einem globalen Spin-1/2 Bad oder mit voneinander unabhängigen Spin-1/2 Bädern wechselwirken. Obwohl es für drei und mehr Qubits kein allgemeines Verschränkungsmaß gibt, stellt sich heraus, dass die Verschränkungsabnahme direkt mit dem Verschränkungsabbau zwischen dem zentralen System und der Umgebung zusammenhängt. Das impliziert die Entstehung eines noch größeren Netzwerkes aus verschränkten Teilchen. Mittels der von-Neumann Entropie und der Wootters-Concurrence, kann ich eine einfache Obergrenze für die verschränkungsbrechende Wirkung des Bades auf die anfänglich maximal verschränkten Vielteilchenzustände ableiten.

# Summary

The main topic of this thesis is the study of many-body effects in strongly correlated one- or quasi one-dimensional condensed matter systems. These systems are characterized by strong quantum and thermal fluctuations, which make mean-field methods fail and demand for a fully numerical approach. Fortunately, a numerical method exist, which allows to treat unusually large one - dimensional system at very high precision. This method is the density-matrix renormalization group method (DMRG), introduced by Steve White in 1992. Originally limited to the study of static problems, time-dependent DMRG has been developed allowing one to investigate non-equilibrium phenomena in quantum mechanics.

In this thesis I present the solution of three conceptionally different problems, which have been addressed using mostly the Krylov-subspace version of the time-dependent DMRG. My findings are directly relevant to recent experiments with ultracold atoms, also carried out at LMU in the group of Prof. Bloch.

The first project aims the ultimate goal of atoms in optical lattices, namely, the possibility to act as a quantum simulator of more complicated condensed matter system. The underline idea is to simulate a magnetic model using ultracold bosonic atoms of two different hyperfine states in an optical superlattice. The system, which is captured by a two-species Bose-Hubbard model, realizes in a certain parameter range the physics of a spin-1/2 Heisenberg chain, where the spin exchange constant is given by second order processes. Tuning of the superlattice parameters allows one to controlling the effect of fast first order processes versus the slower second order ones. The analysis is motivated by recent experiments, where coherent two-particle dynamics with ultracold bosonic atoms in isolated double wells were detected. My project investigates the coherent many-particle dynamics, which takes place after coupling the double well. I provide the theoretical background for the next step, the observation of coherent many-particle dynamics after coupling the double wells. The tunability between the Bose-Hubbard model and the Heisenberg model in this setup could be used to study experimentally the differences in equilibration processes for non-integrable and Bethe ansatz integrable models. It turns out that the relaxation in the Heisenberg model is connected to a phase averaging effect, which is in contrast to the typical scattering driven thermalization in nonintegrable models

In the second project I study a many-body generalization of the original Landau-Zener formula. This formula gives the transition probability between the two states of a quantum mechanical two-level system, where the offset between the two levels is varying linearly in time. In a recent experiment this framework has been extended to a many-body system consisting of pairwise tunnel-coupled one-dimensional Bose liquids. It was found that the tunnel coupling

between the tubes and the intertube interactions strongly modify the original Landau-Zener picture. After a introduction to the two-level and the three-level Landau-Zener problem I present my own results for the quantum dynamics of the microscopic model and the comparison to the experimental results. I have calculated both Landau-Zener sweeps as well as the time-evolution after sudden quenches of the energy offset. A major finding is that for sufficiently large initial density quenches can be efficiently used to create quasi-thermal states of arbitrary temperatures.

The third project is more mathematical and connects the fields of quantum computation and of quantum information. Here, the main purpose is to analyse systematically the effects of decoherence on maximally entangled multi-partite states, which arise typically during quantum computation processes. The bigger the number of entangled qubits the more fragile is its entanglement under the influence decoherence. As starting point I consider first two entangled qubits, whereby one qubit interacts with an arbitrary environment. For this particular case I have derived a factorization law for the disentanglement. Next, I calculate the decrease of entanglement of two, three and four entangled qubits, general  $W$ - and general  $GHZ$ -state, coupled to a global spin-1/2 bath or several independent spin-1/2 baths, one for each qubit. Although there is no appropriate entanglement measure for three and more qubits, it turns out that this decrease is directly related to the increase of entanglement between the central system and the bath. This implies the formation of a much bigger multipartite entangled network. Thus, using the von Neumann entropy and the Wootters concurrence, I derive a simple upper bound for the bath-induced entanglement breaking power of the initially maximally entangled multi-partite states.

# Publication list

During the course of the work for this thesis several articles have been published or made available as preprints on arxiv.org.

- T. Konrad, F. de Melo, M. Tiersch, C. Kasztelan, A. Aragão, and A. Buchleitner: *Evolution equation for quantum entanglement*, Nature Physics **4**, 99 - 102 (2008)
- T. Barthel, C. Kasztelan, I.P. McCulloch, and U. Schollwöck: *Magnetism, coherent many-particle dynamics, and relaxation with ultracold bosons in optical superlattices*, Phys. Rev. A **79**, 053627 (2009)
- C. Kasztelan, S. Trotzky, Y.-A. Chen, I. Bloch, I.P. McCulloch, and U. Schollwöck, and G. Orso: *Landau-Zener dynamics in coupled Bose-Hubbard chains*, in preparation (2010)



# Chapter 1

## Introduction and overview

With the first realization of Bose-Einstein condensation in dilute atomic gases in 1995 [10, 75, 42] a new and very dynamic field of physics emerged. Spectacular experiments with atomic Bose-Einstein condensates have demonstrated the remarkable wave-like nature of this new form of matter. Similar to the emitted light of a laser, which is a perfect realization of a classical electromagnetic wave, a Bose-Einstein condensate can be considered as the perfect realization of a classical matter wave.

The first generation of experiments with Bose-Einstein condensates focused on the coherence properties of these weakly-interacting superfluids. Some of the most important examples are the observation of interference between two overlapping condensates [14], of long-range phase coherence [39], and of quantized vortices and vortex lattices [1]. All of these phenomena can be explained by introducing a so-called macroscopic wave function or order parameter, which reduces the full many-body problem to a nonlinear single particle problem governed by the Gross-Pitaevskii equation for bosons or the Ginzburg-Landau theory for fermions.

Only a few years after the first realization of the BEC two other developments have created much attention among physicists with a background in condensed matter physics, nuclear physics and quantum information science. One is the ability to tune the interaction strength between atoms by means of so-called Feshbach resonances [64, 143], allowing one to enter the strongly interaction regime [302]. The other is the possibility to load ultracold quantum gases into optical lattices [118]. This technique allows to create the perfect periodic structure of arbitrary dimension and tunable tunneling rates. The combination of these two revolutionary techniques allows experimentalists to use cold atoms as quantum simulators, at first advocated by Richard P. Feynmann [99]. The quantum simulator is a highly controllable quantum system which is used to simulate the dynamical behaviour of another more complex quantum system [99]. An optical lattice offers remarkably clean access to a particular Hamiltonian and thereby serves as a model system for testing fundamental theoretical concepts and examples of quantum many-body effects.

Among the various systems, one dimensional and quasi-one dimensional systems are a fantastic playground for quantum phase transitions, with rather unique properties [110]. Contrary to the two and three dimensional cases, interactions play a major role since in one dimension particles cannot move without affecting their neighbours. Hence, any individual motion of the

particles must be transformed into a collective one, leading to a very special universality class for interacting quantum systems, known as Luttinger liquids [181]. Moreover, in one dimension quantum and thermal fluctuations are pushed to a maximum. This provides a severe limitation to mean-field approaches and fully numerical methods are generally needed to understand these physical systems.

Fortunately, in recent years a new numerical exact method, which goes under the name of density-matrix renormalization group (DMRG), allows one to treat unusually large one-dimensional systems at very high precision[242]. Only one decade after the initial DMRG formulation, given in 1992 by Steve White[284], and originally limited to the study of static problems, time-dependent renormalization group techniques have been developed, provide a interesting link between quantum information theory and computational condensed matter physics. This allows one to investigate quantum-many-body systems out of equilibrium, making DMRG a necessary tool to describe current experiments with ultra cold atoms in optical lattices [57].

Optical lattices provide a flexible tool for probing fundamental condensed physics [37, 38], as well as finding applications in quantum optics [144, 175] and quantum information processing [43, 45, 38]. The clear realizations of many Hamiltonians and the high-tunability of the internal parameters allow the creation of many different scenarios, which go beyond those currently achievable in typical condensed-matter physics systems [175]. One can create exotic many-body states [224], which are initially entangled [22] or states with a desired local density [260] as well as systems consisting of different types of bosons or fermions or mixtures between them [204]. By changing the lattice parameters or the whole lattice structure during an experiment it is possible to study exotic phase transitions [118, 128], transport phenomena [281] or non-equilibrium relaxation processes [157, 138] which have been so far unknown, or far from being fully understood.

A fundamental problem in quantum mechanics is the study of relaxation phenomena which occur in system coupled to an environment (open system). Closed systems, which are described by a pure wave function [44], can never relax on a global scale, since their total energy or similar conserved quantities remain constant throughout the whole time-evolution [101]. However, different subsystems of the total system can exchange energy or particles among each other and can therefore relax [24, 66]. These subsystems are simply open systems with respect to the rest of the total system, which acts as an environment. Beside the pure observation of relaxation, it remains an open question, how relaxation occurs in detail and what is the final relaxed state.

The interaction between different parts of system happens due to some flow of particle densities, via hopping, or spin, via spin flips, which depends in highly non-trivial way on the Hamiltonian. All these different processes have in common that they lead to an increase of a quantity called entanglement [139]. As a concrete example one could think about an experiment where the initial state is a so-called domain wall state, i.e. a chain of spins with one half of the spin being spin-ups and the other half being spin-downs. At the beginning of the experiment everything is clear to the observer and a measurement at this point would not lead to a gain of further information. The situation changes rapidly as one turns on interactions, here in form of nearest neighbour spin-flips. This leads to a new description of the total wave function in form of a superposition between different possible states. The redistribution of local quantities between different possible states in a superposition gives rise to entanglement [17]. The longer the sub-



systems stay in contact with each other the more entanglement will be created. Meanwhile, the observer becomes more and more ignorant until he makes a measurement on the system. In contrast to a situation before turning on the spin-flips, a measurement now increases his amount of information about the system.

It is important to say that entanglement is not only a by-product of many-body quantum theory, as it is currently used as the key resource for many applications in quantum engineering [112, 139], like e.g. quantum communication [113] or quantum computing [82]. In a typical scenario one prepares a system consisting of few entangled particles, e.g. spin states, which are used later as the carrier of some quantum information protocol [41, 250]. Since it is in general impossible to isolate this small system from some environment one will encounter all disadvantages of an open system here. As the entanglement between the system and the environment grows the valuable initial few-body entanglement in the system will decrease [163]. Thus, one observes also here a kind of redistribution of the quantity entanglement which comes along with the redistribution of the spins which have been entangled at the beginning.

## 1.1 Goals of this thesis

The aim of this thesis is the investigation of different many-body phenomena and relaxation physics of quantum many-particle lattice systems which are made either of interacting bosons moving in a lattice or, similarly, interacting spins that are localized on the sites of a quasi one-dimensional lattice. The here presented work is, mostly, strongly related to experiments with ultra cold atoms in optical lattices. With the help of the time-dependent DMRG method and, wherever it was possible or useful, other analytical calculations I have tried to:

(i) explain the experimentally observed quantum phenomena in one-dimensional atomic systems. It turns out that very simple questions in quantum mechanics, which has been stated and already solved several decades ago, become fascinating again when put in the context of strongly interacting many-body quantum system. Due to the complexity of the new problems there is often not even a simple picture which could explain the observed behaviour to entire satisfaction. This is in particular true for non-static problems. Despite the possibility to elaborate an answer analytically, e.g. using a mean-field approach, a precise analysis is only possible using the time-dependent DMRG method.

(ii) elaborate theoretical proposal for new and feasible experiments. Numerical analysis helps indeed to find the best parameter regime at which the desired many-body quantum effects are more visible but under the experimental constraints. Here the main purpose is to provide a complete physical picture of the relaxation process of some highly perturbed quantum state to a steady state in the long time limit.

(iii) clarify the question of entanglement evolution, breaking and decoherence effects in real environments. The main motivation was to develop a full theoretical description of the entanglement evolution of two and more initially entangled spin- $\frac{1}{2}$  particles in a spin bath.

## 1.2 Content of the thesis and outlook

The thesis is organized as follows. The first part consisting of two chapters, in which I introduce the DMRG method and in which I give an overview about the field of ultracold atoms in optical lattices, is followed by a second part in which I analyse three concrete problems.

Chapter 2 I give a summary of the density-matrix renormalization group methods in terms of the matrix product state (MPS) description. After introducing the MPS I explain all the necessary tools which are relevant for a successful implementation of a ground state and time-dependent DMRG method. In order to make this preamble more readable, in particular for newcomers in the field of DMRG, I visualise most of the steps using also a simple pictorial language. In particular I present the two mostly used time-evolution methods, namely the Suzuki-Trotter and the Krylov-subspace method. I also provide a detailed formulation of a recently proposed time-evolution method, the so-called folding algorithm.

In Chapter 3 I give an overview on the topic of ultracold gases in optical lattices. In the first part I derive the so-called Gross-Pitaevskii equation for a weakly interacting Bose-Einstein condensate, which allows one to investigate coherent phenomena in ultra cold bosonic gases or macroscopic coherent phenomena. Moreover, I introduce the concepts of ultracold collisions and Feshbach resonances and provide the most important experimental quantities in the so-called Thomas-Fermi limit. In the second part I present the concept of optical lattices and derive the Bose-Hubbard Hamiltonian, which is the simplest model of strong correlated systems. The third and last part describes briefly the most common measurement techniques in optical lattices. I close each of the three parts by an up-to-date overview about the recent development.

In the second part of my thesis I present my results that follow from three different projects. The first two projects have been elaborated in collaboration between the theoretical group of Ulrich Schollwöck and the ultracold atoms group of Immanuel Bloch.

In Chapter 4 I study how well magnetic models can be implemented with ultracold bosonic atoms of two different hyperfine states in an optical superlattice. The system is captured by a two-species Bose-Hubbard model, but realizes in a certain parameter regime actually the physics of a spin- $\frac{1}{2}$  Heisenberg magnet, describing the second order hopping processes. Tuning of the superlattice allows for controlling the effect of fast first order processes versus the slower second order ones. Using the density-matrix renormalization-group method, I provide the evolution of typical experimentally available observables. The validity of the description via the Heisenberg model, depending on the parameters of the Hubbard model, is studied numerically and analytically. The analysis is also motivated by recent experiments [103, 271] where coherent two-particle dynamics with ultracold bosonic atoms in isolated double wells were realized. I provide theoretical background for the next step, the observation of coherent many-particle dynamics after coupling the double wells. Contrary to the case of isolated double wells, relaxation of local observables can be observed. The tunability between the Bose-Hubbard model and the Heisenberg model in this setup could be used to study experimentally the differences in equilibration processes for nonintegrable and Bethe ansatz integrable models. The relaxation in the Heisenberg model is connected to a phase averaging effect, which is in contrast to the typical scattering driven thermalization in nonintegrable models. Finally, I discuss the preparation of magnetic groundstates by adiabatic tuning of the superlattice parameters.

In 1932 L. Landau and C. Zener [170, 297] have derived a formula for the transition probability between the two states of a quantum mechanical two-level system, where the offset between the two levels is varying linearly in time. In Chapter 5 I investigate a many-body generalization of this original Landau-Zener scenario based on a recent experiment [57]. Here, the concept of the two-level system is extended to a system of pairwise tunnel-coupled one-dimensional Bose liquids with an time-dependent offset between the tubes. It turns out that the original Landau-Zener picture can be strongly modified by increasing the intratube and the intertube interactions. A particularly striking result is the breakdown of adiabaticity observed in the inverse sweep, which means that the initially filled tube is the one with higher energy. Contrary to the two-level model it turns out that in the many-body case slower sweeps lead to a lower transfer efficiency. Using the time-dependent DMRG I can qualitatively reproduce the experimental observations for the groundstate sweep as well as for the inverse sweep scenario. Moreover, I monitor the time-evolution of important quantities, e.g. momentum distribution or energies, in order to get a complete picture behind the breakdown. Additionally, I study the time-evolution after sudden quenches of the energy offset. First of all, the quenches give a stroboscopic picture of the sweeps and reduce simultaneously the parameter space, and thus the complexity of the scenario. Second, it turns out that for sufficiently large initial density quenches can be efficiently used to create quasi-thermal states of arbitrary temperatures. The simplicity of the protocol allows for an easy experimental realization of these thermal states. After a introduction to the two-level and the three-level Landau-Zener problem I present my result for the quantum dynamics of the microscopic model and the comparison to the experimental results. I calculate the two possible Landau-Zener scenarios as well as the time-evolution after sudden quenches of the energy offset. A major finding is that for sufficiently large initial density quenches can be efficiently used to create quasi-thermal states of arbitrary temperatures.

Another application of ultracold atoms in optical lattices is the possible realization of a quantum computer a concept which has attracted much attention in recent years. These systems are a formidable starting point for such a realisation of a quantum computer as they already consist of 10000 atoms, which can all be considered to be the carrier of quantum information in form of a qubit, the quantum analogue of the classical bit. A qubit can be realized by any quantum mechanical two-level system, e.g. by a spin- $\frac{1}{2}$  particle. Therefore, I have investigated in chapter 6 the entanglement evolution of initially maximally entangled qubits, i.e. spin- $\frac{1}{2}$  particles, which do interact with a large spin- $\frac{1}{2}$  bath. The here considered initial states are, in the two qubit case, the Bell states and, in the many qubit case, the general  $W$  and  $GHZ$ -state. Due to the existence of a two qubit quantum measure, i.e. the concurrence, it is possible to fully monitor the process of entanglement decrease in that particular case. I will derive an analytical formula for the entanglement decay in the case that only one qubit interacts with an environment. In the case of a few-body system, I consider the systems of three and four qubits. Here a substantial complication arise from the fact that there is no satisfying entanglement measure for mixed states of three or more particles. However, there is not such a problem if the total system is pure and one can measure the entanglement growth between the qubits and the spin bath, a consequence of system-bath-interaction, in terms of the von Neumann entropy. It turns out that the von Neumann entropy, after a trivial normalization by the number of qubits, shows always a universal linear

growth followed by a non-universal convergence to some finite value. At this time scale, the stored quantum state does not exist anymore since it is completely merged with the environment. One can, in general, observe that the bigger the central system is the sooner the entropy saturates. Although it is too difficult to find an analytical exact relation one can definitely exclude an exponential dependence between system size and saturation time.

## Chapter 2

# Matrix Product State, DMRG, Time evolution

Strongly correlated, low-dimensional quantum systems exhibit many extraordinary effects of modern many-body physics. Indeed such one- or two-dimensional structures are not exotic but have been found and studied often in nature. More recently, the advent of highly controlled and tunable strongly interacting ultracold atoms in optical lattices has added an entirely new direction to this field [38].

Now these kind systems are, both analytically and numerically, very hard to study. Exact solutions have been found only in some particular cases, e.g. by the Bethe ansatz in one dimension. Moreover due to the strong interactions in such systems it is not possible to apply perturbation theories. Field theoretical approaches make many severe approximations and need to be additionally validated by numerical methods.

Fortunately, powerful numerical methods has been developed to study strong correlated low-dimensional systems . It was in 1992 when Steve White [283][284] has invented the density-matrix renormalization group (DMRG) method, which turned out to be one the most powerful methods for one-dimensional systems [242]. At the beginning it was only possible to study static properties (energy, order parameters,  $n$ -point correlation functions) of low-lying eigenstates, in particular the ground states. The method has been improved constantly becoming also a powerful tool to the study of dynamic properties of eigenstates, e.g. dynamical structure functions or frequency-dependent conductivities [165] [146], as well as the time-evolution of non-eigenstates under time-dependent and time-independent Hamiltonians [70] [285].

As it turns out, DMRG can be formulated as a variational method on a certain class of ansatz states [205] [242], the so-called matrix product states (MPS) [232] [93].

## 2.1 Matrix Product States

Considering a system with a finite system length  $L$ , e.g. an (anisotropic) Heisenberg antiferromagnetic spin chain with an additional magnetic field,

$$\hat{H} = \sum_{i=2}^{L-1} \frac{J}{2} (S_i^+ S_{i+1}^- + S_i^- S_{i+1}^+) + J^z S_i^z S_{i+1}^z - \sum_{i=1}^L h S_i^z. \quad (2.1)$$

For a sufficient large  $L$  it will be impossible to find an exact solution with, e.g., exact diagonalization methods. The reason for that is an exponential growth of the Hilbert space dimension with the system length. For a chain of spin- $\frac{1}{2}$  particles, with a local state dimension  $d = 2$ , the Hilbert space growth as  $d^L = 2^L$ . Now it turns out that in many situations the relevant physics can be encoded in a much smaller effective Hilbert space using a parametrization provided by matrix product states.

In order to avoid exponential state space growth I assume an upper bound  $D \ll d^L$  for the state dimension. Once state dimension grows above  $D$ , state space has to be truncated down by some procedure. Now imagine that the state is sufficiently large and one therefore has to find a  $D$ -dimensional effective basis to describe it. In a first step I divide the system of the above Hamiltonian cutting it in three parts at some site  $l$ . The state can then be written as a linear combination of the tensor product between a left block  $\{|a_{l-1}\rangle\}$  (sites  $1, \dots, l-1$ ), the local spin state  $\{|\sigma_l\rangle\}$  at site  $l$ , and a right block  $\{|a_{l+1}\rangle\}$  (sites  $l+1, \dots, L$ )

$$|\Psi\rangle = \sum_{a_{l-1}} \sum_{\sigma_l} \sum_{a_{l+1}} \langle a_{l-1} \sigma_l | a_l \rangle |a_{l-1}\rangle |\sigma_l\rangle |a_{l+1}\rangle, \quad (2.2)$$

with  $|a_l\rangle$  being the basis state for the left block together with the local spin state.

Introducing now  $d$  matrices  $A^\sigma$  of dimension  $(D \times D)$  each<sup>1</sup>, I can rewrite the above equation as

$$|\Psi\rangle = \sum_{a_{l-1}} \sum_{\sigma_l} \sum_{a_{l+1}} A_{a_{l-1} a_l}^{\sigma_l} |a_{l-1}\rangle |\sigma_l\rangle |a_{l+1}\rangle, \quad (2.3)$$

where  $A_{a_{l-1} a_l}^{\sigma_l} = \langle a_{l-1} \sigma_l | a_l \rangle$  is an arbitrary rank-3 tensor, as depicted in Fig.(2.1). The advantage of the matrix notation is that it allows for a simple recursion formula to repeat this step for the left  $|a_{l-1}\rangle$  block

$$\begin{aligned} |\Psi\rangle &= \sum_{a_{l-1}} \sum_{\sigma_l} \sum_{a_{l+1}} A_{a_{l-1} a_l}^{\sigma_l} |a_{l-1}\rangle |\sigma_l\rangle |a_{l+1}\rangle \\ &= \sum_{a_{l-1}, a_{l-2}} \sum_{\sigma_{l-1}, \sigma_l} \sum_{a_{l+1}} A_{a_{l-2}, a_{l-1}}^{\sigma_{l-1}} A_{a_{l-1}, a_l}^{\sigma_l} |a_{l-2}\rangle |\sigma_{l-1}\rangle |\sigma_l\rangle |a_{l+1}\rangle \\ &= \sum_{a_1, \dots, a_{l-1}} \sum_{\sigma_1, \dots, \sigma_l} \sum_{a_{l+1}} A_{1, a_1}^{\sigma_1} A_{a_1, a_2}^{\sigma_2} \dots A_{a_{l-1}, a_l}^{\sigma_l} |\sigma_1\rangle |\sigma_2\rangle \dots |\sigma_l\rangle |a_{l+1}\rangle. \end{aligned} \quad (2.4)$$

<sup>1</sup>for open boundary conditions the most left and right  $A^\sigma$  can be smaller



Figure 2.1: Matrix product state representation. The left figure shows the graphical representation of a single  $A^{\sigma_i}$ -tensor with an horizontal leg denoting  $\sigma_i$  the physical and two vertical legs denoting  $a_{i-1}$  and  $a_i$  the row and column index respectively. The graphical representation of the whole matrix product state can be seen on the right.

Repeating the same procedure for the, so far, unchanged right block  $|a_{l+1}\rangle$  I obtain

$$|\Psi\rangle = \sum_{a_i} \sum_{\sigma_i} A_{1,a_1}^{\sigma_1} A_{a_1,a_2}^{\sigma_2} \dots A_{a_{l-1},a_l}^{\sigma_l} A_{a_l,a_{l+1}}^{\sigma_{l+1}} \dots A_{a_{L-1},a_L}^{\sigma_L} |\sigma_1\rangle |\sigma_2\rangle \dots |\sigma_l\rangle |\sigma_{l+1}\rangle \dots |\sigma_L\rangle, \quad (2.5)$$

which in a more general way can be written as

$$|\Psi\rangle = \sum_{\sigma_1, \dots, \sigma_L} \text{Tr}(A^{\sigma_1} \dots A^{\sigma_L}) |\sigma_1\rangle \dots |\sigma_L\rangle. \quad (2.6)$$

Throughout out this chapter, only systems with open boundary conditions are considered. In this case the outer left matrices,  $A^{\sigma_1}$ , and the outer right ones,  $A^{\sigma_L}$ , have the dimension  $1 \times d$  and respectively  $d \times 1$ <sup>2</sup>. Hence the trace becomes trivial and can be omitted

$$|\Psi\rangle = \sum_{\sigma_1, \dots, \sigma_L} A^{\sigma_1} \dots A^{\sigma_L} |\sigma_1\rangle \dots |\sigma_L\rangle. \quad (2.7)$$

Up to now I have introduced the matrix product state by adding piecewise one lattice site from a right block to the left block of the system which make the matrix product state growing from left to right. There are no particular constraints on the matrices  $A^\sigma$  except that their dimensions must match appropriately. However, for certain operations, like the calculation of expectation values or the compressing of a matrix product state, to simplify, I demand that the chosen basis states for each block length are orthonormal to each other. If I assume the growth from left to right I obtain (for each left block) the condition

$$\delta_{a'_l a_l} = \langle a'_l | a_l \rangle = \sum_{a_l} \sum_{a_{l-1}} \sum_{\sigma_l} A_{a'_{l-1}, a'_l}^{\sigma_l \dagger} A_{a_{l-1}, a_l}^{\sigma_l} = \sum_{\sigma_l} (A^{\sigma_l \dagger} A^{\sigma_l})_{a'_l, a_l}. \quad (2.8)$$

The above result can be summarized in a left-normalization condition (and similarly in right-normalization condition, assuming a growth form right to left)

$$\sum_{\sigma} A^{\sigma \dagger} A^{\sigma} = I \quad \text{left-normalization} \quad (2.9)$$

$$\sum_{\sigma} A^{\sigma} A^{\sigma \dagger} = I \quad \text{right-normalization} \quad (2.10)$$

In the following part I will show how to calculate, the overlap, expectation values, correlators in the matrix product state language.

<sup>2</sup>the outer matrices have the form row and column vector

### Overlaps

As a first example of the advantage of MPS formulation I calculate the overlap between the two states  $|\psi\rangle$  and  $|\phi\rangle$ , as depicted in Fig.(2.2). In order to avoid confusion I chose  $A$  to be the tensors of  $|\psi\rangle$  and  $B$  tensors for  $|\phi\rangle$ . Taking the adjoint of  $|\phi\rangle$  the overlap reads

$$\langle\phi|\psi\rangle = \sum_{\sigma} B^{\sigma_1*} \dots B^{\sigma_L*} A^{\sigma_1} \dots A^{\sigma_L}. \quad (2.11)$$

I would like to keep the above product structure between matrices, which is less complicated than a triple sum which includes the indices  $a_i$ . Apparently, the  $B$  and the  $A$  are not in the right order. Fortunately transposing the whole product  $(B^{\sigma_1*} \dots B^{\sigma_L*})^T$  is all one has to do in order to keep a product structure of matrices, but now in an order which makes the calculation much less demanding  $(CD)^T = D^T C^T$

$$\langle\phi|\psi\rangle = \sum_{\sigma} B^{\sigma_L\dagger} \dots B^{\sigma_1\dagger} A^{\sigma_1} \dots A^{\sigma_L}. \quad (2.12)$$

If one decides to contract first over the matrix indices and then over the physical indices, he would have to sum over  $d_L$  strings of matrix multiplications. But this approach is exponentially costly. Now it turns out, that it is much easier to first sum over the physical index  $\sigma$  to obtain a matrix (so matrix multiplication can be used), which in the next step is calculated as product between three matrices. Following the second approach the overlap reads

$$\langle\phi|\psi\rangle = \left( \sum_{\sigma_L} B^{\sigma_L\dagger} \left( \dots \left( \sum_{\sigma_2} B^{\sigma_2\dagger} \left( \underbrace{\sum_{\sigma_1} B^{\sigma_1\dagger} A^{\sigma_1}}_C \right) A^{\sigma_2} \right) \dots \right) A^{\sigma_L} \right). \quad (2.13)$$

$\underbrace{\hspace{10em}}_{BCA}$

The complexity of the whole calculation does not grow anymore after the first step. Performing the operation  $BCA$  as  $(BC)A$  we carrying out  $(2L-1)d$  multiplications, which means that the complexity becomes weak polynomial instead of being exponential.

### Norm

For the calculation of the norm  $\langle\psi|\psi\rangle$  I need simply to replace the matrices  $B$  by  $A$ . Having a left-normalized state it follows from condition [2.9] that the innermost sum (at site 1) is  $C = I$ . This repeats for the following steps in the calculation

$$\begin{aligned} \langle\phi|\psi\rangle &= \left( \sum_{\sigma_L} A^{\sigma_L\dagger} \left( \dots \left( \sum_{\sigma_2} A^{\sigma_2\dagger} \left( \sum_{\sigma_1} A^{\sigma_1\dagger} A^{\sigma_1} \right) A^{\sigma_2} \right) \dots \right) A^{\sigma_L} \right) \\ &= \left( \sum_{\sigma_L} A^{\sigma_L\dagger} \left( \dots \left( \sum_{\sigma_2} A^{\sigma_2\dagger} A^{\sigma_2} \right) \dots \right) A^{\sigma_L} \right) \\ &= \left( \sum_{\sigma_L} A^{\sigma_L\dagger} \left( \dots I \dots \right) A^{\sigma_L} \right) = \dots = 1. \end{aligned} \quad (2.14)$$



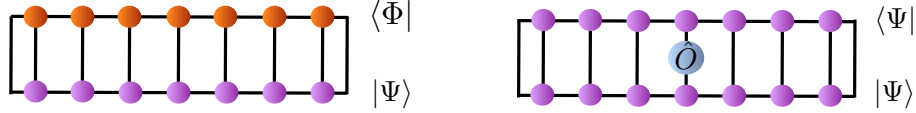


Figure 2.2: Overlap and expectation value. The left figure shows the overlap between two different state. Connecting the most left and right legs of both states is equivalent to the contraction over these indices. The right figure shows the expectation value of  $\hat{O}$ .

### Expectation Values

The general form of an expectation value is given by  $\langle \psi | \hat{O}_i \hat{O}_j \dots | \psi \rangle / \langle \psi | \psi \rangle$ . Since I have already discussed the calculation of the norm [2.14] I can directly proceed to the calculation of a general matrix element  $\langle \phi | \hat{O}_i \hat{O}_j \dots | \psi \rangle$  from which I can then easily deduce the form of the nominator. I start with the assumption having an operator  $\hat{O}$  on every site [see Fig. (2.2)]. In practice  $\hat{O}_i = \hat{I}$  on almost all sites, e.g. for local expectation values or two-site correlators. Thus, considering the operators  $O^{\sigma_1, \sigma'_1} \dots O^{\sigma_L, \sigma'_L}$  the matrix element reads (again we take  $B$  for  $|\phi\rangle$ )

$$\begin{aligned} \langle \phi | \hat{O}_1 \hat{O}_2 \dots \hat{O}_L | \psi \rangle &= \sum_{\sigma} \sum_{\sigma'} B^{\sigma_1^*} \dots B^{\sigma_L^*} O^{\sigma_1, \sigma'_1} \dots O^{\sigma_L, \sigma'_L} A^{\sigma'_1} \dots A^{\sigma'_L} \\ &= \left( \sum_{\sigma_L \sigma'_L} B^{\sigma_L \dagger} \hat{O}^{\sigma_L \sigma'_L} \dots \left( \sum_{\sigma_2 \sigma'_2} B^{\sigma_2 \dagger} \hat{O}^{\sigma_2 \sigma'_2} \left( \sum_{\sigma_1 \sigma'_1} B^{\sigma_1 \dagger} \hat{O}^{\sigma_1 \sigma'_1} A^{\sigma'_1} \right) A^{\sigma'_2} \right) \dots \right) A^{\sigma'_L}, \end{aligned} \quad (2.15)$$

where in last line I have used again the transpose of  $(B^{\sigma_1^*} \dots B^{\sigma_L^*} O^{\sigma_1, \sigma'_1} \dots O^{\sigma_L, \sigma'_L})^T$ .

### Schmidt decomposition and Entanglement

Again, I consider an arbitrary large system (not necessarily one-dimensional) described by the state  $|\Psi\rangle$ . I divide the system in two parts,  $G$  and  $H$ , and assume further that there is some interaction between subsystem  $G$  and subsystem  $H$ . Considering this interaction on a quantum mechanical level I can assume that  $G$  and  $H$  are correlated in non-classical way; one can simply say that  $G$  and  $H$  are entangled. Any pure state  $|\Psi\rangle$  on  $GH$  can be written as

$$|\Psi\rangle = \sum_{ij} \psi_{ij} |i\rangle_G |j\rangle_H, \quad (2.16)$$

where  $\{|i\rangle_G\}$  and  $\{|j\rangle_H\}$  are orthonormal basis of  $G$  and  $H$  with dimension  $N_G$  and  $N_H$  respectively and  $\psi_{ij}$  is some complex coefficient matrix. Now every pure bipartite quantum state can be also written in a more efficient way using the Schmidt decomposition [17][199]. This decomposition is based on the singular value decomposition (SVD) [69], which guarantees for an arbitrary (rectangular) matrix  $A$  of dimensions  $N_G \times N_H$  the existence of a decomposition  $A = USV^\dagger$ . Matrix  $U$  and  $V^\dagger$  can be interpreted as two unitary rotation operators<sup>3</sup>, which act locally

<sup>3</sup>the matrices  $U$  and  $V^\dagger$  are not always quadratic

on  $G$  or  $H$  respectively.  $S$  is a diagonal matrix (connecting  $G$  and  $H$ ) with coefficients  $s_\tau$ , which are called singular values or Schmidt-numbers. Since the singular values describe a normalized quantum state they are all positive and satisfy the condition  $\sum_\tau s_\tau^2 = 1$ . This corresponds to the probability condition of a proper quantum state.

Now if one interprets  $\psi_{ij}$  as a matrix which we singular value decompose, one get

$$\begin{aligned}
|\Psi\rangle &= \sum_{ij} \sum_{\tau=1}^{\min(N_G, N_H)} U_{i,\tau} s_\tau V_{j,\tau}^* |i\rangle_G |j\rangle_H \\
&= \sum_{\tau=1}^{\min(N_G, N_H)} \left( \sum_i U_{i,\tau} |i\rangle_G \right) \left( \sum_j V_{j,\tau}^* |j\rangle_H \right) \\
&= \sum_{\tau=1}^{\min(N_G, N_H)} s_\tau |a_\tau\rangle_G |a_\tau\rangle_H.
\end{aligned} \tag{2.17}$$

Due to the properties of  $U$  and  $V^\dagger$ , the sets  $\{|a_\tau\rangle_G\}$  and  $\{|a_\tau\rangle_H\}$  are orthonormal and can be extended to a full bases of  $G$  and  $H$ . These two orthonormal sets are not unique. One can still apply an additional local rotation acting on  $G$  or on  $H$  without changing the singular values. The numbers  $s_\tau$  connect physical states in  $G$  and  $H$  in a unique way. However, from the purely mathematical point of view the vectors which represent physical basis states, are simple normalized euclidian vectors which contain no further information. Thus, all information about the state  $|\Psi\rangle$  must be encoded in the singular values. This property is the starting point for the renormalization or truncation step of a given state in one-dimensional chain. In the following I restrict the sum to run only over the  $r \leq \min(N_G, N_H)$  positive and nonzero singular values,

$$|\Psi\rangle = \sum_{\tau=1}^r s_\tau |a_\tau\rangle_G |a_\tau\rangle_H. \tag{2.18}$$

The above state has two limits: for  $r = 1$  it corresponds to a product state, for  $r \geq 2$  to an entangled state and finally it corresponds to a maximally entangled state, if  $r = \min(N_G, N_H)$ , The maximal entangled state has then  $s_\tau = \sqrt{1/\min(N_G, N_H)} \quad \forall \tau$ .

One can easily read off the reduced density matrix for  $G$  and  $H$  by tracing over  $H$  and  $G$  respectively, which reveal that both reduced density matrices

$$\hat{\rho}_G = \sum_{\tau=1}^r s_\tau^2 |a_\tau\rangle_G \langle a_\tau|_G \quad \hat{\rho}_H = \sum_{\tau=1}^r s_\tau^2 |a_\tau\rangle_H \langle a_\tau|_H, \tag{2.19}$$

share the same spectrum. This allows to define an entanglement measure of a pure bipartite state, the von Neumann entropy

$$S_{G|H}(|\Psi\rangle) = -\text{Tr} \hat{\rho}_G \log_2 \hat{\rho}_G = -\sum_{\tau=1}^r s_\tau^2 \log_2 s_\tau^2. \tag{2.20}$$

For a general  $D$ -dimensional lattice (e.g. a ball of radius  $l$ ) the maximum entanglement entropy for a subsystem  $G$  in a larger environment  $H$  is

$$S^{\max}(l, D) = \log_2 d\dot{N}_G = \mathcal{O}(l^D), \quad (2.21)$$

i.e., proportional to the subsystem volume. States with a large entanglement entropy dominate in the Hilbert space [222]. Fortunately, many systems of interest often do actually not exploit the maximum number of degrees of freedom. This is reflected in the way the entanglement entropy scales with the subsystem size for the states of interest. A central result is that in ground states of gapped systems with short-range interactions, the entanglement entropy does not scale with the volume of the subsystem as in [Eq.(2.21)], but rather with the subsystem surface area as  $l^D$ , which is called the area law [28][253][48][218][91], or as  $l^D \log l$  for some cases of critical systems.

### Approximate compression of MPS

Various algorithms that can be formulated with MPS lead to substantial increase of the matrix dimensions. One needs a way to approximate a given state (output state after some calculation) with matrix dimensions  $(D'_i \times D'_{i+1})$  by another state with a smaller matrix dimension  $(D_i \times D_{i+1})$ . To this purpose two procedures are available, SVD compression and variational compression. The SVD approach is fast, but it has the disadvantage to be not optimal, since the result at a given site is not independent of the compression at other sites<sup>4</sup>. The slightly slower variational approach is optimal in the sense, that it will always lead to an energy reduction of the total wave function.

The idea behind the SVD compression is the following. Starting at one end of a state  $|\Psi\rangle$  one goes site by site through the MPS such that we can read off the Schmidt coefficients [2.18]. At each step one discards the matrix entries that are smaller than a given bound, i.e. one truncates the lowest weight contributions to the reduced density operators.

I assume that  $|\Psi\rangle$  fulfills the left-normalization condition [2.9]. Starting from the right end of the MPS one performs a singular value decomposition of the matrix  $A^{\sigma_L}$  which leads to

$$\begin{aligned} |\Psi^{(L-1)}\rangle &= \sum_{\sigma} A^{\sigma_1} \dots A^{\sigma_{L-1}} \overbrace{U S V^{\sigma_L \dagger}}^{A^{\sigma_L}} |\sigma_1\rangle \dots |\sigma_L\rangle \\ &= \left( \sum_{\sigma_1 \dots \sigma_{L-1}} A^{\sigma_1} \dots \underbrace{A^{\sigma_{L-1}} U}_{\text{new } A^{\sigma_{L-1}}} |\sigma_1\rangle \dots |\sigma_{L-1}\rangle \right) S \left( \sum_{\sigma_L} V^{\sigma_L \dagger} |\sigma_L\rangle \right). \end{aligned} \quad (2.22)$$

Since  $V^\dagger V = I$  the block  $|a_{L-1}\rangle_H = \sum_{\sigma_L} V^{\sigma_L \dagger} |\sigma_L\rangle$  is already right-normalized, i.e.  $V^{\sigma_L \dagger} \equiv A^{\sigma_L}$ . The states at the left block  $|a_{L-1}\rangle_G = \sum_{\sigma_1 \dots \sigma_{L-1}} A^{\sigma_1} \dots A^{\sigma_{L-1}} U |\sigma_1\rangle \dots |\sigma_{L-1}\rangle$  are also orthogonal as  $U$  is a unitary operation which rotates an orthogonal basis set.

<sup>4</sup>So far there is no mathematical proof for the correctness of the SVD approach.

Thus one arrives at a correct Schmidt decomposition ( $S$  is diagonal):

$$|\Psi^{L-1}\rangle = \sum_{a_{L-1}} s_{a_{L-1}} |a_{L-1}\rangle_G |a_{L-1}\rangle_H. \quad (2.23)$$

It is obvious that repeating this step at the next bond  $L-2$  one gets exactly the same form. The successive repetition of the above steps at each bond while going (without changing the direction) from one end of  $|\Psi\rangle$  to other is called sweep or sweeping procedure<sup>5</sup>. The optimal approximation is provided by keeping during the sweep from right to left the  $D$  largest singular values  $s_{a_{L-1}}, s_{a_{L-2}}, \dots, s_{a_1}$  and set the smaller ones to zero. The right matrix  $A^{\sigma_L}$  conserves in its arrangement of rows the corresponding states on the right (in  $H$ ) one would like to keep. The truncation is then equal to cutting down the right matrix  $A^{\sigma_L}$  by removing their bottom rows and rightmost columns. By repeating this procedure at every bond one obtains  $|\Psi\rangle \rightarrow |\tilde{\Psi}\rangle$  the desired state with dimension  $D$ . The second method, the variational compression, is, from the

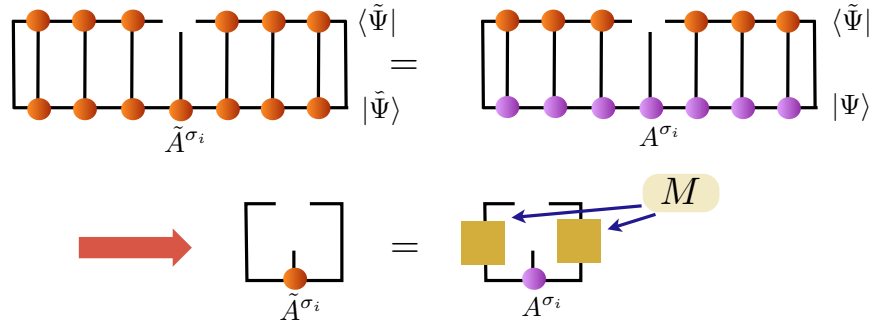


Figure 2.3: Variational compression of an MPS. The upper figure corresponds to the extremization equation Eq.(eq:varioCompression) where I have already removed  $\tilde{A}^{\sigma_i^*}$ . The lower figure corresponds to equation Eq.(2.25) which is the result after a contraction over all indices except  $i$ .

mathematical point of view, a much cleaner approach to approximate a given MPS. Here one tries to minimize  $\| |\Psi\rangle - |\tilde{\Psi}\rangle \|_2^2$ , which is equivalent to the minimization of  $\langle \Psi | \Psi \rangle - \langle \tilde{\Psi} | \Psi \rangle - \langle \Psi | \tilde{\Psi} \rangle + \langle \tilde{\Psi} | \tilde{\Psi} \rangle$  with respect to  $|\tilde{\Psi}\rangle$ . The procedure can be done iteratively as follows. One starts with an initial ansatz state  $|\tilde{\Psi}\rangle$  of the desired reduced dimension  $D'$ . This state can be the output state from the SVD compression approach, which I have explained before. Next, one tries to minimize the distance to the original MPS  $|\Psi\rangle$  to  $|\tilde{\Psi}\rangle$  by changing iteratively the  $\tilde{A}^{\sigma_i}$  matrices ( $\tilde{A}$  correspond to  $|\tilde{\Psi}\rangle$ ) site by site. The new  $\tilde{A}^{\sigma_i}$  can be found by extremizing  $\| |\Psi\rangle - |\tilde{\Psi}\rangle \|_2^2$ <sup>6</sup> with respect to  $\tilde{A}^{\sigma_i^*}$ , which only shows up in  $\langle \tilde{\Psi} | \tilde{\Psi} \rangle - \langle \tilde{\Psi} | \Psi \rangle$ :

$$\begin{aligned} \frac{\partial}{\partial \tilde{A}^{\sigma_i^*}} (\langle \tilde{\Psi} | \tilde{\Psi} \rangle - \langle \tilde{\Psi} | \Psi \rangle) = \\ \sum_{\sigma^*} (\tilde{A}^{\sigma_1^*} \dots \tilde{A}^{\sigma_{i-1}^*})_{1, a_{i-1}} (\tilde{A}^{\sigma_{i+1}^*} \dots \tilde{A}^{\sigma_L^*})_{a_i, 1} \tilde{A}^{\sigma_1} \dots \tilde{A}^{\sigma_i} \dots \tilde{A}^{\sigma_L} - \\ \sum_{\sigma^*} (\tilde{A}^{\sigma_1^*} \dots \tilde{A}^{\sigma_{i-1}^*})_{1, a_{i-1}} (\tilde{A}^{\sigma_{i+1}^*} \dots \tilde{A}^{\sigma_L^*})_{a_i, 1} A^{\sigma_1} \dots A^{\sigma_i} \dots A^{\sigma_L} = 0, \end{aligned} \quad (2.24)$$

<sup>5</sup>The DMRG ground state calculation requires several sweeps forth and back from one end to the other.

<sup>6</sup>This problem can be related to SVD, because the 2-norm of  $|\Psi\rangle$  is identical to the Frobenius norm of the coefficient matrix  $\psi_{ij}$ , with  $|\Psi\rangle = \sum_{ij} \psi_{ij} |i\rangle_G |j\rangle_H$ , i.e.  $\| |\Psi\rangle \|_2^2 = \| \psi_{ij} \|_F^2$

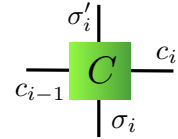
where the sum  $\sigma^*$  runs over all physical sites except  $i$ . Although the above equation looks very complicated it has a simple structure of a linear equation system. Assuming that the left and right block are left- and right-normalized, one may solve this equation (using the transpose operation) keeping the matrix  $\tilde{A}^{\sigma_i}$  explicit and obtains [see Fig.(2.3)]

$$\tilde{A}_{a'_{i-1}, a'_i}^{\sigma_i} = \sum_{a_{i-1}, a_i} M_{a'_{i-1}, a'_i, a_{i-1}, a_i} A_{a_{i-1}, a_i}^{\sigma_i}, \quad (2.25)$$

where  $M$  is the outcome after the calculation of the partial overlap in Eq.(2.24).

### Matrix product operator

The concepts of the matrix product states can be also extended to represent general operators. Any operator which acts on  $|\Psi\rangle$  can be described using so-called matrix product operators which have the big advantage that they leave the form of the MPS invariant. To see this I start with a general matrix product operator (MPO)



$$\hat{O} = \sum_{\sigma} \sum_{\sigma'} C^{\sigma_1, \sigma'_1} \dots C^{\sigma_L, \sigma'_L} |\sigma_1\rangle \langle \sigma'_1| \otimes \dots \otimes |\sigma_L\rangle \langle \sigma'_L|, \quad (2.26)$$

where  $C^{\sigma_i, \sigma'_i}$  are rank-4 tensors. The application of a matrix product operator to a matrix product state is given by

$$\begin{aligned} \hat{O}|\Psi\rangle &= \sum_{\sigma, \sigma'} \sum_{\mathbf{a}, \mathbf{c}} (C_{1, c_1}^{\sigma_1, \sigma'_1} \dots C_{c_{L-1}, c_L}^{\sigma_{L-1}, \sigma'_L}) (A_{1, a_1}^{\sigma'_1} \dots A_{a_{L-1}, a_L}^{\sigma'_L}) |\sigma_1\rangle \dots |\sigma_L\rangle \\ &= \sum_{\sigma, \sigma'} \sum_{\mathbf{a}, \mathbf{c}} (C_{1, c_1}^{\sigma_1, \sigma'_1} A_{1, a_1}^{\sigma'_1}) \dots (C_{c_{L-1}, c_L}^{\sigma_{L-1}, \sigma'_L} A_{a_{L-1}, a_L}^{\sigma'_L}) |\sigma_1\rangle \dots |\sigma_L\rangle \\ &= \sum_{\sigma} \sum_{\mathbf{a}, \mathbf{c}} D_{(1,1), (c_1, a_1)}^{\sigma_1} \dots D_{(c_{L-1}, a_{L-1}), (c_L, a_L)}^{\sigma_L} |\sigma_1\rangle \dots |\sigma_L\rangle. \end{aligned} \quad (2.27)$$

One obtains a new matrix product state at the cost of a multiplication of the matrix dimensions of  $A$  and  $C$ . The result can be summarized as  $|\Phi\rangle = \hat{O}|\Psi\rangle$  with  $|\Phi\rangle$  an MPS built from matrices  $D^{\sigma}$  according to

$$D_{(k,m), (k', m')}^{\sigma} = \sum_{\sigma'} C_{k, k'}^{\sigma, \sigma'} A_{m, m'}^{\sigma'}. \quad (2.28)$$

### Writing Hamiltonians in MPO form

In order to explain how to construct a general Hamiltonian in MPO form I start with trivial case of no interactions. I consider a Hamiltonian  $\hat{H}_{\bullet}$  which can be written as a sum of local operators acting on a single site,

$$\hat{H}_{\bullet} = \sum_{i=1}^L \hat{X}_i. \quad (2.29)$$

where each local operator is given by  $\hat{X}_i = \sum_{\sigma\sigma'} X^{\sigma_i,\sigma'_i} |\sigma_i\rangle\langle\sigma'_i|$ . It turns out that it is not very difficult to express a general Hamiltonian in MPO form, i.e. as product of matrices which act on different sites  $\hat{H} = C^{\sigma_1,\sigma'_1} C^{\sigma_2,\sigma'_2} \dots C^{\sigma_L,\sigma'_L}$ . The Hamiltonian  $\hat{H}_\bullet$  can be encoded by the following operator-valued matrices:

$$C^{\sigma_i,\sigma'_i} = \begin{pmatrix} \delta_{\sigma_i,\sigma'_i} & 0 \\ X^{\sigma_i,\sigma'_i} & \delta_{\sigma_i,\sigma'_i} \end{pmatrix}, \quad \text{for } 1 < i < L, \quad (2.30)$$

and  $C^{\sigma_1,\sigma'_1} = (X^{\sigma_1,\sigma'_1}, \delta_{\sigma_1,\sigma'_1})$  and  $C^{\sigma_L,\sigma'_L} = (\delta_{\sigma_L,\sigma'_L}, X^{\sigma_L,\sigma'_L})^T$ . Thus every Hamiltonian which can be written as sum of local operators can always be represented as a  $2 \times 2$  matrix product operator.

In the next step we consider a Hamiltonian  $\hat{H}_{\bullet\bullet}$  with next-nearest interactions<sup>7</sup>

$$\hat{H}_{\bullet\bullet} = \sum_{i=1}^{L-1} \hat{X}_i \hat{Y}_{i+1}, \quad (2.31)$$

with  $\hat{X}_i$  and  $\hat{Y}_i$  being single site operators. The matrix product operator representation of  $\hat{H}_{\bullet\bullet}$  is now given by:

$$C^{\sigma_i,\sigma'_i} = \begin{pmatrix} \delta_{\sigma_i,\sigma'_i} & 0 & 0 \\ Y^{\sigma_i,\sigma'_i} & 0 & 0 \\ 0 & X^{\sigma_i,\sigma'_i} & \delta_{\sigma_i,\sigma'_i} \end{pmatrix}, \quad \text{for } 1 < i < L, \quad (2.32)$$

and  $C^{\sigma_1,\sigma'_1} = (0, X^{\sigma_1,\sigma'_1}, \delta_{\sigma_1,\sigma'_1})$  and  $C^{\sigma_L,\sigma'_L} = (\delta_{\sigma_L,\sigma'_L}, Y^{\sigma_L,\sigma'_L}, 0)^T$ . This scheme can be generalized to arbitrary Hamiltonians and finite-size operators [215]. For commonly used one-dimensional Hamiltonians the resulting matrix dimensions are small, for instance  $5 \times 5$  for a Heisenberg model in a transverse field [2.1] or  $6 \times 6$  for a fermionic Hubbard model.

Together with the above tools I am ready to make the connection from the matrix product states and operators to the density matrix renormalization method (DMRG) and the time-dependent DMRG methods, which are the main methods of my thesis.

## 2.2 DMRG

Originally, DMRG has been considered as a renormalization group method. The method consists of a systematic truncation of the system Hilbert space. Sweeping site by site, we keep only a small number of important states while minimizing the total energy. The states that are kept in order to construct a renormalization group transformation are the most probable eigenstates of a reduced density matrix and not simply the lowest energy states as in a standard numerical renormalization group (NRG) calculation. Now, DMRG can also be formulated with the help of matrix product states. From this point of view, DMRG can be seen as an algorithm which optimizes variationally some wavefunction with has the structure of a MPS. This formulation of

<sup>7</sup>This example already covers a huge number of models studied in modern literature

DMRG has revealed the deep connection between the density-matrix renormalization approach and quantum information theory and has led to significant extensions of DMRG algorithms, e.g. efficient algorithms for simulating the time-evolution.

There exist two slightly different possibilities to implement the DMRG. The starting point for first approach is a state living on a block-site-site-block configuration  $G \bullet \bullet H$ . This is called two-site DMRG. Alternatively one can consider a block-site-block configuration  $G \bullet H$  (the same as in the introduction of MPS) which is there called one-site DMRG. It turns out that the old formulation of the finite-size one-site DMRG is equal to the groundstate calculation with MPS. In the following we will explain the one-site DMRG.

### Groundstate calculation

The first application area for the DMRG method was to calculate the optimal approximation of the ground state, which means to minimize

$$\frac{\langle \Psi | \hat{H} | \Psi \rangle}{\langle \Psi | \Psi \rangle} \quad (2.33)$$

The idea of the DMRG is very similar to the compression methods in MPS. We start with an ansatz state  $|\Psi\rangle$  and perform in a variational way a local optimization of each  $A^{\sigma_l}$  keeping the matrices on all other sites constant. This naturally introduces several sweepings through the whole state, e.g. going site by site from right to left and then back to the right. This sweep procedure is repeated several times until the state is sufficiently converged.

By keeping at each site the matrices on all other sites constant the variables appear in a quadratic form, for which the determination of the extremum is a linear algebra problem. The minimization of Eq.(2.33) under the constraint of keeping the norm can be reformulated as

$$\frac{\partial}{\partial A^{\sigma_l^*}} (\langle \Psi | \hat{H} | \Psi \rangle - \lambda \langle \Psi | \Psi \rangle) = 0, \quad (2.34)$$

where  $\lambda$  is the Langrangian multiplier of the constraint.

I start with the calculation of the overlap keeping  $A^{\sigma_l}$  explicit. Moreover, I assume that the left block  $|a_{l-1}\rangle_G$  and the right block  $|a_l\rangle_H$  are already left- and right-normalized respectively. According to the result for the calculation of overlap (again using the transpose trick) one finds

$$\begin{aligned} \langle \Psi | \Psi \rangle = & \sum_{\sigma_l} \sum_{\sigma_1, \dots, \sigma_{l-1}} \sum_{\sigma_{l+1}, \dots, \sigma_L} (A^{\sigma_{l-1}^\dagger} \dots A^{\sigma_1^\dagger} A^{\sigma_1} \dots A^{\sigma_{l-1}})_{a'_{l-1}, a_{l-1}} A^{\sigma_l}_{a_{l-1}, a_l} A^{\sigma_l^*}_{a'_{l-1}, a'_l} \times \\ & \times (A^{\sigma_{l+1}} \dots A^{\sigma_L} A^{\sigma_L^\dagger} \dots A^{\sigma_{l+1}^\dagger})_{a_l, a'_{l+1}}, \end{aligned} \quad (2.35)$$

which after applying the normalization condition immediately gives

$$\langle \Psi | \Psi \rangle = \sum_{\sigma_l} \sum_{a_{l-1}, a_l} \delta_{a'_{l-1}, a_{l-1}} A^{\sigma_l}_{a_{l-1}, a_l} A^{\sigma_l^*}_{a'_{l-1}, a'_l} \delta_{a_l, a'_l}. \quad (2.36)$$

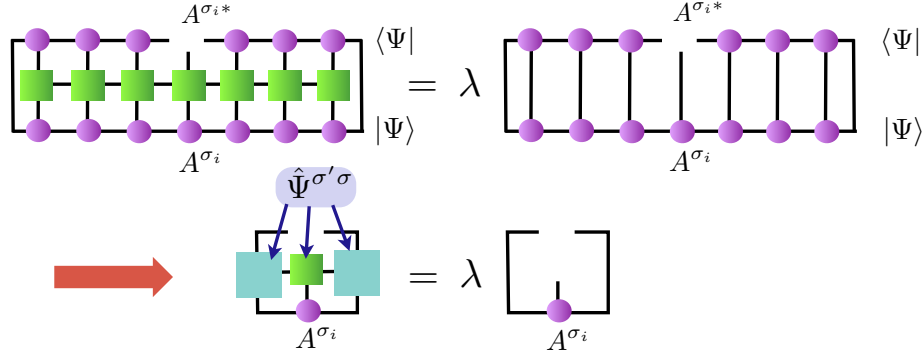


Figure 2.4: One-site DMRG in MPS representation. The upper figure is equivalent to the extremization equation Eq.(2.34). After the contraction over all bond but  $i$  the extremization reduces to equation Eq.(2.39), depicted in the lower figure

In the next step I consider the expectation value  $\langle \Psi | \hat{H} | \Psi \rangle$ , with  $\hat{H}$  in the MPO representation

$$\langle \Psi | \hat{H} | \Psi \rangle = \sum_{\sigma'_i} \sum_{\sigma'_i} \sum_{a'_{l-1}, a'_l} \sum_{a_{l-1}, a_l} \hat{\Psi}_{a'_{l-1} a'_l a_{l-1} a_l}^{\sigma'_i \sigma_i} A_{a'_{l-1}, a'_l}^{\sigma_i*} A_{a_{l-1}, a_l}^{\sigma_i}, \quad (2.37)$$

where  $\hat{\Psi}^{\sigma'_i \sigma_i}$  written in the left-right block representation ( $C$  are the MPO matrices) reads

$$\hat{\Psi}_{a'_{l-1} a'_l a_{l-1} a_l}^{\sigma'_i \sigma_i} = \sum_{k_{l-1} k_l} \hat{\Psi}_{a'_{l-1}, k_{l-1}, a_{l-1}}^G C_{k_{l-1} k_l}^{\sigma'_i \sigma_i} \hat{\Psi}_{a'_l, k_l, a_l}^H. \quad (2.38)$$

The block contributions have a slightly more complicated structure than the normal block structure, e.g. the left block looks similar to  $(A^{\sigma'_{l-1} \dagger} \dots A^{\sigma_{l-1}})(B^{\sigma'_1 \sigma'_1} \dots B^{\sigma'_{l-1} \sigma'_{l-1}})$ . Now if one takes the extremum of the above equation with respect to  $A_{a'_{l-1} a'_l}^{\sigma_i*}$  one obtains after the contraction over all indices but  $i$  [see. Fig.(2.4)]:

$$\sum_{\sigma'_i} \sum_{a_{l-1} a_l} \hat{\Psi}_{a'_{l-1} a'_l a_{l-1} a_l}^{\sigma'_i \sigma_i} A_{a_{l-1} a_l}^{\sigma_i} - \lambda A_{a'_{l-1} a'_l}^{\sigma_i} = 0. \quad (2.39)$$

By introducing the matrix  $H_{\sigma'_i a'_{l-1} a'_l, \sigma_l a_{l-1} a_l} = \hat{\Psi}_{a'_{l-1} a'_l a_{l-1} a_l}^{\sigma'_i \sigma_i}$  and the vector  $v_{\sigma_l a_{l-1} a_l} = A_{a_{l-1} a_l}^{\sigma_l}$ , one arrives at a simple eigenvalue equation

$$Hv - \lambda v = 0. \quad (2.40)$$

In the next step one must solve the above equation. The lowest eigenvalue  $\lambda_0$ , which is current estimate of the ground state, corresponds to the vector  $v_{\sigma_l a_{l-1} a_l}^0$  which is reshaped back to a new  $A_{a_{l-1}, a_l}^{\sigma_l}$ .

Although one could reduce the whole minimization problem to the optimization of a single  $A^{\sigma_l}$  it is in general too demanding to solve the above eigenvalue equation directly. But since one is only interested to find the lowest eigenvalue and eigenstate, it is sufficient to use an iterative



eigensolver, like Lanczos algorithm [169][235][69], which allows for the calculation of the ends of the spectrum. The speed of Lanczos depends very much on the initial starting vector. It turns out that  $A^{\sigma_l} = v$  is already a good guess vector as it is a reasonable approximation of the right solution.

The total algorithm then runs as follows. Starting from some initial guess for  $|\Psi\rangle$ , one sweeps from right and left through the lattice, always improving on one site  $i$ , with the energy going down all the time. Convergence is achieved if energy converges. But the best test, to see whether an eigenstate has been reached, is to consider  $\langle \Psi | \hat{H}^2 | \Psi \rangle - (\langle \Psi | \hat{H} | \Psi \rangle)^2$ .

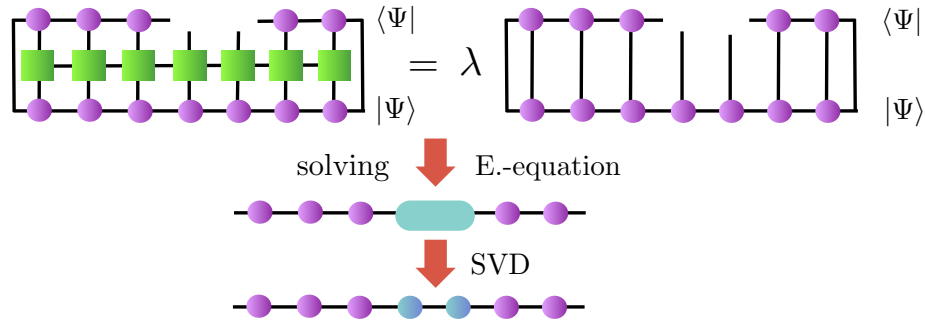


Figure 2.5: Two-site DMRG scheme. In the two-site DMRG one optimizes two bonds at once. This leads to a new object which is not of MPS form. Therefore, the extremization must always be followed by a SVD which produces two new bond operators and thus a proper MPS.

In the two-site DMRG the same optimization takes place on two sites instead of only one site. First one makes a contraction between the two central site matrices  $\sum_{a_l} A_{a_{l-1}, a_l}^{\sigma_l} A_{a_l, a_{l+1}}^{\sigma_{l+1}} = \tilde{A}_{a_{l-1}, a_{l+1}}^{\sigma_l \sigma_{l+1}}$  and obtains a bigger matrix. Next, one optimizes this new central matrix as it was explained for the one-site DMRG. Finally, after the calculation of the lowest  $\lambda$  one has to bring the big matrix back to the initial form of two  $A^{\sigma_l} A^{\sigma_{l+1}}$  matrices by performing a SVD [see Fig.(2.5)]. Now there is small difference between the one-site and two-site approach. While for the one-site DMRG the dimension of the local matrix  $A^{\sigma_l}$  does not increase, it does for the two-site DMRG (dimension becomes  $D \rightarrow dD$ ). Therefore, in order to keep the maximal dimension  $D$  one has to truncate the states, which can be done automatically in the last SVD step before saving the new matrices  $A^{\sigma_l} A^{\sigma_{l+1}}$ .

The ansatz for the ground state calculation for the one-site DMRG is totally variational. Hence, we always reduce the total energy at each step. For the two-site (and more-site) DMRG the same happens until the last step where one has to perform a SVD together with the truncation. By cutting away the local Hilbert space one cannot guarantee that the energy is lowered at each step.

On the other hand one-site DMRG contains also a disadvantage. At each step one takes only into account a local potential. This becomes a problem when treating systems with strong disorder from site to site. This increase the chance that the one-site DMRG can be trapped in some metastable state. Here one has to use the two-site DMRG or modify the one-site DMRG, e.g. by adding a small perturbation term to the local density matrix of the left and right block [284].

## Symmetries

In the previous section I have shown that the ground state calculation can be reduced to the optimization of a single  $A^\sigma$ , which is equal to solving an eigenvalue equation. Independently of the strategy to find a solution for this eigenvalue equation one can profit from symmetries in the system, which reduce the complexity of the eigenvalue problem [see Fig.(2.6)]. In order to accelerate the computation, one can make use of operators that commute with the Hamiltonian. These can be, first of all, the total number of particles  $N$  or the the total spin  $S_{\text{tot}}^z$ , respectively the generators of the  $U(1)$  algebras. Here, by doing a simple bookkeeping for each local site one can decide which  $A$ -matrices must be kept or not. A further reduction of computational cost can be obtained including (wherever it is suitable) non-Abelian symmetries [191][34]. According to the Wigner-Eckart theorem [286] certain laws of conservation correspond to symmetry transformation groups of space. A set of  $2k + 1$  operators  $\{T_q^{(k)} : (-k \leq q \leq k)\}$  which transform under the action under the action of rotation like

$$R(\alpha, \beta, \gamma) T_q^{(k)} R(\alpha, \beta, \gamma)^{-1} = \sum_{q'} D_{q,q'}^k(\alpha, \beta, \gamma) T_{q'}^{(k)}, \quad (2.41)$$

are said to form an irreducible tensor of degree  $k$ . For example a scalar operator  $N$ , which is by definition invariant under rotations,  $R(\alpha, \beta, \gamma) S R(\alpha, \beta, \gamma)^{-1} = S$ , is an irreducible tensor of degree  $k = 0$ . A vector operator  $\hat{V}$  is an irreducible tensor of degree  $k = 1$ , and so on. Knowing the basis vectors of the rotation  $R(\alpha, \beta, \gamma)$  the Wigner-Eckart theorem states that the matrix element  $T^{(k)}_q$  may be written in the form

$$\langle j', m' | T_q^{(k)} | j, m \rangle = (j, k, m, q | j' m') \langle j' || T^{(k)} || j \rangle, \quad (2.42)$$

which is a product between the Clebsch-Gordan coefficient  $(j, k, m, q | j' m')$  and the irreducible matrix element  $\langle j' || T^{(k)} || j \rangle$ , which is independent of  $m, m', q$ . Now, additional to a similar book-

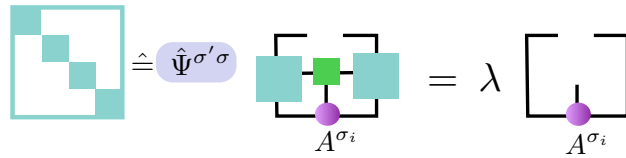


Figure 2.6: Symmetries in DMRG. By using symmetries one can bring  $\Psi^{\sigma'\sigma}$  from the DMRG equation Eq.(2.39) into a block-diagonal form which reduces the diagonalization problem of a huge matrix to a the diagonalization of much smaller matrices.

keeping as for abelian symmetries one writes down the state using a suitable basis (non-abelian) which corresponds to the conserved quantity. Then, in order to evaluate a physical quantity one has to transform back from this non-abelian basis to an abelian one which can be obtained using the above Wigner-Eckart theorem[191].

## 2.3 Time dependent DMRG methods

The DMRG is an excellent method for calculating ground states and also selected eigenstates. We have discussed physical properties which are true equilibrium quantities. However, together with the development in nanoelectronics, ultra cold atoms and many other field of research, problems considering non-equilibrium physical systems became very important during the last two decades. Time-dependent DMRG has been used extensively in the meantime and found to open completely new perspectives on the non-equilibrium behaviour of strongly correlated one-dimensional systems [114] [162] [269] [66].

All time-evolution methods for the DMRG follow one of two strategies. The so-called static Hilbert-space DMRG methods try to enlarge optimally the truncated Hilbert space of  $|\Psi(t=0)\rangle$  such that it is big enough to describe  $|\Psi(t)\rangle$  to a very good approximation [54]. On the other hand, so-called adaptive DMRG tries to change the truncated Hilbert space of  $|\Psi(t)\rangle$  during the time-evolution without increasing the dimension. The methods presented in the following belong to the class of the adaptive ones.

The first implementation of time-dependent DMRG using adaptive Hilbert spaces [285] [70] based on a classical simulation of the time evolution of weakly entangled states, knowing as time-evolving block-decimation (TEBD) algorithm [275]. Both implementations use for the time evolution the so-called Suzuki-Trotter decomposition [107] assuming only nearest neighbor interactions, which is the starting point of the following discussion.

### 2.3.1 Trotter Algorithm

I assume a time-independent Hamiltonian  $\hat{H}$  which only nearest-neighbor interactions<sup>8</sup>

$$\hat{H} = \sum_i \hat{H}_i, \quad (2.43)$$

where  $\hat{H}_i$  is a bond Hamiltonian which connects the sites  $i$  and  $i+1$ , joined by bond  $i$ . One can decompose this Hamiltonian into two parts

$$\hat{H} = \hat{H}_{\text{odd}} + \hat{H}_{\text{even}}, \quad (2.44)$$

with  $\hat{H}_{\text{odd}} = \hat{H}_1 + \hat{H}_3 + \dots$  the Hamiltonian acting on the odd bonds and  $\hat{H}_{\text{even}} = \hat{H}_2 + \hat{H}_4 + \dots$  acting on the even bonds. While all terms in odd and even part commute,  $[\hat{H}_{\text{odd}}, \hat{H}_{\text{even}}] \neq 0$ . The idea is now to apply a sequence of the odd and even Hamiltonian and to factorize the whole time evolution into operators which act only on two bonds. Therefore, dividing the time argument of the time-evolution into infinitesimal time steps  $\Delta t$  leads to

$$e^{-i\hat{H}t} = e^{-i\hat{H}\Delta t} e^{-i\hat{H}\Delta t} e^{-i\hat{H}\Delta t} e^{-i\hat{H}\Delta t} \dots \quad (2.45)$$

Up to here there was no approximation made. Next, one applies the Suzuki-Trotter decomposition which represents a general way of writing a matrix exponential. The exponential of

<sup>8</sup> $\hat{H}$  denotes the full Hamiltonian under which the system will evolve.

two non-commuting operators  $A$  and  $B$  reads in first order  $e^{\delta(A+B)} = \lim_{\delta \rightarrow 0} (e^{\delta A} e^{\delta B} + \mathcal{O}(\delta^2))$ <sup>9</sup>. Thus, replacing  $A$  and  $B$  by the odd and the even part of  $\hat{H}$  and  $\delta$  by  $\Delta t$  (and skipping this part) one arrives at

$$e^{-i\hat{H}t} = e^{-i\hat{H}_{\text{odd}}\Delta t} e^{-i\hat{H}_{\text{even}}\Delta t} e^{-i\hat{H}_{\text{odd}}\Delta t} e^{-i\hat{H}_{\text{even}}\Delta t} \dots \quad (2.46)$$

where one makes an error proportional to  $\Delta t^2$ . According to the above equation the time evolution can be performed as follows [see Fig.(2.7)]. Starting from the left border of the system we apply the odd bond Hamiltonians  $\hat{H}_1, \hat{H}_3, \dots$  sweeping until the right end<sup>10</sup>. Then one performs the reverse sweep from right to left but now with the even bond Hamiltonians  $\hat{H}_2, \hat{H}_4, \dots$ . Finally, before moving to the next time step, one needs to truncate the new MPS to the desired dimension. This steps are repeated until one reaches the total time  $t$ . It is also possible to construct a higher

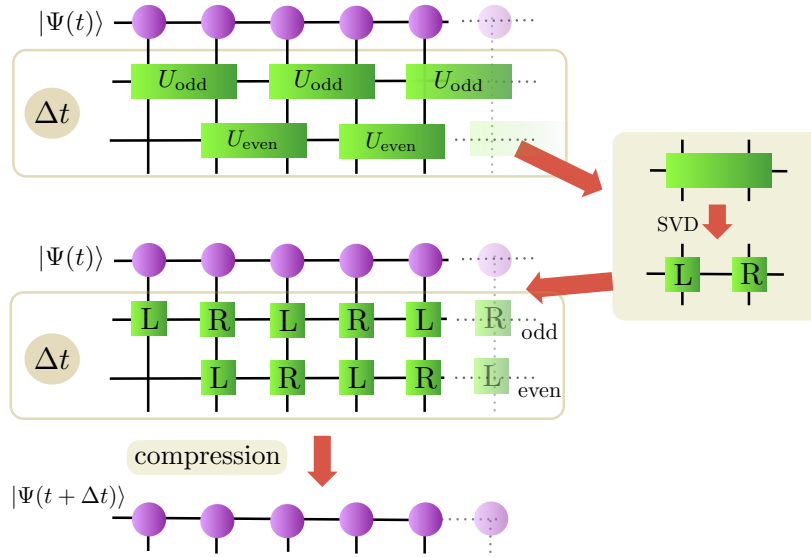


Figure 2.7: The Suzuki-Trotter algorithm in first order. This is the graphical representation of a single calculation step [Eq.(2.46)] during the whole time evolution of  $|\Psi\rangle$ . The upper figure shows the action a two-bond operation of the form  $e^{i\hat{H}\Delta t}$  on a MPS. In order to keep the structure of an MPS and MPO unchanged one can first decompose each two-bond operation into two single bond operations  $L$  and  $R$ , by using a SVD. This creates a valid MPO according to our definition Eq.(2.26), which can then be applied to the MPS by means of Eq.(2.27). After each single time step one has to perform an additional compression of the whole state. This last step which makes the method adaptive, which means that the optimal basis of  $|\Psi(t)\rangle$  is also evolving in time.

order Suzuki-Trotter time evolution at the cost of more than two sweeps. For example the second order Suzuki-Trotter decomposition reads

$$e^{-i\hat{H}t} = e^{-i\hat{H}_{\text{odd}}\Delta t/2} e^{-i\hat{H}_{\text{even}}\Delta t} e^{-i\hat{H}_{\text{odd}}\Delta t/2}, \quad (2.47)$$

<sup>9</sup>For the here considered Hamiltonian  $[A[A, B]] = 0$  and  $[B[B, A]] = 0$  holds and thus one can use the simple version of the Baker-Hausdorff formula  $e^A e^B = e^{A+B} e^{[A, B]/2}$ .

<sup>10</sup>Alternatively to apply a two-site operation followed by a SVD of the 2-block tensors, one can, in order to handle with a proper MPO, first do a SVD of the two-site Hamiltonians before applying them on the  $|\Psi\rangle$ . Doing so one does not need to implement new types of MPOs.

where the error per timestep is only  $\mathcal{O}(\Delta t^3)$ . After each timestep the dimension of the state will be increased. In order to keep a considerably number of states one has to perform a compression of the MPS at the end of each timestep. This compression leads automatically to a new optimal basis, which makes the this time-evolution an adaptive one. The Suzuki-Trotter error together with the error from the truncation are the two sources of error in this algorithm. But while one can reduce the Suzuki-Trotter error by making the time step  $\Delta t$  smaller, the error from the truncation remains.

### 2.3.2 Krylov Algorithm

The following time evolution method, the so-called Krylov time evolution, has become one of the most powerful method for time dependent calculations. In contrast to the Suzuki-Trotter method it bases on a Krylov subspace expansion of the time evolution operator [69], which I will explain in the following. The usual way to calculate the time evolution of the state  $|\Psi\rangle$ , thus

$$|\Psi(t)\rangle = e^{-i\hat{H}t}|\Psi(0)\rangle, \quad (2.48)$$

would be to decompose  $|\Psi(0)\rangle$  in the eigenbasis of  $\hat{H}$ , which then shifts the time evolution from the state to some precoefficients<sup>11</sup>,

$$|\Psi(t)\rangle = \sum_{n=0}^{N-1} a_n e^{-i\lambda_n t} |e_n\rangle, \quad \text{with} \quad |\Psi(0)\rangle = \sum_{n=0}^{N-1} a_n |e_n\rangle, \quad (2.49)$$

where  $\{|e_n\rangle\}$  form the orthonormal eigenbasis of  $\hat{H}$  and  $\dim(\hat{H}) = N$ . Since the Hilbert space of  $\hat{H}$  is usually very large we have to truncate  $\hat{H}$  to some  $\hat{H}_{\text{eff}}$ . It turns out that for a sufficiently small time step  $\hat{H}_{\text{eff}}$  can be very small. Again the first step is to divide the time argument of the time-evolution into infinitesimal time steps  $\Delta t$ . Assuming that one knows a way to build an effective basis, which consists of  $K$  elements, he can rewrite the time-evolution and get

$$\begin{aligned} |\Psi(\Delta t)\rangle &= \mathbf{I}_{\text{eff}} e^{-i\hat{H}\Delta t} |\Psi(0)\rangle \\ &= \sum_{j=0}^{K-1} |k_j\rangle \langle k_j| e^{-i\hat{H}_{\text{eff}}\Delta t} |\Psi(0)\rangle = \sum_{j=0}^{K-1} \langle k_j| e^{-i\hat{H}_{\text{eff}}\Delta t} |\Psi(0)\rangle |k_j\rangle. \end{aligned} \quad (2.50)$$

The above optimistic estimate using  $K$  vectors of with maximal dimension  $D$  is only possible if indeed the  $|k_j\rangle$  are linearly independent [107]. A good guess for such a basis is the Krylov subspace which is spanned by images of  $|\Psi\rangle$  under the first  $K$  powers of  $\hat{H}$ . The Krylov subspace corresponds to the expansion of  $e^{\hat{H}}$  starting from  $\hat{H}^0 = I$ :

$$\mathcal{K}_K(\hat{H}, |\Psi\rangle) = \text{span}\{|\Psi\rangle, \hat{H}^1|\Psi\rangle, \hat{H}^2|\Psi\rangle, \dots, \hat{H}^{(K-1)}|\Psi\rangle\}. \quad (2.51)$$

Unfortunately the vectors tend very quickly to become almost linearly dependent. Hence, methods relying on Krylov subspace involve additionally some orthogonalization scheme, such as the

<sup>11</sup>Again,  $\hat{H}$  denotes the full Hamiltonian

Lanczos iteration [169][69] or the Gram-Schmidt orthogonalization [69]. While Gram-Schmidt takes therefore into account all basis state, the Lanczos algorithm connects at each step a vector with the two previously orthogonalized vectors. The starting point for the iterative orthogonalization of the Krylov subspace is the zeroth Krylov vector  $|k_0\rangle = |\Psi(0)\rangle$ . The next higher Krylov vectors are obtained according the Lanczos iteration scheme

$$\beta_{i+1}|k_{i+1}\rangle = \hat{H}|k_i\rangle - \alpha_i|k_i\rangle - \beta_i|k_{i-1}\rangle, \quad (2.52)$$

where  $\alpha_i$  and  $\beta_i$  are chosen such that the orthonormality condition  $\langle k_i|k_j\rangle = \delta_{ij}$  is fulfilled. Together with the new orthonormal basis set  $\mathcal{K}_N(\hat{H}, |\Psi\rangle) = \text{span}\{|k_0\rangle, |k_1\rangle, |k_2\rangle, \dots\}$  the approximated time-evolution reads

$$|\Psi(\Delta t)\rangle = \sum_{j=0}^{K-1} |k_j\rangle \langle k_j| e^{-i\hat{H}_{\text{eff}}^{\text{Krylov}} \Delta t} |k_0\rangle |k_j\rangle = \sum_{j=0}^{K-1} c_j(\Delta t) |k_j\rangle, \quad (2.53)$$

with  $(\hat{H}_{\text{eff}}^{\text{Krylov}})_{m,n} = \langle k_m|\hat{H}|k_n\rangle$ . Since a product between a MPO and a MPS leads to increase of the dimension of the new state one still has to perform a compression of the final state at each time step. The coefficient  $c_j(\Delta t)$  is used for the effective convergence criterion. Once it drops below a certain value the procedure is stopped. As in the case of the Suzuki-Trotter algorithm the effective Hilbert space is moving during the time evolution adapting the right Hilbert space. The Krylov method can be adapted easily to matrix product states in combination with matrix product operators [cp. Fig.(2.8)]. Each Krylov vector can be stored separately and we can exploit the full local Hilbert space to represent each vector.

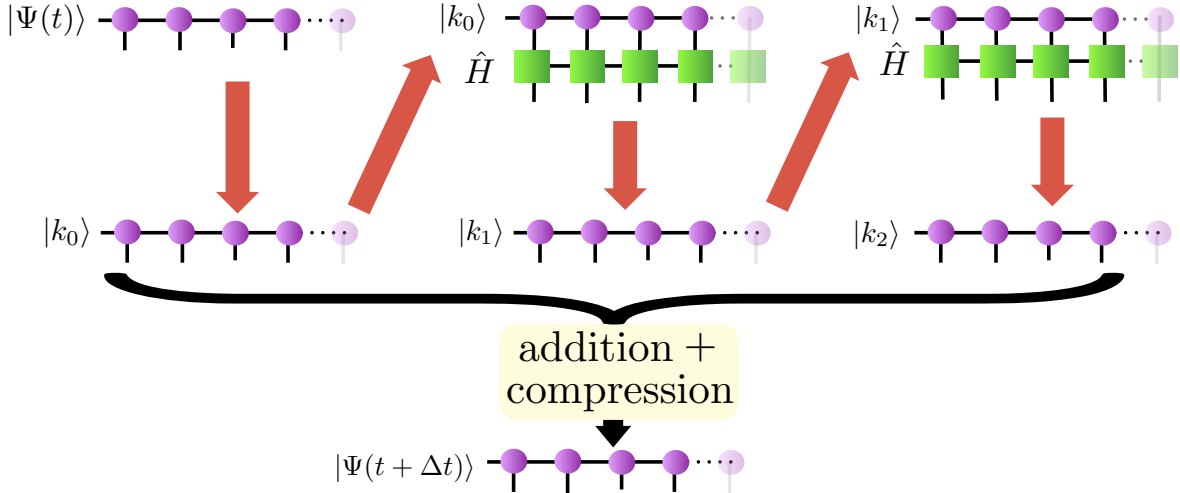


Figure 2.8: Krylov time evolution scheme. Starting from  $|\Psi\rangle$  one calculates an orthogonal Krylov subspace by successive application of  $\hat{H}$  on  $|\Psi\rangle = |k_0\rangle$  followed by an orthogonalization procedure like Lanczos or Gram-Schmidt. Together with the new subspace one can calculate the outgoing state according to Eq.(2.53) which is followed by a compression of the outgoing state. Indeed, it is this last step which makes the method adaptive.

The matrix dimensions for each Krylov vector will become large, especially for higher Krylov vectors. Thus a truncation of the states is needed, limiting the accuracy of the calculated vectors. Another error is induced by limiting the Hamiltonian  $\hat{H}$  to the Krylov subspace

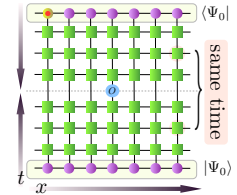
$\hat{H}_{\text{eff}} = \mathbb{I}_{\text{eff}} \hat{H} \mathbb{I}_{\text{eff}}$ . It turns out that for sufficient small time steps  $\Delta t$  the coefficients of the higher Krylov vectors are exponentially suppressed. The error considering a finite number of Krylov vector is roughly proportional to  $c_{K-1}$  the coefficient of  $|k_{K-1}\rangle$  the last Krylov vector. Together with the error induced by the finite dimension of the Krylov subspace, one gets a bound for the total error of the resulting wave function given by

$$\| |\Psi_{j+1}\rangle - e^{-i\hat{H}\Delta t} |\Psi_j\rangle \|^2 < \varepsilon^2, \quad (2.54)$$

with a fixed error bound  $\varepsilon$  for each timestep [136]. The number of Krylov vectors are iteratively increased, while the truncation error of each Krylov vector is adapted such that the error bound [2.54] is fulfilled. It turns out that typically 3-10 Krylov vectors are sufficient for a successful calculation of the time evolution. For bosonic systems the error bound was in between  $10^{-5}$  –  $10^{-4}$ , while for spin systems an error of  $10^{-6}$  was sufficient to maintain convergence.

### 2.3.3 Folding Algorithm

The following procedure, which is called the tensor folding algorithm [19], is based on the normal time-evolution methods, e.g. the Suzuki-Trotter time-evolution. The normal time evolution consists of applying an unitary operation  $e^{-\hat{H}\Delta t}$  on a MPS  $|\Psi(t_0)\rangle$  which gives another MPS  $|\Psi(t_0 + \Delta t)\rangle$  which becomes the new input state in the next step. Now, the here presented method benefits again from matrix product representation of the state and all operators. Drawing the time evolution of some observable leads to a two dimensional rectangular tensor network (right figure). From this perspective it turns out that the calculation of the observable in the time-direction can be performed as well in the spatial direction. This approach is called the transverse contraction and leads to new transverse MPSs and MPOs<sup>12</sup>. Starting from the transverse contraction scheme one can see that two tensors that lie at the same distance from the middle bond correspond to two MPOs from the same time step (bracket in right picture), coming from a certain term and its adjoint in the Trotter decomposition<sup>13</sup>. Originally strongly correlated in time these two tensors become after the rotation two strongly correlated sites. This fact allows one to find a more efficient representation of the entanglement in the transverse MPSs. As I will show below one can group such pairs together in a new MPSs and MPOs by folding the original transverse MPSs and MPOs.



#### Transverse contraction

The basic idea is to look at the quantity that one wants to compute, say the time dependent expectation value of some local operator,  $\langle \Psi(t) | \hat{O} | \Psi(t) \rangle$ , as the contraction of a two dimensional tensor network, and perform it, not along time, but in the direction of space.

The tensor network should be regarded as a theoretical construction, which allows for the study of other evaluation concepts. In the usual time evolution scheme one starts with the initial

<sup>12</sup>The physical aspects of the transverse MPSs and MPOs can probably not be understood very easily.

<sup>13</sup>It could be also any other time-evolution method which can be written as tensor network.

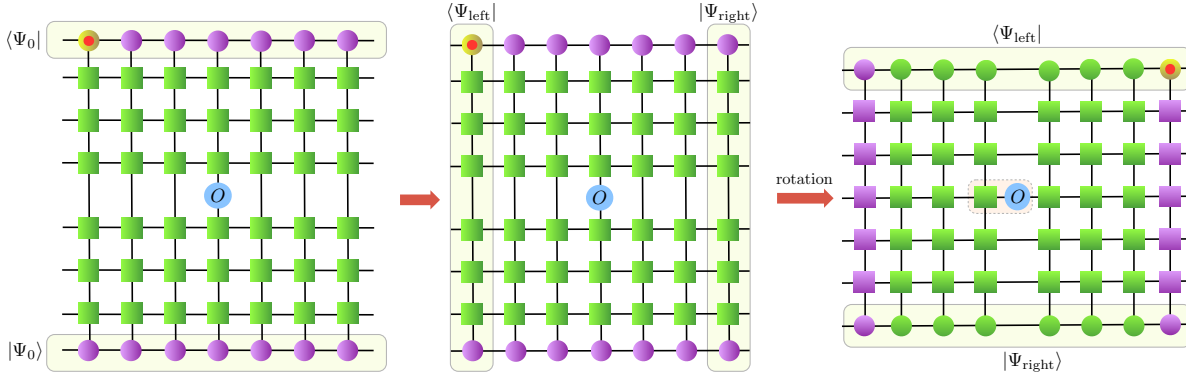


Figure 2.9: Tensor rotation and transverse contraction. The usual tensor network (left figure) consists of two MPSs at the top and the bottom and an equal number of MPOs for both states which represent the time evolution of the state and its complex conjugate. The transverse contraction scheme is equivalent to a rotation of the whole network by 90 degrees. This leads to new MPS at top and bottom and new MPOs which are the starting point of a contraction in the space-direction.

finite size MPS and applies, for every times evolution step, the proper MPOs representing  $e^{i\hat{H}\Delta t}$ . Repeating this for the required number of evolution steps, one arrives at the exact evolved MPS (within the Trotter approximation), as no truncation is carried out. Finally, one adds the local operator  $\hat{O}$  and contract with the Hermitian conjugate of the evolved state [cp. Fig.(2.9)].

The idea of the transverse contraction is to rotate first the tensor network 90 degrees (clock or anti-clockwise), as depicted in Fig.(2.9). This rotation comes along with a total change of indices and thus of the role of the matrix product tensors. The spatial indices (or bond indices) become the new indices of the local dimension and vice-versa. After the rotation one obtains two new states  $\langle\Psi_{\text{left}}|$  and  $|\Psi_{\text{right}}\rangle$  and a two new sets of MPOs, for each new state one. What follows is the usual time evolution scheme in which one applies successively these new *left* and *right* MPOs to  $\langle\Psi_{\text{left}}|$  and  $|\Psi_{\text{right}}\rangle$  respectively.

### Folding algorithm

It turns out that there is a more efficient way to construct a tensor network. The previous rotation of the tensor network is equivalent to changing the time direction into the spacial direction and vice versa. Thus, two initially time-correlated tensors correspond now to two spatially correlated sites [see. Fig.(2.10)]. Under the assumption that the Hamiltonian of original time-evolution contains only homogenous couplings, e.g. an isotropic Heisenberg model, one can even deduce that this particular symmetry also holds for later times (in the rotated picture). By folding the network in the middle of the system one brings strong entangled regions of the network close to each other (ideally on top of each other), as depicted in Fig.(2.10). This concept allows a more efficient representation of the time-evolution, which become noticeable in the benefit of simulation time.

The calculation of the two folded MPS states goes as follow. Setting out from a general MPS



(not necessarily after the transverse operation)

$$|\Psi\rangle = \sum_{\sigma} \sum_{a_1, \dots} A_{1,a_1}^{\sigma_1} A_{a_1,a_2}^{\sigma_2} \dots A_{a_{L-1},1}^{\sigma_L} |\sigma_1 \dots \sigma_L\rangle, \quad (2.55)$$

we obtain the folded MPS

$$\begin{aligned} |\Psi_{\text{fold}}\rangle &= \sum_{\sigma} \sum_{a_1, \dots} A_{1,a_1}^{\sigma_1} A_{a_1,a_2}^{\sigma_2} \dots A_{a_{L/2-1},a_{L/2}}^{\sigma_{L/2}} A_{a_{L/2},a_{L/2+1}}^{\sigma_{L/2+1}} \dots A_{a_{L-1},1}^{\sigma_L} |\sigma_1 \dots \sigma_{L/2} \sigma_{L/2+1} \dots \sigma_L\rangle \\ &= \sum_{\sigma} \sum_{a_1, \dots} \left( A_{1,a_1}^{\sigma_1} (A_{a_{L-1},a_L}^{\sigma_L})^T \right) \left( A_{a_1,a_2}^{\sigma_2} (A_{a_{L-2},a_{L-1}}^{\sigma_{L-1}})^T \right) \dots \\ &\quad \dots \left( A_{a_{L/2-1},a_{L/2}}^{\sigma_{L/2}} (A_{a_{L/2},a_{L/2+1}}^{\sigma_{L/2+1}})^T \right) |(\sigma_1 \sigma_L)(\sigma_2 \sigma_{L-1}) \dots (\sigma_{L/2} \sigma_{L/2+1})\rangle \\ &= \sum_{\Sigma} D^{\Sigma_1} D^{\Sigma_2} \dots D^{\Sigma_{L/2}} |\Sigma_1 \dots \Sigma_{L/2}\rangle. \end{aligned} \quad (2.56)$$

The new MPS  $|\Psi_{\text{fold}}\rangle$  is built from matrices  $D^{\Sigma}$  according to

$$\begin{aligned} D^{\Sigma_i} &= D_{(a_{i-1}a_{L+1-i}), (a_i a_{L-i})}^{(\sigma_{L+1-i} \sigma_i)} = D_{(a_{i-1} \sigma_i, a_{L+1-i} \sigma_{L+1-i}), (a_i a_{L-i})} \\ &= A_{(a_{i-1} \sigma_i), a_i} \otimes A_{(a_{L+1-i} \sigma_{L+1-i}), a_{L-i}} \\ &= A_{a_{i-1}, a_i}^{\sigma_i} A_{a_{L+1-i}, a_{L-i}}^{\sigma_{L+1-i}} \\ &= A_{a_{i-1}, a_i}^{\sigma_i} (A_{a_{L-i}, a_{L+1-i}}^{\sigma_{L+1-i}})^T. \end{aligned} \quad (2.57)$$

An exception are the two sites at the left and right of bend,  $A^{\sigma_{L/2}}$  and  $A^{\sigma_{L/2+1}}$  and thus  $D^{\Sigma_{L/2}}$  the last MPS tensor of the folded state (the two small figure at the right in Fig.(2.10)). One obtains  $D^{\Sigma_{L/2}}$  by an additional contraction over the indices which connect the two  $A$  matrices. In order to get a valid last MPS tensor  $D^{\Sigma_{L/2}}$  one adds a trivial column index with dimension one:

$$\begin{aligned} D^{\Sigma_{L/2}} &= D_{(a_{L/2-1} a_{L/2+1}), 1}^{(\sigma_{L/2+1} \sigma_{L/2})} = D_{(a_{L/2-1} \sigma_{L/2}), (a_{L/2+1} \sigma_{L/2+1})} \\ &= \sum_{a_{L/2}} A_{(a_{L/2-1} \sigma_{L/2}), a_{L/2}} A_{a_{L/2}, (a_{L/2+1} \sigma_{L/2+1})} \\ &= \sum_{a_{L/2}} A_{a_{L/2-1}, a_{L/2}}^{\sigma_{L/2}} A_{a_{L/2}, a_{L/2+1}}^{\sigma_{L/2+1}} \\ &= \sum_{a_{L/2}} A_{a_{L/2-1}, a_{L/2}}^{\sigma_{L/2}} (A_{a_{L/2+1}, a_{L/2}}^{\sigma_{L/2+1}})^T. \end{aligned} \quad (2.58)$$

In a very similar way one constructs the new folded MPO  $F^{\Sigma'_i, \Sigma_i}$  for a given site  $i$ . Assuming  $B^{\sigma'_i \sigma_i}$  to represent the old MPO before the folding the result can be summarized as follows:

$$\begin{aligned} F^{\Sigma'_i, \Sigma_i} &= F_{(a_{i-1} a_{L+1-i}), (a_i a_{L-i})}^{(\sigma'_i \sigma'_{L+1-i}), (\sigma_i \sigma_{L+1-i})} = B_{(a_{i-1} \sigma'_i), (a_i \sigma_i)} \otimes B_{(a_{L+1-i} \sigma'_{L+1-i}), (a_{L-i} \sigma_{L+1-i})} \\ &= B_{a_{i-1}, a_i}^{\sigma'_i, \sigma_i} B_{a_{L+1-i}, a_{L-i}}^{\sigma'_{L+1-i}, \sigma_{L+1-i}} \\ &= B_{a_{i-1}, a_i}^{\sigma'_i, \sigma_i} (B_{a_{L-i}, a_{L+1-i}}^{\sigma'_{L+1-i}, \sigma_{L+1-i}})^T, \end{aligned} \quad (2.59)$$

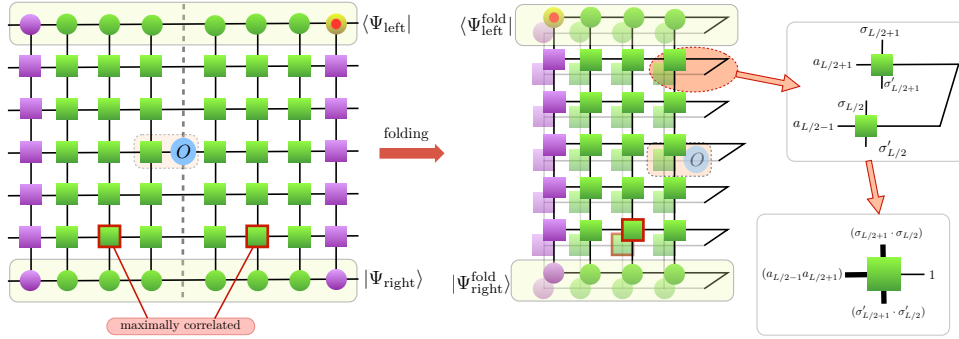


Figure 2.10: Folding scheme. After the rotation of the initial tensor network one can see that there is symmetry around the middle bond of the new MPS. Two bond lying at the same distance from the middle correspond to the same time in the unrotated network from Fig.(2.9). This also holds for the other tensors in the rotated network, which have been perfectly correlated in time before the rotation. By folding the network at the middle bond one can bring these maximally entangled regions on top of each other [see Eqs.(2.56) and (2.59)]. This immediately reduces long distance correlations which makes otherwise the simulations harder. The time evolution of the new folded MPSs and MPOs is done in exact the same way as for the rotated network without a folding. The two small figures on right visualize how one calculates [cp. Eq.(2.58)] the edges of the folded network in order to get proper MPS and MPO objects.

where again one calculates  $D^{\sum'_{L/2} \sum_{L/2}}$  via a contraction over the indices which connect the two  $B$  matrices at the bend and uses the trick adding a trivial column index. As depicted in Fig.(2.10) there is one new MPO which contains the information about the observable  $\hat{O}$ . One can add the information to this MPO by a simple merging of  $\hat{O}$  with one of the neighboring tensors, e.g. the tensor  $B^{\sigma_{L/2}, \sigma'_{L/2}}$ , which leads to a new tensor

$$\tilde{B}^{\sigma''_{L/2}, \sigma_{L/2}} = \sum_{\sigma'_{L/2}} \hat{O}^{\sigma''_{L/2}, \sigma'_{L/2}} B^{\sigma'_{L/2}, \sigma_{L/2}}. \quad (2.60)$$

Apart from this detail one calculates the folded version of this MPO in exact the same way as already explained above.

Together with the new MPS  $\langle \Psi_{\text{left}}^{\text{fold}} |$  and  $| \Psi_{\text{right}}^{\text{fold}} \rangle$  and the new folded MPOs one calculates the time evolution by a successive application of the folded *left* and *right* MPOs on  $\langle \Psi_{\text{left}}^{\text{fold}} |$  and  $| \Psi_{\text{right}}^{\text{fold}} \rangle$  respectively. It turns out that the folding algorithm in combination with the transverse rotation does only require a small modification of the local basis of the old MPS and MPO, which after the transverse step is not anymore a constant for the rotated sites. On the other hand one could also try to implement the whole folding without any rotation of the tensor network.

# Chapter 3

## Ultra Cold Gases

With the realization of Bose-Einstein condensates [10, 42, 75] and of Fermi degeneracy [76, 244, 272] in dilute ultra cold gases a bright source of giant coherent matter waves is available. This has opened up a new chapter in atomic and molecular physics in which the atomic matter waves generated from such condensates can be described by a single macroscopic wave function with typical wave length scale of several micrometers. This allows to directly visualize and investigate quantum mechanical matter wave dynamics.

Some prominent examples include the observation of overlapping condensates [14], of long-range phase coherence [39], the prove of superfluidity through the excitations of vortices [189, 184, 1] and the repulsively bound atom pairs in an optical lattice[287]. The nonlinear behaviour of the BEC was matter wave was demonstrated with the realization of a matter wave amplifier [142] and the excitations of solitons [79].

Gases, in particular dilute gases, were never thought to exhibit strong correlation. Now, two new developments have considerably changed this opinion in the case of ultra cold gases. The first is the ability to tune the interaction strength in cold gases by Feshbach resonances [64, 143]. The second the possibility of generating strong periodic potentials for cold atoms through optical lattices [118]. The two developments allow to enter a regime in which interaction in extremely dilute gases cannot be longer described by a picture based on noninteracting quasiparticles.

Experimentally the strong coupling regime in dilute gases was first reached using Feshbach resonances for bosonic atoms [63]. This approach has one main disadvantage. The increasing the scattering length  $a$  enhances the the three-body collisions (rate varies on average as  $a^4$ ) and thus to a strong decrease of the condensate lifetime [96, 214]. In another approach to the strong coupling regime, an optical lattice has been loaded by BEC [118]. This approach does not suffer from the problems with lifetime of the condensate. By tuning the amplitude of the laser field the BEC has shown a quantum phase transition from a superfluid to a Mott-insulating phase even in the standard regime where the interparticle spacing is much larger scattering length. Other experiments of this type has followed. The realization of a bosonic Luttinger liquid by the observation of a Tonks-Girardeau hard-core Bose gas in 1-D [156, 209]. In two dimensions, a Kosterlitz-Thouless crossover between a normal phase and one with quasi-long-range order [128].

In the following I divide the discussion about ultra cold atoms in three parts. The first con-

cerns the realization of the BEC. In the second part I introduce the concept of optical lattices. Finally, in the third part, I discuss the possible measurement techniques.

### 3.1 Bose Einstein Condensation

The theory of BEC is directly based on the foundations of quantum statistics. The condensation of particles into the ground state of the system without taking into account any interactions was predicted by Einstein in 1925 [90] as a consequence of his extension of Bose's work on photon statistics [40] to massive particles. This section will give an overview of the theory of BEC in ideal and in dilute and weakly interacting gas systems. I will start with qualitative interpretation the phenomenon of BEC followed by a more formally expressed one in terms of quantum statistic of an ideal gas.

Depending on its temperature an atomic cloud of bosons behaves in different ways. At high temperatures, the atoms in the gas behave as point-like particles. When the temperature is lowered, the atoms have to be described as quantum mechanical wave packets with an extent on the order of the de Broglie wavelength

$$\lambda_{\text{dB}} = \frac{h}{\sqrt{2\pi m k_B T}}, \quad (3.1)$$

where  $T$  is the temperature and  $m$  is the mass of the particle. The size of the atomic wavepackets gets larger the further the temperature is lowered. At a certain point, the wavelength of the bosons becomes comparable with the distance between them. The overlap of the atomic wavepackets can be quantified in terms of the phase-space density, defined as the density of the gas  $n$  multiplied by volume occupied by the wavepacket

$$D = n\lambda_{\text{dB}}^3. \quad (3.2)$$

When the phase-space density is on the order of unity, a phase transition will occur and the bosons form a Bose-Einstein condensate, where all atoms occupy the same quantum state. The atoms can then be described by a single macroscopic wave function. The critical temperature for this

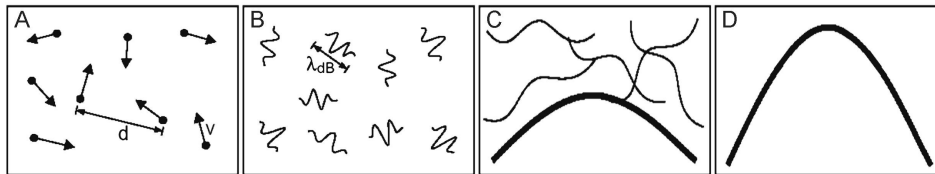


Figure 3.1: The behaviour of a gas of identical bosonic atoms at different temperatures. (A) At high temperatures, the gas can be treated as system of point-like particles. (B) For sufficiently low temperatures, the atoms must be described as wavepackets that scatter according to quantum mechanics. (C) A phase transition to a BEC occurs when the size of the atomic wavepackets is comparable to the mean distance between particles and the wavepackets start to overlap. (D) At zero temperature, all particles are in the same quantum state and can be described by a single macroscopic wave function. Adapted from [154].

phase transition can be directly estimated from [Eq.3.1] and [Eq.3.2]. This critical temperature is usually several orders of magnitude higher than the temperature corresponding to the energy level spacing between the ground and the first excited state of the system. Therefore, BEC has nothing to do with naturally freezing out the atomic motion. It is a true a high-temperature phenomenon. Note that to reach Bose-Einstein condensation, the gas must be sufficiently dilute that it does not become a liquid or a solid when being cooled. Moreover a BEC of atoms is a metastable state, which will eventually decay through the formation of molecules. Several textbooks [217, 213] and review articles [154, 71, 50][173] cover the topic of ultracold gases and Bose-Einstein condensation.

### 3.1.1 BEC of an ideal gas

The most convenient treatment to describe a BEC can be obtained within the framework of quantum statistics using the grand canonical ensemble. In the following I assume an ideal gas of bosons in thermal equilibrium with temperature  $T$ . According to the Bose distribution the mean occupation number  $n_i$  of a single-particle state  $|i\rangle$  is given by

$$n_i = \frac{1}{e^{\beta(\varepsilon_i - \mu)} - 1}, \quad (3.3)$$

where  $\varepsilon_i$  is the energy of the state  $|i\rangle$  and  $\mu$  is chemical potential. For a fixed total number of particles  $N$ , the chemical potential is related to the temperature through the normalization condition  $N = \sum_i n_i$ . The above result provides the important constraint  $\mu < \varepsilon_0$  for the chemical potential of the ideal Bose gas, where  $\varepsilon_0$  is the lowest eigenvalue of the single-particle Hamiltonian. The violation of this equality would result in a negative value for the occupation number of the states with energy smaller than  $\mu$ . Now, when  $\mu \rightarrow \varepsilon_0$  the occupation number of the lowest state

$$N_0 = n_0 = \frac{1}{e^{\beta(\varepsilon_0 - \mu)} - 1} \quad (3.4)$$

becomes increasingly large. This is the mechanism of the Bose-Einstein condensation. The total number of particles can be written as a sum of  $N_0$ , the occupation number in the ground state, and a thermal component  $N_{\text{th}}$ , the number of particles out of the condensate

$$N = N_0 + N_{\text{th}} = N_0 + \sum_{i=1}^{\infty} \frac{1}{e^{\beta(\varepsilon_i - \mu)} - 1}. \quad (3.5)$$

Now, for a fixed temperature,  $N_{\text{th}}(\mu)$  varies smoothly and reaches a maximum for  $\mu = \varepsilon_0$ . Thus the maximum number of particles out of condensate is

$$N_{\text{th,max}} = \sum_{i=1}^{\infty} \frac{1}{e^{\beta(\varepsilon_i - \varepsilon_0)} - 1} \quad (3.6)$$

For very low temperatures  $N_{\text{th,max}}$  can be significantly lower than the total number of particles  $N$ . This implies that a significant amount of particles must occupy the ground state. The temperature

at which the macroscopic occupation of the lowest single-particle state takes place is called the critical temperature  $T_c$ . If the thermal energy is much larger than the spacing between the energy levels  $k_B T \gg \varepsilon_i - \varepsilon_{i-1}$  the sum in equation (3.6) can be replaced by an integral

$$N_{\text{th,max}} = \int_0^\infty \rho(\varepsilon, V(\mathbf{r})) N(\varepsilon), \quad (3.7)$$

with  $\rho(\varepsilon, V(\mathbf{r}))$  the energy of states in a potential  $U(\mathbf{r})$  and  $N(\varepsilon)$  the continuous Bose distribution. It turns out that the critical temperature  $T_c$  depends on the specific confining potential  $V(\mathbf{r})$ . Using the fact that the particle density in a given potential is determined by the particle number and ensemble temperature one can express the critical temperature in dependence of the particle number. For a harmonic trapping potential  $V(\mathbf{r}) = Ar^\alpha$  (with a box potential  $\alpha \rightarrow \infty$ ), the critical temperature turns out to be given by the expression [123, 20]

$$k_B T_c = \hbar \omega_{\text{ho}} \left( \frac{N}{\zeta(3)} \right)^{1/3} = 0.94 \hbar \omega_{\text{ho}} N^{1/3}, \quad (3.8)$$

where I have introduced the geometric average  $\omega_{\text{ho}} = (\omega_x \omega_y \omega_z)^{1/3}$  of the oscillator frequencies.  $\zeta(n)$  is the Riemann function with  $\zeta(3) \approx 1.202$ . Another important quantity is the relative occupation of the ground state

$$\frac{N_0}{N} = 1 - \left( \frac{T}{T_c} \right)^{3/2+3/\alpha}. \quad (3.9)$$

For potential with lower  $\alpha$ , the ground state occupation grows very fast for  $T \rightarrow 0$ . For typical harmonic potentials about 90% of the atoms occupy the ground state at  $T = T_c/2$ . the reason is the following. The potential becomes steeper around its minimum decreasing  $\alpha$ . This leads to a low number of states at low energies with relatively large spacing, which then favors the the occupation of the potential ground state.

### 3.1.2 Ultracold collisions

The differences between an ideal quantum gases and the real quantum gases start with two-particle interaction. Therefore the study of ultracold collisions is a natural starting point for investigation of an interacting quantum gas. Collisions determine two crucial aspects of BEC experiments. The first regards to the evaporative cooling rate necessary for the realization of an BEC. It turns out that this rate depends on the elastic cross section, proportional to the square of the  $s$ -wave scattering length. Second, the sign of the scattering length indicates the stability of the condensate. Positive scattering lengths lead to large stable condensates while negative scattering length do not.

A good approach to describe the scattering of two colliding atoms is to expand their wave function of the relative motion in spherical partial waves. Each of the spherical partial waves is characterized by its angular momentum  $l$ . At sufficiently low energies, the centrifugal barrier prohibits partial waves with nonzero angular momentum and only  $s$ -wave scattering ( $l = 0$ ) needs

to be considered<sup>1</sup>. The scattering is then isotropic and is characterized by the corresponding phase shift  $\delta_0(k)$  between the incoming and the outgoing  $s$ -wave [171]. In the limit of zero collision energy, the scattering is usually parameterized by the scattering length

$$a = \lim_{k \rightarrow 0} \frac{\tan \delta_0(k)}{k}, \quad (3.10)$$

where  $k$  denotes the wave vector of the relative motion of the atoms. In the low-energy limit, the two-body collision problem is then described by one single parameter, the scattering length. This quantity independent of all the details of the interaction potential between the colliding particles. For alkali atoms the typical range of the  $s$ -wave scattering is in between  $10 - 100a_0$ , where  $a_0$  is the Bohr radius.

For two identical bosons, the collisional cross-section is [72]

$$\sigma_c = \frac{8\pi a^2}{1 + k^2 a^2}. \quad (3.11)$$

This expression has two limiting cases. For large scattering lengths, such that  $ka \gg 1$ , the cross section is limited by the collision energy,  $\sigma_c = 8\pi/k^2$ . This is called the unitarity limit. In the limit of small scattering length,  $ka \ll 1$ , the cross section is  $\sigma_c 8\pi a^2$ .

The above cross section, which is exact in the  $s$ -wave limit, corresponds to a point-like scattering potential (pseudopotential)

$$V(r) = g\delta(r), \quad (3.12)$$

where  $r$  is the distance between the colliding particles and the coupling constant  $g$  is proportional to the scattering length

$$g = \frac{4\pi\hbar^2 a}{m}. \quad (3.13)$$

This approximation is valid in many situations, provided no longer-range contributions come into play. For example different forms of dipole-dipole interaction [198][236]. The interaction is repulsive for positive and repulsive for negative scattering lengths.

### Feshbach resonances

In simplified picture, a Feshbach resonance occurs, when the energy of a bound state of the interatomic potential is equal to the kinetic energy of the colliding pair of atoms. This degeneracy can occur only when the bound state exist in a potential that has a higher threshold energy than the energy of the colliding pair. Such a condition can be satisfied for ultracold gases of alkali atoms, due to their hyperfine structure. This concept has been studied in the context of nuclear physics [98] and later applied to atom-atom scattering [264].

---

<sup>1</sup>and  $p$ -wave for fermions

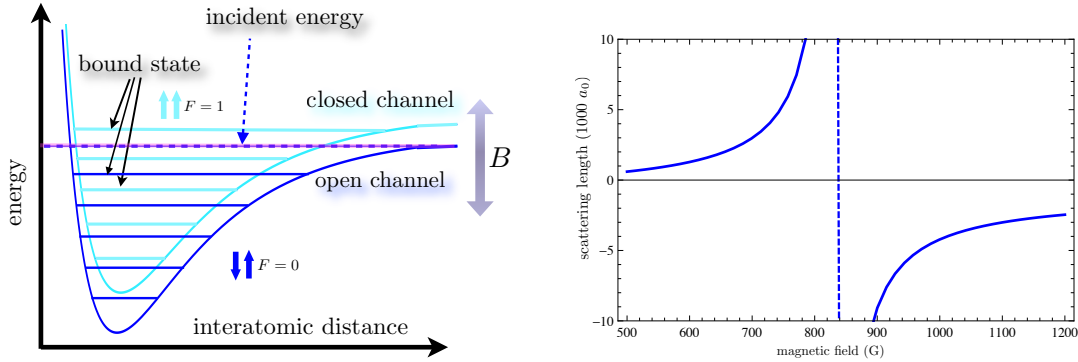


Figure 3.2: Two-channel model for a Feshbach resonance. Two atoms, which are in the lower hyperfine state  $F_1 = 0$  undergo a collision at a low incident energy. In the course of the collision, the open channel is coupled to the closed channel  $F_2 = 1$  via a virtual process (2nd order). When a bound state of  $F_2 = 1$  is close to the kinetic energy of the incoming pair, a scattering resonance occurs. The position of the closed channel can be tuned with respect to the open one, e.g. by varying the magnetic field. The right figure shows the scattering amplitude  $a$  vs. the magnetic field  $B$ . One can tune  $a$  from positive to negative, thus, from repulsive to attractive interactions respectively.

In the following I assume a collision between two atoms which are in the lower hyperfine state  $F_1 = 0$ . The interatomic potential associated with the upper hyperfine state  $F_2 = 1$  may have a bound state close to the kinetic energy of the incoming pair [see Fig.(3.2)]. The different magnetic moments  $m_{F_1}$  and  $m_{F_2}$  one can tune the bound state energy into resonance with the colliding atom energy using an external magnetic field. The elastic scattering physics, i.e. the scattering length  $a$ , can be dramatically altered by tuning an experimentally accessible parameter [258]. Additionally to low collision energy and hyperfine structure, one requires for the existence of a Feshbach resonance a coupling between the open (the continuum energy of this channel is below the total energy of the incoming atom pair) and the closed channel (the continuum energy of this channel is above the total energy of the incoming atom pair). The coupling is provided by the Coulomb interaction, which couples together different hyperfine state at short internuclear distance. As the atoms move together during a collision, the strong electrostatic interaction between the nuclei and the electron overwhelms the relatively weak hyperfine interaction, allowing a spin flip to occur. Due to the symmetry of the two-body system the total magnetic moment  $m_{F_{\text{tot}}} = m_{F_1} + m_{F_2}$  is conserved, while the total spin  $F^{\text{tot}} = F_1 + F_2$  is not! This requirements restrict the number of closed channels that can couple to an open channel.

A Feshbach resonance can be characterized by its position  $B_0$ , the magnetic field where the molecular state crosses the incident scattering state, and its width  $\Delta B$ , which is dependent on the magnetic moment of the bound state and the strength of the coupling between the two scattering channels. On a phenomenological level the scattering length around a Feshbach resonance can be written as

$$a(B) = a_{\text{bg}} \left( 1 - \frac{\Delta B}{B - B_0} \right), \quad (3.14)$$

where  $a_{\text{bg}}$  is the off-resonant background scattering length, which would govern the collision if no resonance would appear in this field range. In general, the variation of the scattering length



by external fields means tuning of the two-body interaction between being effectively attractive and repulsive for sufficient small kinetic energies.

### 3.1.3 BEC of a weakly interacting gas

A dilute Bose gas of interacting particles in a trapping potential  $V(r)$  can at zero temperature (or very low temperature) be treated in a mean-field approach [124][216][217]. At lowest-order and low temperatures one can simply replace the operator  $\hat{\Psi}(\mathbf{r}, t)$  with a classical field  $\Psi(\mathbf{r}, t)$ , also called the order parameter or the wave function of the condensate. The field operator in the Heisenberg representation fulfills the exact equation

$$i\hbar \frac{\partial}{\partial t} \hat{\Psi}(\mathbf{r}, t) = \left[ -\frac{\hbar^2}{2m} \nabla^2 + V_{\text{ext}}(\mathbf{r}) + \int \hat{\Psi}^\dagger(\mathbf{r}', t) V(\mathbf{r}' - \mathbf{r}) \hat{\Psi}(\mathbf{r}', t) d\mathbf{r}' \right] \hat{\Psi}(\mathbf{r}, t) \quad (3.15)$$

Now, if one assumes instead of  $V(\mathbf{r}' - \mathbf{r})$  an effective soft potential  $V_{\text{eff}}^2$  where the Born approximation is applicable one can replace  $\hat{\Psi}(\mathbf{r}, t)$  with  $\Psi(\mathbf{r}, t)$ . Assuming further that  $\Psi(\mathbf{r}, t)$  varies slowly on distances of the order of the range of the interatomic force, one can substitute  $\mathbf{r}'$  for  $\mathbf{r}$  in the arguments of  $\Psi$  and obtains the so-called Gross-Pitaevskii equation

$$i\hbar \frac{\partial}{\partial t} \Psi(\mathbf{r}, t) = \left[ -\frac{\hbar^2}{2m} \nabla^2 + V_{\text{ext}}(\mathbf{r}) + g |\Psi(\mathbf{r}, t)|^2 \right] \Psi(\mathbf{r}, t), \quad (3.16)$$

with the coupling constant  $g = \frac{4\pi\hbar^2 a}{m}$  [cp. Eq.3.13]. the Gross-Pitaevskii equation takes a simple form in the case of stationary solutions. The time dependence of the condensate ground state function is fixed by the chemical potential  $\mu = \frac{\partial E}{\partial N}$ . Thus, the condensate function evolves in time according the law  $\Psi(\mathbf{r}, t) = \Psi(\mathbf{r}) e^{-i\mu t/\hbar}$ . The Gross-Pitaevskii equation then reduces to [177]

$$\mu \psi(\mathbf{r}) = \left[ -\frac{\hbar^2}{2m} \nabla^2 + V_{\text{ext}}(\mathbf{r}) + g |\psi(\mathbf{r})|^2 \right] \psi(\mathbf{r}), \quad (3.17)$$

with  $\mu$  the chemical potential.  $\psi(\mathbf{r})$  can be chosen to be a real function with  $N = N_0 = \int d\mathbf{r} \psi^2$  and thus related to the particle density as  $\psi^2(\mathbf{r}) = n(\mathbf{r})$ . The energy of the system depending on the particle density reads

$$E = \int \left[ \frac{\hbar^2}{2m} |\nabla \sqrt{n}|^2 + nV(\mathbf{r}) + \frac{gn}{2} \right] d\mathbf{r} = E_{\text{kin}} + E_{\text{pot}} + E_{\text{int}}. \quad (3.18)$$

$E_{\text{kin}}$  is the quantum kinetic energy, often referred to as quantum pressure,  $E_{\text{pot}}$  is the potential energy of the system and  $E_{\text{int}}$  is the interaction energy or the mean-field energy. The kinetic and interaction energy terms determine another important parameter, the so-called healing length.

<sup>2</sup>The potential  $V_{\text{eff}}$  should reproduce the same low energy scattering properties given by the bare potential  $V$

The healing length is the distance over which the condensate wave function can compensate for density variations. It is not possible for the condensate density to grow from 0 to  $n$  on arbitrary short distances, since this would lead to a divergence of the quantum pressure  $E_{\text{kin}}$ . The shortest possible distance  $\xi$  for such a change of density is given by the balance of  $E_{\text{kin}} \sim \hbar^2/(2m\xi^2)$  and the interaction energy  $E_{\text{int}} \sim 4\pi\hbar an/m$ , which defines the healing length

$$\xi = \frac{1}{\sqrt{8\pi na}} \quad (3.19)$$

### 3.1.4 Thomas-Fermi approximation

The Gross-Pitaevskii equation only describes the physics for very low temperatures  $T \rightarrow 0$ , thus for the condensate fraction only. While the condensation is taking place in the weakly interacting gas the condensate dynamics is dominated by interactions as the kinetic energy in the lowest quantum state is relatively small and in most cases negligible compared to the interaction energy. These assumptions lead to the Thomas-Fermi approximation which consists in neglecting the kinetic term in the Gross-Pitaevskii equation [3.17], which results in the condensate density

$$n(\mathbf{r}) = \begin{cases} \frac{\mu - V_{\text{ext}}(\mathbf{r})}{g} & \text{for } \mu - V_{\text{ext}}(\mathbf{r}) > 0 \\ 0 & \text{otherwise} \end{cases} \quad (3.20)$$

The Thomas-Fermi approximation allows the determination of several condensate parameters. The central condensate density is given by  $n(0) = \frac{\mu}{g} = \frac{\mu m}{4\pi\hbar^2 a}$ , the chemical potential as a function of particle number  $\mu = \frac{\hbar\omega_{\text{ho}}}{2} \left(\frac{15Na}{a_{\text{ho}}}\right)^{2/5}$ , the mean interaction energy per particle  $\frac{E_{\text{kin}}}{N} = \frac{2}{7}\mu$ , and finally the condensate radii  $R_i = \sqrt{\frac{2\mu}{m\omega_i^2}}$ . These equations are very useful in the discussion of concrete experiments and allow an easy estimation of physical parameters of BEC [280].

### 3.1.5 Recent development

#### Solitons

Solitons are distinguished as wave packet like objects that do not change their shape and propagate with a constant velocity in homogeneous systems. A detailed balance between dispersion induced spreading and a focusing or defocusing mediated by a non-linear interaction stabilizes the soliton as it propagates through a well suited non-linear medium [104]. Long-lived dark and dark-bright solitons with lifetimes of up to several seconds as well as their dynamics has been observed [281, 254, 27].

#### Forming Molecules

A promising approach is to create the molecular gas directly from an ultracold atomic gas. Bosons in Bose-Einstein condensate have been coupled to electronic ground-state molecules

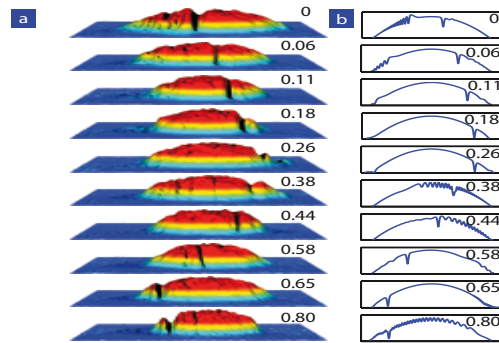


Figure 3.3: Dark soliton oscillations in a trapped BEC. A set of absorption images showing the soliton position at various times after phase imprinting. The soliton propagates to the right and is reflected at the edge of the condensate after  $t = 80$  ms. From [27]

through photoassociation or Feshbach resonances. The availability of atomic Fermi gases offers the prospect of coupling fermionic atoms to bosonic molecules, thus altering the quantum statistics of the system. Such a coupling would be closely related to the pairing mechanism in a fermionic superfluid, predicted to occur near a Feshbach resonance. The first successful experiments [134, 225] produced molecules of fermions using Feshbach resonances. Stimulated adiabatic Raman passage has been used in order to transfer weakly bound molecules (through Feshbach resonances) to ground state which avoids heating the sample [198]. Recently chemical reactions between molecules in this new regime has been studied [204] showing that tiny changes, such as orientation of the single nuclear spin have profound consequences for how chemical reaction occur. There is an intense parallel effort to cool preexisting molecules (which cannot be laser cooled) to the ultracold regime which would allow to study chemically important polar molecules such as ammonia and free radicals.

### BEC-BCS crossover

At very low temperatures the kinetic energy of the atoms is very small and scattering between the atoms can be considered exclusively  $s$ -wave. Since  $s$ -wave scattering is not allowed for identical fermions they are essentially non-interacting particles. This is rather uninteresting<sup>3</sup> and therefore the investigation concerns systems consisting of different kinds of fermions or Bose-Fermi mixtures. Interactions are also important for the cooling. More precisely in its last stage known as evaporative cooling where fast rethermalisation is crucial. This requires naturally strong interactions between atoms, and for this purpose cooling is always performed in mixtures, either of different fermions or more often of fermions and bosons. The Bardeen-Cooper-Schrieffer (BCS) formalism with its particular Ansatz for the ground state wavefunction describes the formation of weakly interacting Cooper pairs as well as strong interacting of a dilute gas of molecules which undergo a BEC [174]. The ability to tune the interaction through a Feshbach resonance allows one to explore the crossover from a BCS superfluid, when the attraction is weak and pairing shows up only in momentum space, to a Bose-Einstein condensate of tightly bound pairs

<sup>3</sup>Actually, non-interacting fermions are of high interest for high-precision atomic clocks.

in real space. A quantum phase transition to the normal state on the weak-coupling side of the BCS-BEC crossover [302] as well as a phase separation in the crossover region [302][211], both driven by density imbalance, have been identified. Contrary to expectations for the weakly interacting case, superfluidity in the resonant region is extremely stable against population imbalance [302]. This opens a path to realize more exotic solutions which allow superfluidity also with imbalanced densities, most notably the FFLO state[49].

## 3.2 BEC in optical lattices

The combination between ultracold atoms and periodic potentials allows to form a physical system which is closely related to many systems in condensed matter physics. In order to have a large tunnel coupling between the neighboring potentials it is highly desirable to keep spacing between individual lattice sites as small as possible. This can be achieved by using the standing wave interference pattern of two counterpropagating laser beams, where the lattice spacing equals half of the laser wavelength. The atoms are can be trapped in the intensity maxima or minima of light field due to the optical dipole force [152].

### 3.2.1 Dipole force

When an atom is placed into laser light, the electric field  $\hat{\mathbf{E}}$  induces an atomic dipole moment  $\hat{\mathbf{d}}$  that oscillates with the driving frequency  $\omega$  [121]. The dipole amplitude  $\tilde{d}$  is simply related to the field amplitude  $\tilde{E}$  by  $\tilde{p} = \alpha(\omega)\tilde{E}$  with  $\alpha$  the complex polarizability. The potential energy of the atom in the field is proportional to the intensity and the real part of the polarizability,

$$V_{\text{dip}} = -\frac{1}{2}\langle\hat{\mathbf{d}}\hat{\mathbf{E}}\rangle = -\frac{1}{2}\text{Re}(\alpha(\omega))I(r), \quad (3.21)$$

where the angular brackets denote the time average over rapid oscillating terms. The field intensity is  $I = 2\epsilon_0 c |\tilde{E}|^2$ , and the factor  $\frac{1}{2}$  takes into account that the dipole moment is an induced and not a permanent one. The dipole force results from the gradient of the interaction potential,

$$\mathbf{F}_{\text{dip}} = -\nabla V_{\text{dip}}(\mathbf{r}) = \frac{1}{2}\text{Re}(\alpha)\nabla I(\mathbf{r}). \quad (3.22)$$

The direction of the force depends on the sign of the polarizability  $\alpha(\omega)$ . In the vicinity of the atomic resonance from ground  $|g\rangle$  to an excited state  $|e\rangle$  at frequency  $\omega_0$ , one can write the polarizability using semiclassical approach as  $\alpha(\omega_L) \approx |\langle e|\hat{\mathbf{d}}|g\rangle|^2/\hbar(\omega_0 - \omega_L)$ . Thus, atoms are attracted to the nodes or the antinodes of the laser intensity for blue- ( $\omega_L > \omega_0$ ) or red-detuned ( $\omega_L < \omega_0$ ) laser light respectively.

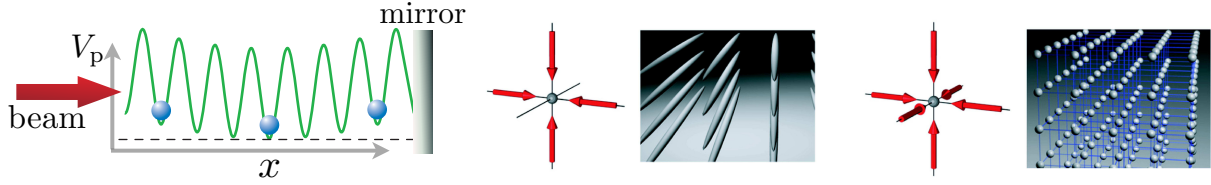


Figure 3.4: Optical lattices. The standing-wave interference pattern creates a periodic potential in which the atoms move by tunnel coupling between the individual wells. The gaussian beam profile of the lasers, a residual harmonic trapping potential, leads to a weak harmonic confinement superimposed over the periodic potential. Thus the overall trapping configuration is inhomogeneous (left). The middle and the right picture show the resulting lattice structure after superimposing two, respectively, three orthogonal standing waves. Illustration from [37]

### 3.2.2 Optical potential

The intensity profile  $I(r, z)$  of a Gaussian laser beam propagating along the  $z$  direction has the form

$$I(r, z) = \left[ \frac{2P}{\pi w^2(z)} \right] e^{-2r^2/w^2(z)}, \quad (3.23)$$

with  $P$  the total power of the laser beam,  $r$  the distance from the center, and  $w(z) = w_0 \sqrt{1 + z^2/z_R^2}$  the  $1/e^2$  radius. This radius is characterized by a beam waist  $w_0$ , which is typically around  $100\mu\text{m}$ , and the Rayleigh length  $z_R$ , which is in the millimeter to centimeter range. Due to the Stark shift, that atoms experience in an off-resonant light field [121], a potential minimum occurs around the intensity maximum of the beam leading to an approximately harmonic potential

$$V_{\text{dip}} \approx -V_{\text{trap}} \left[ 1 - 2(r/w_0)^2 - (z/z_0)^2 \right]. \quad (3.24)$$

The trap depth  $V_{\text{trap}}$  is linearly proportional to the laser power.

### 3.2.3 Optical lattices

Two superimposed counter-propagating narrow-band laser beams will interfere and create an optical standing wave with period  $\lambda/2$ . If the laser beams are far detuned from the atomic resonance and have radially symmetric Gaussian beam profiles, the resulting periodic potential at the beam focus takes the form

$$V(r, z) \simeq -V_0 e^{-2r^2/w^2(r)} \sin^2(kz), \quad (3.25)$$

where  $k = 2\pi/\lambda$  is the wave vector of the laser light. An easy way to create a standing wave is to simply retro-reflect a single beam by a perfect mirror. Due to constructive interference of the two laser beams,  $V_0$  is four times larger than  $V_{\text{trap}}$  (which is not retro-reflected) if the laser power and beam parameters of the two interfering lasers are equal.

Periodic potentials in two dimensions are formed by overlapping two optical standing waves along, not necessarily, orthogonal direction. The resulting optical potential in the center of the

trap is then a simple sum of sinusoidal potential in both directions. In such a configuration atoms are confined to arrays of tightly confining one-dimensional tubes. The trapping potential strength in the radial direction of each tube goes up to 100 kHz. Since the trapping potential strength along the tubes are much weaker, around 10 – 200 Hz, the atoms can only move axially along the tube. Thus, each tube represents a highly tunable one dimensional system of strongly correlated atoms. The first realizations of such quantum wires are [117, 195, 209, 156, 265].

By adding a third optical standing wave, orthogonal to the previous two, one can create a three-dimensional lattice potential. The resulting potential is then given by the sum of the three standing waves. The trapping potential in the center of the trap can be approximated as the sum of a homogeneous periodic lattice potential

$$V_p(x, y, z) = V_0(\sin^2(kx) + \sin^2(ky) + \sin^2(kz)) + V_{\text{trap}}, \quad (3.26)$$

with the harmonic trapping potential

$$V_{\text{trap}} = \frac{1}{2}(m\omega_x^2 x^2 + m\omega_y^2 y^2 + m\omega_z^2 z^2) \quad (3.27)$$

as an additional external harmonic confinement due to the Gaussian laser beam profile.

Coming back to the one dimensional wires created by a two-dimensional optical lattice potential. By superimposing of two weak standing waves with different frequencies along the direction of the tube it is possible to create so-called superlattice structures, e.g. 2D arrays of double-well potentials [248]. The advantage of such superlattice structures is the possibility to manipulate (almost) independently the intrawell and interwell interactions. First main examples for the rich possibilities of superlattices are the study of the superexchange mechanism [103], the spin-dependent transport [172] and the development of a new mapping procedure [249]. Moreover, a variety of lattice structures can be obtained by interfering laser beams under different angles [148, 125].

### 3.2.4 Band structure

The eigenstates for a periodic potential  $V_p(\mathbf{r} + \mathbf{R}) = V_p(\mathbf{r})$  maybe written in terms of the Bloch functions, which are a product between an envelope plane wave function and a periodic function  $u_{n,\mathbf{q}}(\mathbf{r}) = u_{n,\mathbf{q}}(\mathbf{r} + \mathbf{R})$  that has the same periodicity as the as the potential

$$\psi_{n,\mathbf{q}}(\mathbf{r}) = e^{i\mathbf{q}\mathbf{r}} u_{n,\mathbf{q}}(\mathbf{r}). \quad (3.28)$$

The corresponding energy eigenvalue of a periodic potential with periodicity  $\mathbf{Q}$  (the reciprocal lattice vector) is  $\varepsilon_n(\mathbf{q}) = \varepsilon_n(\mathbf{q} + \mathbf{Q})$ . The energies associated with the index  $n$  vary continuously with wavevector  $\mathbf{q}$  and form an energy band identified by band index  $n$ . All distinct values of  $\varepsilon_n(\mathbf{q})$  occur for  $q$ -values within the first Brillouin zone of the reciprocal lattice [15]. The Bloch states form an orthogonal set of eigenstates to the Schrödinger equation delocalized over the entire lattice. This a good choice of basis to work with if the lattice is shallow. However, when working with deep lattices, it is more convenient to work with a set of states localized to a single

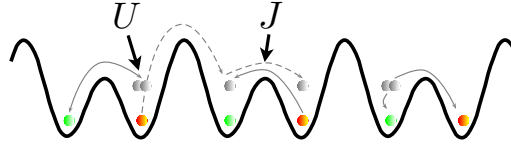


Figure 3.5: Bose Hubbard Hamiltonian in one dimension. This cartoon picture illustrates a system consisting of two different bosonic species in a lattice potential which is described by the interaction  $U$  and the hopping  $J$ .

lattice site  $\mathbf{R}$ . This is provided by the Wannier functions  $w_{n\mathbf{R}}$  which are connected with the Bloch functions by a Fourier transform

$$\psi_{n,\mathbf{q}}(\mathbf{r}) = \sum_{\mathbf{Q}} w_{n\mathbf{R}} e^{i\mathbf{q}\mathbf{R}}. \quad (3.29)$$

The Wannier functions depend only on the relative distance  $\mathbf{r} - \mathbf{R}$ . The Wannier functions form a complete basis for all bands  $n$  and sites  $\mathbf{R}$ . Therefore one can expand the operator  $\hat{\psi}(\mathbf{r})$ , which destroys a particle at an arbitrary point  $\mathbf{r}$ , in the form

$$\hat{\psi}(\mathbf{r}) = \sum_{n,\mathbf{R}} w_n(\mathbf{r} - \mathbf{R}) \hat{a}_{n,\mathbf{R}}, \quad (3.30)$$

where  $\hat{a}_{n,\mathbf{R}}$  is the annihilation operator for particles in the corresponding Wannier states.

### 3.2.5 Bose Hubbard Hamiltonian

One of the first examples demonstrating the possibilities how cold atoms combined with optical lattices can be used to study many body phenomena was the Superfluid-Mott transition for bosonic atoms [118, 100]. A conceptual simple model to describe cold atoms in an optical lattice at finite density is the Bose-Hubbard model. The Bose-Hubbard model is obtained from a general many-body Hamiltonian for bosonic atoms in an external potential

$$\hat{H} = \int d\mathbf{r} \hat{\psi}^\dagger(\mathbf{r}) \left( -\frac{\hbar^2}{2m} \nabla^2 + V_0(\mathbf{r}) + V_{\text{trap}}(\mathbf{r}) \right) \hat{\psi}(\mathbf{r}) + \frac{g}{2} \int d\mathbf{r} \hat{\psi}^\dagger(\mathbf{r}) \hat{\psi}^\dagger(\mathbf{r}) \hat{\psi}(\mathbf{r}) \hat{\psi}(\mathbf{r}), \quad (3.31)$$

with  $V_0(\mathbf{r})$  the optical potential 3.26 and  $V_{\text{trap}}(\mathbf{r})$  an additional (slowly varying) external trapping potential 3.27. The interaction energy is approximated by a short-range contact potential with  $g = \frac{4\pi a \hbar^2}{m}$  3.13. In the following I assume that the thermal and the mean interaction energies at a site are much smaller compared to  $\hbar\omega_0$  the excitation energy to the second band. Expanding the field operators in the Wannier basis 3.30 and keeping only the lowest vibrational states <sup>4</sup>,  $\hat{\psi}(\mathbf{r}) = \sum_{\mathbf{R}} w(\mathbf{r} - \mathbf{R}) \hat{a}_{\mathbf{R}}$ , the general many-body Hamiltonian 3.31 reduces to the Bose-Hubbard model [144]

$$\hat{H} = -J \sum_{\langle \mathbf{R}\mathbf{R}' \rangle} \hat{a}_{\mathbf{R}}^\dagger \hat{a}_{\mathbf{R}'} + \frac{U}{2} \sum_{\mathbf{R}} \hat{n}_{\mathbf{R}} (\hat{n}_{\mathbf{R}} - 1) + \sum_{\mathbf{R}} \varepsilon_{\mathbf{R}} \hat{n}_{\mathbf{R}}, \quad (3.32)$$

<sup>4</sup>the Wannier functions have to decay essentially within a single lattice constant

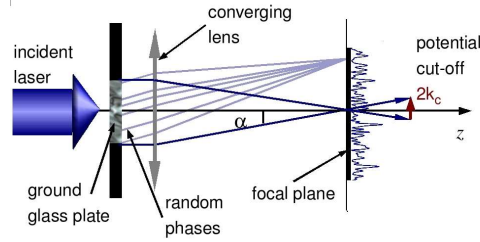


Figure 3.6: Disorder potential created with a glass plate. A coherent laser beam is diffracted through a ground-glass plate and focused by a converging lens. The ground-glass plate transmits the laser light without altering the intensity, but imprinting a random phase profile on the emerging light. Then, the complex electric field on the focal plane results from the coherent superposition of many independent waves with equally-distributed random phases, and is thus a Gaussian random process. Illustration taken from [239].

where  $\langle \mathbf{R}\mathbf{R}' \rangle$  denotes the sum over all lattices  $\mathbf{R}$  and its nearest neighbors. The parameters  $U = g \int d\mathbf{r} |w(\mathbf{r})|^4$  correspond to the strength of the repulsion of two atoms on the lattice site  $\mathbf{R}$ ,  $J = \int d\mathbf{r} w^*(\mathbf{r} - \mathbf{R}) [-\frac{\hbar}{2m} \nabla^2 + V_0(\mathbf{r})] w(\mathbf{r} - \mathbf{R}')$  is the hopping matrix element between neighboring sites, and  $\epsilon_{\mathbf{R}} = \int d\mathbf{R} V_{\text{trap}} |w(\mathbf{r} - \mathbf{R})|^2 \approx V_{\text{trap}}(\mathbf{R})$  describes the energy offset at each lattice site. The Bose-Hubbard model describes the competition between the kinetic energy  $J$  and the on-site interaction  $U$ . The advantage of the optical lattices is that ratio between  $U/J$  can be changed by varying the dimensionless depth  $V_0/E_r$  of the optical lattice, which is controlled by the laser light.

In the following I will consider an optical lattice at very low filling. A pair of atoms at the same site has an energy  $U$  above or below the center of the lowest band. If the interaction energy is attractive  $U < 0$  and sufficiently large the two particles will form a bound state. In the repulsive case the pair is usually expected to be unstable. The two atoms will try to hop onto different lattice sites far from each other. But this process is forbidden if the energy of the two particles is above the energy of the band for a repulsive interaction  $U > U_c$ . The momentum and energy conservation do not allow the two particles to separate because there are simply no free states available which can absorb this energy. Thus the two atoms can also form a repulsive bound pair [287].

### 3.2.6 Recent development

#### BEC in quasiperiodic lattices. Disorder

Current activities in the field of ultracold atoms in optical lattices concerns disorder in interacting quantum systems. Such systems constitute paradigmatic examples of mesoscopic systems where the interplay of interactions, quantum interferences and the external potential give rise to a rich physics. One central aspect for bosonic systems [111] is the competition between disorder, which tends to localize particles [12], and weak repulsive interactions, which instead have a delocalizing effect. Joint theoretical [73, 234, 238, 237] and experimental efforts [183, 61, 246, 89] has been made and recently Anderson localization has been observed in one and two-dimensional systems of ultracold atoms [168, 35, 247]. It is impossible to completely eliminate it in real physical



systems, but its effect on the microscopic components of matter is not as negative as it was previously thought. Recently the effect of disorder on superconductivity and quantum magnetism has been investigated [239].

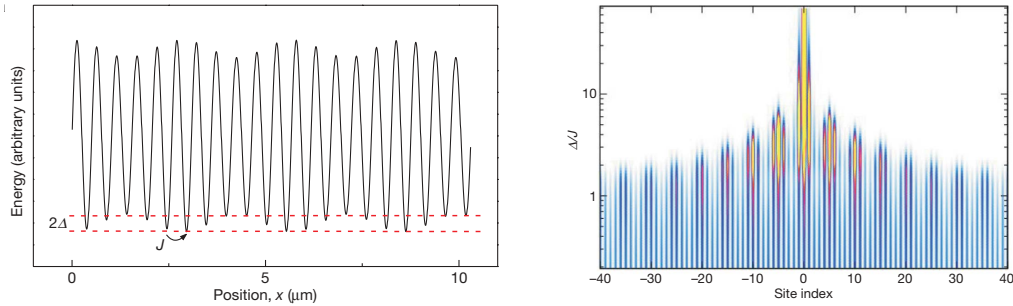


Figure 3.7: Quasi-periodic optical potential and Anderson localization. The left figure shows the resulting quasi-periodic lattice structure of a one dimensional lattice which is perturbed by a second, weak incommensurate lattice. The hopping energy  $J$  describes the tunnelling between different sites of the primary lattice and  $2\Delta$  is the maximum shift of the on-site energy induced by the secondary lattice. The right figure shows the calculated density of a low-lying eigenstate of the bichromatic potential, as a function of  $\Delta/J$  (vertical axis). For small values of  $\Delta/J$  the state is delocalized over many lattice sites. For  $\Delta/J > 7$  the state becomes exponentially localized on lengths smaller than the lattice constant. Illustrations from [230].

### Dipolar gases in optical lattices

Atoms or molecules having a permanent dipole moment (either magnetic or electric) interact not only via short-range potentials, but also via the dipole-dipole interaction. Contrary to the case of usual quantum degenerate bosonic gases, where  $s$ -wave scattering dominates (often replaced by a contact potential proportional to the scattering length  $a$ ) the physics of dipolar gases is governed by the interaction potential being long-range and anisotropic. There are several candidates to realize experimentally a dipolar quantum gas: Rydberg atoms [291], which can have very large induced electric dipole moments, molecules having a permanent electric dipole moment  $d$  [204, 203], or ground state atoms, e.g. chromium [120], having a large magnetic moment  $\mu$ . Recently dipolar effects has been observed in alkali atoms [94, 273]. This longer range interaction will allow access to a new regime of strongly correlated quantum gases with unique phase transitions, such as to supersolid phases for bosons [115] and to topological superfluid phases for fermions [62]. Dipolar atoms in two-dimensional lattices can be used in order to create controllable states, robust against small local imperfections, aimed to be quantum memories [224] used for quantum information processing.

### Quantum simulator

Conventional computers lack the processing power to calculate the behavior of complex quantum systems. For the general description of a quantum spin system with 300 particles a computer would need more memory than there is available in the world. Atoms in an optical lattice are a nearly perfect quantum simulator for solids, as they offer a very flexible model-system in a clean

and well-controlled environment. Recent development in this field go beyond the realization of simple cubic structures. More complex lattice configuration such as arrays of fully controllable double wells [271] has opened a way for study of magnetic systems [23] or the Landau-Zener phenomenon [56]. A possibility to generate artificially generated vector gauge potentials was demonstrated in [178] which shows possible to study the fractional quantum hall effect [129]. In the same fashion one can create ladder systems or 2D checkerboard structures studying topological effects on single plaquettes [208] or d-wave pairing and superconductivity [226]. The realization of triangular and hexagonal structures [26] exhibit very rich new phases showing, e.g. supersolidity [193, 282], quantum stripe ordered states, exotic superconducting states [188] or graphene-like physics [151]. Recently it was proposed how frustrated quantum magnets can be realized within a triangular optical lattice [87].

### Quantum Information Processing

Atoms in an optical lattice in the Mott insulator regime serve as a large qubit [16] register. Neutral atoms present two essential advantages for quantum information processing. They are relatively weakly coupled to the environment, so that decoherence can be controlled better than in most other systems [43]. A simple 1D model for quantum computation based on an optical lattice with one atom per lattice site and coherent manipulation between two different atomic ground states has been proposed in [207]. Another proposal for a massively parallel quantum gate array, which allows the creation of a highly entangled many-body cluster state through coherent collisions between atoms on neighboring lattice sites has been made [270]. Based on a double well potential a technique has been developed to address spatially dense field-intensitive qubit register and perform quantum gates [180].

### Relaxation Physics

Recent experiments, especially with ultracold gases, have revived the interest on relaxation physics of non-integrable and integrable systems. For integrable systems, the time evolution can cause a dephasing effect, leading for finite subsystems to certain steady states [24]. It is an open question whether a given integrable system in a certain initial state will evolve to any steady state and whether this will be a thermal state  $\rho \approx e^{-\sum_k a_k \hat{O}_k}$ . Such experiments with integrable systems have shown the absence of thermalization [157, 138]. An analytical prove under what circumstances integrable systems relax to non-canonical steady states has been given [24]. Whether or how thermalization occurs in non-integrable systems is in general unclear [228]. In the study of relaxation processes in coherent non-equilibrium dynamics of quenched quantum systems, ultracold atoms in optical superlattices with periodicity two provide a very fruitful test ground [101, 66]. While the global system preserves the information about the initial condition, local quantities, like local magnetization [24], relax to the state having maximum entropy respecting the constraints of the initial condition.

### Bose-Fermi mixtures

Mixtures between bosonic and fermionic gases in optical lattices form novel quantum many-body systems. Such mixtures occur frequently in nature, where usually bosons act as carriers of force between fermionic particles<sup>5</sup>. Since cooling of fermions very difficult due to the lack of  $s$ -wave scattering (three-body processes are very unlikely) most cooling strategies for fermions use evaporation of bosons. Thus, Bose-Fermi mixtures come across with experiments on ultracold fermions.

Pairing of fermions with one or more bosons opens a path to new quantum phases in one and more dimensions [202, 127, 221]. These mixtures also suggest fundamental relevance for a broad range of phenomena, like high- $T_C$  [141], but also exotic systems such as neutron stars and quark-gluon plasmas [259]. Recently a Bose-Fermi mixture was used as a playground for the investigation of chemical reactions [204].

## 3.3 Measurement in optical lattices

The primary tool of detecting and characterizing cold atom systems are interference experiments [32, 67]. First experiments have been focused on demonstrating macroscopic coherence of large Bose Einstein condensates [14]. Subsequent work has used interference experiments to explore more interesting phases and phenomena. To name only few examples, the interference in time-of-flight experiments was used to explore the superfluid to Mott insulator transition in optical lattices [118], analysis of fluctuations in low-dimensional systems [128, 138], and studies of phase diffusion and decoherence in dynamically split condensates [14, 137, 249]. But these interference patterns can also contain information about second- and higher-order coherence [6]. The analyse of second-order correlation and anticorrelations within the interference patterns has been used to demonstrate the Hanbury Brown Twiss [130] type of bunching of bosonic [102, 206, 252, 240, 126] and antibunching and fermionic atoms [231, 147, 119].

### 3.3.1 Time-of-flight and adiabatic measurement

There exist two possible methods to release ultracold gases from optical lattice. The first way is turn off the potential abruptly. Assuming that the atoms do not interact after the release a given Bloch state with quasimomentum  $q$  will expand according to its momentum distribution as a plane wave with momenta  $p_n = \hbar q \pm n2\hbar k$ . After a certain time of flight a laser beam illuminates the falling atoms and the resulting shadow is imaged on a CCD chip [154]. The amount of light absorbed is related to the column density of the atom cloud, and by comparing the shadow image to a reference image taken with no atoms present, the density distribution and atom number can be determined. The absorption imaging is destructive and one must rerun the experiment for every picture. The density distribution observed after a fixed time of flight at position  $\mathbf{x}$  (on the

<sup>5</sup>A prominent example of such systems is the conventional Bardeen-Cooper-Schrieffer superconductivity, caused by an effective interaction between fermions induced by the electron-phonon coupling.

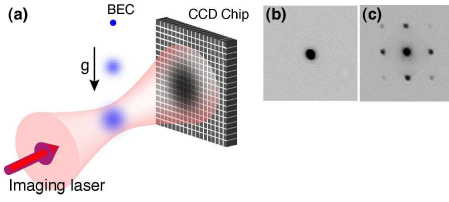


Figure 3.8: Time of flight measurement. A BEC is released from the harmonic trap (a) and, while expanding, falls down due to the gravitation force. After some time of flight an absorption image of the expanding cloud is taken, which can be seen in (b) and (c). Illustration from [37].

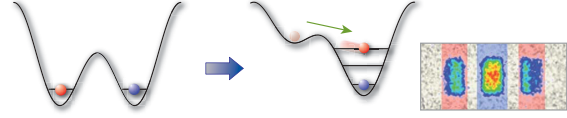


Figure 3.9: Density measurement via band mapping technique. The population of the left well is lifted by the help of a superlattice. As soon as the tunnel barrier between the left and right well becomes very small the particles from the left well can tunnel to right well where they initially occupy a higher band. During the adiabatic ramp down of the confining potential the quasi momentum is conserved. The Bloch wave in the  $n$ th energy band in the right well is mapped onto a free particle with momentum  $p$  in the  $n$ th Brillouin zone [271].

CCD chip) corresponds to the momentum distribution of the particles

$$n(\mathbf{x}) = (m\hbar t)^3 |w(\mathbf{k})|^2 \mathcal{G}(\mathbf{k}), \quad (3.33)$$

with  $\mathbf{k} = m\mathbf{x}/\hbar t$  due to the assumption of a ballistic expansion.  $w(\mathbf{k})$  is the Fourier transform of the Wannier function. All coherence properties are characterized by the Fourier transform

$$\mathcal{G}(\mathbf{k}) = \sum_{\mathbf{R}, \mathbf{R}'} e^{i\mathbf{k}(\mathbf{R}-\mathbf{R}')} G(\mathbf{R}, \mathbf{R}') \quad (3.34)$$

of the one-particle density matrix  $G(\mathbf{R}, \mathbf{R}') = \langle \hat{a}_{\mathbf{R}}^\dagger \hat{a}_{\mathbf{R}'} \rangle$ . However, the measured momentum distribution can deviate from the distribution in the optical lattice if one cannot neglect the interactions during the time of flight or if the expansion time is not long enough to guarantee that the initial size of the cloud can be neglected (far-field approximation) [212, 109].

Now, the second way to release the atoms profits from the big advantage of optical lattice potentials that the lattice depth can be dynamically controlled by simply tuning the laser power. By adiabatically opening a deep lattice and converting it into a shallow one the quasi-momentum  $\mathbf{q}$  is preserved. After releasing the atoms completely the Bloch-wave in the  $n$ th energy band is mapped onto a corresponding free-particle momentum  $\mathbf{p}$  in the  $n$ th Brillouin zone [152, 117, 160]. The homogeneously filled lowest energy band then corresponds to a fully occupied central Brillouin zone (a square of width  $2\hbar k$ ). If higher bands are populated one also observes populations in higher Brillouin zones. This is a very efficient method to visualize the distribution of particles over the Bloch states in different energy bands. It has been also applied successfully in combination with a double well potential to measure the population of the left and the right double well in a superlattice structure [249].

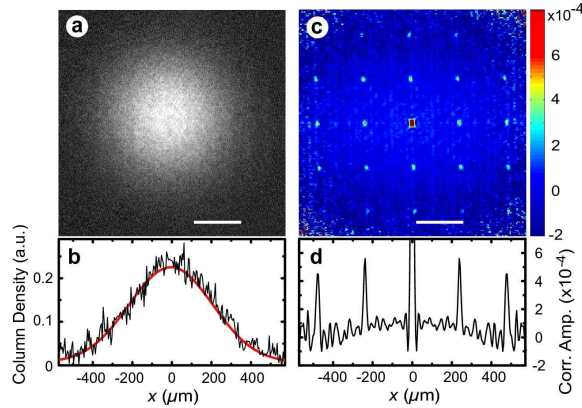


Figure 3.10: Noise correlations of a Mott insulator released from a 3 d lattice. Figure (a) shows the image of a single shot and a cut through the image (b). A statistical analysis over several single shot picture is shown in (c) together a cut through it (d). Figures are taken from [102].

### 3.3.2 Noise correlations

The successful study of an interacting many-body quantum system requires detection methods which are sensitive to higher-order correlations. Quantum fluctuations in many-body observable as fluctuation patterns in the momentum distribution after release from trap contain information about initial correlated quantum state [6, 220, 298, 122]. Among these noise-correlation techniques the most developed and used ones give information about the first- and the second-order correlation properties. The main reason why higher-order correlations are difficult to detect is due to the low intensity of the observed signal. Typically the observed signal is around  $10^{-3} - 10^{-4}$  and deviates significantly from the theoretically predicted value of 1. The development of CCD chips with a higher spatial and temporal resolution can overcome such limitations and also evaluate higher-order correlations.

Let us consider a quantum gas released from a trapping potential. After a certain flight time  $t$  the resulting density cloud yield a density distribution  $\hat{n}(\mathbf{x})$ . Assuming that there are no interactions after releasing the atoms and that the time-of-flight  $t$  is sufficiently large in order to use the far field approximation the average density distribution (repeating the experiment several times) is related to the quantum state in the trap (before the release) via

$$\langle \hat{n}(\mathbf{x}) \rangle_{\text{TOF}} = \langle \hat{a}^\dagger(\mathbf{x}) \hat{a}(\mathbf{x}) \rangle_{\text{TOF}} \approx \langle \hat{a}(\mathbf{k}) \hat{a}(\mathbf{k}) \rangle_{\text{trap}} = \langle \hat{n}(\mathbf{k}) \rangle_{\text{trap}}. \quad (3.35)$$

The above equation connects the density distribution after the time-of-flight with the momentum distribution reflecting first-order coherence properties of the state in the trap. However there is another source of fluctuations of the interference pattern which is purely quantum nature. Each pixel in the image records on average a substantial number of atoms. For each of those pixels the number of atoms recorded in a single realization of experiment will exhibit shot-noise fluctuations<sup>6</sup>. Shot noise is especially strong in systems with short-range single particle correlations, in particular in fermionic systems [122]. Probing coherence properties using interference

<sup>6</sup>This analog to the double slit experiment with single photons. For each run the position of the photon is random

is much more difficult in such systems than in system with a long- or quasi-long-range order. Here the shot noise is less important than the low wavelength thermal or quantum fluctuations [219] However when interactions have been enhanced , e.g. by Feshbach resonance, or a high density sample is prepared, Eq. [3.35] is not valid anymore.

So far I have only discussed the first-order coherence properties. The next order of coherences are encoded in the density-density correlations in the expanding cloud. Doing a similar analysis as in the first-order case one can find a relation between the density-density correlators in the cloud and the momentum density-density correlators of the state in the trap

$$\langle \hat{n}(\mathbf{x})\hat{n}(\mathbf{x}') \rangle_{\text{TOM}} \approx \langle \hat{a}^\dagger(\mathbf{k})\hat{a}(\mathbf{k})\hat{a}^\dagger(\mathbf{k}')\hat{a}(\mathbf{k}') \rangle_{\text{trap}} = \langle \hat{a}^\dagger(\mathbf{k})\hat{a}^\dagger(\mathbf{k}')\hat{a}(\mathbf{k}')\hat{a}(\mathbf{k}) \rangle_{\text{trap}} + \delta_{\mathbf{k}\mathbf{k}'} \langle \hat{a}^\dagger(\mathbf{k})\hat{a}(\mathbf{k}) \rangle_{\text{trap}}. \quad (3.36)$$

The last term in Eq. [3.36] only enters for  $\mathbf{x} = \mathbf{x}'$  and contains no more information about the initial quantum state than the momentum distribution [3.35] itself.

### 3.3.3 Recent development

#### Probing fermionic superfluidity

A new method for detecting paired states in either bosonic or fermionic systems has been proposed using interference experiments with independent or weakly coupled low dimensional systems [122]. Under the assumption of weakly coupled condensates (Josephson coupling) and region dependent noise measurement one is able to detect *s*-wave, *d*-wave and FFLO-like pairing.

#### Photoemission and Raman spectroscopy

In analogy to the photoemission spectroscopy in electronic systems a pulse of radio-frequency drives atoms into an unoccupied Zeeman spin state, where they are counted to yield a spectrum of counts versus radio-frequency frequency [225] [58]. While the first implementation of photoemission spectroscopy could not resolve the single-particle excitation spectrum (fundamental theoretical property), the elementary excitations and energy dispersion could be probed recently [256]. A similar but no identical technique is to use Raman transition, by using a weak external field, to change the internal states of atoms from a magnetically trapped state to an untrapped state. Afterwards the atoms can be extract from a trap to a free space [182, 190]. The output-coupling current from a Bose gas in the optical lattice can be directly related with single-particle correlation functions of the Bose-Hubbard model. Recently the Raman transition method has been successfully implemented for fermions [290] probing as well the momentum distribution [74] of the condensate.

#### Bragg spectroscopy

There exist several ways to sample the excitation spectrum of a complex system. This spectrum gives often crucial information about the many-body dynamics of this system. The Bragg spectroscopy [92] uses elementary excitations in ultra-cold atomic gases via the inelastic scattering of

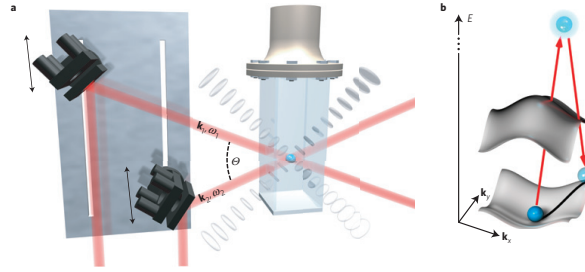


Figure 3.11: Bragg spectroscopy of a trapped condensate. A condensate was exposed to two counterpropagating laser beams and analyzed using time of flight absorption. If the momentum and energy of the laser beams is resonant with a two-photon transition in the atomic sample a transition occurs within the lowest phononic band. In this way one can obtain the whole dispersion relation of the system.

two laser light beams by the atomic sample. The light scattering process occurs when the energy transfer  $\varepsilon$  and the momentum transfer  $\mathbf{q}$  given by the laser beams is resonant with a two-photon transition (between the lowest bands) in the atomic sample. The two-photon transition does not change the internal state of the atoms. Bragg spectroscopy allows to extract information about the dynamical structure factor  $S(\mathbf{q}, \omega)$  and about the one-particle spectral function  $A(\mathbf{q}, \omega)$  and could be extended to study more exotic correlated phases of ultracold atoms [60].

### Real space microscopy

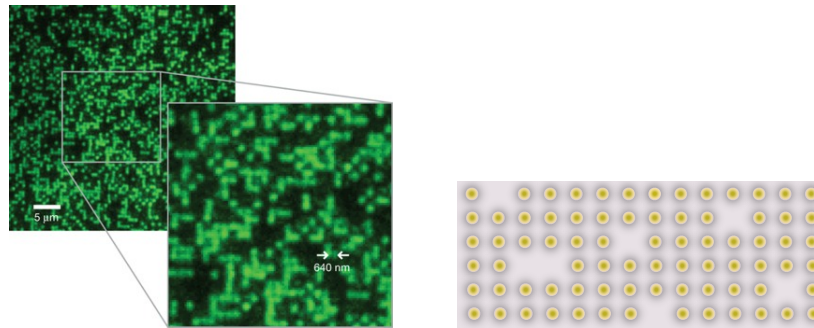


Figure 3.12: Direct microscopy of trapped atoms. The left picture is taken from a recent experiment by [21]. During an experiment the position of the atoms is frozen by making the whole lattice deeper. Next, the atoms are illuminated by a highly focused probe beam. The scattered fluorescence light is collected by an objective lens and projected onto a CCD. The additional knowledge about the possible positions of the atoms allows to obtain a resolution which is below the wave length of the probe beam. The same technique allows in principle to manipulate the atoms e.g. to create holes in order to study transport phenomena (right figure).

Recently the first successful attempt to visualize atoms in real space has been realized. By the implementation of a high-resolution optical imaging system, single atoms have been detected on individual sites of a Hubbard regime optical lattice [21]. In order to get an image of the system one has to freeze the position of the atoms by making the lattice very deep. Next, a highly focused probe beam scans the system and the scattered fluorescence light is collected by an objective lens and projected onto a CCD. Now, it turns out that together with the information about the

possible positions of the atoms one can find an atom even at a lattice spacing which is smaller than the wave length of the probe beam. Taking the fluorescence picture one can use advanced techniques from image analysis which allow for an identification of an atom out of the noisy picture. Moreover, it should be possible to use the probe beam in order to create holes in a regular structure and also to perform two-site operation which are the basis for quantum computing. So far, a direct microscopy of a whole setup will in general destroy the whole experiment. Therefore, in order to get a time-evolution one has to repeat the experiment a couple times.



## Chapter 4

# Magnetism, coherent many-particle dynamics, and relaxation with ultracold bosons in optical superlattices

One of the most exciting recent events in physics has been the increasing overlap between two previously disjoint fields, quantum optics and condensed matter physics. This has become possible due to the enormous progress in cooling dilute bosonic and also fermionic gases down to temperatures where respectively Bose-Einstein condensation and Fermi degeneracy (temperatures well below the Fermi energy) are reached.

A very attractive feature of this new class of experiments is that they provide the arguably cleanest realization of the (bosonic) Hubbard model [144], which with nearest-neighbor hopping and onsite interaction is the minimal model of strong correlation physics [140].

Here, I describe and analyze numerically a particular setup with ultracold bosons of two species in an optical superlattice, described by a Bose-Hubbard model. In the limit of strong onsite interactions, the system can be described by the spin-1/2 Heisenberg antiferro- or ferromagnet, depending on the parameters of the superlattice [23]. The motivation is fourfold:

(i) In the vein of Feynman's idea to simulate quantum systems by other quantum systems [99], it would be a great achievement to implement models of magnets like the Heisenberg model with ultracold atoms in optical lattices. In condensed matter systems, collective magnetism arises from the Coulomb interaction and the particle statistics which cause (super)exchange processes [132, 80, 133, 81, 164, 11, 13]. In particular, exchange interactions resulting from second order hopping processes in the Fermi-Hubbard model dominate its behavior in the limit of strong onsite interaction and are captured by an effective spin model, namely the Heisenberg antiferromagnet [13, 55, 95].

While collective magnetism has been widely studied in solids over the decades, several experimental restrictions apply quite generally: It is generally far from clear to what extent the typical simplified models are quantitatively realistic, and how to obtain the interaction parameters. External control of these parameters is very difficult. Moreover, quantum magnetism becomes particularly interesting in low dimensions. In real effectively low-dimensional solids it is however hard to control or assert the effect of the weaker interactions in the second and/or

third dimension. Last but not least, solids give us only access to the linear response regime as sampled e.g. by neutron scattering. Questions of out-of-equilibrium many-body dynamics are essentially inaccessible.

Experiments with ultracold atoms in optical lattices constitute clean and well-tunable manifestations of the Bose- or Fermi-Hubbard model [144, 38]. To implement magnetic systems, the most straight forward approach would hence be to use a gas of ultracold fermions. However, cooling of fermionic gases to the quantum regime is a considerably harder task due to the lack of s-wave scattering among identical fermions [76, 77, 201, 160, 59]. Hence it is desirable to develop an alternative route via gases of ultracold bosons. The here presented investigations follow this idea [166, 84, 7, 106, 22]. Although I focus here on one dimension, analogous setups in higher dimensions [248] could be used to investigate a plethora of frustrated spin systems that are hard to access analytically and numerically.

(ii) The superlattice structure chosen in the following setup (in analogy to the recent experiments [103, 271]) allows in contrast to [84, 7] for the tuning of the effective spin-spin interaction by changing an alternating scalar potential  $\Delta$ ; Fig 4.1. With the hopping strength  $t$  and the onsite interaction  $U$  of the Hubbard model, the coupling in the corresponding effective spin model is then  $4t^2U/(U^2 - \Delta^2)$ . This allows on the one hand to switch for the effective model between the Heisenberg ferro- and antiferromagnet. On the other hand one might hope to increase for a fixed onsite interaction  $U$  the effective coupling, by choosing  $\Delta \sim U$ . In this case, the relevant physics would become visible at correspondingly higher temperatures. However, the validity of the effective model breaks down in the vicinity of  $\Delta \sim U$ . So one has to balance the validity of the Heisenberg description and the temperatures needed to observe the quantum effects. To this purpose, the parameter  $\Delta$  can be easily varied and used to tune to the Heisenberg regime in controlled fashion.

(iii) In recent experiments [103, 271] by the Bloch group, the same optical superlattice as the one discussed here was used. But its parameters were chosen such that the superlattice decomposed actually into isolated double wells. The experiments analyzed dynamics in these double wells and contrasted in particular first order (hopping) processes (Hubbard regime) versus slower second order processes (Heisenberg regime). The next step would be to observe coherent many-particle dynamics after coupling the double wells. We analyze such a situation by the time-dependent density matrix renormalization group method (DMRG) [70, 285]. I focus on the coherent evolution of an initial Néel state and the differences between the Heisenberg and the Hubbard regimes and present the experimentally available observables.

(iv) Besides testing the coherence in the experiments, the setup allows to address questions of non-equilibrium many-particle systems, which is in general difficult for all present analytical and numerical methods. Contrary to the setup of isolated double wells, one observes for the many-particle dynamics in the here considered setup a relaxation of local quantities. This is an indicator for convergence of subsystems with finite real-space extent to a steady state. Recently, the mechanism of how such a relaxation may occur was clarified for (free) integrable systems in [24]. Corresponding examples can also be found in [229, 53, 65, 105]. For a few nonintegrable systems the question was analyzed numerically in [161, 186, 66] and analytically e.g. in [194, 88]. In general one expects that in nonintegrable models, thermalization occurs (due to scattering processes), and that in integrable models, relaxation (to a nonthermal steady state) occurs via

phase averaging effects [24]. This is demonstrated here analytically for the Heisenberg model. The setup could be used to study experimentally such relaxation processes – in particular, the qualitative differences between nonintegrable systems, here the Bose-Hubbard model, and Bethe ansatz integrable models [33, 296], here the Heisenberg model.

The here presented work also fill a certain gap of current literature on such topics (see e.g. [84, 7, 106]) by emphasizing that the Heisenberg spins of the effective model, obtained by the Schrieffer-Wolff transformation [245, 23], should not be identified directly with the two boson species. A spin up of the effective model corresponds rather to a particle of species 1 dressed by hole-double-occupancy fluctuations. The analogy holds only for small  $t/(U \pm \Delta)$ . The consequences for experimentally available observables are surprisingly strong. Recently in [22] a setup of coupled double wells ( $\Delta = 0$ , but alternating hopping  $t \neq t'$  in Fig. 4.1) was analyzed numerically – in particular, the possibilities to generate entangled pairs of particles were studied. Again, a perfect mapping to a spin model was assumed from the outset.

The chapter is organized as follows. Section 4.1 describes the experimental setup and how it can be described by a Bose-Hubbard model. Restricting to half filling, Section 4.2 derive by a Schrieffer-Wolff transformation for the limit of large onsite interactions an effective model which is the Heisenberg antiferro- or ferromagnet. In Section 4.3, I investigate by time-dependent density-matrix renormalization-group (DMRG) the evolution of typical observables like magnetization, momentum-space and real-space correlators, where the first two are also available experimentally. The focus is on contrasting the differences between the full Hubbard dynamics and the corresponding effective spin model, and also the differences to the case of isolated double wells [103, 271]. Indications for (local) relaxation to steady states can be observed. This is discussed in Section 4.4 where I also explain how the relaxation for the Heisenberg model is connected to a phase averaging effect. Section 4.5 addresses in more detail the question why and under what circumstances the effective model is a valid description for the full Hubbard Hamiltonian, especially for the dynamics. In Section 4.6 I argue that the groundstate of the Heisenberg antiferromagnet could be prepared by tuning an alternating hopping parameter of the superlattice adiabatically. Section 4.7 gives a short conclusion.

## 4.1 Setup and model

In the following, I present a setup of ultracold bosonic atoms in a one-dimensional optical superlattice that reduces in certain parameter regimes, where first order hopping processes are suppressed, to the Heisenberg ferro- or antiferromagnet. The use of bosons is motivated by the fact that experimentally, access to the low energy quantum physics is at the moment still much harder for fermionic systems. In analogy to the fermionic case, for which the antiferromagnetic Heisenberg model describes the effective low-energy physics of the fermionic Hubbard model, I choose to have two species  $\sigma \in \{\uparrow, \downarrow\}$  of bosons in the lattice – two hyperfine states of a bosonic atom. At half filling ( $N$  sites,  $N_\uparrow = N_\downarrow = N/2$ ), the effective low energy model is, as one will see later, the ferromagnetic Heisenberg model. To allow for tuning the effect of first order processes and to switch between a ferromagnetic and antiferromagnetic regime, I employ an alternating onsite potential  $\Delta_i$  and call the two sublattices  $\mathcal{A}$  and  $\mathcal{B}$ . The potential minima differ by a value

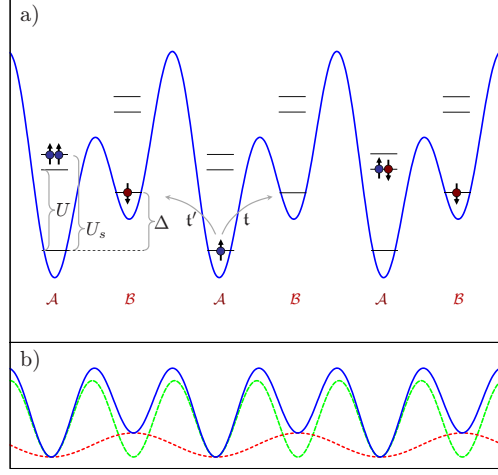


Figure 4.1: a) Tight-binding system parameters for the here considered system of ultracold bosons of two species ( $\uparrow, \downarrow$ ) in a one-dimensional optical superlattice (4.1). b) If the phase shift between the two laser potentials (dashed lines) is zero, the minima of the full potential (solid line) are equidistant, the Wannier wave functions for each site are reflection symmetric, and hopping parameters  $t$  and  $t'$  are hence equal.

$\Delta > 0$ . Such superlattices can be generated by the superposition of two laser frequencies of ratio 1 : 2, see Ref. [9, 103, 271] and Fig. 4.1. Further, the tight-binding approximation with restriction to the first Bloch band (one Wannier function per site) is assumed. Then the system is described by the two-species Bose-Hubbard Hamiltonian

$$\hat{H} = -t \sum_{\sigma, \langle ij \rangle} (a_{\sigma i}^\dagger a_{\sigma j} + H.C.) + \sum_{\sigma, i} \Delta_i n_{\sigma, i} + U \sum_i n_{\uparrow i} n_{\downarrow i} + \frac{U_s}{2} \sum_{\sigma, i} n_{\sigma i} (n_{\sigma i} - 1), \quad (4.1)$$

In particular, I choose

$$\Delta_i = \begin{cases} -\Delta/2 & \text{for even } i \\ \Delta/2 & \text{for odd } i. \end{cases} \quad (4.2)$$

The superlattice potential is of the form [cp. Eq.3.26]

$$V(x) = V_0 \sin^2(kx) + V_1 \sin^2(kx/2 + \phi). \quad (4.3)$$

The amplitude  $V_1$  of the second potential can be used to tune  $\Delta$ ; for my purposes,  $V_1 \ll V_0$ . In (4.1) it was assumed that hopping from a site  $i$  to its neighbors  $i \pm 1$  occurs with equal amplitude  $t$ . In principle, the hopping depends exponentially on the distance between the potential minima [144, 301]. Only if one chooses the phase difference  $\phi$  to vanish as in Fig. 4.1b, the positions of the potential minima will be equidistant for all  $V_1$ , and the Wannier wave functions for all sites are reflection symmetric. In this case, the hopping will hence be of equal strength for all bonds, i.e.  $t = t'$  in Fig. 4.1. This situation is considered in the following.

For the actual analysis of dynamics in Section 4.3, I will choose equal inter- and intra-species interaction,  $U = U_s$ . This is at the moment the standard situation for the corresponding experiments. With  $U = U_s$ , the effective Heisenberg models, describing the second order physics, will

turn out to be isotropic. The onsite potential  $\Delta$  and interaction  $U$  can be calculated in harmonic approximation of the lattice potential around its minima. For  $\phi = 0$  in (4.3), the corresponding oscillator frequencies are  $\hbar\omega_{\pm} = 2\sqrt{E_r(V_0 \pm V_1/4)} \approx 2\sqrt{E_r V_0}(1 \pm \frac{1}{8}\frac{V_1}{V_0})$ , where  $E_r \equiv \frac{\hbar^2 k^2}{2m}$  is the recoil energy of the laser potential with the shorter wave length. For the dependence of the onsite potential on the lattice parameters follows

$$\Delta = V_1 - \frac{\hbar}{2}(\omega_+ - \omega_-) \approx V_1 \left(1 - \frac{1}{4}\sqrt{\frac{E_r}{V_0}}\right). \quad (4.4)$$

In order to achieve an effectively one-dimensional lattice,  $V(x)$  is superimposed with two transversal laser beam potentials of a (higher) amplitude  $V_{\perp}$ . Within the harmonic approximation, and with the s-wave scattering length  $a_s$ , the resulting onsite interactions for two neighboring sites are [301]

$$U_{\pm} = \sqrt{\frac{8}{\pi}} a_s k \left( \frac{(V_0 \pm V_1/4)V_{\perp}^2}{E_r^3} \right)^{\frac{1}{4}} E_r. \quad (4.5)$$

They are in principle not identical. Irrespective of this, the effective spin model derived in Section 4.2 would be isotropic and translation invariant. As I will show in the following for a set of realistic experimental parameters, one finds for the case  $V_1 = 0$  ( $\Rightarrow \Delta = 0$ ) that  $V_0 \gg E_r$  and  $V_0 \gg U$ . The onsite potentials  $\Delta$  considered in the here presented numerical simulations of the Hubbard model (4.1) are from the interval  $\Delta \in [0, 4U]$ . According to (4.4),  $V_1$  will for nonzero  $\Delta$  hence obey  $V_0 \gg V_1$  and one can thus use  $U_+ = U_- \equiv U$  in good approximation.

For the tight-binding approximation to hold, one needs that energies  $t$ ,  $U$ , and  $\Delta$  are well below  $\hbar\omega_{\pm} \approx 2\sqrt{E_r V_0}$ , the energy scale for vibrations of an atom in one minimum of the laser potential. With the hopping  $t = \frac{4}{\sqrt{\pi}} (V_0 V_{\perp}^2 / E_r^3)^{1/4} e^{-2\sqrt{V_0/E_r}} E_r$  [301, 38], one has for example with  $\lambda = 2\pi/k = 800nm$ , Rubidium atoms (i.e.  $a_s k \approx \pi 0.01$ ),  $V_0 \approx 8.7E_r$  and  $V_{\perp} \approx 30E_r$  (cmp. e.g. to [103]) that  $t \approx 0.06E_r$ ,  $U \approx 8t$  and  $\hbar\omega_0 \approx 100t$ . So as long as  $\Delta$  is also well below  $100t$ , the tight-binding approximation for (4.1) using the lowest Bloch band is valid.

## 4.2 Effective model

To go to a regime where the physics of the two-species Bose-Hubbard model (4.1) reduces to that of a Heisenberg magnet, I choose half filling

$$N_{\downarrow} = N_{\uparrow} = N/2, \quad (4.6)$$

( $N$  is the total number of lattice sites) and assume the large- $U$  limit

$$t \ll |U \pm \Delta|. \quad (4.7)$$

In this limit, occupation of a single site by more than one boson is energetically unfavorable and will occur only in short lived intermediate states. This means that single (first order) hopping processes are suppressed. Besides some hybridization effects, exactly one boson sits on each lattice site and can be identified with an effective spin on that site (up and down orientations

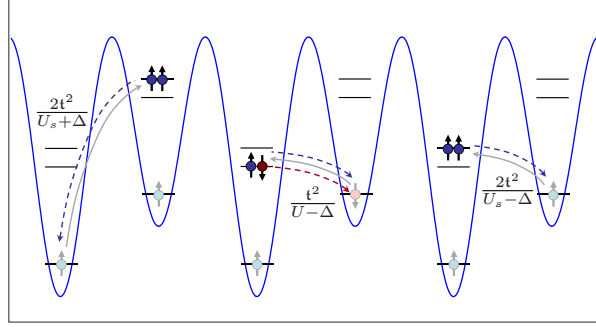


Figure 4.2: Some second order hopping processes (superexchange) contributing to the effective spin model (4.9) when first order hopping processes in the full Hubbard model (4.1) are suppressed. The figure displays possible initial states (light color) with one particle per site and intermediate states (dark color) with doubly occupied and empty sites.

corresponding each to one of the boson species). The second order hopping processes as depicted in Fig. 4.2 lead then to nearest neighbor spin-spin interactions.

I will show below, how the effective Hamiltonian can be derived by a Schrieffer-Wolff transformation. While this is a well-known procedure, there is an interesting twist to the interpretation of the result. For the moment I will work with the naive identification of spins up and down of the effective model with the two boson species of the full model (4.1). I want to derive an effective Hamiltonian describing the physics of the Hubbard Hamiltonian (4.1) in the subspace  $\mathcal{H}_1$  of singly-occupied sites.

$$\mathcal{H}_1 := \text{span}\{|\uparrow\rangle, |\downarrow\rangle\}^{\otimes N} \quad (4.8)$$

The effective Hamiltonian can be deduced from the following simple recipe: With exactly one spin per site, the onsite interaction is ineffective. Hopping processes occur only in second order, leading to a spin-spin interaction

$$\hat{H}_{\text{eff}} = -J \sum_{\langle ij \rangle} (\hat{S}_i^x \hat{S}_j^x + \hat{S}_i^y \hat{S}_j^y) + (J - J_s) \sum_{\langle ij \rangle} \hat{S}_i^z \hat{S}_j^z. \quad (4.9)$$

The corresponding coupling strengths  $J$  and  $J_s$  are obtained by dividing for each possible second order process (Fig. 4.2) the product of the transition matrix elements  $t \cdot t$  for the hopping to a neighboring site and back by the energy difference  $U \pm \Delta$  ( $U_s \pm \Delta$ ) to the intermediate state, and adding all such terms that contribute to the same effective spin-spin interaction (see also [271]).

$$J = \frac{2t^2}{U + \Delta} + \frac{2t^2}{U - \Delta} = \frac{4t^2 U}{U^2 - \Delta^2}, \quad J_s = 2 \frac{4t^2 U_s}{U_s^2 - \Delta^2}. \quad (4.10)$$

The effective Hamiltonian (4.9) is the XXZ model. From now on I specialize to  $U = U_s$ , i.e.  $J - J_s = -J$  and have hence the isotropic Heisenberg ferromagnet for  $\Delta < U$  ( $J > 0$ ) and the isotropic antiferromagnet for  $\Delta > U$  ( $J < 0$ ). Note that the effective Heisenberg Hamiltonian would also be isotropic and translation invariant if the onsite interaction  $U$  would be different for

even and odd sites. If the hopping would be alternating ( $t \neq t'$ ), one would obtain the dimerized Heisenberg model.

A common mathematical approach for the deduction of such effective models is the Schrieffer-Wolff transformation [245]. I am interested in the physics of the subspace  $\mathcal{H}_1$  with exactly one particle per site. The Hubbard Hamiltonian couples this subspace in first order of the hopping  $t$  to the rest of the Hilbert space (states with doubly occupied and empty sites). The Schrieffer-Wolff transformation,

$$\hat{H}_{\text{eff}}^{\text{full}} := e^{i\hat{\mathcal{S}}} \hat{H} e^{-i\hat{\mathcal{S}}}, \quad \mathcal{H}_1^{\text{orig}} := e^{-i\hat{\mathcal{S}}} \mathcal{H}_1, \quad (4.11)$$

is a unitary transformation with generator  $\hat{\mathcal{S}}$  chosen such that the transformed Hamiltonian  $\hat{H}_{\text{eff}}^{\text{full}}$  does not contain terms anymore that couple  $\mathcal{H}_1$  to the rest of the Hilbert space, or at least only in some higher order of  $t$ . Together with the appropriate generator [23]

$$\hat{\mathcal{S}} = \mathcal{O}\left(\frac{t}{U \pm \Delta}\right), \quad (4.12)$$

one obtains the effective Hamiltonian

$$\hat{H}_{\text{eff}} = \hat{H}_{\text{eff}}^{\text{full}}|_{\mathcal{H}_1} = -J \sum_{\langle ij \rangle} \hat{S}_i \cdot \hat{S}_j + \mathcal{O}(t^4). \quad (4.13)$$

The full effective Hamiltonian  $\hat{H}_{\text{eff}}^{\text{full}}$  still contains a term  $i[\hat{\mathcal{S}}, \hat{H}_t^0]$  representing the remaining coupling of the subspace  $\mathcal{H}_1$  to the rest of the Hilbert space which is of order  $t^2$ .

The method is based on the smallness of  $\hat{\mathcal{S}}$ . According to (4.12), it hence breaks down when  $U \sim |\Delta|$ . The effective Hamiltonian (4.13) is only valid for  $|U \pm \Delta| \gg t$ . Only in this regime, the first order hopping processes leading out of  $\mathcal{H}_1$  are suppressed. See the discussion in Section 4.5.

Often spin up (down) states of the effective model are then identified with a boson of species  $\uparrow$  (species  $\downarrow$ ) on the corresponding sites. However, with respect to the original model, Eq. (4.1), it is *not*  $\mathcal{H}_1$  itself that is weakly coupled to the rest of the Hilbert space and evolves according to the Heisenberg Hamiltonian but the subspace  $\mathcal{H}_1^{\text{orig}}$  defined in Eq. (4.11). A spin up in the effective model corresponds rather to a boson of species  $\uparrow$  with a cloud of hole-double-occupancy fluctuations  $a_{\sigma i} \rightarrow e^{i\hat{\mathcal{S}}} a_{\sigma i} e^{-i\hat{\mathcal{S}}}$ ; see also Fig. 4.3. The experimental consequences are surprisingly strong, as I will show in the next section.

## 4.3 Time-evolution from the Néel state

In the following, numerical results for the evolution of the system where the initial state is the Néel state

$$|\phi\rangle := |\uparrow\downarrow\uparrow\downarrow\uparrow\downarrow\dots\rangle \in \mathcal{H}_1 \quad (4.14)$$

are presented. This parallels recent experimental investigations [103, 271] of the evolution of corresponding states  $|\uparrow\downarrow\rangle$  in isolated double wells.

To compare the effect of first and second order processes, the evolution was done twice for each set of parameters ( $t = 1$ ,  $U = 8$ , various  $\Delta$ ; see Section 4.1), once with the corresponding

Heisenberg model (in the subspace  $\mathcal{H}_1$ ) and once with the full Hubbard Hamiltonian (in the full Hilbert space), where the initial state (4.14) was in fact chosen as the tensor product of alternatingly having one boson of species  $\uparrow$  or  $\downarrow$  on each site. The two different time scales of first and second order processes become clearly visible. The qualitative differences to the isolated double well situation (as analyzed in [103, 271]) and resulting interesting questions for experimental investigations are discussed.

### 4.3.1 Errors through experimental limitations in state preparation and measurement

I shortly want to discuss how well the dynamics of the magnetic model, the Heisenberg model, can be implemented experimentally by those of the two-species Bose-Hubbard model. In the literature on magnetism via ultracold two-species atom gases in optical lattices [84, 7, 22], spins up and down of the magnetic system are usually identified directly with atoms of species  $\uparrow$  and  $\downarrow$  of the ultracold gas. In this vein, evolution of the Néel state (4.14) with the Heisenberg Hamiltonian would be translated into evolution of the state  $|\uparrow\downarrow\uparrow\downarrow\uparrow\downarrow\dots\rangle$  with the Hubbard Hamiltonian. This is actually correct only to zeroth order in  $\mathcal{S}$ .

I want to implement the evolution of a state  $|\phi\rangle \in \mathcal{H}_1$ , (4.8), under the effective Hamiltonian  $\hat{H}_{\text{eff}} = e^{i\mathcal{S}}\hat{H}e^{-i\mathcal{S}}|_{\mathcal{H}_1}$  by the evolution of a state  $|\psi\rangle = e^{-i\mathcal{S}}|\phi\rangle \in \mathcal{H}_1^{\text{orig}}$ , (4.11), under the Bose-Hubbard Hamiltonian  $\hat{H}$ . The state  $|\psi\rangle$  is  $|\phi\rangle$ , superimposed with states where starting from  $|\phi\rangle$ , pairs of doubly occupied sites and empty sites were created (e.g. Eq. (4.18) and Fig. 4.3 below). This can also be interpreted as constructing the Néel state with effective spins, each corresponding to a boson accompanied by a cloud of hole-double-occupancy fluctuations  $a_{\sigma i} \rightarrow e^{i\mathcal{S}} a_{\sigma i} e^{-i\mathcal{S}}$ . The decisive point is now that it seems not possible to prepare such states from  $\mathcal{H}_1^{\text{orig}}$  (and has to my knowledge never been done), but only some specific states from  $\mathcal{H}_1$ . Hence, instead of starting the experiment from the initial state  $|\psi\rangle$ , one is forced to neglect the Schrieffer-Wolff transformation and start from the state  $|\phi\rangle$  – in my example the Néel state. For observables that do not change the number of doubly occupied sites, this results in an error of  $\mathcal{O}(\mathcal{S}^2)$ .

If one had determined the exact Schrieffer-Wolff transformation  $e^{-i\mathcal{S}}$  (i.e.  $\mathcal{S}$  exact to all orders in  $\mathfrak{t}$ ) and could actually implement it e.g. by time evolution in the experiment, all measurements would be exact. One could prepare the state  $|\phi\rangle$ , apply the Schrieffer-Wolff transformation by time evolution to obtain  $|\psi\rangle$ , evolve with the Hubbard Hamiltonian for some time  $t$ , apply the inverse Schrieffer-Wolff transformation and measure the observable  $\hat{O}$ . This would yield the exact equality

$$\langle\phi|e^{-\hat{H}_{\text{eff}}t/i\hbar}\cdot\hat{O}\cdot e^{\hat{H}_{\text{eff}}t/i\hbar}|\phi\rangle = \langle\phi|e^{i\hat{S}}e^{-\hat{H}t/i\hbar}e^{-i\hat{S}}\cdot\hat{O}\cdot e^{i\hat{S}}e^{\hat{H}t/i\hbar}e^{-i\hat{S}}|\phi\rangle, \quad (4.15)$$

where  $\hat{H}_{\text{eff}}$  would now of course be a generalization of the Heisenberg model with longer ranged interactions.

Using a  $\mathcal{S}$  which is determined to first order in  $\frac{\mathfrak{t}}{U_{\pm\Delta}}$  instead of the exact one<sup>1</sup>, the remaining

<sup>1</sup>and correspondingly  $\hat{H}_{\text{eff}}$  to first order in the effective coupling  $J$



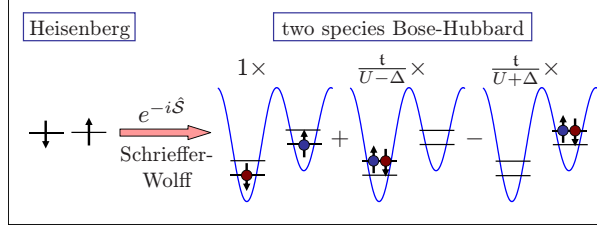


Figure 4.3: Spin up (down) states of the effective magnetic model are not to be identified directly with a boson of species  $\uparrow$  (species  $\downarrow$ ) in the experimentally realized Bose-Hubbard model. A spin up in the effective model corresponds rather to a boson of species  $\uparrow$  with a cloud of hole-double-occupancy fluctuations  $a_{\sigma i} \rightarrow e^{i\hat{\mathcal{S}}} a_{\sigma i} e^{-i\hat{\mathcal{S}}}$ . In the vicinity of  $\Delta = U$ , the correspondence breaks down.

errors [23] in the observables are of order  $\hat{\mathcal{S}}^4$ , i.e.  $\mathcal{O}((\frac{t}{U \pm \Delta})^4)$ . However, failing to implement the Schrieffer-Wolff transformation completely, i.e. measuring  $\langle \phi | e^{-\hat{H}t/i\hbar} \cdot \hat{O} \cdot e^{\hat{H}t/i\hbar} | \phi \rangle$  instead of (4.15), leads to errors of order  $\hat{\mathcal{S}}^2$ . This will be demonstrated in an example (Section 4.3.4). In addition to the error from neglecting or truncating the Schrieffer-Wolff transformation, there is the error from truncating the effective Hamiltonian (4.13). This accumulates with time and is in principle of order  $J^2 t$ , but may also just result in a sort of rescaling of the time axis. Also the local observables considered relax relatively quickly, making this second source of error less important.

In the remainder of the article, the initial state (4.14), evolved with the Heisenberg Hamiltonian (4.13) will be called  $\phi(t)$ . If it is evolved with the Hubbard Hamiltonian (4.1), it will be called  $\tilde{\phi}(t)$ .

$$|\phi(t)\rangle := e^{\hat{H}_{\text{eff}}t/i\hbar} |\phi\rangle \quad \text{and} \quad |\tilde{\phi}(t)\rangle := e^{\hat{H}t/i\hbar} |\phi\rangle, \quad (4.16)$$

and concerning observables I have explained that

$$\langle \hat{O} \rangle_{\tilde{\phi}} = \langle \hat{O} \rangle_{\phi} + \mathcal{O}(\hat{\mathcal{S}}^2). \quad (4.17)$$

To illustrate the considerations above, I shortly regard the case of an isolated double well (two sites). Hamiltonian and  $\hat{\mathcal{S}}$  read

$$\begin{aligned} \hat{H} &= \hat{H}_t + \hat{H}_0 \\ \hat{H}_0 &= (U + \Delta) |0, \uparrow \downarrow\rangle \langle 0, \uparrow \downarrow| + (U - \Delta) | \uparrow \downarrow, 0\rangle \langle \uparrow \downarrow, 0| \\ \hat{H}_t &= -t(|0, \uparrow \downarrow\rangle \langle \uparrow, \downarrow| + | \uparrow \downarrow, 0\rangle \langle \downarrow, \uparrow| + H.C.) \\ \hat{\mathcal{S}} &= \frac{it}{U - \Delta} | \uparrow \downarrow, 0\rangle (\langle \downarrow, \uparrow| + \langle \uparrow, \downarrow|) - \frac{it}{U + \Delta} |0, \uparrow \downarrow\rangle (\langle \downarrow, \uparrow| + \langle \uparrow, \downarrow|) + H.C.. \end{aligned}$$

With this, the effective Hamiltonian and the transformed initial state are

$$\begin{aligned} \hat{H}_{\text{eff}} &= -\frac{4t^2 U}{U^2 - \Delta^2} \hat{S}_1 \cdot \hat{S}_2 + \mathcal{O}(\hat{\mathcal{S}}^4) \\ e^{-i\hat{\mathcal{S}}} | \uparrow, \downarrow \rangle &= (1 - i\hat{\mathcal{S}}) | \uparrow, \downarrow \rangle + \mathcal{O}(\hat{\mathcal{S}}^2) \\ &\simeq | \uparrow, \downarrow \rangle + \frac{t}{U - \Delta} | \uparrow \downarrow, 0 \rangle - \frac{t}{U + \Delta} |0, \uparrow \downarrow \rangle. \end{aligned} \quad (4.18)$$

So a magnetic state with one particle per site corresponds in the experimentally realized Hubbard model to the magnetic state plus an admixture of states with doubly occupied and empty sites, Fig. 4.3. The original Hamiltonian generates with  $\hat{H}_t$  doubly occupied sites to first order in  $t$ . Conversely, in the (full) effective model, such terms are at least of order  $t^2$  (in the two site case here, actually of order  $t^4$ ).

### 4.3.2 Symmetry between the ferromagnetic and the antiferromagnetic cases

The Néel state  $|\phi\rangle$ , (4.14), and the effective Hamiltonian (4.13) are both real in the  $\{S_i^z\}_i$ -eigenbasis  $\mathcal{B} := \{|\sigma\rangle = |\sigma_1\sigma_2\dots\rangle\}$  (real coefficients and matrix elements). Typical observables  $\hat{O}$  of interest like  $\hat{S}_i^z$  for the magnetization or  $\hat{S}_i^z\hat{S}_j^z$  and  $\hat{S}_i^+\hat{S}_j^- + \hat{S}_j^+\hat{S}_i^-$  for correlators are real in that basis and selfadjoint. It follows that the corresponding expectation values  $\langle\hat{O}\rangle_{\phi(t)}$  are identical for the Heisenberg ferromagnet ( $J = 1$ ) and antiferromagnet ( $J = -1$ ): Let  $o_{\sigma,\sigma'} := \langle\sigma|\hat{O}|\sigma'\rangle$ ,  $\phi_\sigma := \langle\sigma|\phi\rangle$ , and  $u_{(a)\text{fm},\sigma,\sigma'}(t) := \langle\sigma|\hat{U}_{(a)\text{fm}}(t)|\sigma'\rangle$  for the time evolution operator of the (anti)ferromagnetic Heisenberg model. Then

$$\mathbb{R} \ni \langle\phi|U_{\text{fm}}^\dagger(t) \cdot \hat{O} \cdot U_{\text{fm}}(t)|\phi\rangle = \left(\phi^\dagger u_{\text{fm}}^\dagger(t) \cdot o \cdot u_{\text{fm}}(t)\phi\right)^* \quad (4.19)$$

$$= \phi^\dagger (u_{\text{fm}}^\dagger(t))^* \cdot o \cdot (u_{\text{fm}}(t))^* \phi \quad (4.20)$$

$$= \langle\phi|U_{\text{afm}}^\dagger(t) \cdot \hat{O} \cdot U_{\text{afm}}(t)|\phi\rangle. \quad (4.21)$$

The evolution of the corresponding observable under the full Hubbard Hamiltonian  $\langle\hat{O}\rangle_{\tilde{\phi}(t)}$  will obey this symmetry to zeroth order in  $\mathcal{S}$ . Typically, the resulting curve will coincide well with the corresponding Heisenberg curve. The smaller  $|U^2 - \Delta^2|$  is chosen, the worse the effective model will capture the actual dynamics and the stronger deviations from the corresponding Heisenberg results will be. The specific form of the deviations, however, will depend on the choice of  $U$ ,  $\Delta$ , and  $t$ . In particular they show no symmetry when switching between the antiferromagnetic and the ferromagnetic regimes ( $\Delta \gtrless U$ ). To illustrate this further, several plots contain the two curves  $\Delta = 0$  and  $\Delta = \sqrt{2}U$  which have according to (4.10) the same effective spin spin interaction strength  $J$ , except for the opposite sign (FM, AFM, respectively).

### 4.3.3 Numerical method and parameters

For the numerical simulation, a Krylov subspace variant [210, 136] of the time-dependent DMRG algorithm is used [285, 70, 243]. For the Hubbard model, the site basis is restricted to a maximum of two particles for each species. Insensitivity of observables to the chosen maximum number of bosons per site was affirmed. I chose a lattice sizes of  $L = 33$  for the Bose-Hubbard model and  $L = 65$  sites for the Heisenberg model. Odd numbers are useful here to have reflection symmetric states.

As a matter of fact, boundary effects are much less problematic here than in groundstate calculations, as the initial state is a product state and correlations between sites are generated inside a causal cone (the analogon of a light cone; see Section 4.3.5, in particular Figs. 4.9

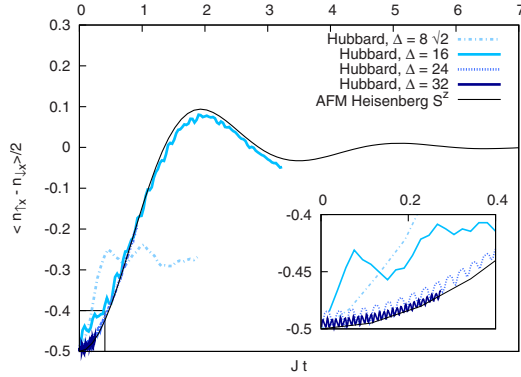


Figure 4.4: Evolution of the magnetization on a particular site  $x$ , starting from the Néel state and evolving with respect to the full Hubbard Hamiltonian with  $U = 8$  and  $\Delta > U$ , and the isotropic Heisenberg antiferromagnet, respectively. The first order processes occur on the time scale  $t = 1$  (here  $1/J$  due to the rescaling of the time axis, where time is given in units of the effective coupling  $J$ ) and their amplitude decreases quickly with increasing  $|U^2 - \Delta^2|$ .

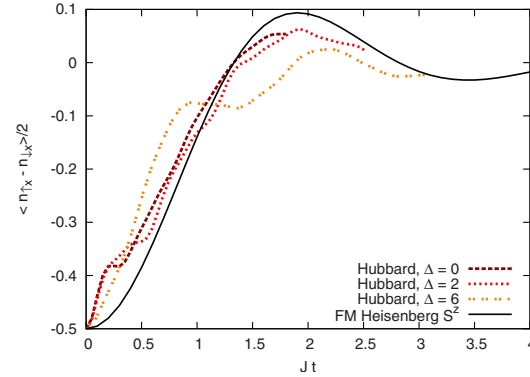


Figure 4.5: Evolution of the magnetization on a particular site  $x$ , starting from the Néel state and evolving with respect to the full Hubbard Hamiltonian with  $U = 8$  and  $\Delta < U$ , and the isotropic Heisenberg ferromagnet, respectively. The first order processes occur on the time scale  $t = 1$ . Here the contributions of the first order processes cannot be made arbitrarily small as one is limited by  $|U^2 - \Delta^2| \leq U^2$ . The Heisenberg curve here is identical to the one of the antiferromagnet in Fig. 4.4 due to symmetry, see Section 4.3.2.

and 4.11). So as long as measurements are done in the middle of the system, outside of the causal cones starting from the boundary sites, results are except for exponentially small contributions identical to those of an infinite system (thermodynamic limit).

In the time evolution, the absolute difference per physical time unit between exactly evolved state and the state evolved via DMRG  $\|\psi_{dt}^{\text{exact}} - \psi_{dt}^{\text{DMRG}}\|/dtN$  is bounded from above by  $\varepsilon = 10^{-4}$  to  $\varepsilon = 10^{-6}$  and the time step chosen appropriately between  $dt = 0.1$  and  $0.01$ . The errors are determined in a rigorous fashion, by calculating the exact value of  $\| |k+1\rangle - \hat{H}|k\rangle \|$ , where  $|k\rangle$  are the Krylov vectors. For all calculated observables, convergence in the error bound and  $dt$  was checked. The resulting number of basis states, used to represent the time-evolved state, is  $\lesssim 3000$ .

### 4.3.4 Site magnetization

Figures 4.4–4.6 show the evolution of the site magnetization  $m_x = \langle \hat{S}_x^z \rangle_\phi$  in the Heisenberg model and the corresponding quantity  $\tilde{m}_x = \langle n_{\uparrow x} - n_{\downarrow x} \rangle_{\tilde{\phi}} / 2$  ( $= \langle \hat{S}_x^z \rangle_\phi + \mathcal{O}(\mathcal{J}^2)$ ) according to Section 4.3.1) for the full Hubbard Hamiltonian. For the latter, times are rescaled by the coupling constant  $J$ , (4.10), of the corresponding effective spin model. Site  $x$  is chosen to be in the middle of the system in order to avoid finite size effects (cf. Section 5.2.1). For the Heisenberg model (in the thermodynamic limit), the site magnetization obeys for symmetry reasons  $m_{x+1} = -m_x$ . Analogously, due to invariance under translations by an even number of sites and particle number conservation, one has for the Hubbard model (again in the thermodynamic limit)  $\langle n_{\sigma x} + n_{\sigma x+1} \rangle_{\tilde{\phi}} = 1 \forall t$  and hence  $\tilde{m}_{x+1} = -\tilde{m}_x$ , and  $\langle n_{\uparrow x+1} + n_{\downarrow x+1} \rangle_{\tilde{\phi}} = 2 - \langle n_{\uparrow x} + n_{\downarrow x} \rangle_{\tilde{\phi}}$  for all

times. As discussed in Section 5.2.1, deviations of the numerical results from the thermodynamic limit are negligible, although the simulations are carried out with finite lattice sizes.

The larger  $|U^2 - \Delta^2|$  is (for fixed  $t = 1$ ), the better the curves for the full Hubbard Hamiltonian coincide with those of the Heisenberg model. This is consistent with Sec. 4.2 as the perturbative derivation of the effective model becomes exact in this limit. Note that the deviations between the measurements stem from two contributions here: (a) failure of preparing the correct  $\mathcal{H}_1^{\text{orig}}$  state, i.e. applying the Schrieffer-Wolff transformation at  $t = 0$ , (b) failure of measuring  $\hat{S}_x^z$  instead of  $e^{-i\hat{\mathcal{S}}}\hat{S}_x^ze^{i\hat{\mathcal{S}}} = \hat{S}_x^z - i[\hat{\mathcal{S}}, \hat{S}_x^z] + \mathcal{O}(\hat{\mathcal{S}}^2)$ . The weight of those errors which are of order  $\hat{\mathcal{S}}^2$  vanishes only far away from  $|\Delta| = U$ .

For the Heisenberg model, one observes relaxation of the site magnetization from  $\pm 1/2$  to 0. The oscillations of this observable occur on the time scale  $1/J$ . The relaxation is possible due to the continuous spectrum of the Heisenberg model (in the thermodynamic limit). Here, the convergence to a steady state is connected to a phase averaging effect, as is typical for integrable systems. Analytically this can be seen in a time-dependent mean field treatment of the Heisenberg model which I present in Section 4.4.2. For the staggered magnetization ( $m_x$ ) one obtains (in this approximation) a damped oscillation with the amplitude decaying as  $\sim 1/t^{3/2}$ . This coincides well with the DMRG data, giving support to the mean field approach; see Section 4.4.2, Fig. 4.17.

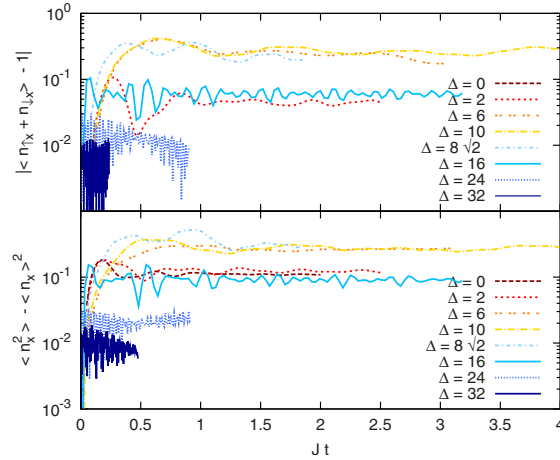


Figure 4.6: Evolution of the occupation number  $\langle n_{\uparrow x} + n_{\downarrow x} \rangle - 1$  (upper panel) and its variance  $\langle n_x^2 \rangle - \langle n_x \rangle^2$  (lower panel) on a particular site  $x$ , starting from the Néel state and evolving with respect to the full Hubbard Hamiltonian with  $U = 8$  and several  $\Delta$ . The two quantities should be exactly zero, if the analogy to the spin model is exact. The analogy breaks when  $|U^2 - \Delta^2|$  goes to zero. In the special case  $\Delta = 0$ , the system is (additionally to the invariance under translations by two sites) invariant under translation by one site plus interchange of particle species. Hence  $\langle n_{\uparrow x} + n_{\downarrow x} \rangle = 1 \forall_t$  for  $\Delta = 0$ .

For large  $|U^2 - \Delta^2|$  the Hubbard dynamics clearly follow the curves obtained with the Heisenberg model (second order processes); Fig. 4.4 and 4.5. On the shorter time-scale  $1/t = 1$  ( $J/t$  in the rescaled plots), corresponding to first order processes, small oscillations around the Heisenberg curves are visible. Their amplitude decreases with increasing  $|U^2 - \Delta^2|$ . The perturbative treatment of the system, leading to the isotropic Heisenberg model, breaks down for  $|\Delta| \sim U$ . In

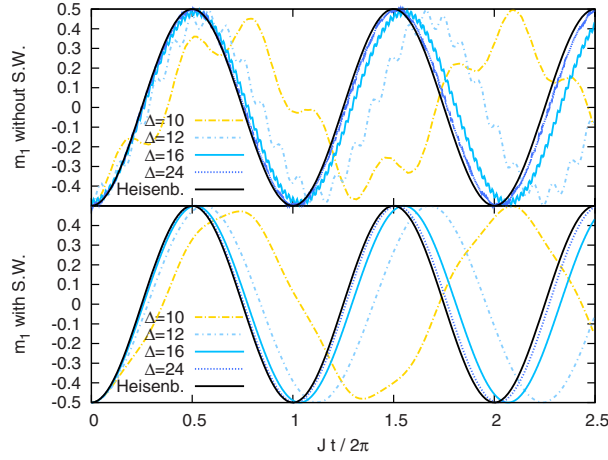


Figure 4.7: Evolution of the magnetization ( $\hat{m}_1 := (n_{\uparrow 1} - n_{\downarrow 1})/2$ ) on one site of an isolated double well, starting from the Néel state and evolving with respect to the full two-site Hubbard Hamiltonian with  $U = 8$  and  $\Delta = 10, 16, 24, 32$ , and the isotropic Heisenberg antiferromagnet, respectively. Contrary to the case of an infinite lattice, the magnetization does not relax here. The upper panel shows  $\langle \hat{m}_1 \rangle_{\hat{\phi}} \equiv \langle \phi | e^{-\hat{H}t/i\hbar} \hat{m}_1 e^{\hat{H}t/i\hbar} | \phi \rangle$ . In the lower panel shows  $\langle \phi | e^{i\hat{S}} e^{-\hat{H}t/i\hbar} e^{-i\hat{S}} \hat{m}_1 e^{i\hat{S}} e^{\hat{H}t/i\hbar} e^{-i\hat{S}} | \phi \rangle$ , i.e. there the Schrieffer-Wolff transformation was accounted for ( $\hat{\mathcal{S}}$  correct to  $\mathcal{O}(\frac{t}{U \pm \Delta})$ ). As discussed in Section 4.3.1, the stretching in the curves w.r.t. time results from terms of order  $J^2$  in the effective Hamiltonian. They originate from fourth-order hopping processes.

this case, the two boson species cannot be interpreted as spin up or down states anymore and one has an appreciable amount of double occupancies in the system as demonstrated in Fig. 4.6.

Finally, I want to compare those results to the dynamics for isolated double wells as addressed experimentally in [103, 271]. Fig. 4.7 shows for this case the dynamics of the site magnetization again for the Hubbard model at various  $\Delta > U$  and the corresponding antiferromagnetic Heisenberg model. The decisive difference is that no equilibration is possible in this case. This is due to the fact that the Hamiltonian has only a few discrete eigenvalues here, as opposed to a gapless continuous spectrum for the lattice systems in the thermodynamic limit. In the two-site Heisenberg model there are only two states in the basis of the  $S^z = 0$  Hilbert space. The two eigenstates have energy difference  $J$ . The magnetization curve for the Heisenberg curve is hence just a cosine with frequency  $J$  and constant amplitude 1. The dynamics of the corresponding two-site Hubbard model is determined by three (discrete) incommensurate frequencies. The magnetization is hence not completely periodic, but due to the relation to Heisenberg model, a frequency  $\sim J$  is still dominating. No sign of relaxation is visible.

As mentioned above, the differences between Hubbard and Heisenberg dynamics stem from the fact that the two Schrieffer-Wolff transformations in (4.3.1) have been neglected. Fig. 4.7 shows in the lower panel the site magnetization for the case where both error sources (a) and (b) have been corrected. Although this should be hard to implement experimentally, it is unproblematic for the numerical analysis. Applying the Schrieffer-Wolff transformation, correct up to  $\mathcal{O}(\frac{t}{U \pm \Delta})$ , to the initial state before the Hubbard time evolution and its inverse before the measurement. As discussed in Section 4.3.1, the remaining deviations from the Heisenberg curve are then only of order  $\mathcal{S}^4$ ; Fig. 4.7.

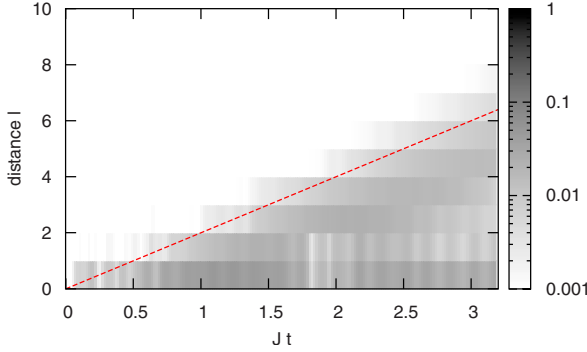


Figure 4.8: Evolution of the analogon  $\frac{1}{4}(\langle n_{\uparrow x} - n_{\downarrow x} \rangle (n_{\uparrow x+\ell} - n_{\downarrow x+\ell}))_{\tilde{\phi}} - \frac{1}{4} \langle n_{\uparrow x} - n_{\downarrow x} \rangle_{\tilde{\phi}} \langle n_{\uparrow x+\ell} - n_{\downarrow x+\ell} \rangle_{\tilde{\phi}}$  of the magnetization-magnetization correlation function, starting from the Néel state and evolving with respect to the full Hubbard Hamiltonian with  $U = 8$  and  $\Delta = 16$ . The plot shows the absolute value of the correlator in logarithmic scaling. The line denotes the maximum group velocity  $2J$  of the Heisenberg model.

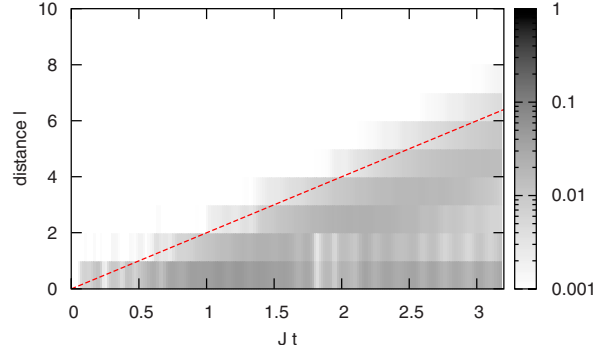


Figure 4.9: Evolution of the magnetization-magnetization correlation function  $\langle \hat{S}_x^z \hat{S}_{x+\ell}^z \rangle_{\phi} - \langle \hat{S}_x^z \rangle_{\phi} \langle \hat{S}_{x+\ell}^z \rangle_{\phi}$ , starting from the Néel state and evolving with respect to the isotropic Heisenberg antiferromagnet. The plot shows the absolute value of the correlator in logarithmic scaling. The line denotes the maximum group velocity  $2J$  of the Heisenberg model.

### 4.3.5 Correlation functions

The correlation functions in Figs. 4.8–4.11 support on the one hand the results already obtained from the magnetization dynamics in Section 4.3.4. On the other hand one also sees here explicitly that correlations spread out inside a causal cone (analogon of a light cone) defined by the maximum group velocity. The latter coincides for large  $|U^2 - \Delta^2|$  with the maximum group velocity  $2J$  of the Heisenberg model. One also notes here that equilibration to a steady state occurs first for small subsystems. This issue will be discussed in Section 4.4.

### 4.3.6 Momentum distribution and correlators

Experimental access to onsite magnetization or, correspondingly, the particle number difference (“spin imbalance”) has already been demonstrated [103, 271]. However there is no direct access to the real-space correlators. As it turns out, the standard experimental observable [see. Sec.3.3.2] for experiments with ultracold atoms, the momentum distribution  $\langle n_k \rangle = \langle n_{\uparrow k} + n_{\downarrow k} \rangle$ , is to zeroth order in  $\mathcal{J}$  constant in time. It measures to this order simply the particle density which is in the limit of Heisenberg dynamics  $\Delta \gg U$  very close to one.

$$n_k = \frac{1}{N} \sum_i n_i + \frac{1}{N} \sum_{\sigma, i \neq j} e^{ik \cdot (r_i - r_j)} a_{\sigma i}^{\dagger} a_{\sigma j} \quad (4.22)$$

It follows with (4.17)

$$\langle n_k \rangle_{\tilde{\phi}} = \langle n_k \rangle_{\phi} + \mathcal{O}(\mathcal{J}^2) = 1 + \mathcal{O}(\mathcal{J}^2). \quad (4.23)$$

Hence one needs to go beyond the measurement of the momentum distribution. By analysis of shot-noise of absorption images taken by time-of-flight measurements [cp. Sec.3.3], one obtains momentum-space particle density correlation functions [6, 102]. Experimentally available

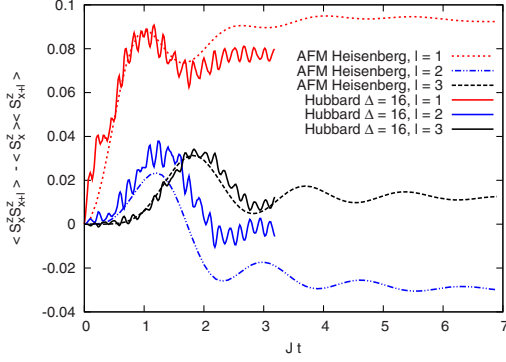


Figure 4.10: Evolution of short range magnetization-magnetization correlation function (distances  $\ell = 1, 2, 3$ ), starting from the Néel state and evolving with respect to the full Hubbard Hamiltonian with  $U = 8$  and  $\Delta = 16$  and the isotropic Heisenberg antiferromagnet, respectively. With increasing time, deviations between Heisenberg and Hubbard dynamics become more pronounced than for the magnetization in Fig. 4.4. However, in both cases tendency toward equilibration to a steady state is visible.

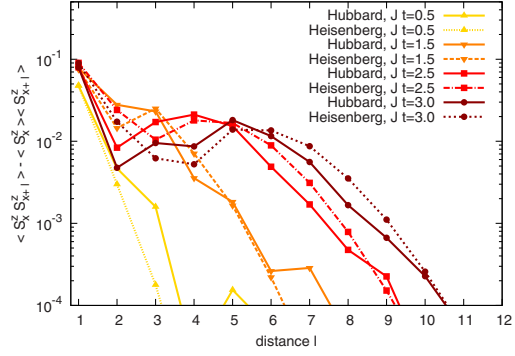


Figure 4.11: Evolution of the magnetization-magnetization correlation function, starting from the Néel state and evolving with respect to the full Hubbard Hamiltonian with  $U = 8$  and  $\Delta = 16$  and the isotropic Heisenberg antiferromagnet, respectively. See also Fig. 4.10.

are  $\langle n_{\sigma k} n_{\sigma' k'} \rangle$  and  $\langle n_k n_{k'} \rangle = \sum_{\sigma \sigma'} \langle n_{\sigma k} n_{\sigma' k'} \rangle$  and hence also  $\sum_{\sigma} \langle n_{\sigma k} n_{-\sigma k'} \rangle$ . In the following, I will again use the approximation  $\langle \hat{O} \rangle_{\tilde{\phi}} = \langle \hat{O} \rangle_{\phi} + \mathcal{O}(\mathcal{J}^2) \simeq \langle \hat{O} \rangle_{\phi}$ .

$$\langle n_{\sigma k} n_{\sigma' k'} \rangle_{\tilde{\phi}} = \frac{1}{N^2} \sum_{ij, nm} e^{ik \cdot (r_i - r_j)} e^{ik' \cdot (r_m - r_n)} \langle a_{\sigma i}^{\dagger} a_{\sigma j} a_{\sigma' m}^{\dagger} a_{\sigma' n} \rangle_{\tilde{\phi}} \quad (4.24)$$

Those give information about long-range spin correlations.

$$\begin{aligned} \langle a_{\uparrow i}^{\dagger} a_{\uparrow j} a_{\uparrow m}^{\dagger} a_{\uparrow n} \rangle_{\tilde{\phi}} &\simeq \langle \delta_{ij} \delta_{mn} n_{\uparrow i} n_{\uparrow m} + (1 - \delta_{ij}) \delta_{in} \delta_{jm} a_{\uparrow i}^{\dagger} a_{\uparrow j} a_{\uparrow j}^{\dagger} a_{\uparrow i} \rangle_{\phi} \\ &= \langle \delta_{ij} \delta_{mn} (\frac{1}{2} + \hat{S}_i^z) (\frac{1}{2} + \hat{S}_m^z) + (1 - \delta_{ij}) \delta_{in} \delta_{jm} (\frac{1}{2} + \hat{S}_i^z) (\frac{3}{2} + \hat{S}_j^z) \rangle_{\phi} \end{aligned} \quad (4.25)$$

for the observable  $\langle n_{\uparrow k} n_{\uparrow k'} \rangle$  and

$$\begin{aligned} \sum_{\sigma} \langle a_{\sigma i}^{\dagger} a_{\sigma j} a_{-\sigma m}^{\dagger} a_{-\sigma n} \rangle_{\tilde{\phi}} &\simeq \langle \delta_{ij} \delta_{mn} \sum_{\sigma} n_{\sigma i} n_{-\sigma m} + (1 - \delta_{ij}) \delta_{in} \delta_{jm} \sum_{\sigma} a_{\sigma i}^{\dagger} a_{\sigma j} a_{-\sigma j}^{\dagger} a_{-\sigma i} \rangle_{\phi} \\ &= \langle \delta_{ij} \delta_{mn} (\frac{1}{2} - 2\hat{S}_i^z \hat{S}_m^z) + (1 - \delta_{ij}) \delta_{in} \delta_{jm} 2(\hat{S}_i^x \hat{S}_m^x + \hat{S}_i^y \hat{S}_m^y) \rangle_{\phi} \end{aligned} \quad (4.26)$$

for the observable  $\sum_{\sigma} \langle n_{\sigma k} n_{-\sigma k'} \rangle$ . This also reflects the fact that to zeroth order of  $\mathcal{J}$ , there are no double occupancies with respect to the original basis. However, there is an admixture of them, contributing in second order of  $\mathcal{J}$ ,  $\langle n_{\uparrow i} n_{\downarrow i} \rangle_{\tilde{\phi}} = \mathcal{O}(\mathcal{J}^2)$ . Inserting (4.25) and (4.26) to (4.24) yields

$$\begin{aligned} \langle n_{\uparrow k} n_{\uparrow k'} \rangle_{\tilde{\phi}} &\simeq \frac{1}{4} - \frac{1}{N} + \frac{3}{4} \delta_{kk'} + \langle \hat{S}_{\Delta k}^z \hat{S}_{-\Delta k}^z \rangle_{\phi} \\ &= \langle n_{\downarrow k} n_{\downarrow k'} \rangle_{\phi} \end{aligned} \quad (4.27)$$

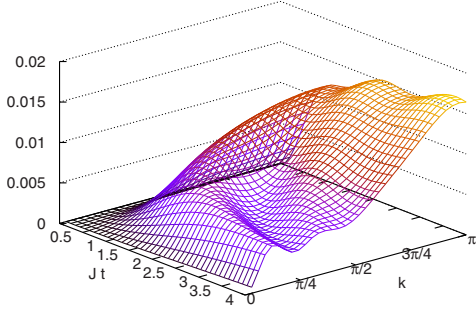


Figure 4.12: Evolution of the momentum-space spin-spin correlator  $\langle \hat{S}_{\Delta k}^z \hat{S}_{-\Delta k}^z \rangle_{\phi}$  for the Heisenberg antiferromagnet. The correlator corresponds according to Eq. (4.27) to the density-density correlator in the Hubbard model and is available in experiments with ultracold atoms [6]. The initial state (4.14) is uncorrelated. Correlations build up on the time scale  $1/J$ . Finite-size effects have been corrected (see text).

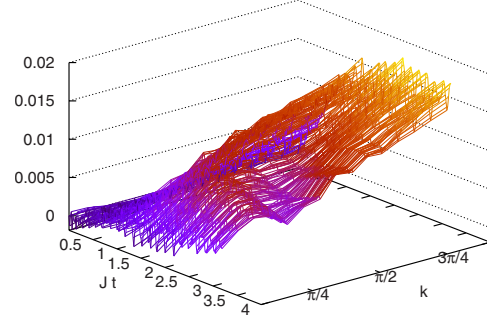


Figure 4.13: Evolution of the momentum space density-density correlator  $\frac{1}{N_k} \sum_k \langle n_{\uparrow k+\Delta k} n_{\uparrow k} \rangle_{\phi}$  (minus the trivial parts on the right hand side of Eq. (4.27)) in the Hubbard model with  $U = 8$  and  $\Delta = 16$ . Except for quick oscillations on the time scale  $t = 1/t$ , the result reflects the evolution of the corresponding spin-spin correlator in the Heisenberg model, Fig. 4.12. Finite-size effects have been corrected and first order hopping contributions entering through the nearest neighbor correlator  $\langle a_i^\dagger a_j \rangle_{\phi}$  are removed (see text).

and

$$\sum_{\sigma} \langle n_{\sigma k} n_{-\sigma k'} \rangle_{\phi} \simeq \frac{1}{2} - \frac{1}{N} + 2 \langle \hat{S}_{\Delta k}^x \hat{S}_{-\Delta k}^x + \hat{S}_{\Delta k}^y \hat{S}_{-\Delta k}^y \rangle_{\phi}, \quad (4.28)$$

where  $\Delta k \equiv k - k'$ ,  $\hat{S}_q^{\alpha} \equiv \frac{1}{N} \sum_i e^{iq \cdot r_i} \hat{S}_i^{\alpha}$ ,  $\hat{S}^{\alpha} \equiv \frac{1}{N} \sum_i \hat{S}_i^{\alpha}$ , and  $\hat{S}^z |\phi(t)\rangle = 0$  are used.

A numerical comparison of the evolution of the momentum-space spin-spin (density-density) correlator for the Heisenberg and the Hubbard models is given in Figs. 4.12-4.14. To achieve such a good agreement, two corrections are necessary. First of all one needs to correct for finite size effects. Secondly, single particle Green's functions  $\langle a_i^\dagger a_j \rangle$  enter which are trivial when evolving with the Heisenberg model ( $\langle a_i^\dagger a_j \rangle_{\phi} = \delta_{ij} n_{\uparrow i}(t)$ ), but have contributions of  $\mathcal{O}(\mathcal{P}^2)$ , when evolving with the Hubbard Hamiltonian. In the comparison of both evolutions, they can hence be understood as a major carrier of disturbance, reflecting first order processes in the Hubbard model. To achieve comparability it would be desirable to remove contributions from  $\langle a_i^\dagger a_j \rangle$  completely. This would be possible for the numerical analysis. In a corresponding experiment however, the quantities are not available. Hence I remove only the contributions from nearest neighbor correlators  $\langle a_i^\dagger a_{i\pm 1} \rangle$ . As Figures 4.12-4.14 demonstrate that this is already sufficient and Fig. 4.15 that it is necessary. The experimental observation of the nearest-neighbor correlators is within reach [101].

The specific form of the momentum-space correlation function can be understood with the causal cone behavior of the corresponding real-space correlators discussed in Section 4.3.5. At the beginning of time evolution, correlations for small distances build up (e.g. due to the spin flip terms  $\hat{S}_i^+ \hat{S}_{i\pm 1}^-$  in the Heisenberg model). This corresponds in the momentum space representation to correlations for large  $\Delta k$ . As the correlations spread out in real-space, correlations for smaller momenta  $\Delta k$  build up.



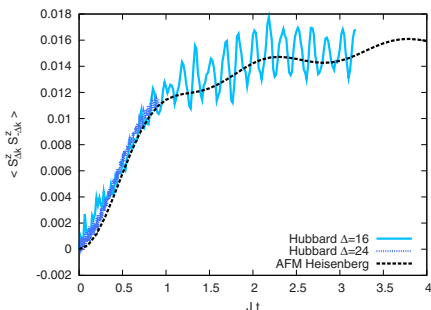


Figure 4.14: Evolution of the momentum space density-density correlator  $\frac{1}{N_k} \sum_k \langle n_{\uparrow k+\pi} n_{\uparrow k} \rangle_{\tilde{\phi}}$  for  $\Delta k = \pi$  (minus the trivial parts on the right hand side of Eq. (4.27)) in the Hubbard model with  $U = 8$  and  $\Delta = 16, 24$ . The Hubbard results follow once more the Heisenberg curves, except for some quick oscillations due to first order hopping processes which die out for  $|\Delta|$  far from  $U$ .

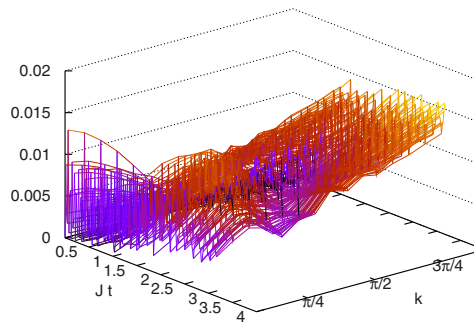


Figure 4.15: The same observable as in Fig. 4.13 except, that the observable has *not* been corrected for finite size effects and the effects of the correlator  $\langle a_i^\dagger a_j \rangle_{\tilde{\phi}}$ . One can see here clearly, that those corrections of the raw data are important to achieve comparability to the corresponding Heisenberg result in Fig. 4.12.

## 4.4 Relaxation to steady states

### 4.4.1 General features

Contrary to the setup of isolated double wells, one observes for the many-particle dynamics in the setup a relaxation for local quantities. This may be seen as an indicator for convergence of the states of subsystems with finite real-space extent to a steady state. Recently, the mechanism of how such a relaxation may occur was clarified for (free) integrable systems [24]. Corresponding examples can also be found in [229, 53, 66, 105]. The setup considered in this paper could be used to study experimentally such relaxation processes – in particular, the differences for the nonintegrable Bose-Hubbard model and the Bethe ansatz integrable Heisenberg model. Experimental investigations would be very useful here, as the fast entanglement growth during time evolution, Fig. 4.16, prohibits numerical access to long times and for Bethe ansatz integrable systems, analytical results are also relatively limited for such purposes.

Integrable many-particle systems do not relax to the well known canonical, or “thermal”, ensembles (a fact that was already observed experimentally e.g. in [157]). If they relax the steady state is due to the integrals of motion to a much more constrained ensemble [229, 24]. This could be detected experimentally by comparing the steady state correlation functions after time evolution to those obtained for the corresponding thermal ensemble. The temperature should be chosen such as to have the same energy in both states. For (free) integrable models, the relaxation occurs due to a phase averaging (“dephasing”) effect [24]. In Section 4.4.2, the relaxation in the Bethe ansatz integrable Heisenberg model is treated within a mean field approximation. Also in this case, relaxation is connected to a phase averaging effect.

Nonintegrable systems are generally believed to relax to a thermal ensemble due to effective scattering processes. Recent numerical analysis of such systems [186, 161, 66] is not yet fully conclusive due to limitations on maximum observation times (density-matrix renormalization-

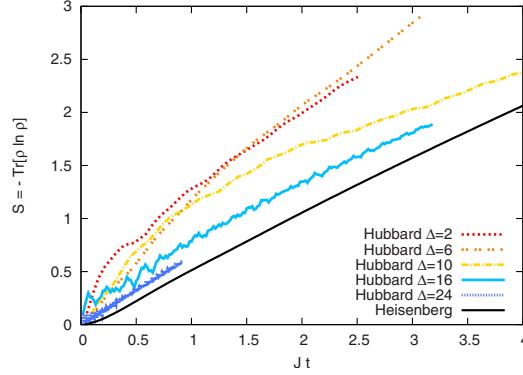


Figure 4.16: For the initial state (4.14), evolution of the entanglement entropy with respect to a partition of the system into left and right half. The growth is roughly linear in time (compare e.g. to [47]) resulting in an exponential increase in the computation time required for the simulation. The more important first order processes are, the faster the entanglement entropy increases. The tuning from the Heisenberg model ( $|U^2 - \Delta^2| \rightarrow \infty$ ), where no first order processes occur, to the regime  $|\Delta| \sim U = 8$  can be understood as a smooth increase in the number of relevant degrees of freedom, resulting in a stronger entanglement growth. The entanglement entropies for the Heisenberg ferro- and antiferromagnet are identical, because the corresponding density matrices are in the  $\{\hat{S}_i^z\}$ -eigenbasis simply related by complex conjugation; cf. Section 4.3.2.

group) or system size (exact diagonalization). Analytical approaches are usually restricted to rather exotic models or limiting cases. See e.g. [88, 194] for investigations by dynamical mean-field theory (DMFT).

In the here considered setup, the nonintegrable two-species Bose-Hubbard model could be tuned so close to the Heisenberg regime (large  $|U^2 - \Delta^2|$ ) that thermalization occurs very slowly. One might hence observe first a relaxation to a nonthermal (almost) steady state due to the integrable Heisenberg dynamics, which would then be followed by slower thermalization due to the remaining nonintegrable first order processes of the full Bose-Hubbard Hamiltonian.

#### 4.4.2 Relaxation for the Heisenberg magnet in mean field approximation

In this section, the relaxation of the Heisenberg magnet with the initial state being the Néel state (4.14) will be investigated. In particular I will derive that the (staggered) magnetization decays as  $1/t^{3/2}$  due to a phase averaging effect.

The model is Bethe ansatz integrable [33, 296]. However, it is in general not possible to solve the equations of motion for arbitrary initial states. With appreciable numerical effort this has been achieved recently (only) for the initial state being the groundstate plus a one-particle excitation [51]. To investigate the dynamics nevertheless, I hence employ a mean field approximation for the  $\hat{S}_i^z \hat{S}_{i+1}^z$  term.

$$\begin{aligned} \hat{H} &= \sum_i \left( \frac{1}{2} (\hat{S}_i^+ \hat{S}_{i+1}^- + \hat{S}_i^- \hat{S}_{i+1}^+) + \hat{S}_i^z \hat{S}_{i+1}^z \right) \\ &\rightarrow \sum_i \left( \frac{1}{2} (\hat{S}_i^+ \hat{S}_{i+1}^- + \hat{S}_i^- \hat{S}_{i+1}^+) - 2(-1)^i \rho_\pi(t) \hat{S}_i^z \right) \end{aligned} \quad (4.29)$$

where the order parameter  $\rho_\pi$  is the staggered magnetization

$$\rho_\pi \equiv \frac{1}{N} \sum_x (-1)^x \langle \hat{S}_x^z \rangle = \frac{1}{N} \sum_x (-1)^x \langle n_x - \frac{1}{2} \rangle. \quad (4.30)$$

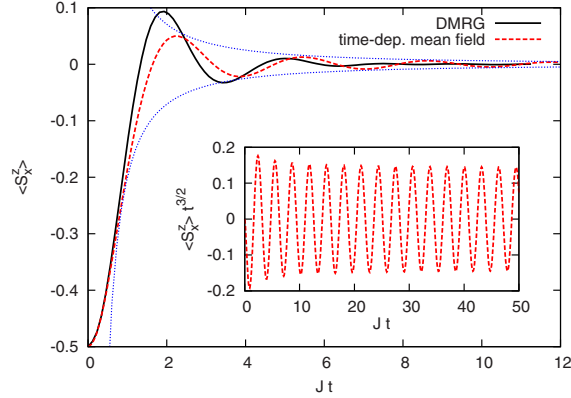


Figure 4.17: Evolution of the magnetization on a particular site  $x$ , starting from the Néel state and evolving with respect to the isotropic Heisenberg Hamiltonian, once with DMRG and once in the mean field approximation. The (staggered) magnetization shows a  $1/t^{3/2}$  decay (blue). In the mean field approach one sees that local relaxation is connected to a phase averaging effect as is typical for integrable models [24]; see text.

After a Fourier and a Jordan-Wigner transformation [149, 176] with  $c_i := (-1)^{\sum_{n=1}^{i-1} (\hat{S}_n^z + \frac{1}{2})} \hat{S}_i^-$  and  $\hat{S}_i^z = c_i^\dagger c_i - \frac{1}{2}$ , the mean field Hamiltonian and the staggered magnetization read with  $\varepsilon_k := \cos k$

$$\hat{H}(t) = \sum_{-\frac{\pi}{2} \leq k < \frac{\pi}{2}} (\varepsilon_k c_k^\dagger c_k - 2\rho_\pi(t) c_{k+\pi}^\dagger c_k), \quad (4.31)$$

$$\rho_\pi(t) = \frac{1}{N} \sum_{-\frac{\pi}{2} \leq k < \frac{\pi}{2}} 2\Re \langle c_k^\dagger c_{k+\pi} \rangle. \quad (4.32)$$

The initial state is the Néel state (4.14) and reads in the fermionic operators for  $t = 0$  with  $u_k(0) = v_k(0) = 1/\sqrt{2}$

$$|\phi(t)\rangle = \prod_{-\frac{\pi}{2} \leq k < \frac{\pi}{2}} (u_k(t) c_k^\dagger + v_k(t) c_{k+\pi}^\dagger) |0\rangle. \quad (4.33)$$

So each mode  $c_k$  is in the initial state only correlated with mode  $c_{k+\pi}$ . As the mean field Hamiltonian (4.31) couples for every  $k$  also just those two modes, the state remains in the form (4.33) for all times. With  $i\hbar \partial_t c_k(t) = [c_k, \hat{H}(t)]$  one obtains the equations of motion ( $\hbar = 1$ )

$$i\partial_t u_k(t) = \varepsilon_k \cdot u_k(t) - 2\rho_\pi(t) \cdot v_k(t), \quad (4.34a)$$

$$i\partial_t v_k(t) = -\varepsilon_k \cdot v_k(t) - 2\rho_\pi(t) \cdot u_k(t), \quad (4.34b)$$

a system of  $N$  coupled nonlinear differential equations.

Those can be integrated numerically, yielding for the staggered magnetization  $\rho_\pi(t)$  a damped oscillation decaying as  $1/t^{3/2}$ . Fig. 4.17 compares  $\rho_\pi(t)$  from the mean field analysis to the corresponding DMRG result (Fig. 4.4) and shows good qualitative agreement.

As demonstrated in [131], where the same equations of motion were obtained for the evolution of a system of spinless fermions, Eq. (4.34) is equivalent to the equations of motion of the

classical Hamiltonian

$$H_S = - \sum_{-\pi \leq k < \pi} 2\varepsilon_k S_k^z + \frac{2}{N} \sum_{k,k'} (S_k^x S_{k'}^x + S_k^y S_{k'}^y) \quad (4.35)$$

with the Anderson pseudospin variables  $S_k^+ = v_k^* u_k$ ,  $S_k^z = \frac{1}{2}(|v_k|^2 - |u_k|^2)$  for  $-\frac{\pi}{2} \leq k < \frac{\pi}{2}$  and  $S_{k+\pi}^x = S_k^x$ ,  $S_{k+\pi}^{y,z} = -S_k^{y,z}$ , [12, 131]. This Hamiltonian occurred in the mean field analysis of quenches in fermionic condensates; see e.g. [279, 263, 294, 295]. From this, it is known that (4.35) and hence (4.34) are integrable [295] due to the  $N/2$  integrals of motion  $L_k^2$ ,

$$L_k \equiv e_z + 2 \sum_{k \neq k'} \frac{S_{k'}}{\varepsilon_k - \varepsilon_{k'}}, \quad \partial_t L_k^2 = 0. \quad (4.36)$$

One can now argue that the  $x$  and  $y$  components of the vectors  $L_k$  will vanish for large times, as done in [131]. From this one can determine the (nonthermal) steady state, by equating  $(L_k^z(t \rightarrow \infty))^2$  with  $L_k^2(t=0)$ . The result is  $\lim_{t \rightarrow \infty} S_k^z(t) = \frac{1}{2} \cos k$ . With  $S_k^z = \frac{1}{2}(|v_k|^2 - |u_k|^2)$  and  $|v_k|^2 + |u_k|^2 = 1 \forall t$ , it follows that

$$\lim_{t \rightarrow \infty} |u_k(t)| = \sqrt{1 - \cos k} / \sqrt{2}, \quad (4.37)$$

$$\lim_{t \rightarrow \infty} |v_k(t)| = \sqrt{1 + \cos k} / \sqrt{2}. \quad (4.38)$$

With the knowledge of the steady state, the  $1/t^{3/2}$  decay of the magnetization  $\rho_\pi$  can now be derived.

To this purpose let us first recall the general dephasing scenario for  $d$ -dimensional (free) integrable models. In [24] it was demonstrated that local observables  $G(t)$  (i.e. correlators) lead in general to expressions of the form

$$G(t) = G_0 + \int d^d k e^{i\varphi(k)t} f(k), \quad (4.39)$$

where the amplitude  $f(k)$  is determined by the chosen observable, the initial state, and the eigenbasis of the Hamiltonian. The phase function  $\varphi(k)$  is determined by the spectrum of the Hamiltonian. Now, the quantity  $G(t)$  relaxes to  $G_0$  for large times if the phase function varies quickly enough in regions of the  $k$  space where the amplitude  $f(k)$  is nonzero. Whether and how quickly an observable relaxes is in particular determined by contributions from points where  $\varphi(k)$  is stationary or  $f(k)$  diverges. For the paradigmatic scenario of  $\varphi(k) \sim \varphi_0 + |k|^\ell$ ,  $f(k) \sim 1/k^m$  near a stationary point  $k_0 = 0$ , the integral in (4.39) behaves as

$$e^{i\varphi_0 t} \int d^d k \frac{1}{|k|^m} e^{i|k|^\ell t} \sim \int dq \frac{1}{q^\chi} e^{iqt}, \quad \chi = \frac{m+\ell-d}{\ell}. \quad (4.40)$$

Hence the time-dependent contribution to  $G(t)$ , for  $t \rightarrow \infty$ , does not vanish if  $\chi \geq 1$ , vanishes as  $1/t^{1-\chi}$  if  $0 < \chi < 1$ , and at least as  $1/t$  if  $\chi < 0$ ,<sup>2</sup>

<sup>2</sup>For free systems, the (Gaussian) state of any subsystem is fully characterized by its one-particle Green's function. This was exploited in [24] to derive conditions on the relaxation of subsystem states, based on the relaxation of the Green's function.

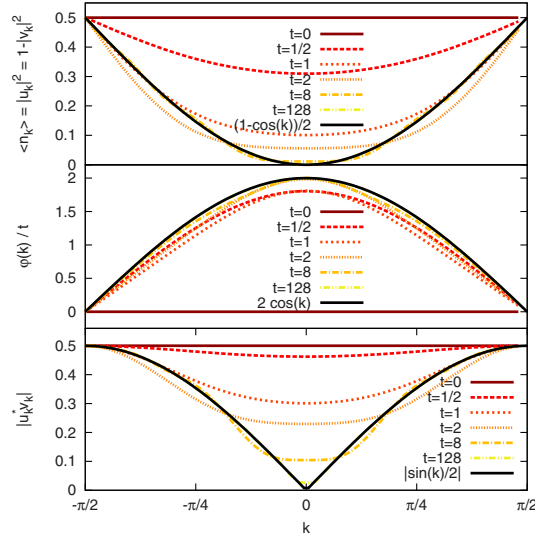


Figure 4.18: Evolution of the occupation number  $\langle n_k \rangle = 1 - \langle n_{k+\pi} \rangle$ , phase  $\varphi(k) = \arg(u_k^*(t)v_k(t)) - \arg(u_{\pi/2}^*(t)v_{\pi/2}(t))$  of the wavefunction, and  $|u_k^* v_k|$  for each pair of modes  $c_k, c_{k+\pi}$ . The initial state, the Néel state with  $u_k = v_k = 1/\sqrt{2}$ , is evolved with the mean field approximation of the isotropic Heisenberg Hamiltonian (4.31). Except for the lowest panel, the curves for  $t = 128$  coincide (within resolution of the plots) with the limiting curves for  $t \rightarrow \infty$  which are  $\frac{1 - \cos k}{2}$ ,  $2 \cos k$ , and  $|\sin k|/2$ , respectively.

Now I come back to the staggered magnetization. Expressed in the variables  $u$  and  $v$ , it reads after going to the thermodynamic limit

$$\rho_\pi(t) = \int dk \mathfrak{R}(u_k^* v_k) = \int dk \mathfrak{R}(e^{i\varphi(k)t} f(k, t)). \quad (4.41)$$

This is, except for the additional time dependence of the amplitude function  $f(k, t)$ , an integral of the form (4.39). Presuming that  $\rho_\pi$  vanishes for long times, it follows from the equations of motion (4.34) that for large  $t$ , the phases of  $u_k$  and  $v_k$  are roughly  $\pm \varepsilon_k \cdot t$  and hence  $\varphi(k) \approx \varepsilon_k - \varepsilon_{k+\pi} = 2 \cos k$ , which is stationary (with  $\ell = 2$ ) at  $k = 0$ ; cf. Fig. 4.18. For finite times, the amplitudes of  $u_k$  and  $v_k$  are finite as  $|u_k|^2 = \langle n_k \rangle$  and  $|v_k|^2 = \langle n_{k+\pi} \rangle = 1 - \langle n_k \rangle$ . Hence  $m = 0$  for  $k = 0$  which is also confirmed numerically in Fig. 4.18. The dephasing of the staggered magnetization (4.41) is determined by the stationary point  $k = 0$  of  $\varphi$ . With  $d = 1$ ,  $m = 0$ , and  $\ell = 2$  one has  $\chi = \frac{m + \ell - d}{\ell} = \frac{1}{2}$ . The phase averaging accounts hence for a factor of  $1/t^{1-\chi} = 1/t^{1/2}$  for the decay of the staggered magnetization. Linearizing the equations of motion around the steady state one finds that  $|u_0^* v_0| (f(k, t))$  around  $k = 0$  decays as  $1/\sqrt{t}$  and further that only a vicinity  $|k| \lesssim 1/\sqrt{t}$  of  $k = 0$  is contributing to (the leading order of) the integral (4.41). Taking all this together, one infers the  $1/t^{3/2}$  decay of the staggered magnetization.

## 4.5 Validity of the effective spin model

One may be wondering why the restriction to the single-occupancy space  $\mathcal{H}_1$ , (4.8), is justified (if the initial state of the system is in  $\mathcal{H}_1$  and I evolve with the effective Hamiltonian), although

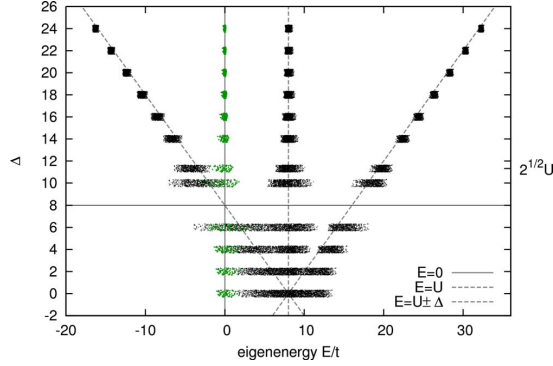


Figure 4.19: The many-particle spectrum of the effective Hamiltonian  $\hat{H}_{\text{eff}}^0$  for the subspaces  $\mathcal{M}^0$  (green) and  $\mathcal{M}^1$  (black) with  $U = 8$  and  $\Delta = 2, 4, 6, 8, 10, \sqrt{2}U, 14, 16, \dots$  as obtained from exact diagonalization in the  $S^z = 0$  sector for  $N = 8$  sites ( $\dim \mathcal{M}^0 = 70$ ,  $\dim \mathcal{M}^1 = 2800$ ). Each dot corresponds to an eigenenergy. For the plot, small random numbers are added to the  $\Delta$  values to give a rough impression of the density of states. The subspace  $\mathcal{M}^1$  is separated energetically into  $\mathcal{M}_{0,0}^1 \cup \mathcal{M}_{0,1}^1$  around  $E = U$  and  $\mathcal{M}_{1,1}^1, \mathcal{M}_{-1,0}^1$  around  $E = U \pm \Delta$ .

the coupling to the rest of the Hilbert space has the same strength as the coupling for dynamics inside the subspace  $\mathcal{H}_1$  and although parts of the rest of the Hilbert space overlap energetically with  $\mathcal{H}_1$ . There could be considerable transition rates out of the subspace with (predominantly) one particle per site, rendering a description or comparison with dynamics of the effective model derived for that subspace useless. I will assess here that this is not the case (for the large- $U$  limit).

First of all, the numerical results of Section 4.3 showed that for large  $|U^2 - \Delta^2|$ , the Hubbard curves follow quite precisely the Heisenberg curves, indicating very little transitions to other subspaces. One can also give a somewhat handwaving but rather suggestive argument. I will show in the following that transition matrix elements leading out of  $\mathcal{H}_1$  occur predominantly to states with energy difference  $\sim U$ , and diminish in the large- $U$  limit. Those yield therefore finite small transition amplitudes. In higher orders of the perturbation theory, there are also transitions to states with energy  $\sim U \pm \Delta$ , which will lead to a small (controllable) transition rate out of  $\mathcal{H}_1$ .

In the full effective Hamiltonian (4.9), I regard the term  $\hat{V} = i[\hat{\mathcal{S}}, \hat{H}_t^0]$  that generates or destroys double occupancies, i.e. generates transitions between subspace  $\mathcal{M}^n$  with  $n$  doubly occupied sites as a perturbation.

$$\hat{H}_{\text{eff}}^{\text{full}} = \hat{H}_{\text{eff}}^0 + \hat{V} \quad (4.42)$$

The subspaces  $\mathcal{M}^n$  separate (energetically) further into  $\mathcal{M}_{m-\mu, m}^n$  with  $m$  doubly occupied and  $\mu$  empty sites on sublattice  $\mathcal{A}$  ( $n - m$  doubly occupied and  $n - \mu$  empty sites on sublattice  $\mathcal{B}$ ); i.e.  $\mathcal{H}_1 \equiv \mathcal{M}_{0,0}^0$ . Fig. 4.19 shows the many-particle spectrum of the effective Hamiltonian  $\hat{H}_{\text{eff}}^0$  for the subspaces  $\mathcal{M}^0$  and  $\mathcal{M}^1$  as obtained from exact diagonalization in the  $S^z = 0$  sector for  $N = 8$  sites.

The single (quasi-)particle excitations in these subspaces have energies of order  $\mathcal{O}(J, t)$  – spinwaves and hopping of doubly occupied and empty sites. However, the subspaces overlap energetically (in the thermodynamic limit) as, in a qualitative picture, one can have  $\sim N$  quasi-particle excitations resulting in the width  $\sim N|J| \gg U$  of the spectrum for each subspace. Specif-

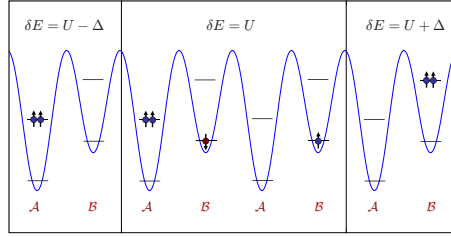


Figure 4.20: The subspace  $\mathcal{M}^1$ , with exactly one doubly occupied and one empty site separates energetically into three different subbands  $\mathcal{M}_{1,1}^1$ ,  $\mathcal{M}_{0,0}^1 \cup \mathcal{M}_{0,1}^1$ , and  $\mathcal{M}_{-1,0}^1$ . The operator  $\hat{V} = i[\hat{\mathcal{S}}, \hat{H}_t^0]$  maps states from  $\mathcal{M}^0$  to states from  $\mathcal{M}_{0,0}^1 \cup \mathcal{M}_{0,1}^1$  that differ in energy by  $\sim U$  (see text).

ically for  $\mathcal{M}^0$ , the lower and upper bounds on the spectrum are determined by the ground state energies of the ferromagnetic and the antiferromagnetic Heisenberg models. Those are in the thermodynamic limit  $E_{\text{fm}} = -\frac{1}{4}JN$  and  $-E_{\text{afm}} = (\ln 2 - \frac{1}{4})JN$ , [33, 192].

If one acts on a state  $|\psi\rangle \in \mathcal{M}^0$  of energy  $E$  with the operator  $\hat{V} = i[\hat{\mathcal{S}}, \hat{H}_t^0]$  (cf. Appendix ??), firstly,  $\hat{\mathcal{S}}$  generates a double occupancy and an empty site;  $|\sigma_i, \sigma_{i+1}\rangle \mapsto |\sigma_i \sigma_{i+1}, 0\rangle$  on two neighboring sites  $i$  and  $i+1$ . Secondly, a corresponding hopping term from  $\hat{H}_t^0$  acts on  $i$  (or  $i+1$ ) and  $i-1$  (or  $i+2$ ) such that e.g.  $|\sigma_{i-1}, \sigma_i \sigma_{i+1}, 0\rangle \mapsto |\sigma_{i-1} \sigma_i, \sigma_{i+1}, 0\rangle$  or  $|\sigma_i \sigma_{i+1}, 0, \sigma_{i+2}\rangle \mapsto |\sigma_i \sigma_{i+1}, \sigma_{i+2}, 0\rangle$ . Hence both, the doubly occupied and the empty site are on the same sublattice  $\mathcal{A}$  or  $\mathcal{B}$  and the resulting state  $\hat{V}|\psi\rangle \in \mathcal{M}_{0,0}^1 \cup \mathcal{M}_{0,1}^1$  has energy  $E \sim E + U$ ; see Fig. 4.20.

Let us consider transitions from  $\mathcal{M}^0$  to  $\mathcal{M}^1$ . For any initial eigenstate  $|i\rangle \in \mathcal{M}^0$  the transition amplitude, to a state  $|f\rangle \in \mathcal{M}^1$  is in the Born approximation given by

$$c_f(T) = \frac{-i}{\hbar} \int_{t_0}^T dt \langle f | \hat{V} | i \rangle e^{i\omega_{fi}t} = \mathcal{O}\left(\frac{t^2}{U \pm \Delta} \cdot \frac{1}{U}\right). \quad (4.43)$$

This estimate of a small (oscillating) transition amplitude follows from the consideration that nonvanishing transition elements exist only for states with energy differences  $\hbar\omega_{fi} = \mathcal{O}(U)$ . I have pointed out that the subspaces  $\mathcal{M}^0$  and  $\mathcal{M}^1$  ultimately overlap energetically. However, states  $|f\rangle$  and  $|i\rangle$  with comparable energy will have a vanishing transition matrix element: As argued above, the operator  $\hat{V}$  generates states from  $\mathcal{M}^1$  and causes a change of  $\sim U$  in energy. Besides this it can create or destroy in a qualitative picture only a small number of quasi-particle excitations as it is a product of only four ladder operators. This will change the energy only by a small amount of  $\mathcal{O}(J, t)$ . So  $\hbar\omega_{fi}$  will indeed be of order  $\mathcal{O}(U)$  for all nonvanishing transition amplitudes  $\langle f | \hat{V} | i \rangle$ .

To illustrate this, Figs. 4.21 and 4.22 show the transition matrix elements  $\langle f | \hat{V} | i \rangle$  between eigenstates of the effective Hamiltonian  $\hat{H}_{\text{eff}}^0$  for the subspaces  $\mathcal{M}^0$  and  $\mathcal{M}^1$  as obtained from exact diagonalization in the  $S^z = 0$  sector for  $N = 8$  sites.

Small matrix elements to states with energy difference  $U \pm \Delta$  remain. For unfortunate choice of  $U$  and  $\Delta$  one may hence encounter nonvanishing transitions to states in  $\mathcal{M}^{n>0}$  with  $\hbar\omega_{fi} \sim 0$ . Consider e.g.  $\Delta = 2U$ . In this case, two actions of the operator  $\hat{V}$  may end up in a state  $|f\rangle$  with comparable energy ( $U + (U - \Delta) = 0$ ) and hence to a (finite but small) transition rate out of  $\mathcal{M}^0$ . By appropriate choice of the ratio  $U/\Delta$ , one can achieve that the effect occurs only in higher

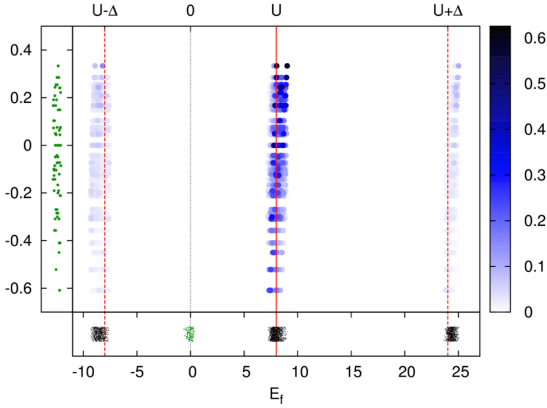


Figure 4.21: Transition matrix elements  $\langle f|\hat{V}|i\rangle$  between eigenstates of the effective Hamiltonian  $\hat{H}_{\text{eff}}^0$  for the subspaces  $\mathcal{M}^0$  and  $\mathcal{M}^1$  with  $U = 8$  and  $\Delta = 16$  as obtained from exact diagonalization in the  $S^z = 0$  sector for  $N = 8$  sites. Each dot corresponds to a nonzero transition matrix element. The narrow panels to the left and bottom show the corresponding eigenenergies. Nonvanishing matrix elements exist only for states with energy difference of  $\mathcal{O}(U)$ .

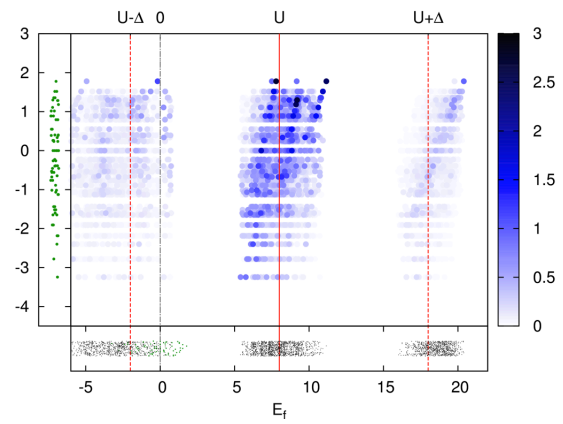


Figure 4.22: Transition matrix elements  $\langle f|\hat{V}|i\rangle$  between eigenstates of the effective Hamiltonian  $\hat{H}_{\text{eff}}^0$  for the subspaces  $\mathcal{M}^0$  and  $\mathcal{M}^1$  with  $U = 8$  and  $\Delta = 10$  as obtained from exact diagonalization in the  $S^z = 0$  sector for  $N = 8$  sites. Still nonvanishing matrix elements exist only for states with energy difference of  $\mathcal{O}(U)$ . But as  $\Delta$  is closer to  $U$  here, the matrix elements are larger in amplitude, (4.43), and the spectral subbands are broader due to a larger effective coupling  $J$ .

orders  $\hat{V}$ , resulting in a small transition rate. Further, the transition matrix elements itself can be made small by going to the large- $U$  limit (4.7).

## 4.6 Preparation of the antiferromagnetic groundstate by adiabatic evolution

In the Sections 4.3 and 4.5 I have given arguments and gathered numerical support for the fact that transition rates from the single-occupancy subspace  $\mathcal{H}_1^{\text{orig}}$ , (4.11), to the rest of the Hilbert space can be made small for time evolution with the Hubbard Hamiltonian. If this can also be realized experimentally for sufficiently long times, it would be possible to prepare for example the ground state of the antiferromagnetic Heisenberg model by adiabatically switching on the coupling  $t'$  between initially isolated double wells, Fig. 4.1, i.e. switching from  $t' = 0$  to  $t' = t$ , while  $t$  is kept constant. As demonstrated in [103, 271] for the initial situation of isolated double wells, the groundstate of the single occupancy subspace (4.8) can be prepared experimentally.

For the adiabatic approximation [153, 18] to be applicable, the system needs to be gapped on the whole path in the space of system parameters except for the end point, where the gap has to close abruptly enough. As argued in Section 4.5, transitions to other subspaces with (quasiparticle) double occupancies can be neglected for a certain period of time  $T$  that can be made very large. So one only needs to worry about transitions from the  $\mathcal{H}_1^{\text{orig}}$  groundstates to excited states inside the subspace, i.e. one needs to derive conditions on the dependence of the



corresponding energy gap on the hopping  $t'$  between initially isolated double wells such that  $t' = t$  can be reached adiabatically in a finite amount of time  $\tau < T$ .

The quantitative condition for adiabaticity is generally stated as

$$\left| \frac{\langle E_0(t) | \frac{d\hat{H}}{dt} | E_n(t) \rangle}{E_0(t) - E_n(t)} \right| \ll 1 \quad \forall_{t \in [0, \tau], n \neq 0}, \quad (4.44)$$

where  $|E_n(t)\rangle$  label the energy eigenstates and  $|E_0(0)\rangle$  is the initial state. Recently, substantial problems were pointed out [187, 266] and two more conditions added [267]

$$\int_0^\tau dt \left| \frac{d}{dt} \frac{\langle E_0(t) | \frac{d\hat{H}}{dt} | E_n(t) \rangle}{E_0(t) - E_n(t)} \right| \ll 1, \quad (4.45)$$

$$\int_0^\tau dt \left| \frac{\langle E_0(t) | \frac{d\hat{H}}{dt} | E_n(t) \rangle}{E_0(t) - E_n(t)} \right| |\langle E_n(t) | \frac{d\hat{H}}{dt} | E_m(t) \rangle| \ll 1. \quad (4.46)$$

If one has one time-dependent system parameter  $p(t)$ , namely the dimerization  $p = \delta$ , where

$$\delta := \frac{1 - |J'/J|}{1 + |J'/J|} = \frac{1 - |t'/t|^2}{1 + |t'/t|^2}, \quad (4.47)$$

and one part of the Hamiltonian is linear in that parameter (this is the case for the effective Hamiltonian and  $\delta \rightarrow 0$ ), the numerators of (4.44)-(4.46) are proportional to the sweeping speed  $v(t) := dp(t)/dt$ . The denominator is the spectral gap  $E_g(t)$ . Only points  $p(\tau)$  in parameter space where the gap vanishes are problematic. If the gap vanishes as

$$E_g(t) \propto |p(\tau) - p(t)|^\nu, \quad \nu > 0, \quad (4.48)$$

$\nu$  should (for  $t$  close to  $\tau$ ) be reduced as  $c|\tau - t|^\mu$ . According to (4.44),

$$1 \gg \frac{c|\tau - t|^\mu}{E_g(t)} \propto \frac{|\tau - t|^\mu}{|\int_0^{\tau-t} ds \cdot s^\mu|^\nu} \propto |\tau - t|^{\mu - \nu(\mu+1)}. \quad (4.49)$$

Hence, only for  $\nu < 1$ , i.e. for gaps that close abruptly enough, adiabaticity can be reached with  $\mu \geq \frac{\nu}{1-\nu}$ . The second condition, (4.45), is in this scenario fulfilled automatically, the third, (4.46), implies  $\mu > \frac{\nu-1}{2-\nu}$  which is also true.

For  $J' \simeq J$ , a situation which was examined intensively in the context of spin-Peierls systems, the model was first treated by Jordan-Wigner transformation and subsequent bosonization [68]. The precise result for the excitation gap can be obtained by a mapping to the four-state Potts model [36] or conformal field theory [2] (see also [167]). The gap is given by

$$E_g(\delta) \propto \frac{\delta^{2/3}}{|\ln \delta|^{1/2}} = \mathcal{O}(\delta^{2/3}). \quad (4.50)$$

That means one has a gap with  $\nu = 2/3 < 1$  and hence the gap can be closed in a finite amount of time with exponent  $\mu = 2$ . This means that the dimerization  $\delta$  has to be varied with

speed  $v(t) = c|\tau - t|^2$ , hence  $\delta(t) = \frac{\epsilon}{2}|\tau - t|^3$ . One needs thus the time  $\tau = (2/c)^{1/3}$ . The smaller  $c$  is, the farther one is in the adiabatic regime but the longer one needs for the preparation. An analysis of how small  $c$  is to be chosen to achieve a given accuracy of the prepared state could be carried out along the lines of Ref. [269].

Note that in [159], it was recently discussed within a mean-field approach, how the antiferromagnetic phase of the three-dimensional Fermi-Hubbard model could be reached by adiabatic tuning of the lattice potential.

## 4.7 Conclusion

A setup of two species of ultracold bosonic atoms in an optical superlattice has been studied. This setup realizes in a certain parameter regime the Heisenberg ferro- and antiferromagnet. The focus was in particular on time evolution of nonequilibrium states. The numerical results and analytical considerations showed that the physics of Bose-Hubbard model implemented in the experiment differs for certain parameter ranges considerably from the physics of the effective Heisenberg models. Note that this would also be true for alternative suggestions as in [166, 84, 7, 106, 22]. The spin states up and down can in general not be identified directly with a bosonic particle of one specific species. The regime where the correspondence between the two models is good, implies higher requirements on cooling and coherence (coherence time) in an experimental realization. The explicit form of the Schrieffer-Wolff transformation was used to analyze the transition rates out of the magnetic subspace of the full Hilbert space.

In contrast to the accomplished experiments [103, 271] for isolated double-wells (filled each with two particles), the setup of coupled double-wells discussed here allows for relaxation of the many-particle state. In the numerics one can observe indications for (local) relaxation to steady states. For the Heisenberg model in a mean field approximation, are explained how the relaxation is connected to a phase averaging effect. This is typical for integrable models which have nonthermal steady states. Nonintegrable models are generally believed to thermalize due to effective scattering effects. The here considered setup can be tuned from the nonintegrable Bose-Hubbard model to the Bethe ansatz integrable Heisenberg model and could hence be used to study the differences of the relaxation processes experimentally.

Finally I argued that the groundstate of the Heisenberg antiferromagnet could be prepared by tuning an alternating hopping parameter of the superlattice adiabatically.

## Chapter 5

# Landau Zener dynamics on a ladder with ultra cold bosons

Current ultracold atomic systems offer an entirely new perspective on low-dimensional quantum liquids. The extremely precise tunability of optical lattices allows one to focus on non-equilibrium dynamical behaviour of bosonic and fermionic many-body systems. Compared to the equilibrium properties, the theoretical understanding of dynamics in such systems is far more rudimentary since, in general, it is very difficult to obtain full analytical expressions for the dynamics of quantum mechanical systems; in particular if the Hamiltonian is time-dependent. One of the few analytically solved exceptions is the famous Landau-Zener problem [170, 297]. The Landau-Zener problem describes the dynamics of a time-dependent two-level quantum system, which can be described by

$$\hat{H}(t) = \begin{pmatrix} 0 & J \\ J & 2\varepsilon \end{pmatrix}, \quad (5.1)$$

where  $J$  is the coupling between the two levels and  $2\varepsilon = 2\alpha t$  is the energy offset. The Landau-Zener problem can be found in applications in physics and theoretical chemistry. For the latter the Landau-Zener formula was important for the understanding of atomic and molecular scatter processes for which non-adiabatical transitions between potential barriers became important [200, 86, 108, 255]. Indeed, this was the original context for which the Landau-Zener scenario was formulated independently by Landau [170], Zener [297] and Stückelberg [261] in 1932. In the same year Majorana has described the dynamic of a spin- $\frac{1}{2}$  particle in an inhomogeneous magnetic field [185, 233]<sup>1</sup>.

The Landau Zener formulation plays a crucial role in experiments with ultracold atoms in magneto-optical traps, where non-adiabatical spin flips lead to a loss of atoms [262]. Further examples can be found in the field of semiconductor physics [46], in particle physics [268] and nuclear physics [135]. One of the most important and probably most investigated phenomenon is the interaction between single atoms or molecules and laser light. In such a typical scenario the

---

<sup>1</sup>The Landau-Zener formula should be rather called the Landau-Zener-Stückelberg-Majorana formula, which is definitely too long

original Landau-Zener formula describes an atom approximately as a two-level system, which is driven by an external time-dependent laser field [5, 251]. The adiabatic dynamics induced by the laser field is used in order to change coherently the occupation probability between the two internal states. By the help of additional lasers one can induce the AC-Stark shift and to change the relative position between the initial and the final levels. This is the famous Stark Chirped Rapid Adiabatic Passage (SCRAP) [276, 289, 227]<sup>2</sup>, which was later extended the Stimulated Raman Adiabatic Passage (STIRAP) [31] the adiabatic transition via a third level (dark-state). Moreover, it turns out that the influence of a constant external force on the dynamics in periodic structures leads not only to Bloch oscillations in the lowest energy band but also to Landau-Zener-type oscillations between different Bloch bands. These effects has been experimentally observed in semi-conductor systems having a superlattice structure [97] and for ultracold atoms in optical lattices [29].

There exist many complicated systems for which the original Landau-Zener description holds. However, many other applications and scenarios cannot be described by a simple two-level model. Generalizations assuming more than two coupled modes are often not solvable analytically. The problem might be treated then using approaches known from field of open quantum systems. Here the most difficult part is to define a bath which leads to the correct damping factors in the evolution of the original two-level problem.

In the present chapter I introduce a particular Landau-Zener scenario which has been studied recently with ultracold bosons in an optical lattice [57]. This experiment addresses a direct many-body generalization of the Landau-Zener problem. The system at hand consists of pairwise tunnel-coupled one-dimensional Bose liquids. By tuning the correlations of the one-dimensional gases, via a change of the tunnel coupling between the tubes and the inter-tube interactions it is possible to switch between regimes which go far beyond the original Landau-Zener picture.

The aim of the here presented work is twofold. First, using the time-dependent DMRG method it is possible to verify the experimental results obtained in [57]. Second, the numerical exact method allows for the extraction of important quantities, e.g. real space correlators, which help clarifying the microscopic understanding of the physical system.

## 5.1 Mean field description

The two-body problem Eq. (5.1) has been first solved independently in 1932 by Landau [170], Zener [297], Stückelberg [261] and Majorana [185] and later rediscovered by Wannier [278] in 1964. The time-dependent two-level Hamiltonian Eq. (5.1) has the eigenvalues  $E_{1,2} = \varepsilon \mp \sqrt{\varepsilon^2 + J^2}$  and the eigenvectors  $|\phi_{1,2}\rangle = \frac{1}{w_{1,2}} \begin{pmatrix} 1 \\ v_{1,2} \end{pmatrix}$  with  $v_{1,2} = E_{1,2}/J$  and the normalization constant  $w_{1,2} = \sqrt{(E_{1,2}/J)^2 + 1}$ . The eigenstates of the uncoupled system  $|e_L\rangle = \begin{pmatrix} 1 \\ 0 \end{pmatrix}$  and  $|e_R\rangle = \begin{pmatrix} 0 \\ 1 \end{pmatrix}$  ( $J = 0$ ) are called the standard basis states.

<sup>2</sup>The original realization of the adiabatic transfer, known as Rapid Adiabatic Passage [179], has changed the

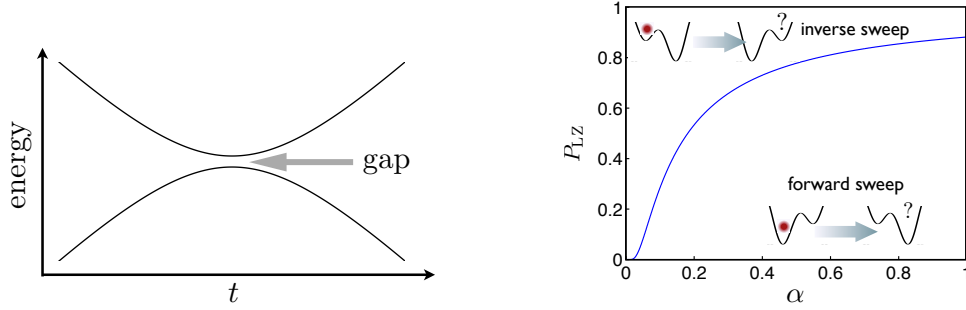


Figure 5.1: The left figure shows the energies of the two-level problem Eq. (5.1) as a function of time. The smaller the gap between the energies the more adiabatic must be the transition. On the right one can see a typical curve for the transition probability  $P_{LZ}$  as a function of the transition speed. For the simple case of a two-level model there is no difference between the forward sweep and the inverse sweep scenario which are depicted as an insert; in both scenarios  $P_{LZ}$  has the same dependence on  $\alpha$ .

### 5.1.1 Landau-Zener formula

In the following I will derive the Landau Zener formula under the assumption that the system changes linearly in time, starting at large negative time and evolving to a large positive time. Moreover, I assume that for  $t = 0$  the system starts in one of its eigenstates. During the time evolution the system is given as linear combination between the two standard basis states

$$|\psi(t)\rangle = \psi_1(t) \begin{pmatrix} 1 \\ 0 \end{pmatrix} + \psi_2(t) \begin{pmatrix} 0 \\ 1 \end{pmatrix}. \quad (5.2)$$

I assume now without loss of generality that  $|\psi_1(t \rightarrow -\infty)| = 1$ . Together with time-evolution described by  $i\hbar|\dot{\psi}(t)\rangle = \hat{H}(A(t))|\psi(t)\rangle$  one obtains the two coupled first order differential equations

$$\begin{aligned} i\hbar\dot{\psi}_1 &= J\psi_2 \\ i\hbar\dot{\psi}_2 &= J\psi_1 + 2\alpha t\psi_2, \end{aligned} \quad (5.3)$$

which can be put together into a single second order differential equation using  $\psi_2 = \frac{i}{J}\dot{\psi}_1$  and  $\dot{\psi}_2 = \frac{i}{J}\ddot{\psi}_1$ :

$$\ddot{\psi}_1 + 2i\alpha t\dot{\psi}_1 + J^2\psi_1 = 0. \quad (5.4)$$

Together with the ansatz  $\psi(t) = U(t)e^{f(t)}$  and its derivations one obtains

$$\begin{aligned} \ddot{U} + \dot{U}(2\dot{f} + 2i\alpha t) + U(\ddot{f} + \dot{f}^2 + 2i\alpha t\dot{f} + J) &= 0 \\ \ddot{U} + U(J^2 - i\alpha + (i\alpha t)^2) &= 0 \end{aligned} \quad (5.5)$$

where in the last line I used the identity  $\dot{f} = -i\alpha t$  and therefore  $f = -\frac{i}{2}\alpha t^2 + C$  which makes  $\dot{U}$  in the first line vanish. The linear transformation  $z = e^{i\frac{\pi}{4}}(2\alpha)^{\frac{1}{2}}t$  leads to the so-called normal

---

couplings between the levels.

form of the Weber differential equation

$$\frac{d^2}{dz^2}U(z) + \left( \nu + \frac{1}{2} - \frac{1}{4}z^2 \right) U(z) = 0 \quad \text{with } \nu = \frac{iJ^2}{2\alpha}. \quad (5.6)$$

The above equation can be solved by means of a simple linear combination between the two Weber functions  $D_\nu(z)$  and  $D_\nu(-z)$  for which the asymptotic behavior [25] at large large times  $|t|$  is known<sup>3</sup>. Assuming that  $\alpha > 0$  and under the constrain that  $0 \leq |\psi_1(t \rightarrow +\infty)|^2 \leq 1$  one finds the only possible solution to be  $D_\nu(z)$  which leads together with the original ansatz to the solution<sup>4</sup>

$$\psi_1(t) = A \exp\left(-\frac{i}{2}\alpha t\right) D_\nu\left(e^{i\frac{\pi}{4}}(2\alpha)^{\frac{1}{2}}t\right). \quad (5.7)$$

The normalization constant  $A$  can be calculated from the asymptotic solution as

$$|\psi_1(t \rightarrow -\infty)|^2 = 1 = |A|^2 \left| D_\nu\left(e^{i\frac{\pi}{4}}(2\alpha)^{\frac{1}{2}}t, t \rightarrow -\infty\right) \right|^2 = |A|^2 e^{\frac{3\pi J^2}{4\alpha}} \quad (5.8)$$

Now, together with above equation one can easily find the Landau-Zener formula  $P_{LZ} = |\psi_1(t \rightarrow +\infty)|^2$ , which gives the transition probability between the initial ground and the excited state (or vice versa):

$$P_{LZ} = e^{-\frac{3\pi J^2}{4\alpha}} \left| D_\nu\left(e^{i\frac{\pi}{4}}(2\alpha)^{\frac{1}{2}}t, t \rightarrow +\infty\right) \right|^2 = e^{-\frac{3\pi J^2}{4\alpha}} e^{-\frac{\pi J^2}{4\alpha}} = e^{-\frac{\pi J^2}{\alpha}} \quad (5.9)$$

In a similar way one can also derive for  $\alpha < 0$  the same Landau-Zener probability as for  $\alpha > 0$ . Thus, one finally arrives at the known expression

$$P_{LZ} = e^{-\frac{\pi J^2}{|\alpha|}}. \quad (5.10)$$

## 5.1.2 Extensions of the Landau-Zener formula

### Two-level system coupled to an infinitely large bath

After the discussion of the pure Landau-Zener problem for a closed two-level quantum system I would like to consider a more realistic scenario of a two-level system coupled to an infinitely large bath. The coupling to the bath leads to a decay of the population of the two internal states. It turns out that such a simple coupling which results in an constant decay rate does not change the Landau-Zener formula Eq.(5.10). Nevertheless, in order to model a more convenient environment it is important to know why the Landau-Zener formula is not affected by such a bath.

<sup>3</sup>The two Weber functions are linear independent iff  $\nu \neq \mathbb{N}$

<sup>4</sup>The derivation is similar for  $\alpha < 0$ .

In the following I assume that the right standard basis state  $|e_R\rangle$  decays with a constant rate. The system is now governed by the non-hermitian Hamiltonian

$$\hat{H}(t) = \begin{pmatrix} 0 & J \\ J & 2\varepsilon - 2i\gamma \end{pmatrix} \quad \text{with } \gamma > 0. \quad (5.11)$$

Similar to the hermitian case the time-evolution of the above system can be described through a set of two coupled differential equation

$$\begin{aligned} i\hbar\dot{\psi}_1 &= J\psi_2 \\ i\hbar\dot{\psi}_2 &= J\psi_1 + 2\alpha t\psi_2 - 2i\gamma\psi_2, \end{aligned} \quad (5.12)$$

which leads to the following second order differential equation for  $\psi_1$ :

$$\ddot{\psi}_1 + 2(i\alpha t - \gamma)\dot{\psi}_1 + J^2\psi_1 = 0. \quad (5.13)$$

In an analogous way to Eq. (5.5) one obtains together with the ansatz state

$$\psi_1(t) = A \exp\left(-\frac{i}{2}\alpha t^2 - \gamma t\right) U(t) \quad (5.14)$$

the following pre-Weber differential equation

$$\ddot{U} + (J^2 - i\alpha + (\alpha t - i\gamma)^2)U = 0. \quad (5.15)$$

Finally, after the transformation  $z = e^{i\frac{\pi}{4}}(2\alpha)^{\frac{1}{2}}(t - i\frac{\gamma}{2})$  one obtains the Weber equation. For  $\nu = -iJ^2/(2\alpha)$  and thus  $\alpha > 0$  one gets the solution in terms of the Weber functions:

$$\psi_1(t) = \psi_1(t) = A \exp\left(-\frac{i}{2}\alpha(t - i\frac{\gamma}{2})^2\right) D_\nu\left(e^{i\frac{\pi}{4}}(2\alpha)^{\frac{1}{2}}(t - i\frac{\gamma}{2})\right). \quad (5.16)$$

After the determination of  $A$  from the asymptotic behaviour at  $t \rightarrow -\infty$  one obtains the Landau-Zener probability from the opposite limit of  $t$  as

$$P_{LZ} = e^{-\frac{\pi J^2}{|\alpha|}}, \quad (5.17)$$

which is totally independent of  $\gamma$ .

### Three level Landau-Zener

It seems that that the probability  $P_{LZ}$  to find the system after a time-evolution in its initial state does not depend on the details of the coupling between the other standard basis state and some arbitrary large bath. However, this is, in general, not true. Considering different system-bath-couplings, and thus decay mechanisms which are different to the one which assumes an arbitrary large continuum, one obtains changes in the Landau-Zener probability [277, 3]. Motivated by this results I will try in the following another approach to model a bath. Instead of a local or

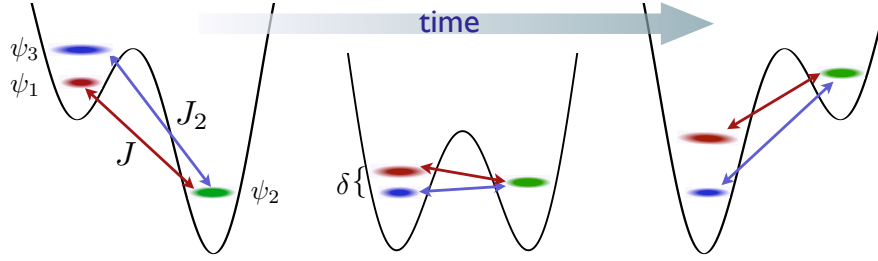


Figure 5.2: Three level Landau-Zener sweep in a double well. Schematic sketch of the model in Eq. (5.18) with respect to the experiment in [57]. At the beginning of the simulation (left figure)  $|\psi_1|^2 = 1$  (red) and the energy levels are  $\varepsilon_2 \ll \varepsilon_1 < \varepsilon_3$ . According to the Hamiltonian (5.18) the first energy level is zero during the whole simulation. The two transition speeds  $\alpha > 0$  and  $\beta < 0$  and  $\delta$  are chosen in such a way that an energy-crossing occurs in the vicinity of  $\varepsilon_2(t) = 0$ . The right figure shows the situation at  $t \rightarrow +\infty$ . The order of the energies is completely inverse with respect to the initial situation.

global bath which couples to the two states I assume a third state which couples with the second but not with the first state. Inspired by the recent experiment of Chen [57] I assume also the third state to change its relative energy in time. Such a system can be described by

$$\hat{H}(t) = \begin{pmatrix} 0 & J & 0 \\ J & \varepsilon_2(t) & J_2 \\ 0 & J_2 & \varepsilon_3(t) \end{pmatrix}, \quad (5.18)$$

with  $\varepsilon_2(t) = \Delta_2 + \alpha t$ , where  $|\alpha| = \frac{2\Delta_2}{T}$  is the so-called sweep rate and  $T$  is the so-called sweep time, i.e. the time-evolution runs between  $0 \leq t \leq T$  with speed  $\alpha$ . Finally,  $\varepsilon_3(t) = \Delta_3 + \delta + \beta t$  with  $|\beta| = \frac{2\Delta_3}{T}$  and  $\delta$  a small additional energy offset.  $J_2$  couples the second with the third level. To give some numbers, in the following numerical simulations,  $J = J_2 = -0.1$ ,  $\Delta_2 = -30$  with  $\alpha > 0$  and  $\Delta_3 \approx +1$  with  $\beta < 0$ . The energy offset will be  $\delta \approx -0.1$ . Assuming that the third standard basis state has constant energy, i.e.  $\beta = 0$ , one would obtain again the Landau-Zener Eq.(5.10). Indeed, this model has been already solved [78] and belongs to the class of the so-called equal slope  $N$ -level models.

Now, I consider the three level case with  $\beta \neq 0$ . It turns out that this scenario is too difficult for a derivation of a Landau-Zener probability law from simple consideration of the adiabatic theorem at the crossing points of the three involved energies. With regard to the breakdown of the Landau-Zener formula [see Chap.(5.4)] for the so-called inverse sweep in [57], which means the case of an adiabatic transfer of the excited state and not the ground state<sup>5</sup>, I model the initial state and the time evolution in the following way. The initial state in [57] consists of a BEC in one tube and a second empty tube, which has an additional negative energy shift. For most of the time during the adiabatic transport of bosons from the filled to the empty tube the effective coupling between the two tubes is zero. While the effective coupling is zero the two tubes are independent from each other and the BEC state in the filled tube can be considered to be the ground state. This means for the three level model, that at  $t = 0$  the energy of the second state is far below the

<sup>5</sup>In the simple two-level model the Landau-Zener probabilities for the excited state and for the ground state are the same.



energy of the first state  $\varepsilon_2(t=0) = \Delta_2 \ll 0 = \varepsilon_1$  and on the other hand the energy of third state, the additional channel for a decay, is slightly above first state energy  $\varepsilon_3(t=0) = \Delta_3 + \delta > 0$ .

According to the experiment I choose for the time-evolution  $\alpha = \frac{2\Delta_2}{T}$  and  $\beta = -\frac{2\Delta_3}{T}$ , which leads to  $\varepsilon_2(t=0) = -\Delta_2 \rightarrow \varepsilon_2(T) = +\Delta_2$  and  $\varepsilon_3(t=0) = \Delta_3 - \delta \rightarrow \varepsilon_3(T) = -\Delta_3 + \delta$  and, thus, to the final situation where  $\varepsilon_3 < \varepsilon_1 \ll \varepsilon_2$ . The choice of sign in  $\alpha$  and  $\beta$  (and the relatively small  $\delta \approx -0.1$ ) leads to two energy-crossings during the time-evolution, which take place when  $\varepsilon_2 \approx 0$ . With the additional offset  $\delta$  one can avoid the situation that both energy-crossings take place at the same point, which would also mean that all three energies are the same. The choice of  $\delta < 0$  also provides that already at the symmetric point, i.e. the situation after the half sweep,  $\varepsilon_1 > \varepsilon_3$ . This is a reasonable due to the fact that at this point the initial BEC is certainly not the ground state anymore. In figure Fig.(5.3) shows the fidelity  $|\psi_2|^2$  as a function of the inverse sweep rate  $\alpha$  for different choices of  $\delta$ . The other parameters are  $J = J_2 = -0.1$ ,  $\Delta_2 = -30$ ,  $\Delta_3 = 1$ . One observes for fast sweeps (large  $\alpha$  corresponds to a small  $T$ ) a monotonic increase of the fidelity which then, for slower sweeps, is followed by its decrease. The smaller  $|\delta|$  the faster does the downturn occur and the stronger is decrease of the fidelity. This simple model could serve as a starting point for the interpretation of the observed downturn in the coupled-tubes scenario in [57], which I will discuss in the second part of this chapter.

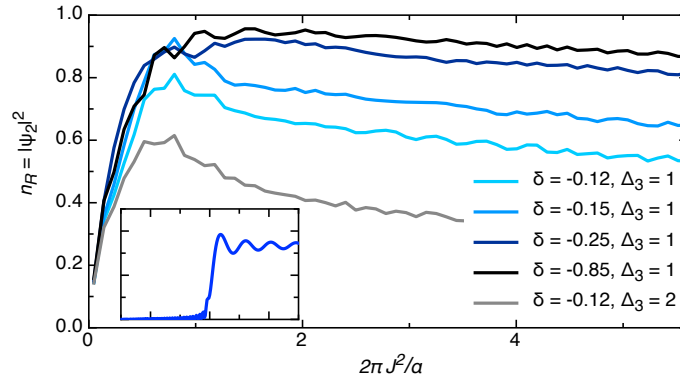


Figure 5.3: The three level model inverse sweep scenario. The plots are calculated by a simple direct integration for the parameter:  $J = J_2 = -0.1$ ,  $\Delta_2(t=0) = -30$ . Apart the grey curve the blue curves differ in the detuning of the auxiliary energy level  $\delta$ . The curves show an universal behaviour for very large sweep rates. The later observed deviation from the universality occurs sooner for smaller  $\delta$ . The insert show exemplary curve for a single sweep. See also the inverse sweep with the bosonic ladder [Fig. (5.7)]

After the discussion of the original Landau-Zener scenario and the two extensions in terms of a constant decay rate to an infinitely large bath and the assumption of a third state I will now proceed with a more precise analysis of the Landau-Zener scenario in two coupled one-dimensional bosonic condensates [57] using the time-dependent DMRG method.

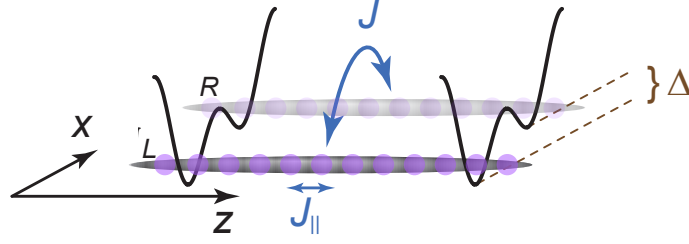


Figure 5.4: The bosonic ladder scheme. The Bose ladder model with the intratube hopping  $J_{\parallel}$  ( $z$ -axis), the onsite interaction  $U$ , the intertube hopping  $J$  ( $x$ -axis) and the variable offset  $\Delta$  on the right tube.

## 5.2 Setup and model for the time-dependent DMRG calculations

I consider a bosonic ladder system made of two coupled one-dimensional tubes, the left  $L$  and the right  $R$  tube, made of an optical lattice. Additionally to the intratube hopping  $J_{L,\parallel} = J_{R,\parallel} = J_{\parallel}$  (axial  $z$ -direction) and the onsite interaction  $U$ , there is a superlattice potential in the (transversal)  $x$ -direction of the form

$$V(z) = V_0 \sin^2(kz) + V_1 \sin^2(kz/2 + \phi), \quad (5.19)$$

where by simply varying  $V_1$  and the phase  $\phi$  one can tune the intertube hopping  $J$  and create an additional offset  $\Delta$  between the potential energy in the left and the right tube [cp. Fig. (5.4)]. The superlattice structure can be generated by the superposition of two standing waves [103, 271] generated with two lasers with the frequency ratio 1:2. Assuming the tight-binding approximation with restriction to the first Bloch band (one Wannier function per site) the system is then described by the Bose-Hubbard Hamiltonian

$$\begin{aligned} \hat{H}(t) = & J_{\parallel} \sum_{i,\sigma=L,R} (\hat{b}_{i,\sigma}^{\dagger} \hat{b}_{i+1,\sigma} + h.c.) + J \sum_i (\hat{b}_{i,L}^{\dagger} \hat{b}_{i,R} + h.c.) \\ & + \frac{U}{2} \sum_{i,\sigma=L,R} \hat{n}_{i,\sigma} (\hat{n}_{i,\sigma} - 1) + \Delta(t) \sum_i \hat{n}_{i,R}, \end{aligned} \quad (5.20)$$

For the initial system one calculates the ground state at  $\Delta = 100J$ , i.e. all bosons sit in the left tube and quenches the ground state from  $\Delta = 100J$  to the desired initial value  $\Delta(t_0) = \Delta_0$ . Next, the simulation is done by varying linearly  $\Delta$  in time according to

$$\Delta(t) = \Delta_0 + \frac{\Delta_f - \Delta_0}{T} t = \Delta_0 + \alpha t, \quad \text{where } 0 \leq t \leq T, \quad (5.21)$$

until one reaches the final  $\Delta(T) = \Delta_f = -\Delta_0$ . In the following I call such a simulation a sweep. There are two types of sweeps. I use the term forward sweep (or ground state sweep) if  $\Delta_0 > 0$  and the term inverse sweep if  $\Delta_0 < 0$ . In the following I will always consider situations where the energy offset  $\Delta_0$  is the largest energy scale, namely,  $|\Delta_0| \gg J \gg U$

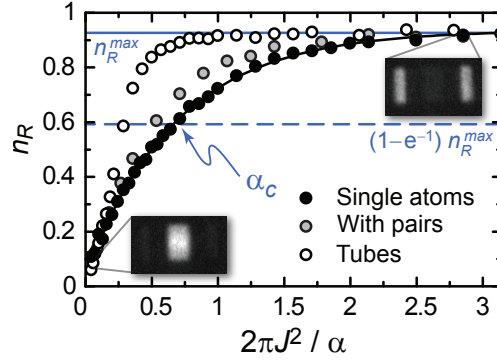


Figure 5.5: Forward sweep. The transfer efficiency, also called fidelity here, calculated for the single particle in a double well [cp. Fig. (5.1)], for two particle in a double well and the experimentally obtained data for the coupled tubes. Sweep fidelity is measured with the characteristic rate  $\alpha_c$ , which is the sweep rate to achieve a transfer efficiency of  $1 - e^{-1} \approx 63\%$  with respect to the maximal measured value  $n_R^{\max}$ . Figure adapted from [57].

### 5.2.1 Numerical method and parameters

For the numerical simulation, a Krylov subspace variant [210, 136] of the time-dependent DMRG algorithm was used [285, 70, 243]. For the Hubbard model, the site basis was restricted to a maximum of three particles for each species. Insensitivity of observables to the chosen maximum number of bosons per site was affirmed. The investigated sizes of the ladder system are in between of  $L = 8 \times 2$  and  $L = 16 \times 2$ . In the time evolution, the absolute difference per physical time unit between exactly evolved state and the state evolved via DMRG  $\|\psi_{dt}^{\text{exact}} - \psi_{dt}^{\text{DMRG}}\|/dtN$  was bounded from above by  $\varepsilon = 10^{-4}$  and the time step chosen appropriately between  $dt = 0.05$  and  $0.005$ . The errors were determined in a rigorous fashion, by calculating the exact value of  $\| |k+1\rangle - \hat{H}|k\rangle \|$ , where  $|k\rangle$  are the Krylov vectors. I have simulated the sweep with  $\hat{H}(t)$  by a step wise calculation with a static Hamiltonian. For this purpose it was sufficient to divide  $\Delta_f - \Delta_0$  and the sweep time  $T$  into 100 sub-steps for the forward and 200 – 400 sub-steps for the inverse sweep. For all calculated observables, convergence in the error bound and  $dt$  was checked. The resulting number of basis states, used to represent the time-evolved state, was  $\lesssim 4000$ .

## 5.3 Forward sweep

I start the discussion of the ground state sweeps, where  $\Delta_0 > 0$ , i.e. the filled left tube is the one with lower energy. The comparison of transfer efficiencies  $n_R$ , which I also call fidelity, for pairwise coupled dot-like lattice sites (or equivalently  $J_{\parallel} = 0$  for the tubes) and one-dimensional tubes as a function of sweep rate has been done in [57] and can be seen in Fig. (5.5). The fidelity  $n_R$  can be directly associated with  $1 - P_{LZ}$ , the probability to stay in the ground state. Except the general monotonic increase of  $n_R$  [see inverse sweep Chap. (5.4)] in all cases, one observes an enhance of this transfer with increasing interaction strength. In order to quantify the sweep fidelity with a single number, one can defines the characteristic rate  $\alpha_c$  as the sweep rate to achieve a transfer efficiency of  $1 - e^{-1} \approx 63\%$  with respect to the maximal measured value.

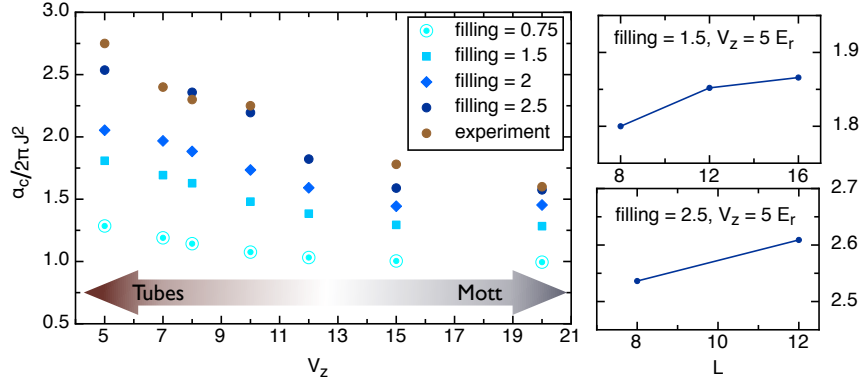


Figure 5.6: Forward sweep. Characteristic rates  $\alpha_c$  for the transverse lattice depth  $V_x = 15E_r$  and a different axial lattice depths  $V_z$  for different initial fillings. The points have been obtained on a  $L = 8 \times 2$  lattice. For the initial filling  $n_{L,0} = 2.5$  one gets the best agreement with the experimental data where the average filling is around  $n_{L,0} = 2.6$ . For large  $V_z$  (decoupled double wells) one recovers the two-level Landau-Zener result. The two additional plots at the right show the dependence of the here presented results on the system length  $L$ . As expected, the bigger the interactions the more important are finite size effects. Nevertheless, the error between  $L = 8 \times 2$  and  $L = 16 \times 2$  is less than 5%.

Therefore, larger  $\alpha_c$  correspond to higher transfer rates. In the case of single atoms in the dot-like sites, the result almost matches with the Landau-Zener formula. Here,  $\alpha_c = 2\pi J^2$  sets the natural scale for the sweep rate. If the filling is increased, one finds an enhanced value of  $\alpha_c$ . This enhancement is even more pronounced in the case of the pairwise coupled tubes filled with up to 100 atoms which leads to the conclusion that interactions are crucial for such enhancement. Indeed, a non-interacting BEC, i.e.  $J_{\parallel}$ , would result in the same transfer rate as is the case for a single particle.

In Fig. (5.6) one can see the characteristic rates  $\alpha_c$  for the transverse lattice depth  $V_x = 15E_r$  and a different axial lattice depths  $V_z$  calculated using the time-dependent DMRG method. To give some numbers,  $V_z = 4$  is equivalent to  $J_{\parallel} = 0.63J$  and  $U = 4.03J$  while  $V_z = 15$  corresponds to  $J_{\parallel} = 0.06J$  and  $U = 5.7J$ . The dependence of  $\alpha_c$  on the transverse  $z$ -lattice depths accounts well for the trends observed in the experiments. One observes a significant jump  $V_z \approx 8$  when going from small lattice depths to large depths, where the condensate is significantly depleted and driven towards the Mott transition of the quantum ladder. Deep in the Mott regime all Bose enhancement in the tunneling process is lost and one essentially recovers the single-particle Landau-Zener results.

## 5.4 Inverse sweep

After the discussion of the results for the ground state, or forward sweep, I will present, in the following, the results for the simulation of the so-called inverse sweep. The inverse sweep scenario aims the question of the probability for a successful transfer of an excited state from the left to right tube. According to the preparation scheme [cp. Chap. (5.2)] the initial state is obtained by a quench of  $\Delta_i \rightarrow -\Delta_0 < 0$  at  $t = 0$ . The filled left tube lies energetically above the

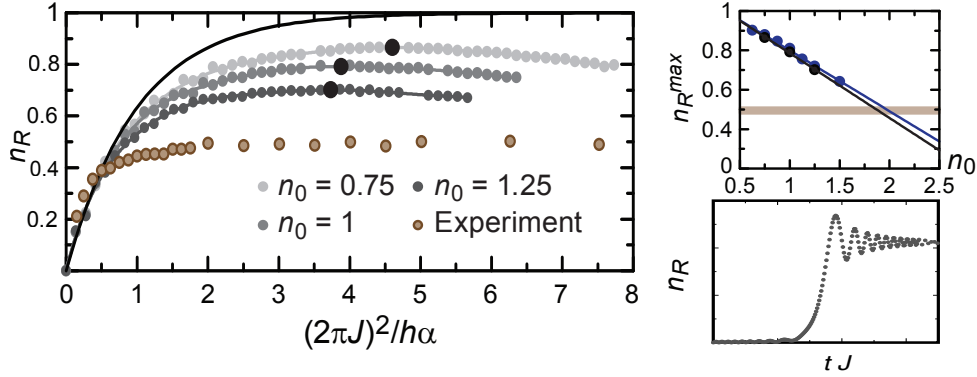


Figure 5.7: Fidelity in the inverse sweep. The left figure shows the fidelity  $n_R$  as a function of the sweep rate  $\alpha$ . The solid black curve shows the Landau-Zener solution for a single particle problem in a double well. The grey curves show the result of the time-dependent DMRG calculation for a  $L = 8 \times 2$  ladder at  $J_{\parallel} = 0.38J$ ,  $U = 1.58J$  and  $\Delta_0 = 9.1J$  for three initial fillings  $n_{L,0} = 0.75$  (light grey),  $n_{L,0} = 1$  (grey),  $n_{L,0} = 1.25$  (dark grey). For a quantitative comparison I have plotted the data from the experiment (brown dots). The big discrepancy between the experiment and the simulation comes from the fact that it was possible to reach the typical experimental densities  $n_{L,0}^{\text{exp}} \approx 2$ . However, the position and the absolute value of the maximum of  $n_R(\alpha)$  moves towards the experimentally observed value as one increases the number of bosons, which corresponds to an increase of the effective interaction along the tubes. The bigger this intratube interaction the sooner does the fidelity curve deviate from the single particle solution. The upper right figure shows  $n_R^{\text{max}}$  as a function of the initial density  $n_{L,0}$  (black dots). The extracted curve coincides very well with the experimentally obtained position of  $n_R^{\text{max,exp}}$  (brown line). The smaller dark blue dots correspond to the numerical calculation with  $L = 12 \times 2$ . The finite size effects (at least at this densities) are in the range of few percent. The upper lower figure shows a typical sweep of  $n_R$  in real time. The final value of  $n_R$  is averaged over the last few (damped) oscillations.

empty right tube.

The results of the fidelity  $n_R$  as a function of the sweep rate  $\alpha$ , for different initial densities, are depicted in Fig. (5.7). The parameters in units of the intertube hopping  $J$  are  $U = 1.58J$ ,  $J_{\parallel} = 0.38J$  and  $\Delta_i = -\Delta_0 = -9.1J$  or equivalent  $V_x = 12E_r$  and  $V_z = 4E_r$ . After a monotonic increase of  $n_R$  for large  $\alpha$  the fidelity starts to saturate at around some maximum value. Then, contrary to the forward sweep scenario,  $n_R$  does not approach the maximal fidelity but starts to decrease with a decreasing sweep rate. This downturn disappears in the case of non interacting bosons [cp. the two-level Landau-Zener in Chap. (5.1.1)], where forward and inverse sweeps lead to a monotonically increasing fidelity. The solid black curve in the upper figure in Fig. (5.7) shows the result of a single particle in a double well (or equivalently for tubes  $J_{\parallel} = 0$ ) for both, the forward and the inverse sweep. The surprising downturn effect must be a direct consequence of interactions along the tubes ( $z$ -direction). As one can see in Fig. (5.7) the bigger the initial density, and thus the overall interaction strength, the sooner does the fidelity break off the single particle result. Moreover, with increasing interactions the maximal value of  $n_R$  is smaller and occurs at a higher rates  $\alpha$ . Figure (5.7) shows also the experimental data for the same parameter regime (brown dots). The typical densities in the experiments are around  $n_{L,0}^{\text{exp}} \approx 2$ . It turns out that such high densities and related time scales are not accessible by the time-dependent DMRG method used in this project. Nevertheless, a simple linear extrapolation of the position of the maxima as a function of  $n_{L,0}$  does almost perfectly coincide with the experimental value [see

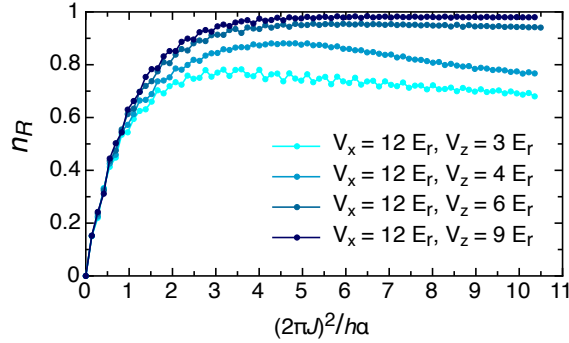


Figure 5.8: Dependence of the inverse sweep relaxation on the intratube coupling  $J_{\parallel}$ . The four curves show the fidelity as function of the inverse sweep rate  $\alpha$  for four different intratube couplings  $V_z$ . For large  $V_z = 9E_r$  (corresponds to  $J_{\parallel} = 0.02$ ) the double wells are not sufficiently connected and, thus, the curve shows basically the single double well result. In particular, there is no downturn visible. As soon as one turns on the intratube hopping the relaxation effect becomes more and more visible.

upper right figure in Fig.(5.7)]. The dependence of the relaxation on the intratube hopping is also shown in figure (5.8). Here, I have plotted four different curves starting with the uncoupled double wells case ( $V_z = 9E_r$ ), where a relaxation is not visible, and going down to smaller  $V_z$  which correspond to an increase of  $J_{\parallel}$ .

In the following I will try to explain the observed downturn and relaxation process for the inverse sweep. The initial state in the left tube describes approximately a Bose-Einstein condensate and is, thus, a macroscopic object. For fast sweeps, or equivalently, for short coupling times, the function of fidelity follows the  $P_{LZ}$  as calculated for a single double well. The intratube hopping  $J_{\parallel}$  is three time smaller than  $J$  and therefore not important for fast sweeps. However, as the sweep rate  $\alpha$  decreases the intratube hopping becomes more and more relevant. The fidelity starts to deviate from the single double well picture [see Fig. (5.7)]. During a single sweep [see the lower right figure in Fig. (5.7)] bosons swap from left to empty right tube and oscillate afterwards until an equilibration in both tubes. While the first turnover is still a coherent process, which does not destroy the BEC, the subsequent intertube oscillations already involve non-coherent scattering process and intratube hopping; the condensate forms here a highly excited state [see Chap.(5.5)]. While the fraction of the initial condensate which swaps from left to right becomes bigger as one increases the sweep time, the following intertube oscillations have a more or less constant amplitude [see lower right figure in Fig(5.7)]. This oscillations lead to the redistribution of momenta caused by collisions among the bosons under the restriction of a conserved total momentum. As long as the double wells are not coupled, i.e.  $J_{\parallel} \approx 0$  there is no possibility for the bosons to change their momenta after a scattering event. Once the double wells are coupled, bosons are allowed to change their momenta during a collision, which is equivalent to an additional intertube hopping. I have already mentioned that the total state, as well as the left and right states, correspond to highly excited configuration throughout the whole sweep process. As I will show in the next chapter [see Chap.(5.5)] a highly excited system of bosons, e.g. all bosons of the system sit in the energetically higher tube, has always the tendency to equilibrate around fifty-fifty occupation, i.e. half of the bosons sit in the left and the other half in the right tube. This is exactly what

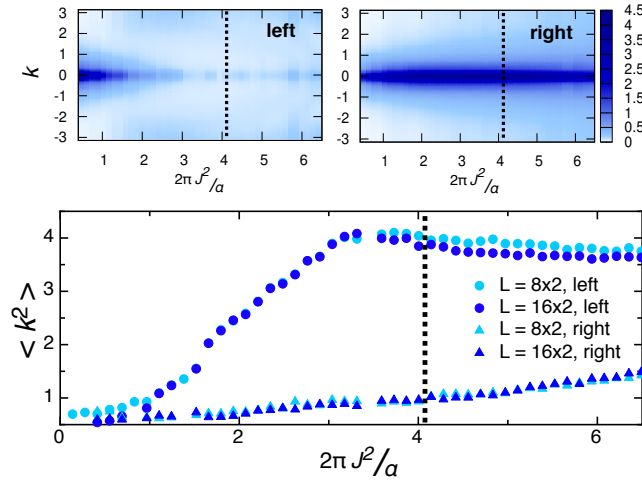


Figure 5.9: Momentum distribution of the inverse sweep. The two upper plots show the momentum distribution  $n_k$  in the left and in the right tube as a function of the sweep rate. Since the initial state in the left tube is a BEC one observes a large peak at  $k = 0$ . A fast inverse sweeps lead to a separation of the initial condensate among both tubes collisions with a redistribution of momenta are not allowed. This is not anymore the case for longer sweeps. The hopping along the tubes open a possibility for scattering processes with a high momentum exchange. Collisions with a high momentum are favoured since the particles can then absorb most of the systems energy and put it into kinetic energy along the tubes. The number of bosons which participate is much smaller than the total number of bosons in the right tube. While the initial signal of the condensate, i.e.  $k = 0$ , survives much longer and in the right tube (upper right), it disappears in the left tube, which make the observation of peaks at  $k = \pi$  possible (upper left). The lower figure shows the broadening of  $n_k$  in the left and in the right tube. While  $n_{k,L}$  is already completely broaden for moderate large sweep times the right tube shows the memory about the initial condensate even for longer sweep times. Nevertheless, one can see a constant growth of the broadening also here. Finally, for very large sweep times the left and right tube should have exactly the same distribution, since they stay long enough in contact with each other.

happens during an inverse sweep. Bosons will always try to reach the fifty-fifty configuration as long as the majority of them occupy the higher excited tube and, this is crucial, as long as the two tubes are effectively coupled. Although there is finite intertube coupling  $J$  during the whole sweep, there is only a certain parameter (or time) window when bosons are allowed to jump from left to right and vice versa. Once the system passes this window the fidelity is locked and there are only intratube processes going on.

The whole curve can be explained as follows. The increase for fast sweeps is a more or less modified version of the isolated double well case. For longer sweeps the fidelity starts to deviate from the Landau-Zener result for a single particle, since intratube hopping are allowed. The energy of the system is redistributed into excitation along the tubes via collisions between the bosons. The best way to redistribute the energy is to put it into the highest momentum modes, i.e.  $k = \pi, -\pi$ . As one increases the sweep time further the system follows more and more the dynamic of the quenches, i.e. the sweep can be seen as a sequence of several quenches.

There is a small difference between the left and right tube. While the fraction of oscillating bosons at the end of each single sweep are much smaller than the total number of bosons in the right tube, it is of the same order as the number of bosons in the left tube. Therefore, this highly

excited bosons cause a much faster broadening in the left than in the right tube, where there are still enough bosons in the BEC state with  $k = 0$  [see figure at bottom of Fig.(5.9)]. Finally, for infinitely long sweeps the broadening of the left and right tube must be the same as there will be an infinitely large number of intertube hopping processes during single sweep.

## 5.5 Time-evolution after quenches

The forward and inverse sweep in a bosonic ladder system can be seen as one particular example of the Landau-Zener problem, i.e. the scenario of coupled double wells. The fact that bosons are, now, strongly correlated along the legs of the ladder leads in the case of the inverse sweep scenario to a remarkable deviation from the expected single double well result. While it is possible to find a simple physical picture for the observed relaxation it turns out that a more detailed explanation is a much harder task due to the large number of parameters combined with the fact that the Hamiltonian, which governs the dynamic, is time-dependent. One possible way to decrease the complexity of the problem is by studying systematically quench scenarios, i.e. instantaneous quenches of the initial setup with all bosons sitting in the left tube, to a Hamiltonian with a constant  $\Delta_f = \text{const}$ . However, the fact that quenches allow for a clean stroboscopic picture of the Landau-Zener problem is not the only reason for their investigation. Another important reason is the possibility to create a quasi-thermal state<sup>6</sup> using a simple experimental setup. Before starting the discussion about the quenches there are two general remarks. Contrary to the sweeps the total energy in the quench scenarios is a conserved quantity. Second, despite the fact that  $J \neq 0$  the effective hopping process can only occur in the vicinity of  $\Delta_f = 0$ . Due to the energy conservation no hopping is allowed if  $|\Delta_f|$  is too large.

As for the sweeps the following discussion will mainly relay on the results for the fidelity and the broadening of the momentum distribution. The figure at the bottom of Fig. (5.10) shows the broadening  $\langle k^2 \rangle$  as a function of  $\Delta_f$  for different fillings. For a sufficient large initial filling  $n_{L,0}$ , the broadening  $\langle k^2 \rangle$  grows in a monotonic way. First of all  $\langle k^2 \rangle$  is very small for very large positive  $\Delta_f$ . This is the regime where the initial state corresponds nearly to the true ground state of the system, i.e. a quasi perfect condensate with a strong peak at  $k = 0$ . Now, decreasing  $\Delta_f \rightarrow 0$  and further to  $\Delta_f < 0$  is equivalent to start with a more and more excited state, which then can be associated to an effective temperature  $T_{\text{eff}} > 0$ . As expected, the broadening becomes here larger and larger since the momentum distribution starts to become flatter the larger  $T_{\text{eff}}$ . The largest possible value for  $\langle k^2 \rangle$ , i.e.  $\langle k^2 \rangle = \pi$  for a totally flat momentum distribution, is reached approximately around  $\Delta_f \approx -2J$ . Figure (5.10) shows also the broadening of a thermal state (red dots) with filling  $n_{L,0} = 1.5$ , calculated by the finite temperature DMRG calculation. The agreement between the latter and steady state results for  $n_{L,0} = 1.5$  is very good. This is not the case anymore for smaller fillings. As one can see in [Fig.(5.10)] a peculiarity occurs in the vicinity of the symmetric point ( $\Delta_f = 0$ ); the broadening drops down to the initial value before the quench. Since the resonance between the energy levels in the left and right tube is here the biggest a dilute condensate can easy tunnel with the loss of coherences. For low fillings

<sup>6</sup>A steady state with almost the same properties like a true thermal state.



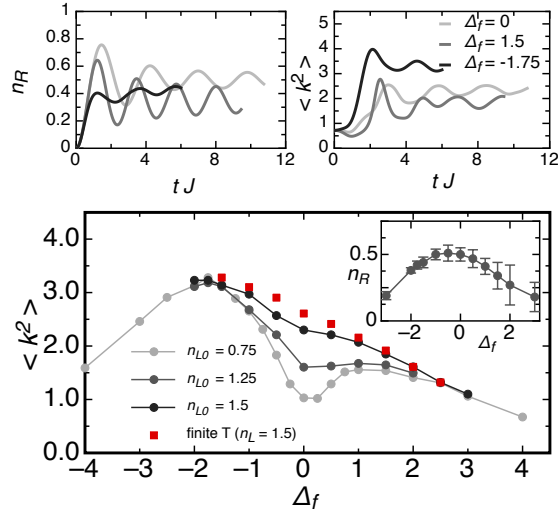


Figure 5.10: Quench scenario. The figure at the bottom shows the broadening of the momentum  $\langle k^2 \rangle$  as a function  $\Delta_f$ . For a sufficiently large filling  $n_{L,0}$  the broadening (here the filling is 1.5, dark grey dots) of the steady state after the quench is almost the same as for the thermal state with the same filling (red dots). For  $\Delta_f > 0$  the initial state is almost the exact ground state of the system. Therefore, there is no much broadening visible. The opposite effect occurs for  $\Delta_f < 0$ , where the initial system is highly excited. The intertube oscillation comes along with a fast redistribution of energy into all momenta states along the tubes, i.e. this leads to large broadening of  $k$ . If  $n_{L,0}$  is too small a particularity occurs in the vicinity of the totally symmetric point  $\Delta_f = 0$ . Here, the energy states in the left and in the right tube are in perfect resonance. Additionally, there are not enough bosons for a fast redistribution of energy through two-body collisions. Hence, the particles can move almost independently between the two tubes and without any intratube excitation. The small insert on the lower figure shows the fidelity as a function of  $\Delta_f$ . As one approaches  $\Delta_f = 0$  the normalized fidelity approaches  $n_R = 0.5$ . Since  $n_R = 0.5$  is equivalent to the most effective exploitation of space the fidelity does not grow as one goes further to  $\Delta_f < 0$  but stays constant. Finally, for large negative  $\Delta$  the fidelity becomes smaller again as the two tubes become more and more decoupled. The two figures at the top show the fidelity (upper left) and the broadening (upper right) for three different  $\Delta_f$ . The final value of  $n_R$  and  $\langle k^2 \rangle$  is calculated from the average over the last oscillation.

the number of interbosonic collisions drops rapidly which leads to a stable coherent intertube tunneling. However, also for lower filling it is only a matter of time until  $\langle k^2 \rangle$  reaches the value of the thermal state. For a larger  $\Delta_f$  (approximately around  $|\Delta_f| > 2.5J$ ) the tunneling rate decreases rapidly since then a hopping process would violate the energy conservation in the system.

The small inset in the lower picture in figure (5.10) shows the final fidelity after a quench for a system with the filling 1.5. There is a strong asymmetry between the positive and the negative  $\Delta_f$  which has been also observed experimentally. As expected the fidelity grows monotonically, starting at zero for  $\Delta_f \gg 0$ , as one approaches  $\Delta_f = 0$  for which  $n_R = 0.5$ . In this regime one can assume that two energy bands in the left and right tube are in resonance. This resonance leads to a oscillation of some condensate fraction. Since the two tube evolve different in time and due to the fact that bosons can collide and redistribute momenta, one observes an additional damping of the oscillation. Now, things change a little bit as one goes further to negative  $\Delta_f$ . The fidelity remains more or less constant for  $0 > \Delta_f > -1.75$ . The reason for this plateau comes from the fact that a fifty-fifty distribution of bosons guarantees the most optimal exploitation of space. The

energy gain from this delocalization is redistributed into kinetic energy along the tubes. Finally, for even smaller negative  $\Delta_f$  the fidelity starts to decrease slowly to zero as one approaches the parameter regime for which the two tubes are (energy conservation) decoupled. The two upper figures in [Fig. (5.10)] show exemplary the fidelity (upper left) and the broadening (upper right) for three different  $\Delta_f$  for system with the initial filling  $n_{L,0} = 1.5$ . The final value of the steady state is calculated taking the average over the last oscillation of each individual run.

The above quench scenario allows for the generation of a system of ultracold bosons with any desired thermal distribution. The simplicity of the method allows for an easy experimental implementation and has moreover the advantage that a desired temperature can be adjust by the choice of the right  $\Delta_f$ . The steady state after a few intertube oscillations can be used further for other experiments where one would like to check the temperature dependence of some effect. As long as the initial density is large enough there is no problem to generate this thermal ensemble on fast time scales and without bigger loss of particles.

Finally, I would like to connect the results from the quench scenarios with the sweeps, and here in particular, with the inverse sweep. A typical sweep consists of a large bosonic swap from the left to the right tube followed by several intertube oscillations with a smaller amplitude [see Fig.(5.7)]. As long as the time scale of the intertube tunneling is smaller than the sweep rate  $\alpha$ , i.e. fast sweeps, one observes only few intertube oscillations. Moreover, the first intertube boson swap happens more or less when  $\Delta(t) = 0$ . Thus, the fast sweep can be explained with the results from the quenches to  $\Delta_f \geq 0$ . For example, one observes only a small broadening during the fast sweep. The situation changes when the sweep time becomes smaller than the tunnel rate. Here, the initial swap of bosons from left to right ( $\Delta(t) = 0$ ) is followed by a backflow to the left tube at  $\Delta > 0$ . However, the situation when bosons moves from to right to the almost empty left tube is similar to a quench at  $\Delta_f < 0$ , thus, the region where the broadening  $\langle k^2 \rangle$  becomes maximally large. Only a small fraction of bosons is involved in the backflow and all the additional oscillations. The remaining bosons in the right tube keep the initially imprinted information about the condensate, i.e. the momentum distribution remains peaked around  $k = 0$ . Therefore, one observes a much faster broadening in the left than in the right tube.

## Chapter 6

# Entanglement and Decoherence of Multi-Qubit-Systems in external Baths

The main difference between the classical and the quantum description of world is the concept of superposition. Although the description in terms of quantum mechanics apply for the microscopic as well as for the macroscopic materia<sup>1</sup>, direct effects of superposition have been observed only in the further. Interactions among the particles lead to two new characteristics of quantum mechanics: the entanglement and the effects of decoherence [300].

Entanglement is a property of the quantum mechanical state of a system containing two or more objects, where the objects that make up the system are linked in a way that one cannot adequately describe the quantum state of a constituent of the system without full mention of its counterparts, even if the individual objects are spatially separated [139]. This interconnection leads to non-classical correlations between observable physical properties of remote systems, often referred to as nonlocal correlations [8]. Entanglement is a precious resource in quantum information processing. It is e.g. believed to be the ingredient of the quantum speed-up in quantum computation [83] and communication. Moreover several quantum protocols, as teleportation [30] just to mention an important example, can be realized exclusively with the help of entangled states [41]. On the other hand it is the entanglement which makes it very difficult to study many-body physics analytically as well as numerically on classical computers. This becomes obvious when using DMRG methods which are working good as long as the entanglement between two parts of the considered system does not grow exponentially fast.

Decoherence or dephasing is a mechanism that appears when a quantum system  $S$  interact with an environment  $B$ . As long as a system does not interact with the environment it is considered to be closed. One can describe this closed state by a pure wave function, which in its in general contain phase coherent superpositions, i.e. the general wave function reads  $|\Psi\rangle_S = \alpha_0|\phi_0\rangle_S + \alpha_1|\phi_1\rangle_S + \dots$ . Now, the interaction between the system  $S$  and the environment  $B$  creates entanglement between  $S$  and  $B$ . This has an important consequence for the system  $S$ . The initial superpositions disappear slowly and a collapse of the wave function occurs. The

---

<sup>1</sup>Due to the lack of a good criterion to distinguish between quantum and classical, an identification of the classical with the macroscopic has often been accepted. A counter example is the cryogenic version of the Weber bar gravity-wave detector, which must be treated as a quantum harmonic oscillator even though it may weight a ton [52]

system  $S$  (as well as  $B$ ) is now described by an ensemble of classically weighted wave vectors, i.e.  $\rho_S = \sum_i p_i |\psi_i\rangle\langle\psi_i|_S$ . This description is equivalent to the outcome after a full measurement on the initial system. The environment acts as a kind of measurement device which, within the formulation of quantum mechanics, reads out information about the initial system at cost of the destruction of phase coherent superpositions. Decoherence is the mechanism by which the classical limit emerges out of a quantum starting point and it determines the location of the quantum-classical boundary [300]. Although the two phenomena, i.e. entanglement and decoherence, are strongly connected with each other they are not the same. Entanglement is a much stronger property on a quantum state than many-body coherence.

I have already mentioned that entanglement is a crucial ingredient for many applications in quantum engineering. Some of these applications like secure quantum communication, also called quantum cryptography [112], have already been demonstrated in experiment. This has encouraged scientists to put effort in developing a more complex quantum device, the so-called quantum computer. Computers which make direct use of quantum mechanical phenomena<sup>2</sup> allow to approach problems of a completely different complexity class [150] as classical computers. In particular, it has been predicted that quantum computers should find the prime numbers of a given number in polynomial time only [250].

In general one cannot build a quantum device which is completely decoupled from the environment. As mentioned above these interactions create entanglement between system and environment at the cost destruction of the superpositions and the entanglement in the system. In the context of quantum computing the main experimental challenge is to protect the system's coherence until the end of the performed algorithm. A quantum computer, as well as a classical one, consists of computational steps and the storage of the input and the outcome [257]. One can prove that all quantum algorithms can be reduced to sequence of operations on two or one qubits [82]. Qubits, or quantum bits, the most basic entity of a quantum computer, are simply quantum mechanical two-level systems. These can be for example, spin- $\frac{1}{2}$  particles, vertically and horizontally polarized photons or the two energetically lowest states of an atom. Now, during the runtime of some quantum algorithm the qubits in  $S$  will interact with the environment  $B$ . This interaction introduces noise into the system  $S$  and leads to a discrepancy between the real and the theoretical predicted outcome. This part of the computation has already been studied intensively deducing several lower bounds in terms of the fidelity, i.e. the overlap of the real and the predicted state. On the other hand, the storage of the input and the outcome, thus problems concerning more than two qubits<sup>3</sup>, are much more difficult to investigate. The reason for that is the following: although the investigation of entanglement has been intensified during the last two decades, proper mathematical tools for an exact quantification of many-body entanglement are still missing, i.e. in particular for the quantification of the entanglement of more than two qubits. However, there has made a lot progress in the field of quantum computation during the last few years [158][292] and a new proposals for the implementation of a quantum computer has been demonstrated successfully [299] [196].

<sup>2</sup>Classical computers do also follow the laws of quantum mechanics. In contrast to those, a quantum computer uses directly the superposition and entanglement of quantum states.

<sup>3</sup>The successful storage requires the coherence of superposition of many qubits. In the case of the factorization algorithm [250] the number qubits depends on the length of prime numbers one needs to factorize.

In the following I consider the storage problem of many-body entangled states in a solid, e.g. qubits on quantum dots. System and bath interact via a Heisenberg-like coupling. It has been conjectured [223] that the typical time scales of total decoherence of a  $N$ -qubit state in a spin environment decrease exponentially with  $N$ . These leads to the assumption that quantum computer could save a  $N$ -qubit state for exponentially short time scales only. I focus on the open question about the relation between decoherence time an and the size of the entangled many-qubit state.

## 6.1 Quantifying Entanglement and Decoherence

In the following I will consider the situation where a system  $S$  consisting of one to few qubits  $N_S > 1$  and a bath  $B$  of  $N_B$  qubits ( $N_B > N_S$ ). The total system containing  $N = N_S + N_B$  particles is governed by  $H^S$  the system,  $H^B$  the bath and  $H^{S,B}$  the interaction Hamiltonian between  $S$  and  $B$ . The initial state, which consists of two or more qubits is maximal entangled. Moreover, I assume that initially the system was not in contact with the bath, i.e. the wave function of  $S$  and  $B$  at time  $t = 0$  is a product state  $|\Psi\rangle_{SB} = |\psi\rangle_S |\psi\rangle_B$ . In our general scenario the system  $S$  starts to build up entanglement with the bath  $B$ . This destroys the coherence of the system and even more the entanglement between parts within the system. One can say that one generates  $(N_S + N_B)$ -body entanglement at the cost of  $N_S$ -body entanglement. The information about the system  $S$  will be in general contained in a density operator  $\rho_S$ .

I have already mentioned that the study of entanglement of an arbitrary many-body state turns out to be a very hard task. Despite the enormous effort in the investigation of entanglement these phenomenon is still not completely understood. This becomes evident when studying the enormous number of different measures of this phenomenon. They all have the disadvantage of being non-extendable to a general situation. A roughly overview over the possible entanglement measures is given below ( $n$  denotes the number of entangled particles with the dimension  $d$ ):

	pure state $ \Psi\rangle$	mixed state $\rho$
$n = 2$	exists for all dimensions $d$	exist only for $d = 2$ <sup>4</sup> no easy measure for $d > 2$
$n > 2$	exists for special states with $d = 2$	good measure does not exist

Due to the lack of applicable entanglement measures I must restrict the investigation of systems made of three and more qubits [see Sec.(6.3)] to the study of their coherence properties and two-qubit entanglement within the system. One has to keep in mind that coherence and entanglement are two distinct phenomena. A total disentanglement of a system will happen on much faster time scale then the total decoherence.

### Quantification of Decoherence

The quantification of the coherence in a system  $S$  comes along with the study of entanglement between  $S$  and an environment  $B$ , thus a bipartite and pure system. Unlike for the entanglement,

in the following, one is not restricted to a specific number of qubits in  $S$ . The general form of the wave function (at some time  $t$ ) for  $S$  and  $B$  using the Schmidt decomposition reads

$$|\Psi^{SB}\rangle = \sum_{\tau} s_{\tau} |\alpha_{\tau}\rangle_S |\alpha_{\tau}\rangle_B, \quad (6.1)$$

with  $\{|\alpha_{\tau}\rangle_S\}$  and  $\{|\alpha_{\tau}\rangle_B\}$  being two orthonormal basis sets and  $s_{\tau}$  the Schmidt coefficients. Now, the whole information about the system  $S$  is contained in the reduced density operator  $\rho_S = \text{Tr}_B[|\Psi\rangle_{SB}\langle\Psi|_{SB}] = \sum_{\tau} s_{\tau}^2 |\alpha_{\tau}\rangle\langle\alpha_{\tau}|_S$ . The origin of decoherence is the interaction between  $S$  and  $B$ , which can be interpreted as a sequence of indirect measurements on the system  $S$  performed by the measuring apparatus called environment  $B$ . In analogy of the so-called von Neumann measurement where this happens abruptly, correlations between states in  $S$  and  $B$  are build up at cost of a damping of the superpositions in  $S$ <sup>5</sup>. Considering the density matrix again we observe in general small dampings of the diagonal elements, i.e. the population of the density matrix, and very fast decay of the off-diagonal elements which indicate the coherences in the system. As shown in the first chapter there exist a quantum measure for the entanglement of  $|\Psi\rangle_{SB}$ , the so-called von Neumann entropy [cp. Eq.(2.21)] which is based on the Schmidt coefficients<sup>6</sup>:

$$E(|\Psi\rangle_{SB}) := S(\rho_S) = - \sum_{\tau} s_{\tau}^2 \log_2 s_{\tau}^2. \quad (6.2)$$

Now, the loss of the off-diagonal elements of  $\rho_S$  comes along with the grow of the diagonal elements and hence the increase of the entanglement. Therefore I will also study the von Neumann entropy [Eq.(6.2)] which is a good indicator of loss of coherences for all system sizes.

### Bipartite entanglement measures. Concurrence

The traditional entanglement measure for pure bipartite state  $|\Psi\rangle_{SB}$  is given by  $E(|\Psi\rangle_{SB})$  the von Neumann entropy Eq.(6.2). A maximal von Neumann entropy is equivalent to a maximal entanglement between  $S$  and  $B$ . If the total wave function  $|\Psi\rangle_{SB}$  is a product state and is thus described by one Schmidt coefficient  $s_1 = 1$  only,  $E(|\Psi\rangle_{SB}) = 0$  as required. Since the Schmidt decomposition exists for pure states only,  $E(|\Psi\rangle_{SB})$  cannot be directly used for mixed states  $\rho_{SB}$ <sup>7</sup>. According to [274], a possible extension of any pure state entanglement measure to a measure of mixed state entanglement can be obtained by calculating the so-called convex roof. For the von Neumann entropy  $E(|\Psi\rangle_{SB})$  this extension is known as the entanglement of formation [288]:

$$E_F(\rho_{SB}) := \inf_{\{p_i, |\phi_i\rangle_{SB}\}} \left\{ \sum_i p_i E(|\phi_i\rangle_{SB}) \mid \rho_{SB} = \sum_i p_i |\phi_i\rangle\langle\phi_i|_{SB} \right\}. \quad (6.3)$$

<sup>5</sup>In the case of the von Neumann measurement the quantum mechanical states in  $S$  couple with macroscopical pointer states in  $B$ . We do not go into the details of the modern measurement theory. A recent review on this topic can be found here [241].

<sup>6</sup>The idea behind all bipartite pure state measurements is that from the quantum informational point of view an orthonormal basis set does not contain any secret information. Thus, the information of entanglement must be a function of the Schmidt coefficients only.

<sup>7</sup>Assuming the separable mixed state  $\rho_{SB} = \rho_S \otimes \rho_B = \mathbf{I}_S \otimes \mathbf{I}_B$  we find by tracing out over  $B$  that  $E(\rho_{SB}) \neq 0$ , which is simply wrong.

The entanglement of formation of a mixed state is defined as the minimum average entanglement of an ensemble of pure states  $\{|\phi_i\rangle\}$  that represents the given mixed state  $\rho_{SB}$ . Unfortunately there exist infinitely many decompositions of  $\rho_{SB}$  which makes it very hard to solve the above equation. Remarkably, it turns out that in the case of two entangled qubits  $E_F$  can be written as a function of the so-called concurrence [288]

$$C(\rho_{SB}) = \max \left\{ 0, \sqrt{\lambda_1} - \sqrt{\lambda_2} - \sqrt{\lambda_3} - \sqrt{\lambda_4} \right\}, \quad (6.4)$$

with  $\lambda_i$  being the eigenvalues (in descending order) of matrix  $\rho = \rho_{SB}\tilde{\rho}_{SB}$  and  $\tilde{\rho}_{SB} = \sigma_y^S \otimes \sigma_y^B (\rho_{SB}^*) \sigma_y^S \otimes \sigma_y^B$ . Since  $E_F(\rho_{SB}) = f(C(\rho_{SB}))$  and hence  $C(\rho_{SB})$  has also the properties of a good quantum measure I will use exclusively the concurrence in the following discussion of the time-evolution of the entanglement.

### Quantum channels, Kraus representation

There exist several ways how to describe the time-evolution of an open system [44]. All of them have certain advantages (and certainly also disadvantages) and it depends very much on the considered problem which description is preferred. In particular, for problems considering entanglement and general aspects of quantum theory and quantum information the concept of the so-called dynamical maps has been established. Dynamical maps describe the environment as a black box for an incoming state giving back an outgoing state and can therefore be seen as a snapshot of the time-evolution [4]. Starting from general considerations of time-evolution of a closed system consisting of system  $S$  and environment  $B$  I will derive a correct mathematical representation of the time-evolution of the open quantum system  $S$  alone.

Let us assume the initial state of  $S$  and  $B$  to be a pure product state  $|\Psi(t=0)\rangle_{SB} = |\psi\rangle_S |\psi\rangle_B$  where  $|\psi\rangle_S$  and  $|\psi\rangle_B$  are the wave functions of the system and environment, respectively. The transformation which describes the change of  $|\psi\rangle_S$  at time  $t > 0$  is given by

$$\rho_S(0) \longrightarrow \rho_S(t) = \$(t)\rho_S(0) \equiv \text{Tr}_B \left[ U(t,0)(\rho_S \otimes \rho_B)U(t,0)^\dagger \right], \quad (6.5)$$

with  $\rho_S(0) = |\psi\rangle\langle\psi|_S$  and  $\rho_B(0) = |\psi\rangle\langle\psi|_B$ . The above relation defines a map within the space of density matrices  $\$(t) : \mathcal{S}(\mathcal{H}_S) \rightarrow \mathcal{S}(\mathcal{H}_S)$ . It follows from [Eq.(6.5)] that in order to obtain the map  $\$$  we have to trace out of the degrees of freedom in  $B$ . All we need for this purpose is the spectral decomposition of  $\rho_B$  at a given time  $t > 0$  (cp. Eq. (6.1)),

$$\rho_B = \sum_{\tau} s_{\tau} |\alpha_{\tau}\rangle\langle\alpha_{\tau}|_B, \quad (6.6)$$

with  $\{|\alpha_{\tau}\rangle\}$  being an orthonormal basis set in  $B$  and  $\sum_{\tau} s_{\tau} = 1$ . This leads to the so-called operator-sum representation of the mapping  $\$$ :

$$\$(t)\rho_S = \sum_{ij} W_{i,j}(t)\rho_S W_{i,j}(t)^\dagger, \quad (6.7)$$

where  $W_{i,j} = \sqrt{s_\tau} \langle \alpha_i | U(t,0) | \alpha_j \rangle$  are operators acting on  $S$ . The above equation can be further simplified through a unitary basis transformation of  $\{|\alpha_\tau\rangle\}$  which leads to the so-called Kraus representation

$$\$(t)\rho_S = \sum_i K_i(t)\rho_S K_i(t)^\dagger. \quad (6.8)$$

A dynamical map  $\$$  is called a complete positive map (CPM) or equivalently a quantum channel[4], if it satisfies the following conditions:

- it maps Hermitian matrices to Hermitian matrices (Hermiticity preserving)
- it maps positive (semi-definite) matrices  $\rho \geq 0$  to positive (semi-definite) matrices (positivity preserving)
- completely positive if and only if for any state  $\rho_{SB}$ :  $\$ \otimes \mathbf{1}(\rho_{SB}) \geq 0$ .

Describing the action of  $B$  on  $S$  by a quantum channel allows for a very general analysis of the disentangling action of arbitrary environments. In particular in the case of two entangled qubits one can obtain a closed expression for the time-evolution of the entanglement. Together with the definition of a quantum channel I can introduce now the Jamiołkowski isomorphism which is an isomorphism between quantum channels and density matrices. This allows for a pictorial proof of a general law of time-evolution of an entangled pair of qubits.

### Jamiołkowski isomorphism

The concept of quantum channels allows to describe the time-evolution of  $\rho_S$  in form of a black box like picture. An incoming state  $\rho_{\text{in}} = \rho_S(t=0)$  is mapped by  $\$(t)$  onto an outgoing state  $\rho_{\text{out}} = \rho_S(t)$ . It turns out that this concept is directly related with the phenomenon of quantum teleportation in which some unknown and arbitrary properties of an incoming states are copied onto an outgoing state<sup>8</sup>. The original teleportation scheme [30] which assumes the existence of a maximally entangled pair of qubits as the resource for the transmission of quantum information leads to perfect fidelity between  $\rho_{\text{in}}$  and  $\rho_{\text{out}}$ <sup>9</sup>. In terms of dynamical maps this perfect teleportation would correspond to the trivial quantum channel  $\mathbf{1}$ , i.e. no interaction between environment  $B$  and system  $S$ . This invariance is depicted in Fig.(6.2) Hence interactions between  $S$  and  $B$  lead to an imperfect or noisy quantum channel which correspond to a non maximally entangled state for the quantum teleportation.

This duality between maps and density matrices is given by the Jamiołkowski-Choi isomorphism [145]  $\mathbf{J}$ . The mapping from bipartite density matrices  $(\rho_\$)_{CC'}$  to the linear maps  $\$$  and is defined as

$$\$(\rho_{\bar{C}}) := d\text{Tr}_{\bar{C}C} \left[ \rho_{\bar{C}} P_{\bar{C}C}^{\Phi^+} (\rho_\$)_{CC'} \right], \quad (6.9)$$

<sup>8</sup>The quantum teleportation teleports properties of one state to another. The outgoing object must already exist before the teleportation.

<sup>9</sup>In the original paper by Bennett  $\rho_{\text{in}}$  and  $\rho_{\text{out}}$  are both pure states for which the fidelity equals the overlap between both states.



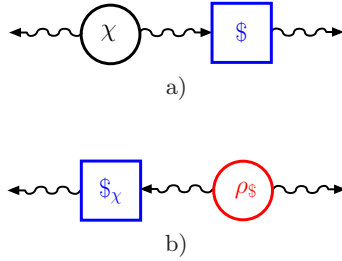


Figure 6.1: Entanglement decay scenarios. a) Laboratory scenario: one of the qubits of the initial state  $|\Psi\rangle$ , the right one, undergoes the action of a general quantum channel  $\$$ . b) Dual scenario: the same end result is obtained by inter-changing the role of states and channels: the left qubit of a mixed state  $\rho_s$  undergoes the action of the quantum channel  $\$ \psi$ . Circles represent sources of entangled states, squares symbolize channels.

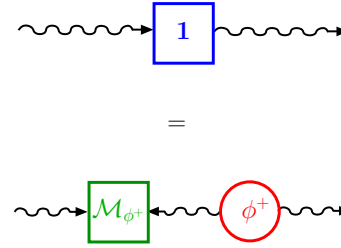


Figure 6.2: Quantum Teleportation identity. The teleportation protocol transfers the incoming state from the left to the outgoing state on the right. The procedure consists of a composite Bell measurement on the incoming qubit and on one qubit of an auxiliary, maximally entangled state  $|\Phi^+\rangle$ . I restrict to the case where the measurement results in a projection  $\mathcal{M}_{\phi^+}$  on the state  $|\Phi^+\rangle$ .

with  $P_{\bar{C}C}^{\Phi^+} = |\Phi^+\rangle\langle\Phi^+|_{\bar{C}C}$  being the projector onto the maximally entangled state  $|\Phi^+\rangle = \frac{1}{\sqrt{d}} \sum_i |i\rangle_{\bar{C}} |i\rangle_C$  and  $d$  the dimension of all three subspaces<sup>10</sup>. The r.h.s of the above equation is equivalent to the formulation of a quantum teleportation scheme via  $(\rho_{CC'})$ . The inverse mapping from the linear maps to density matrices reads

$$(\rho_s)_{CC'} = \mathbf{1} \otimes \$ (|\Phi^+\rangle\langle\Phi^+|_{CC'}). \quad (6.10)$$

By sending one part of a maximal entangled pure state through the channel  $\$$  one can encode all information of  $\$$  in a density matrix  $\rho_s$ , see Fig.(6.3).

## 6.2 General entanglement law for entangled qubit pairs

Before starting with the numerical study of few-qubits decoherence and entanglement evolution in arbitrary spin baths I will discuss a scenario for which a closed expression of the time-evolution of entanglement in terms of concurrence has been found [163]. I consider entangled states of qubit pairs, with one qubit being subject to an arbitrary channel  $\$$  which may represent the influence of an environment, of a measurement, or of both. In order to illustrate the situation, I consider a source which emits a particle to the left and another one to the right. Each particle on its own carries one qubit of quantum information (in general a superposition or mixture of two basis states  $|0\rangle$  and  $|1\rangle$ ). I therefore also refer to the particles as left and right qubit. Let the particles leaving the source be in a pure state  $|\Psi\rangle$ :

$$|\Psi\rangle = \sqrt{\omega}|00\rangle + \sqrt{1-\omega}|11\rangle, \quad (6.11)$$

with  $0 \leq \omega \leq 1$ , i.e., for values of  $\omega$  between zero and one the particles are in a coherent superposition of both being in state  $|0\rangle$  and being in state  $|1\rangle$ . Any pure state can be written in this

<sup>10</sup>For simplicity I assume that  $\bar{C}, C$  and  $C'$  have the same dimension  $d$ .

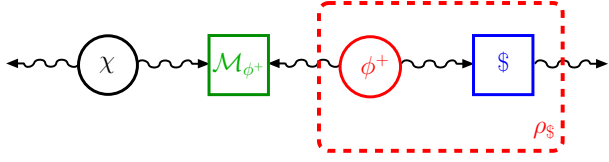


Figure 6.3: Building in the teleportation identity. The right qubit of  $|\Psi\rangle$  undergoes the action of a quantum channel  $\$$ , after intermediate teleportation. The maximally entangled state  $|\Phi^+\rangle$  together with the action of the channel  $\mathbf{1} \otimes \$$  yield the source of the mixed state  $\rho_S$ .

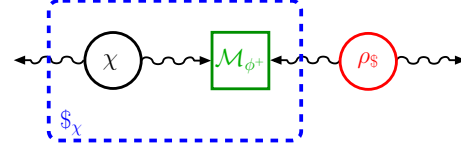


Figure 6.4: Entanglement swapping. Transfer of entanglement between the qubit pairs of  $|\Psi\rangle$  and  $\rho_S$ , respectively, to entanglement between the outgoing pair of qubits. The Bell measurement  $M_{\Phi^+}$  together with the source of the entangled state  $|\Phi^+\rangle$  constitute the quantum channel  $\$_\Psi$  for the left qubit of state  $\rho_S$ .

form, modulo local unitary operations, without loss of generality. The concurrence of the state  $|\Psi\rangle$  equals  $C(|\Psi\rangle) = 2\sqrt{\omega(1-\omega)}$ . For  $\omega$  in Eq.(6.11) equal to zero or one, the state's entanglement and hence its concurrence vanishes;  $\omega = 1/2$  implies  $|\Psi\rangle = |\Phi^+\rangle$ , one of the maximally entangled Bell states, with maximal concurrence  $C(|\Psi^+\rangle) = 1$ .

Now the right qubit traverses an arbitrary quantum channel  $\$$ , as illustrated in Fig. (6.1a). In order to calculate the concurrence hereafter I use the fact that the qubits' final state must be the same as in the dual picture, yielded by the Jamiołkowski isomorphism  $\mathbf{J}$ , in which the roles of initial state  $|\Psi\rangle$  and channel  $\$$  are interchanged, as depicted in Fig.(6.1b). Thus, the two-qubit state  $|\Psi\rangle$  is identified with the qubit channel  $\$_\Psi$ , and the qubit channel  $\$$  with the two-qubit state  $\rho_S$ . Symbolically:

$$(\mathbf{1} \otimes \$)|\Psi\rangle\langle\Psi| = (\$_\Psi \otimes \mathbf{1})\rho_S. \quad (6.12)$$

More precisely, one obtains a new initial state  $\rho_S = (\mathbf{1} \otimes \$)|\Phi^+\rangle\langle\Phi^+|$  and a new noisy channel  $\$_\Psi(\rho) = (M_\Psi \otimes \mathbf{1})\rho(M_\Psi^\dagger \otimes \mathbf{1})$  with  $M = (\sqrt{\omega}|0\rangle\langle 0| + \sqrt{1-\omega}|1\rangle\langle 1|)/\sqrt{2}$  a filtering operation used in weak measurement scenarios. The left and the right hand side of Eq.(6.12) correspond to the equivalence between Fig.(6.3) and Fig.(6.4) respectively. The advantage of Eq.(6.12) is that the entanglement evolution induced by the particular channel  $\$_\Psi$  can be deduced more easily, as I will demonstrate now. The concurrence of the final state  $\rho_f = (\mathbf{1} \otimes \$)|\Psi\rangle\langle\Psi|$  is a function of the eigenvalues of the matrix [cp. Eq.(6.4)]:

$$\rho_f \tilde{\rho}_f = (M_\Psi \otimes \mathbf{1})\rho_S \cdot [M_\Psi \sigma_y M_\Psi \otimes \sigma_y] \cdot \rho_S^* \cdot [M_\Psi \sigma_y \otimes \sigma_y], \quad (6.13)$$

where I have used Eq.(6.12) and the fact that  $M = M^\dagger = M^*$ . For invertible  $M$ , it follows that the eigenvalues of  $\rho_f \tilde{\rho}_f$  and  $\rho_S \tilde{\rho}_S$  are proportional, because

$$\begin{aligned} \det[\rho_f \tilde{\rho}_f - \lambda \mathbf{I}] &= \det[(M_\Psi \otimes \mathbf{1})^{-1}] \det[M_\Psi \otimes \mathbf{1}] \det[\rho_f \tilde{\rho}_f - \lambda \mathbf{I}] \\ &= \det[(M_\Psi \otimes \mathbf{1})^{-1} \rho_f \tilde{\rho}_f (M_\Psi \otimes \mathbf{1}) - \lambda \mathbf{I}] \\ &= \det[\omega(1-\omega)\rho_S \tilde{\rho}_S - \lambda \mathbf{I}], \end{aligned} \quad (6.14)$$

where I have used  $M_S \sigma_y M_\Psi = \sqrt{\omega(1-\omega)}\sigma_y/2$  to obtain the last equality. Otherwise, for  $\omega = 0$  or  $\omega = 1$  the concurrence vanishes because  $M_S \sigma_y M_\Psi = 0$ .

Together with the definition of  $\rho_S$ ,  $\rho_f$  and the concurrence  $C(|\Psi\rangle) = 2\sqrt{\omega(1-\omega)}$  one can obtain the following factorization law:

$$C[(\mathbf{1} \otimes \$)|\Psi\rangle\langle\Psi|] = C[(\mathbf{1} \otimes \$)|\Phi^+\rangle\langle\Phi^+|]C(|\Psi\rangle). \quad (6.15)$$

The entanglement reduction under a one-sided noisy channel is independent of the initial state  $|\Psi\rangle$  and completely determined by the channels action on the maximally entangled state. Thus, if one knows the time evolution of the Bell states entanglement, one knows it for any pure initial state. This result can also be interpreted in terms of entanglement swapping between a pure state  $|\Psi\rangle$  and a mixed state  $\rho_S$  leading to the final state  $\rho_f$ , owing the equivalence of the processes represented in Fig.(6.4).

The factorization law Eq.(6.15) can be generalized for mixed initial states  $\rho_0$  and to two-sided quantum channel  $\$_L \otimes \$_R$  in form of an inequality<sup>11</sup>, which gives us an upper bound for the final entanglement [163].

The scenario of an entangled qubit pair under the action of a one-sided quantum channel can be found in some important applications like long distance quantum communication or teleportation, where one qubit is sent from a sender to a receiver far away. Nevertheless, for the study of decoherence and entanglement in the context of quantum computing it is necessary to study more involved scenarios, where more than two qubits interact with an common environment. In the next part I will take a closer look on such scenarios discussing qualitative and quantitative results which have been obtained using the time dependent DMRG method [see Chapter ??].

## 6.3 Few qubits in a general spin bath

In the following I will consider a total system  $SB$  consisting of one or few qubits which mimic our central system  $S$ , thus some entangled state which is stored for a further quantum computation operation, and a big bath  $B$  of spin- $\frac{1}{2}$  particles<sup>12</sup>. The evolution of  $SB$  is governed by the following three Hamiltonians  $\hat{H}_S$  for the central system  $S$ ,  $\hat{H}_B$  for the bath  $B$  and  $\hat{H}_I$  describing the interactions between  $SB$ . Further I assume that, in comparison with a long storage time, the quantum operations happen on a time scale which is much faster then the typical interaction times between  $S$  and  $B$ . The initial state at  $t = 0$  is thus a product state  $|\Psi(t=0)\rangle_{SB} = |\psi_0\rangle_S |\psi_0\rangle_B$  between the wave functions describing  $S$  and  $B$ ; existing entanglement at  $t = 0$  is neglected. Together with the total number of system qubits  $N_S$  and bath spins  $N_B$  the initial Hamiltonian

<sup>11</sup>The simple factorization law Eq.(6.15) results from the trivial form of  $\$_\Psi$  (it consist of exactly one Kraus operator) to the corresponding channel to  $|\Psi\rangle$ . To find the corresponding channel for a general initial mixed state  $\rho_0$  is a difficult variational problem of the same form as for the Entanglement of Formation Eq.(6.3)

<sup>12</sup>In the here considered scenario, the qubits of  $S$  can be some free electrons on a quantum dot which are coupled to a bath of nuclear spin- $\frac{1}{2}$  particles, which could be called qubits as well. In order to make a distinction between  $S$  and  $B$  I call the particles in  $S$  qubits and the particles in  $B$  bath spins.

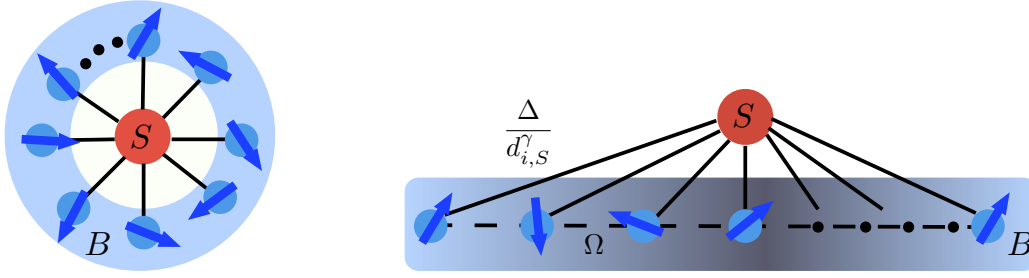


Figure 6.5: The two models. The left picture corresponds to non decaying interactions between central system and bath  $\gamma = 0$ . A distance between qubits and bath spins does not exist. The right picture shows the situation where  $\gamma = 2$ , which is equivalent to decaying interaction strength and thus to a distance between system and bath spins.

reads

$$\begin{aligned}
 H_S &= - \sum_{i=1}^{N_S-1} \sum_{j=i+1}^{N_S} \sum_{\alpha=x,y,z} J_{i,j}^\alpha S_i^\alpha S_j^\alpha, \\
 H_B &= - \sum_{i=1}^{N_B-1} \sum_{j=i+1}^{N_B} \sum_{\alpha=x,y,z} \Omega_{i,j}^\alpha I_i^\alpha I_j^\alpha, \\
 H_I &= - \sum_{i=1}^{N_S} \sum_{j=1}^{N_B} \sum_{\alpha=x,y,z} \frac{1}{d_{i,j}^\gamma} \Delta_{i,j}^\alpha S_i^\alpha I_j^\alpha.
 \end{aligned} \tag{6.16}$$

The interaction strengths between the particles in  $S$ ,  $B$  are given by the couplings  $J_{i,j}^\alpha$  and  $\Omega_{i,j}^\alpha$ , respectively. Additionally to  $\Delta_{i,j}^\alpha$  the coupling between central qubits and bath's spins we add  $\frac{1}{d^\gamma}$  a factor which mimics a decay of the interaction strength, with  $d$  a fictive distance between the central qubits and some baths spin. A typical example is a central system consisting of one or few qubits sitting on a quantum dot where qubits interact with the nuclear spins [155]. Typically the damping constant  $\gamma$  is a complicated function of the interactions and of the dimension of the system. Moreover, the above model does not consider interaction between more than two particles since they are less probable.

In order to reduce the large number of free parameters I make a few restrictions on the total system. I assume that all two-qubit calculation steps have been already performed and thus  $\hat{H}_S(t \geq 0) = 0$ , i.e. the system  $S$  does not evolve unitary. Furthermore I investigate only the case where all couplings are isotropic, i.e.  $\Delta_{i,j}^x \Delta_{i,j}^y \Delta_{i,j}^z = \Delta_{i,j}$  and analogous for  $\Omega$ . Since then  $[\mathbf{I}_i, \mathbf{I}_j] = 0$  and  $[\mathbf{S}_i, \mathbf{I}_j] = 0$  for all  $i, j$  and together with the relation  $[AB, C] = A[B, C] + [A, C]B$  it follows that  $[\hat{H}_I, \hat{H}_B] = 0$ . Therefore, the decoherence process is solely determined by the interaction  $\hat{H}_I$  which makes a discussion of  $\Omega$  needless [293] (in all simulations  $\Omega = -1$ ).

It is well known, that a totally polarized bath would suppress decoherence completely since the necessary spin-flip operations between  $S$  and  $B$  are not possible anymore. Unfortunately, the maximal experimentally achieved polarization, e.g. in a quantum dot, is around 30%. Therefore, I further assume the bath to be totally unpolarized  $\sum_i \langle S_i^z \rangle = 0$ . I have already mentioned the quantum dot scenario which typically consists of  $10^4 - 10^5$  nuclear spins. This number of bath spins is simply to large to be simulated with DMRG. But fortunately it turns out that the evolution

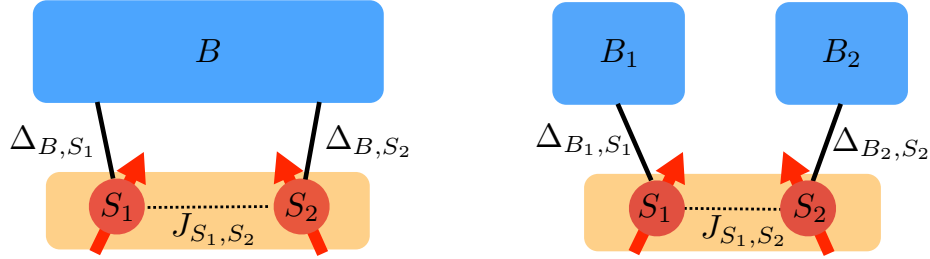


Figure 6.6: The two types of baths. The left picture shows the situation where both central qubits interact with a global bath  $B$ . The right shows the general situation of two local baths  $B_1$  and  $B_2$ , one for each qubit. A non existing bath, or equivalently  $\Delta = 0$ , corresponds to a trivial time evolution with  $\mathcal{S} = \mathbf{1}$ .

of  $S$  is mostly affected by a small number of strongly coupled bath spins in the vicinity  $S$ . The here considered baths size of  $N_B = 40$  and  $N_B = 60$  is sufficient in order to reveal the most important qualitative and quantitative effects.

Finally, considering a quantum dot situation where the central qubits sits on two-dimensional lattice I choose  $\gamma = 2$ . The assumption behind this value is the following: the interaction between the central qubits and the bath spins goes as  $1/d^3$ , which leads to a fast decay of the interaction [257]. For a DMRG calculation one has to map this two-dimensional lattice onto a one-dimensional chain. All spins which lie at a certain distance on a ring around the center of system  $S$  are multiplied by the weight factor which leads to reduction of  $\gamma = 3$  to  $\gamma = 2$ . This model corresponds to strongly localized central qubits.

The initial bath is a superposition of several states with randomly distributed bath spins with zero total magnetization. At the beginning of the simulation the total wave function a product state  $|\Psi(t=0)\rangle_{SB} = |\psi_0\rangle_S |\psi_0\rangle_B$ . Additionally, the cases where the number of qubits  $N_S \geq 2$  the central state will be maximally entangled.

### 6.3.1 The two qubit case, Bell states

As a first example, I will discuss the entanglement evolution of maximally entangled qubit pairs  $S$  interacting with some bath  $B$ . The advantage of this particular case is that the entanglement for pure and mixed states is well defined in terms of the concurrence [cp. Eq.(6.4)]. Moreover, one can study the decoherence of the central system using the von Neumann entropy and thus the entanglement creation between  $S$  and  $B$ . It is well known that there exist a basis for all pure two qubit states in term of the so-call Bell states. The total basis consist of four Bell states  $|\Phi^\pm\rangle = (|00\rangle \pm |11\rangle)/\sqrt{2}$  and  $|\Psi^\pm\rangle = (|01\rangle \pm |10\rangle)/\sqrt{2}$ . In the following I will consider the initial state to be  $|\Phi^+\rangle_S$  or  $|\Psi^+\rangle_S$ . These two states have both total spin  $S_{\text{tot}}^z = 1$  and belong to the so-called spin triplet. The spin singlet  $|\Psi^-\rangle_S$ , on the other hand, shows a completely different evolution. Since  $S_{\text{tot}}^z = 0$  the state  $|\Psi^-\rangle_S$  evolves rather trivial which becomes obvious when one calculates the time evolution of  $|\Psi^-\rangle_S$  and some bath spin  $|0_j\rangle_B$  (or equivalently  $|1_j\rangle_B$ ) for a short

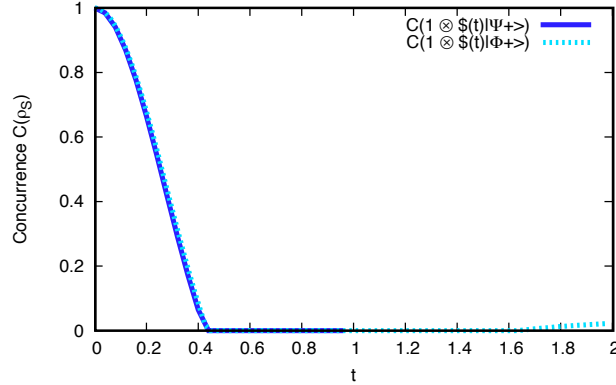


Figure 6.7: Evolution of Concurrence for one-side quantum channels. The parameters are  $\Delta_i = -1$  and  $\gamma = 0$ . The bath' length is  $N_B = 40$ . In perfect agreement with the factorization law both states the same entanglement evolution.

time  $t$ :

$$\begin{aligned}
& \exp(i(H_I^{S_1 B_j} + H_I^{S_2 B_j})t) |\Psi^-\rangle_S |0_j\rangle_B \\
& \cong \left( \mathbf{1} + i[H_I^{S_1 B_j} + H_I^{S_2 B_j}]t \right) |\Psi^-\rangle_S |0_j\rangle_B \\
& = |\Psi^-\rangle_S |0_j\rangle_B + \\
& \quad + \frac{1}{\sqrt{2}} \frac{1}{4} |010_j\rangle_{SB} + \frac{1}{4} |100_j\rangle_{SB} - \frac{1}{2} |001_j\rangle_{SB} + \\
& \quad + \frac{1}{2} |001_j\rangle_{SB} - \frac{1}{4} |010_j\rangle_{SB} - \frac{1}{4} |100_j\rangle_{SB} \\
& = |\Psi^-\rangle_S |0_j\rangle_B. \tag{6.17}
\end{aligned}$$

As long as the interactions between  $S$  and  $B$  are isotropic the initial central system  $|\Psi^-\rangle_S$  will not change. Since I consider only two-body interactions between  $S$  and  $B$  the above result will not change even if I would assume a bigger bath.

In general, there exist two possible bath' scenarios [see Fig.(6.3.1)]. In the first scenario both qubits interact with one common bath  $B$ , also called a global bath. This situation is the case when the two central qubits are very close to each other, e.g. both qubits sit on the same quantum dot. The second scenario deals with two local baths  $B_1$  and  $B_2$  for each qubit. Here one can imagine the situation in which one qubit remains at the source while the other is sent to some receiver, e.g. quantum communication or teleportation. The second qubit interacts with completely different environment than the first one. Since I am interested in the storage of some few-qubits state I will investigate, in the following, the scenario of a global bath  $B$ . But first, I want to present the results for the case where only one qubit interacts with a local bath. These result confirm perfectly the factorization law [cp. Eq.(6.4)] for the entanglement decay.

### Constant interaction $\gamma = 0$ and one-side channels

Let us start with scenario in which one qubit of our qubit pair, e.g. qubit  $S_2$ , interacts with a local bath  $B_2$  while the other is completely decoupled from any environment. This situation

is directly related to the factorization law for entanglement evolution of qubit pairs [Eq.(6.4)]. Indeed, it turns out that the results completely agree with the factorization law. Of course, one could understand this fact by doing a straight-forward calculation of the time-evolution but this is in general a hard task. It turns out that a simpler calculation of the short time-evolution under the assumption that the bath consists of two spins only already reveals the qualitative behavior of the central system  $S$ . Taking into account more bath spins would therefore change the prefactors but not the general form of  $\rho_S^{\Psi^+}$ :

$$\begin{aligned} (\mathbf{1} + i\delta t \mathbf{1} \otimes (H_I^{S_2 B_j} + H_I^{S_2 B_k})) |\Psi^+\rangle_S |0_j 1_k\rangle_B &= \\ &= 2 |\Psi^+\rangle_S |0_j 1_k\rangle_B + i\delta t \frac{1}{\sqrt{2}} \left[ \frac{1}{2} |00\rangle_S |1_j 1_k\rangle_B + \frac{1}{2} |11\rangle_S |0_j 0_k\rangle_B \right] \\ &\stackrel{LU}{=} (\mathbf{1} + i\delta t \mathbf{1} \otimes (H_I^{S_2 B_j} + H_I^{S_2 B_k})) |\Phi^+\rangle_S |0_j 1_k\rangle_B. \end{aligned} \quad (6.18)$$

Since all maximally entangled qubit pairs are mathematically equivalent under a local unitary operations, i.e. for the here considered states  $|\Phi^+\rangle = \sigma_x \otimes \mathbf{1} |\Psi^+\rangle$ , and obviously then  $[\sigma_x \otimes \mathbf{1}, \mathbf{1} \otimes \$] = 0$ , the final result is also equivalent under a local unitary operation<sup>13</sup>. Taking the trace over the bath spins leads to the final state

$$\rho_S^{\Psi^+}(t) = p_0(t) \underbrace{|\Psi^+\rangle\langle\Psi^+|_S}_{\text{nothing happens}} + p_1(t) \underbrace{[|00\rangle\langle 00|_S + |11\rangle\langle 11|_S]}_{\text{outcome after projective measurement}}, \quad (6.19)$$

which is again a mixture between the maximally entangled state  $|\Psi^+\rangle$  and a total mixed state. Roughly speaking  $\rho_S^{\Psi^+}(t)$  will be entangled as long as  $p_0(t) > p_1(t)$  or equivalently as long as the entangled part  $|\Psi^+\rangle\langle\Psi^+|$  dominates over the total mixture. As already mentioned one can easily obtain the result for  $\Phi^+$  by applying  $\sigma_x \otimes \mathbf{1}$  on  $\rho_S^{\Psi^+}(t)$ . Indeed one can see in Fig.(6.7) that both initial states have the same entanglement evolution. This is consistent with the factorization law [Eq.(6.4)] which must be valid for all maximally entangled states.

### Two-side channels with constant interaction strength $\gamma = 0$

The effect of a single local bath, i.e. a one-sided quantum channel can be completely explained with the factorization law for the entanglement evolution. In particular one can prove that the law does not depend on the choice of the initial maximally entangled state. Now, this law is in general not valid if one considers the scenario in which both qubits interact with an environment [see Fig.(6.3.1)]. Hence, one can expect that a global bath leads to a different disentanglement for different initial states. In the following I consider the situation of one global bath  $B$  for both central qubits. It turns out that the entanglement evolution of  $|\Psi^+\rangle_S$  is completely different from the evolution of  $|\Phi^+\rangle_S$ .

Let us start with calculation of the general form of  $\rho_S^{\Psi^+}(t)$  after the time-evolution for a short time. The general form does not depend on the number of bath spins. Hence, assuming two bath

<sup>13</sup>For the here considered case we can also write  $(\mathbf{1} \otimes \$)|\Psi^+\rangle = \sigma_x \otimes \mathbf{1}[(\mathbf{1} \otimes \$)|\Phi^+\rangle]$ .

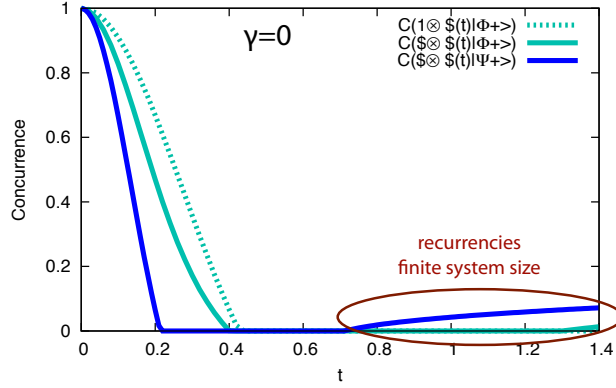


Figure 6.8: Evolution of concurrence for two-side channels. The parameters are  $\Delta_i = -1$  and  $\gamma = 0$ . The bath's length is  $N_B = 40$ . The behavior of the entanglement for the two initial states  $|\Psi^+\rangle$  and  $|\Phi^+\rangle$  is now different. In the here considered situation one can find at least a simple relation between the entanglement evolution of  $|\Psi^+\rangle$  under the action of  $\mathbf{1} \otimes \$$  and the  $\$ \otimes \$$ . For the latter the entanglement decays twice as fast as for the farther,  $C[(\mathbf{1} \otimes \$(2 \cdot t))|\Psi^+\rangle] = C[(\$ \otimes \$(t))|\Psi^+\rangle]$ . Due to a finite system size one observes recurrences of entanglement for longer times.

spins only, one obtains

$$\begin{aligned} & (\mathbf{1} + i\delta t(H_I^{S_1 B_j} + H_I^{S_1 B_k}) \otimes (H_I^{S_2 B_j} + H_I^{S_2 B_k}))|\Psi^+\rangle_S |0_j 1_k\rangle_B \\ & = 2|\Psi^+\rangle_S |0_j 1_k\rangle_B + i\delta t \frac{1}{\sqrt{2}} [ |00\rangle_S |1_j 1_k\rangle_B + |11\rangle_S |0_j 0_k\rangle_B ]. \end{aligned} \quad (6.20)$$

As one can already guess from the form of the above equation, the reduced density matrix corresponding to Eq.(6.20) is similar to the reduced density matrix for a one-side channel. After tracing out the environment one obtains a similar expression as in Eq.(6.19) with the only difference of new probabilities  $p'_0(t)$  and  $p'_1(t)$ . According to the initial considerations the result for the other Bell state  $|\Phi^+\rangle$ , i.e. for  $\rho_S^{\Phi^+}(t)$ , must be different from  $\rho_S^{\Psi^+}(t)$ . Indeed, one obtains after a similar calculation as in Eq.(6.20) followed by a trace over  $B$ ,

$$\rho_S^{\Phi^+}(t) = p''_0(t)|\Phi^+\rangle\langle\Phi^+|_S + p''_1(t)|\Psi^+\rangle\langle\Psi^+|_S. \quad (6.21)$$

The above state  $\rho_S^{\Phi^+}(t)$  is a mixture between the two maximal entangled states  $|\Phi^+\rangle_S$  and  $|\Psi^+\rangle_S$  and becomes totally disentangled for  $p''_0(t) = p''_1(t)$ . In Fig.(6.8) one can see the different evolution of entanglement of  $|\Psi^+\rangle_S$  and  $|\Phi^+\rangle_S$ . It turns out that for the here considered scenario the concurrence of  $(\$ \otimes \$)|\Psi^+\rangle$  decreases twice as fast as for a one-sided bath  $\mathbf{1} \otimes \$$ , and thus to:

$$C[(\$ \otimes \$(t))|\Psi^+\rangle_S] = C[(\mathbf{1} \otimes \$(2 \cdot t))|\Psi^+\rangle_S]. \quad (6.22)$$

### Two-side channels with decaying interaction strength $\gamma = 2$

Up to now I have considered only the situation for which  $\gamma = 0$ . In the present section I will discuss the more realistic case  $\gamma = 2$ . Due the fast decay of interaction strength the evolution of



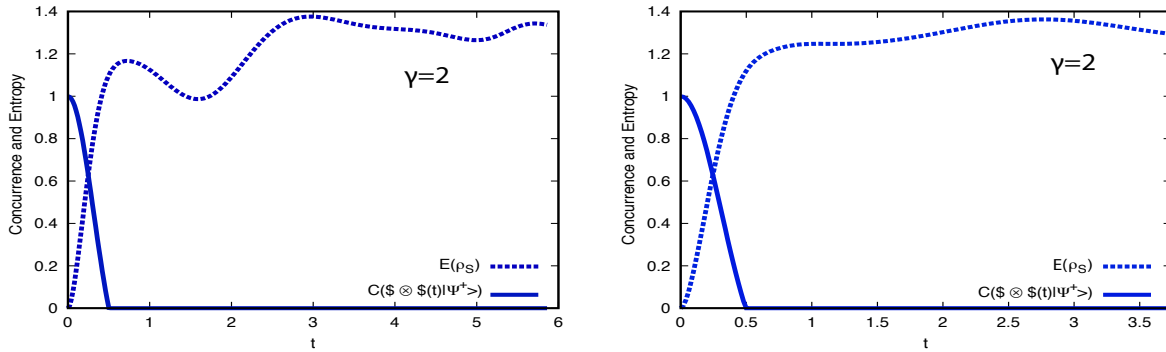


Figure 6.9: Evolution of concurrence and von Neumann entropy for  $(\mathcal{S} \otimes \mathcal{S}(t))|\Psi^+\rangle$ . The parameters are  $\Delta_i = -1$  and  $\gamma = 2$ . The bath's length is  $N_B = 40$ . The left and the right figure represent two arbitrary bath configurations. One can see that time when the entropy reaches the first maximum coincide with the total disentanglement. This point marks the time scale at which the central system become completely entangled with the bath.

entanglement will be dominated by a small part of the bath in the vicinity of the central system. As already mentioned, I initialize the bath spin configuration of the bath randomly for each simulation. As a consequence the time-evolution of entanglement and the decoherence process vary for each individual run. These differences can be seen in Fig.(6.9) and Fig.(6.10) for both  $|\Psi^+\rangle$  and  $|\Phi^+\rangle$ , respectively. For both initial states I present the results from two exemplary simulations. As expected the concurrence as well as the one-qubit and the two-qubit coherences have completely different characteristics. Nevertheless, both figures reveal a general law which will be important for the investigation of more than only two central qubits. One can observe in all cases that the entanglement decays on a faster time scale than the less fragile coherences of the central system  $S$ , which are measured in terms of the von Neumann entropy  $E$  [cp. Eq.(6.2)]. This is a very important result with regard to the following analysis of three and more central qubits for which a simple entanglement measure does not exist.

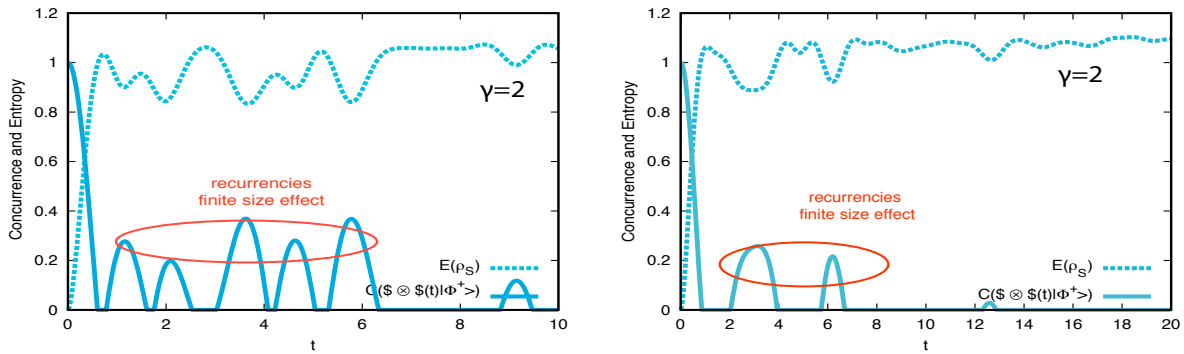


Figure 6.10: Evolution of concurrence and von Neumann entropy for  $(\mathcal{S} \otimes \mathcal{S}(t))|\Phi^+\rangle$ . The parameters are  $\Delta_i = -1$  and  $\gamma = 2$ . The bath's length is  $N_B = 40$ . The same behavior same as in Fig.(6.9) can be observed. Maximal entanglement between system and bath is equivalent to total disentanglement of the two qubits. The left and the right figure represent two arbitrary bath configurations. Again, at longer time recurrences occurs.

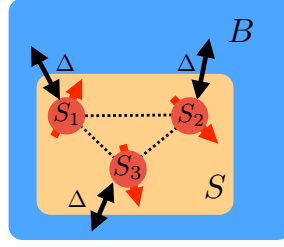


Figure 6.11: Three entangled qubits in a global bath. This cartoon picture shows three qubits in  $S$  surrounded by a global bath  $B$ . Each qubit interacts with the surrounding bath spins as well as with each other. In the here considered situation the central qubits are initially entangled.

### 6.3.2 The three and more qubit case, general $W$ - and $GHZ$ -state

Contrary to the case of entangled qubit pairs there are, so far, no applicable entanglement measures for systems with three or more qubits. Although there exist various proposals [139, 8] how to quantify many-body entanglement, none of these measures can satisfy the following criteria: 1.) general validity for pure and in particular mixed states. 2.) simple accessibility and 3.) scalability. In particular for mixed states, which are the central objects of investigation, entanglement measures exist only as convex-roof constructions of pure state measures. These constructions requires an optimization over infinitely many decompositions of the mixed state [see the definition of the entanglement of formation Eq.(6.3)].

Fortunately it turns out that the lack of an adequate entanglement measure does not restrict one to investigate the question whether a many-body state is still entangled or not. Entanglement is a phenomenon which depends on the quantum coherences in a system. As long as the system contains such coherences it can in priciple contain few-body entanglement. On the other hand the total lost of coherences due to system-enviroment interactions denotes the point of a total disentanglement. The results from the previous section, where I could monitor the time-evolution of entanglement and decoherence, are in complete agreement with this upper bound on the entanglement [see Fig.(6.9) and Fig.(6.10)].

In the following, I concentrate on two famous examples of maximally entangled many-body states , the general  $W$ -state [199],

$$|W_n\rangle \propto |1000\dots\rangle + |0100\dots\rangle + |0010\dots\rangle + \dots , \quad (6.23)$$

and the general Greenberger-Horne-Zeilinger, or  $GHZ$ -state[116],

$$|GHZ_n\rangle \propto |0000\dots\rangle + |1111\dots\rangle , \quad (6.24)$$

where  $n$  denotes the number of qubits in  $S$ , i.e. here  $n = N_S$ . The two previously studied Bell states  $|\Psi^+\rangle_S$  and  $|\Phi^+\rangle_S$  are obviously incorporated in the above definitions of  $|W_n\rangle$  and  $|GHZ_n\rangle$ . This allows to combine the results for the time evolution of decoherence with respect to an entanglement breakdown for 2 qubits with the case of 3 and 4 qubits interacting with a global bath  $B$ . The simulations has been performed taking  $N_B = 44$  bath spins into account.

Going back to Figs. (6.9) and (6.10) in the previous chapter one can see that entanglement breaking occurs at the same time when the von Neumann entropy  $E(\rho_S)$  saturates for the first

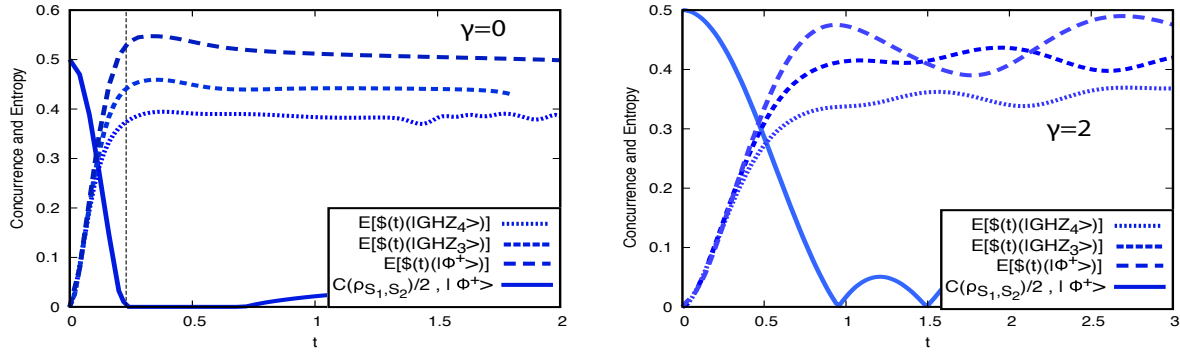


Figure 6.12: Evolution of Concurrence and the normalized von Neumann entropy for  $|W\rangle$ -states in a global bath. The bath length is  $N_B = 40$ , the number of entangled qubits is  $N_S = 2, 3, 4$  and  $\Delta_i = -1$ . The left and the right figure represent the two cases of non-decaying,  $\gamma = 0$ , and decaying interactions,  $\gamma = 2$ . In both pictures one can see the universal behavior of the normalized entropies, thus a linear growth followed by a convergence to the maximal possible value of entropy. This maximum marks the point of total entanglement breaking. To stress this fact I have also plotted the Concurrence of  $|\Psi^+\rangle$ . The bigger  $N_S$  the sooner the entropy deviates from the linear part. Thus, the fragility of many-body entanglement increases with the number of entangled parts. Due to the finite system size one observes recurrences of entanglement.

time: the two qubit state  $S$  is completely entangled with the bath  $B$ . The total information, which was initially stored in the non-local correlations between the two qubits, must be now located in the quantum correlations between the system  $S$  and the bath  $B$ . Thus, the entanglement between  $S$  and  $B$  serves as an indirect measure of the entanglement within  $S$  only. This observation is independent of whether  $\gamma = 0$  or  $\gamma = 2$  and can, of course, be expanded to bigger systems  $S$ .

Figure (6.12) compares the time evolution of  $E(\rho_S)$  for  $W$ -like initial states for system sizes  $N_S = 2, 3, 4$ . In order to compare the entropy for different numbers of qubits I will plot the entropy per qubit, i.e.  $E(\rho_S)/N_S$ , in the following. The evolution of entropy can be divided in three steps. First, at short time scales, it growth slowly followed then by a linear increase at intermediate times and finally by a saturation to some maximal value. The deviation from the linear increase of the normalized entropy thereby depends on the number of qubits  $N_S$ . As long as the entropy  $E(\rho_S)$  grows linearly the system  $S$  still contains entanglement. With the beginning of the saturation of  $E(\rho_S)$  the entanglement of the system is definitely lost and the state  $\rho_S$  cannot be used anymore as a quantum resource. The total coherence is distributed among  $n$  particles which all interact independently with a bath. Roughly speaking the influence of the bath on the coherence of  $S$  is threefold. Therefore, it is no surprise that with the increasing number of qubits (and assuming that all qubits interact) the coherences disappear faster.

The above observations are also valid in the case of the  $GHZ$ -like states. Figure (6.13) compares  $E(\rho_S)/N_S$  the von Neumann entropies normalized by the number of central qubits  $N_S$ . Also in this case the saturation of the entropy marks the time when the central system  $S$  is completely disentangled and thus not usable anymore as quantum memory. This behavior is completely independent on whether  $\gamma = 0$  or  $\gamma = 2$ .

In general, the linear increase of the entropy agrees with the bounds given by the so-called Lieb-Robinson theorem [197], a theorem about the entanglement growth in dynamical systems

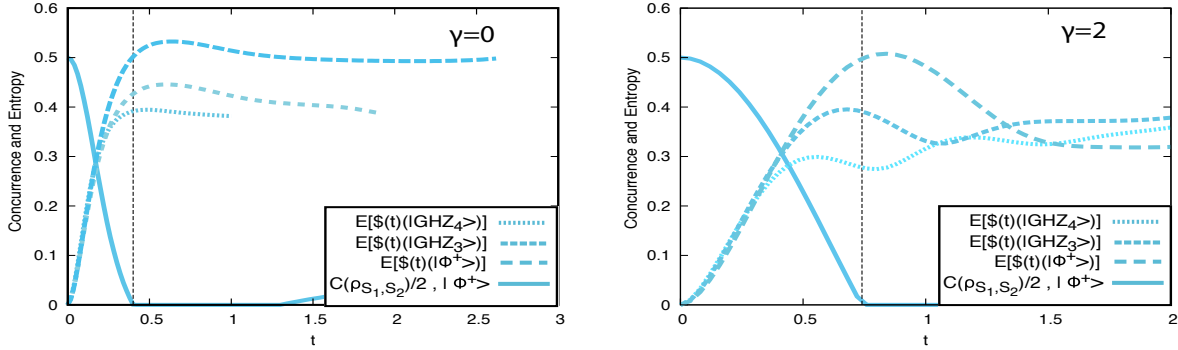


Figure 6.13: Evolution of Concurrence and the normalized von Neumann entropy for  $|GHZ\rangle$ -states in a global bath. The bath's length is  $N_B = 40$ , the number of entangled qubits is  $N_S = 2, 3, 4$  and  $\Delta_i = -1$ . The left and the right figure represent the two cases of non-decaying,  $\gamma = 0$ , and decaying interactions,  $\gamma = 2$ . The universal linear behavior of the normalized entropy, already discussed in Fig.(6.12), can be seen also for the  $GHZ$ -like state, independently of  $\gamma$ . Also here recurrences arise due to the finite system size.

[see Chapter ??]. The saturation of the entropy corresponds to the time scales at which  $\rho_S(t)$  has minimal fidelity with the initial state. The state itself is definitely a mixed state from the very first contact with the environment  $B$ . However, for short times it is still possible to extract an entangled pure state out this mixture  $\rho_S(t)$  using appropriate purification techniques[85]. Nevertheless, the question, how much mixedness is tolerable in  $\rho_S$ , will depend on the algorithms and error correction schemes.

The attempt to extract a general law for  $T(N_S)$  the time of the complete entanglement breaking was not successful. however, the simulations suggest that  $T(N_S)$  does not grow exponentially fast. Whether the correspondence is polynomial or even logarithmic could not be extracted from the small number of data points. On the other hand, a fixed time  $T$  gives a non-exponential bound to the maximal storable number of qubits  $N_S$  (if one tolerates the total loss of system's entanglement).

However, it is more realistic to believe that one can tolerate a certain entanglement loss only. The exact amount of entanglement does certainly not depend in a general way on the used algorithms [257] and error correction schemes [85]. Let assume that a certain loss per qubit is tolerable. Then the total storage time remains a constant up to maximal number of qubits  $N_S^{\max}$ . Otherwise the storage time will definitely reduce by a further factor  $N_S$ . As long as the von Neumann entropy growth linearly this factor would look like  $1/N_S$ . However, at very small time scales one observes a slow transient effect which suggests that  $f(N_S) > 1/N_S$  and thus a weaker suppression of the time scale of a successful storage.

At least for the here considered central systems and baths one always finds an increasing fragility of the saved many-body state, which, however, is not exponentially fast. Due to the limited methods of investigation it remains an open question whether this non-exponential result is still valid for  $N_S \rightarrow \infty$ . Nevertheless, this thermodynamical limit has no relevance for the experimentally aimed number of qubits  $N_S$ .

### 6.3.3 Summary and outlook

With regard to a possible storage of entangled states, I have investigated the entanglement evolution and decoherence properties of initially maximally entangled many-body quantum states using the time-dependent DMRG method together with available analytical tools. The here presented work assumes the central state and the bath to be spin- $\frac{1}{2}$  particles. Due to the general complexity of the bath as well as the stored state a definite answer to the storage question has not been found. Another substantial complication arise from the fact that, albeit intensive effort over the last two decades, there is no satisfying entanglement measure for mixed states with three or more particles.

In order to reduce the immense number of possible scenarios I have concentrated on situations which are typical for the storage of states in quantum dots. Despite the dependence of the quantitative results on the parameter of the system it turns out that qualitative findings are can be summarized in general law.

The here considered initial states are, in the two qubit case, the Bell states and, in the many qubit case, the  $W$  and  $GHZ$ -state. All these states are maximally entangled and have been therefore the object of countless investigations on quantum information and computation.

Due to the existence of a two qubit quantum measure, i.e. the concurrence, it is possible to fully characterize the process of entanglement decrease in that particular case. It turns out that this decrease is directly related to the increase of entanglement between the central system and the bath which corresponds to the creation of a much bigger multipartite entangled network. The information which was initially stored in the non-local correlations between the qubits is now redistributed over the whole environment. It is exactly this entanglement growth which makes the environment act as a measuring device and which forbids the description of the central state by a pure wave function. In general, one will need to apply additional error correction protocols in order to restore some part of the initial state.

In the case of a few-body system, I have considered the systems of three and four qubits. It turns out that the von Neumann entropy, after a trivial normalization by the number of qubits, shows always a universal linear growth followed by a non-universal convergence to some finite value. It is in the nature of the following state that the maximal possible linear entropy can never be reached. However, at this time scale, the stored quantum state does not exist anymore since it is completely merged with the environment. One can, in general, observe that the bigger the central system is the sooner the entropy saturates. Although it is too difficult to find an analytical exact relation one can definitely exclude an exponential dependence between system size and saturation time. 1

In a scenario, in which it is possible to store a state up to some time  $T$ , the number of qubits will be limited by  $N_S^{\max}$  a number which does not increase exponentially in time. For a smaller amount of qubits  $N_S < N_S^{\max}$  the upper bound is a result of the tolerable entanglement loss<sup>14</sup>. If the upper bound is given by the entanglement loss per qubit, then, due to the universal linear growth of the entropy, the maximal number of qubits is  $N_S^{\max}$ . While for a bound which is given by the global entanglement loss the total storage time reduces by a factor  $f(N_S) > 1/N_S$ .

<sup>14</sup>The limit is given by the error correction schemes.



# Bibliography

- [1] J.R. Abo-Shaeer, C. Raman, J.M. Vogels und W. Ketterle, *Science (New York, N.Y.)* **292** (2001), 476.
- [2] I. Affleck, D. Gepner, H.J. Schulz und T. Ziman, *Journal of Physics A: Mathematical and General* **22** (1989).
- [3] V. Akulin und W. Schleich, *Physical Review A* **46** (1992), 4110.
- [4] R. Alicki und M. Fannes: *Quantum Dynamical Systems*. Oxford University Press, USA, 2001.
- [5] L. Allen und J.H. Eberly: *Optical Resonance and Two-Level Atoms*. Dover Publications, 1987.
- [6] E. Altman, E. Demler und M. Lukin, *Physical Review A* **70** (2004), 013603.
- [7] E. Altman, W. Hofstetter, E. Demler und M.D. Lukin, *New Journal of Physics* **5** (2003), 113.
- [8] L. Amico, R. Fazio, A. Osterloh und V. Vedral, *Reviews of Modern Physics* **80** (2008), 517.
- [9] M. Anderlini, J. Sebby-Strabley, J. Kruse, J.V. Porto und W.D. Phillips, *Journal of Physics B: Atomic, Molecular and Optical Physics* **39** (2006), S199.
- [10] M.H. Anderson, J.R. Ensher, M.R. Matthews, C.E. Wieman und E.A. Cornell, *Science (New York, N.Y.)* **269** (1995), 198.
- [11] P. Anderson, *Physical Review* **79** (1950), 350.
- [12] P. Anderson, *Physical Review* **109** (1958), 1492.
- [13] P.W. Anderson, *Physical Review* **115** (1959), 2.
- [14] M.R. Andrews, *Science* **275** (1997), 637.
- [15] N.W. Ashcroft und N.D. Mermin: *Solid State Physics*. Brooks Cole, 1976.

- [16] J. Audretsch: *Verschrankte Welt: Faszination Der Quanten (German Edition)*. Wiley-VCH Verlag GmbH, Weinheim, 2002.
- [17] J. Audretsch: *Verschrankte Systeme: Die Quantenphysik Auf Neuen Wegen (German Edition)*. Wiley-VCH Verlag GmbH, 2005.
- [18] J.E. Avron, R. Seiler und L.G. Yaffe, *Communications in Mathematical Physics* **110** (1987), 33.
- [19] M. Bañuls, M. Hastings, F. Verstraete und J. Cirac, *Physical Review Letters* **102** (2009).
- [20] V. Bagnato, D. Pritchard und D. Kleppner, *Physical Review A* **35** (1987), 4354.
- [21] W.S. Bakr, J.I. Gillen, A. Peng, S. Fölling und M. Greiner, *Nature* **462** (2009), 74.
- [22] P. Barmettler, A. Rey, E. Demler, M. Lukin, I. Bloch und V. Gritsev, *Physical Review A* **78** (2008), 012330.
- [23] T. Barthel, C. Kasztelan, I. McCulloch und U. Schollwöck, *Physical Review A* **79** (2009).
- [24] T. Barthel und U. Schollwöck, *Physical Review Letters* **100** (2008).
- [25] H. Bateman: *Higher Transcendental Functions*. Krieger Pub Co, 1981.
- [26] C. Becker, P. Soltan-Panahi, J. Kronjäger, S. Dörscher, K. Bongs und K. Sengstock, (2009), 19.
- [27] C. Becker, S. Stellmer, P. Soltan-Panahi, S. Dörscher, M. Baumert, E.M. Richter, J. Kronjäger, K. Bongs und K. Sengstock, *Nature Physics* **4** (2008), 496.
- [28] J. Bekenstein, *Physical Review D* **7** (1973), 2333.
- [29] M. Ben Dahan, E. Peik, J. Reichel, Y. Castin und C. Salomon, *Physical Review Letters* **76** (1996), 4508.
- [30] C. Bennett, G. Brassard, C. Crépeau, R. Jozsa, A. Peres und W. Wootters, *Physical Review Letters* **70** (1993), 1895.
- [31] K. Bergmann, H. Theuer und B. Shore, *Reviews of Modern Physics* **70** (1998), 1003.
- [32] P.R. Berman: *Atom Interferometry*. Academic Press, 1996.
- [33] H. Bethe, *Zeitschrift für Physik* **71** (1931), 205.
- [34] L.C. Biedenharn und J. Louck: *Angular Momentum in Quantum Physics: Theory and Application*. Addison-Wesley Publishing Company, 1981.
- [35] J. Billy, V. Josse, Z. Zuo, A. Bernard, B. Hambrecht, P. Lugan, D. Clément, L. Sanchez-Palencia, P. Bouyer und A. Aspect, *Nature* **453** (2008), 891.



- [36] J.L. Black und V.J. Emery, *Physical Review B* **23** (1981), 429.
- [37] I. Bloch, *Nature Physics* **1** (2005), 23.
- [38] I. Bloch, J. Dalibard und W. Zwerger, *Reviews of Modern Physics* **80** (2008), 885.
- [39] I. Bloch, T. Hansch und T. Esslinger, *Nature* **403** (2000), 166.
- [40] S.N. Bose, *Annalen der Physik. Leipzig* **26** (1924), 178.
- [41] D. Bouwmeester, J.W. Pan, K. Mattle, M. Eibl, H. Weinfurter und A. Zeilinger, **390** (1997), 575.
- [42] C. Bradley, C. Sackett, J. Tollett und R. Hulet, *Physical Review Letters* **75** (1995), 1687.
- [43] G. Brennen, C. Caves, P. Jessen und I. Deutsch, *Physical Review Letters* **82** (1999), 1060.
- [44] H.P. Breuer und F. Petruccione: *The Theory of Open Quantum Systems*, 2002.
- [45] H.J. Briegel, T. Calarco, D. Jaksch, I. Cirac und P. Zoller, *Journal of Modern Optics* **47** (2000).
- [46] Y.A. Bychkov und A.M. Dykhne, *Sov. Phys. JETP* **21** (1965).
- [47] P. Calabrese und J. Cardy, *Journal of Statistical Mechanics: Theory and Experiment* **2005** (2005), P04010.
- [48] C. Callan, *Physics Letters B* **333** (1994), 55.
- [49] R. Casalbuoni und G. Nardulli, *Reviews of Modern Physics* **76** (2004), 263.
- [50] Y. Castin. *Bose-Einstein condensates in atomic gases: simple theoretical results*. EDP Sciences and Springer-Verlag, 2001. Seiten 1–136.
- [51] J.S. Caux und J.M. Maillet, *Physical Review Letters* **95** (2005), 077201.
- [52] C. Caves, K. Thorne, R. Drever, V. Sandberg und M. Zimmermann, *Reviews of Modern Physics* **52** (1980), 341.
- [53] M. Cazalilla, *Physical Review Letters* **97** (2006).
- [54] M. Cazalilla und J. Marston, *Physical Review Letters* **88** (2002).
- [55] K.A. Chao, J. Spalek und A.M. Oles, *Journal of Physics C: Solid State Physics* **10** (1977).
- [56] Y.A. Chen, S. Huber, S. Trotzky, I. Bloch und E. Altman, *arXiv:1003.4956v1* (2010).
- [57] Y.A. Chen, S.D. Huber, S. Trotzky, I. Bloch und E. Altman, (2010), 13.

- [58] C. Chin, M. Bartenstein, A. Altmeyer, S. Riedl, S. Jochim, J.H. Denschlag und R. Grimm, *Science (New York, N.Y.)* **305** (2004), 1128.
- [59] J.K. Chin, D.E. Miller, Y. Liu, C. Stan, W. Setiawan, C. Sanner, K. Xu und W. Ketterle, *Nature* **443** (2006), 961.
- [60] D. Clément, N. Fabbri, L. Fallani, C. Fort und M. Inguscio, *Journal of Low Temperature Physics* **158** (2009), 5.
- [61] D. Clément, A. Varón, M. Hugbart, J. Retter, P. Bouyer, L. Sanchez-Palencia, D. Gangardt, G. Shlyapnikov und A. Aspect, *Physical Review Letters* **95** (2005), 170409.
- [62] N.R. Cooper und G.V. Shlyapnikov, *Physical Review Letters* **103** (2009), 155302.
- [63] S. Cornish, N. Claussen, J. Roberts, E. Cornell und C. Wieman, *Physical Review Letters* **85** (2000), 1795.
- [64] P. Courteille, R. Freeland, D. Heinzen, F. van Abeelen und B. Verhaar, *Physical Review Letters* **81** (1998), 69.
- [65] M. Cramer, C. Dawson, J. Eisert und T. Osborne, *Physical Review Letters* **100** (2008), 030602.
- [66] M. Cramer, A. Flesch, I. McCulloch, U. Schollwöck und J. Eisert, *Physical Review Letters* **101** (2008).
- [67] A. Cronin, J. Schmiedmayer und D. Pritchard, *Reviews of Modern Physics* **81** (2009), 1051.
- [68] M. Cross und D. Fisher, *Physical Review B* **19** (1979), 402.
- [69] W. Dahmen und A. Reusken: *Numerik für Ingenieure und Naturwissenschaftler (Springer-Lehrbuch) (German Edition)*. Springer, 2008.
- [70] A.J. Daley, C. Kollath, U. Schollwöck und G. Vidal, *Journal of Statistical Mechanics: Theory and Experiment* **2004** (2004), P04005.
- [71] F. Dalfovo, S. Giorgini, L. Pitaevskii und S. Stringari, *Reviews of Modern Physics* **71** (1999), 463.
- [72] J. Dalibard. *Collisional dynamics of ultra-cold atomic gases*. IOS Press Amsterdam, 1999.
- [73] B. Damski, J. Zakrzewski, L. Santos, P. Zoller und M. Lewenstein, *Physical Review Letters* **91** (2003), 080403.
- [74] T.L. Dao, A. Georges, J. Dalibard, C. Salomon und I. Carusotto, *Physical Review Letters* **98** (2007), 240402.

- [75] K. Davis, M. Mewes, M. Andrews, N. van Druten, D. Durfee, D. Kurn und W. Ketterle, *Physical Review Letters* **75** (1995), 3969.
- [76] B. DeMarco, *Science* **285** (1999), 1703.
- [77] B. DeMarco, J. Bohn, J. Burke, M. Holland und D. Jin, *Physical Review Letters* **82** (1999), 4208.
- [78] Y.N. Demkov und V.I. Osherov, *Sov. Phys. JETP* **26** (1968).
- [79] J. Denschlag, *Science* **287** (2000), 97.
- [80] P.A.M. Dirac, *Proceeding of the Royal Society A* **112** (1926), 661 .
- [81] P.A.M. Dirac, *Proceedings of the Royal Society A* **123** (1929), 714 .
- [82] D. DiVincenzo, *Physical Review A* **51** (1995), 1015.
- [83] D.P. DiVincenzo, *Science* **270** (1995), 255.
- [84] L.M. Duan, E. Demler und M. Lukin, *Physical Review Letters* **91** (2003), 090402.
- [85] W. Dür und H.J. Briegel, *Reports on Progress in Physics* **70** (2007), 1381.
- [86] A.M. Dykhne und A.V. Chaplik, *Sov. Phys. JEPT* **16** (1963).
- [87] A. Eckardt, P. Hauke, P. Soltan-Panahi, C. Becker, K. Sengstock und M. Lewenstein, *EPL (Europhysics Letters)* **89** (2010), 10010.
- [88] M. Eckstein und M. Kollar, *Physical Review Letters* **100** (2008).
- [89] E. Edwards, M. Beeler, T. Hong und S. Rolston, *Physical Review Letters* **101** (2008), 260402.
- [90] A. Einstein, *Sitzungsberichte der Preussischen Akademie der Wissenschaften* **1** (1925), 3.
- [91] J. Eisert, M. Cramer und M.B. Plenio, *Reviews of Modern Physics* **82** (2010), 277.
- [92] N. Fabbri, D. Clément, L. Fallani, C. Fort, M. Modugno, K. van der Stam und M. Inguscio, *Physical Review A* **79** (2009), 043623.
- [93] F. Fannes, B. Nachtergaele und R.F. Werner, *Jurnal of Physics A: Mathematical ang General* **24** (1991).
- [94] M. Fattori, G. Roati, B. Deissler, C. DErrico, M. Zaccanti, M. Jona-Lasinio, L. Santos, M. Inguscio und G. Modugno, *Physical Review Letters* **101** (2008), 190405.
- [95] P. Fazekas: *Lecture Notes on Electron Correlation and Magnetism (Series in Modern Condensed Matter Physics, Vol. 5)*. World Scientific Pub Co Inc, 1999.

- [96] P. Fedichev, M. Reynolds und G. Shlyapnikov, *Physical Review Letters* **77** (1996), 2921.
- [97] J. Feldmann, K. Leo, J. Shah, D. Miller, J. Cunningham, T. Meier, G. von Plessen, A. Schulze, P. Thomas und S. Schmitt-Rink, *Physical Review B* **46** (1992), 7252.
- [98] H. Feshbach, *Annals of Physics* **5** (1958), 357.
- [99] R.P. Feynman, *International Journal of Theoretical Physics* **21** (1982), 467.
- [100] M. Fisher, P. Weichman, G. Grinstein und D. Fisher, *Physical Review B* **40** (1989), 546.
- [101] A. Flesch, M. Cramer, I. McCulloch, U. Schollwöck und J. Eisert, *Physical Review A* **78** (2008).
- [102] S. Fölling, F. Gerbier, A. Widera, O. Mandel, T. Gericke und I. Bloch, *Nature* **434** (2005), 481.
- [103] S. Fölling, S. Trotzky, P. Cheinet, M. Feld, R. Saers, A. Widera, T. Müller und I. Bloch, *Nature* **448** (2007), 1029.
- [104] D.J. Frantzeskakis, (2010), 82.
- [105] D. Gangardt und M. Pustilnik, *Physical Review A* **77** (2008).
- [106] J. García-Ripoll, M. Martin-Delgado und J. Cirac, *Physical Review Letters* **93** (2004).
- [107] J.J. García-Ripoll, *New Journal of Physics* **8** (2006), 305.
- [108] T.F. George und Y.W. Lin, *Journal of Chemical Physics* **60** (1974).
- [109] F. Gerbier, S. Foelling, A. Widera und I. Bloch, (2007).
- [110] T. Giamarchi, (2010).
- [111] T. Giamarchi und H. Schulz, *Physical Review B* **37** (1988), 325.
- [112] N. Gisin, G. Ribordy, W. Tittel und H. Zbinden, *Reviews of Modern Physics* **74** (2002), 145.
- [113] N. Gisin und R. Thew, *Nature Photonics* **1** (2007), 165.
- [114] D. Gobert, C. Kollath, U. Schollwöck und G. Schütz, *Phys. Rev. E* **71** (2005), 36102.
- [115] K. Góral, L. Santos und M. Lewenstein, *Physical Review Letters* **88** (2002), 170406.
- [116] D. Greenberger, M. Horne und A. Zeilinger. *Bells Theorem, Quantum Theory, and Conceptions of the Universe*. Kluwer Academics, Dodrecht, NL, 1989. Seiten 73 – 76.
- [117] M. Greiner, I. Bloch, O. Mandel, T. Hänsch und T. Esslinger, *Physical Review Letters* **87** (2001).

- [118] M. Greiner, O. Mandel, T. Esslinger, T.W. Hänsch und I. Bloch, *Nature* **415** (2002), 39.
- [119] M. Greiner, C. Regal, J. Stewart und D. Jin, *Physical Review Letters* **94** (2005), 110401.
- [120] A. Griesmaier, J. Werner, S. Hensler, J. Stuhler und T. Pfau, *Physical Review Letters* **94** (2005), 160401.
- [121] R. Grimm, M. Weidenmüller und Y. Ovchinnikov, *Adv. At. Mol. Opt. Phys.* **42** (2000).
- [122] V. Gritsev, E. Demler und A. Polkovnikov, *Physical Review A* **78** (2008), 063624.
- [123] S.R. de Groot, G.J. Hooyman und C.A. ten Seldam, *Proceedings of the Royal Society of London. Series A, Mathematical and Physical Sciences (1934-1990)* **203** (1950), 266.
- [124] E.P. Gross, *Il Nuovo Cimento* **20** (1961), 454.
- [125] G. Grynberg und C. Robillard, *Phys. Rep.* **355** (2001), 335 .
- [126] V. Guarrera, N. Fabbri, L. Fallani, C. Fort, K. van Der Stam und M. Inguscio, *Physical Review Letters* **100** (2008), 250403.
- [127] K. Günter, T. Stöferle, H. Moritz, M. Köhl und T. Esslinger, *Physical Review Letters* **96** (2006), 180402.
- [128] Z. Hadzibabic, P. Krüger, M. Cheneau, B. Battelier und J. Dalibard, *Nature* **441** (2006), 1118.
- [129] M. Hafezi, A. Sørensen, E. Demler und M. Lukin, *Physical Review A* **76** (2007), 023613.
- [130] R. Hanbury Brown und D.R.Q. Twiss, *Nature* **178** (1956), 1046.
- [131] M.B. Hastings und L.S. Levitov, (2008).
- [132] W. Heisenberg, *Zeitschrift für Physik* **39** (1926), 499.
- [133] W. Heisenberg, *Zeitschrift für Physik* **49** (1928), 619.
- [134] J. Herbig, T. Kraemer, M. Mark, T. Weber, C. Chin, H.C. Nägerl und R. Grimm, *Science* **301** (2003), 1510 .
- [135] D. Hill und J. Wheeler, *Physical Review* **89** (1953), 1102.
- [136] M. Hochbruck und C. Lubich, *SIAM Journal on Numerical Analysis* **34** (1997), 1911.
- [137] S. Hofferberth, I. Lesanovsky, B. Fischer, T. Schumm und J. Schmiedmayer, *Nature* **449** (2007), 324.
- [138] S. Hofferberth, I. Lesanovsky, T. Schumm, A. Imambekov, V. Gritsev, E. Demler und J. Schmiedmayer, *Nature Physics* **4** (2008), 489.

- [139] R. Horodecki, P. Horodecki, M. Horodecki und K. Horodecki, *Reviews of Modern Physics* **81** (2009), 865.
- [140] J. Hubbard, *Proceedings of the Royal Society A: Mathematical, Physical and Engineering Sciences* **276** (1963), 238.
- [141] F. Illuminati und A. Albus, *Physical Review Letters* **93** (2004), 090406.
- [142] S. Inouye, *Science* **285** (1999), 571.
- [143] S. Inouye, M.R. Andrews, J. Stenger, H.J. Miesner, D.M. Stamper-Kurn und W. Ketterle, **392** (1998), 151.
- [144] D. Jaksch, C. Bruder, J. Cirac, C. Gardiner und P. Zoller, *Physical Review Letters* **81** (1998), 3108.
- [145] A. Jamiokowski, *Rep. Math. Phys.* **3** (1972), 275 .
- [146] E. Jeckelmann, *Physical Review B* **66** (2002).
- [147] T. Jelte, J.M. McNamara, W. Hogervorst, W. Vassen, V. Krachmalnicoff, M. Schellekens, A. Perrin, H. Chang, D. Boiron, A. Aspect und C.I. Westbrook, *Nature* **445** (2007), 402.
- [148] P.S. Jenness und I.H. Deutsch, *Adv. At. Mol. Opt. Phys.* **37** (1996).
- [149] P. Jordan und E. Wigner, *Zeitschrift für Physik* **47** (1928), 631.
- [150] S.P. Jordan, (2008), 144.
- [151] G. Juzelinas, J. Ruseckas, M. Lindberg, L. Santos und P. Öhberg, *Physical Review A* **77** (2008), 011802.
- [152] A. Kastberg, W. Phillips, S. Rolston, R. Spreuw und P. Jessen, *Physical Review Letters* **74** (1995), 1542.
- [153] T. Kato, *Journal of the Physical Society of Japan* **5** (1950), 435 .
- [154] W. Ketterle, D. Durfee und D. Stamper-Kurn. *Making, probing and understanding Bose-Einstein condensates*. IOS Press Amsterdam, 1999. Seiten 67–176.
- [155] A.V. Khaetskii, D. Loss und L. Glazman, *Phys. Rev. Lett.* **88** (2002), 186802.
- [156] T. Kinoshita, T. Wenger und D.S. Weiss, *Science (New York, N.Y.)* **305** (2004), 1125.
- [157] T. Kinoshita, T. Wenger und D.S. Weiss, *Nature* **440** (2006), 900.
- [158] E. Knill, R. Laflamme und G.J. Milburn, *Nature* **409** (2001), 46.

- [159] A. Koetsier, R. Duine, I. Bloch und H. Stoof, *Physical Review A* **77** (2008).
- [160] M. Köhl, H. Moritz, T. Stöferle, K. Günter und T. Esslinger, *Physical Review Letters* **94** (2005), 080403.
- [161] C. Kollath, A. Läuchli und E. Altman, *Physical Review Letters* **98** (2007), 180601.
- [162] C. Kollath, U. Schollwöck, J. von Delft und W. Zwerger, *Physical Review A* **71** (2005).
- [163] T. Konrad, F. de Melo, M. Tiersch, C. Kasztelan, A. Aragão und A. Buchleitner, *Nature Physics* **4** (2007), 14.
- [164] H. Kramers, *Physica* **1** (1934), 182.
- [165] T. Kühner und S. White, *Physical Review B* **60** (1999), 335.
- [166] A. Kuklov und B. Svistunov, *Physical Review Letters* **90** (2003).
- [167] M. Kumar, S. Ramasesha, D. Sen und Z. Soos, *Physical Review B* **75** (2007).
- [168] Y. Lahini, A. Avidan, F. Pozzi, M. Sorel, R. Morandotti, D. Christodoulides und Y. Silberberg, *Physical Review Letters* **100** (2008), 013906.
- [169] C. Lanczos, *J. Res. Nat. Bur. Standards* **45** (1950), 255 .
- [170] L. Landau, *Physics of the Soviet Union* **2** (1932), 46.
- [171] L.D. Landau und L.M. Lifshitz: *Quantum Mechanics Non-Relativistic Theory, Third Edition: Volume 3*. Butterworth-Heinemann, 1981.
- [172] P. Lee, M. Anderlini, B. Brown, J. Sebby-Strabley, W. Phillips und J. Porto, *Physical Review Letters* **99** (2007).
- [173] A. Leggett, *Reviews of Modern Physics* **73** (2001), 307.
- [174] A.J. Leggett, *J. Phys. (Paris)* **41** (1980), C7/19.
- [175] M. Lewenstein, A. Sanpera, V. Ahufinger, B. Damski, A. Sen und U. Sen, *Advances in Physics* **56** (2007), 243.
- [176] E. Lieb, T. Schultz und D. Mattis, *Annals of Physics* **16** (1961), 407.
- [177] E. Lieb, R. Seiringer und J. Yngvason, *Physical Review A* **61** (2000).
- [178] Y.J. Lin, R. Compton, A. Perry, W. Phillips, J. Porto und I. Spielman, *Physical Review Letters* **102** (2009), 5.
- [179] M. Loy, *Physical Review Letters* **32** (1974), 814.

- [180] N. Lundblad und J. Porto: *Quantum Information Processing with Double-Well Optical Lattices - OSA Technical Digest (CD)*. *Quantum Information Processing with Double-Well Optical Lattices - OSA Technical Digest (CD)*, In *Conference on Lasers and Electro-Optics/International Quantum Electronics Conference*. Optical Society of America (Mai 2009) Seite IWG2.
- [181] J.M. Luttinger, *Journal of Mathematical Physics* **4** (1963), 1154.
- [182] D. Luxat und A. Griffin, *Physical Review A* **65** (2002), 043618.
- [183] J. Lye, L. Fallani, M. Modugno, D. Wiersma, C. Fort und M. Inguscio, *Physical Review Letters* **95** (2005), 070401.
- [184] K. Madison, F. Chevy, W. Wohlleben und J. Dalibard, *Physical Review Letters* **84** (2000), 806.
- [185] E. Majorana, *Nuovo Cim.* **9** (1932).
- [186] S. Manmana, S. Wessel, R. Noack und A. Muramatsu, *Physical Review Letters* **98** (2007).
- [187] K.P. Marzlin und B. Sanders, *Physical Review Letters* **97** (2006).
- [188] L. Mathey, S.W. Tsai und A. Castro Neto, *Physical Review B* **75** (2007), 174516.
- [189] M. Matthews, B. Anderson, P. Haljan, D. Hall, C. Wieman und E. Cornell, *Physical Review Letters* **83** (1999), 2498.
- [190] I. Mazets, *Physical Review A* **71** (2005), 023806.
- [191] I.P. McCulloch und M. Gulácsi, *Europhysics Letters* **57** (2002), 852.
- [192] D. Medeiros und G. Cabrera, *Physical Review B* **43** (1991), 3703.
- [193] R. Melko, A. Paramekanti, A. Burkov, A. Vishwanath, D. Sheng und L. Balents, *Physical Review Letters* **95** (2005), 127207.
- [194] M. Moeckel und S. Kehrein, *Physical Review Letters* **100** (2008), 175702.
- [195] H. Moritz, T. Stöferle, M. Köhl und T. Esslinger, *Physical Review Letters* **91** (2003).
- [196] J.J.L. Morton, A.M. Tyryshkin, R.M. Brown, S. Shankar, B.W. Lovett, A. Ardavan, T. Schenkel, E.E. Haller, J.W. Ager und S.A. Lyon, *Nature* **455** (2008), 1085.
- [197] B. Nachtergaele, Y. Ogata und R. Sims, *Journal of Statistical Physics* **124** (2006), 1.
- [198] K.K. Ni, S. Ospelkaus, M.H.G. de Miranda, A. Pe'er, B. Neyenhuis, J.J. Zirbel, S. Kotochigova, P.S. Julienne, D.S. Jin und J. Ye, *Science (New York, N.Y.)* **322** (2008), 231.



- [199] M.A. Nielsen und I.L. Chuang: *Quantum Computation and Quantum Information*. Cambridge University Press, 2000.
- [200] E. Nikitin und S. Umanskii: *Theory of Slow Atomic Collisions (Springer Series in Chemical Physics)*. Springer, 1984.
- [201] K.M. O'Hara, S.L. Hemmer, M.E. Gehm, S.R. Granade und J.E. Thomas, *Science (New York, N.Y.)* **298** (2002), 2179.
- [202] C. Ospelkaus, S. Ospelkaus, L. Humbert, P. Ernst, K. Sengstock und K. Bongs, *Physical Review Letters* **97** (2006), 120402.
- [203] S. Ospelkaus, K.K. Ni, G. Quéméner, B. Neyenhuis, D. Wang, M.H.G. de Miranda, J.L. Bohn, J. Ye und D.S. Jin, *Physical Review Letters* **104** (2010), 030402.
- [204] S. Ospelkaus, K.K. Ni, D. Wang, M.H.G. de Miranda, B. Neyenhuis, G. Quéméner, P.S. Julienne, J.L. Bohn, D.S. Jin und J. Ye, *Science (New York, N.Y.)* **327** (2010), 853.
- [205] S. Östlund und S. Rommer, *Physical Review Letters* **75** (1995), 3537.
- [206] A. Öttl, S. Ritter, M. Köhl und T. Esslinger, *Physical Review Letters* **95** (2005), 090404.
- [207] J. Pachos und P. Knight, *Physical Review Letters* **91** (2003), 107902.
- [208] B. Paredes und I. Bloch, *Physical Review A* **77** (2008), 023603.
- [209] B. Paredes, A. Widera, V. Murg, O. Mandel, S. Fölling, I. Cirac, G.V. Shlyapnikov, T.W. Hänsch und I. Bloch, *Nature* **429** (2004), 277.
- [210] T.J. Park und J.C. Light, *The Journal of Chemical Physics* **85** (1986), 5870.
- [211] G.B. Partridge, W. Li, R.I. Kamar, Y.A. Liao und R.G. Hulet, *Science (New York, N.Y.)* **311** (2006), 503.
- [212] P. Pedri, L. Pitaevskii, S. Stringari, C. Fort, S. Burger, F. Cataliotti, P. Maddaloni, F. Minardi und M. Inguscio, *Physical Review Letters* **87** (2001).
- [213] C.J. Pethick und H. Smith: *Bose-Einstein Condensation in Dilute Gases*. Cambridge University Press, 2001.
- [214] D. Petrov, C. Salomon und G. Shlyapnikov, *Physical Review Letters* **93** (2004), 090404.
- [215] B. Pirvu, V. Murg, J.I. Cirac und F. Verstraete, *New Journal of Physics* **12** (2010), 025012.
- [216] L. Pitaevskii, *Sov. Phys. JETP* **13** (1961), 451.
- [217] L. Pitaevskii und S. Stringari: *Bose-Einstein Condensation*. Oxford University Press, Oxford, 2003.

- [218] M. Plenio, J. Eisert, J. Dreißig und M. Cramer, *Physical Review Letters* **94** (2005).
- [219] A. Polkovnikov, *Europhys. Lett.* **78** (2007).
- [220] A. Polkovnikov, E. Altman und E. Demler, *Proceedings of the National Academy of Sciences of the United States of America* **103** (2006), 6125.
- [221] L. Pollet, C. Kollath, U. Schollwöck und M. Troyer, *Physical Review A* **77** (2008), 023608.
- [222] S. Popescu, A.J. Short und A. Winter, *Nature Physics* **2** (2006), 754.
- [223] N. Prokof'ev und P. Stamp, *Reports on Progress in Physics* **63** (2000), 669.
- [224] P. Rabl, D. DeMille, J. Doyle, M. Lukin, R. Schoelkopf und P. Zoller, *Physical Review Letters* **97** (2006), 033003.
- [225] C.A. Regal, C. Ticknor, J.L. Bohn und D.S. Jin, *Nature* **424** (2003), 47.
- [226] A.M. Rey, R. Sensarma, S. Foelling, M. Greiner, E. Demler und M. Lukin, *EPL (Europhysics Letters)* **87** (2009), 60001.
- [227] T. Rickes, L.P. Yatsenko, S. Steuerwald, T. Halfmann, B.W. Shore, N.V. Vitanov und K. Bergmann, *The Journal of Chemical Physics* **113** (2000), 534.
- [228] M. Rigol, V. Dunjko und M. Olshanii, *Nature* **452** (2008), 854.
- [229] M. Rigol, V. Dunjko, V. Yurovsky und M. Olshanii, *Physical Review Letters* **98** (2007), 050405.
- [230] G. Roati, C. D'Errico, L. Fallani, M. Fattori, C. Fort, M. Zaccanti, G. Modugno, M. Modugno und M. Inguscio, *Nature* **453** (2008), 895.
- [231] T. Rom, T. Best, D. van Oosten, U. Schneider, S. Fölling, B. Paredes und I. Bloch, *Nature* **444** (2006), 733.
- [232] S. Rommer und S. Östlund, *Physical Review B* **55** (1997), 2164.
- [233] N. Rosen und C. Zener, *Physical Review* **40** (1932).
- [234] R. Roth und K. Burnett, *Journal of Optics B: Quantum and Semiclassical Optics* **5** (2003), S50.
- [235] Y. Saad: *Iterative Methods for Sparse Linear Systems, Second Edition*. Society for Industrial and Applied Mathematics, 2003.
- [236] J. Sage, S. Sainis, T. Bergeman und D. DeMille, *Physical Review Letters* **94** (2005).
- [237] L. Sanchez-Palencia, D. Clément, P. Lugan, P. Bouyer und A. Aspect, *New Journal of Physics* **10** (2008), 045019.

- [238] L. Sanchez-Palencia, D. Clément, P. Lugan, P. Bouyer, G. Shlyapnikov und A. Aspect, *Physical Review Letters* **98** (2007), 210401.
- [239] L. Sanchez-Palencia und M. Lewenstein, *Nature Physics* **6** (2010), 87.
- [240] M. Schellekens, R. Hoppeler, A. Perrin, J.V. Gomes, D. Boiron, A. Aspect und C.I. Westbrook, *Science (New York, N.Y.)* **310** (2005), 648.
- [241] M. Schlosshauer, *Reviews of Modern Physics* **76** (2005), 1267.
- [242] U. Schollwöck, *Reviews of Modern Physics* **77** (2005), 259.
- [243] U. Schollwöck, *Rev. Mod. Phys.* **77** (2005), 259.
- [244] F. Schreck, L. Khaykovich, K. Corwin, G. Ferrari, T. Bourdel, J. Cubizolles und C. Salomon, *Physical Review Letters* **87** (2001).
- [245] J. Schrieffer und P. Wolff, *Physical Review* **149** (1966), 491.
- [246] T. Schulte, S. Drenkelforth, J. Kruse, W. Ertmer, J. Arlt, K. Sacha, J. Zakrzewski und M. Lewenstein, *Physical Review Letters* **95** (2005), 170411.
- [247] T. Schwartz, G. Bartal, S. Fishman und M. Segev, *Nature* **446** (2007), 52.
- [248] J. Sebby-Strabley, M. Anderlini, P. Jessen und J. Porto, *Physical Review A* **73** (2006).
- [249] J. Sebby-Strabley, B. Brown, M. Anderlini, P. Lee, W. Phillips, J. Porto und P. Johnson, *Physical Review Letters* **98** (2007).
- [250] P.W. Shor, *SIAM Review* **41** (1999), 303.
- [251] B.W. Shore: *The Theory of Coherent Atomic Excitation, 2 Volume Set*. Wiley-Interscience, 1990.
- [252] I. Spielman, W. Phillips und J. Porto, *Physical Review Letters* **98** (2007), 080404.
- [253] M. Srednicki, *Physical Review Letters* **71** (1993), 666.
- [254] S. Stellmer, C. Becker, P. Soltan-Panahi, E.M. Richter, S. Dörscher, M. Baumert, J. Kronjäger, K. Bongs und K. Sengstock, *Physical Review Letters* **101** (2008), 120406.
- [255] S. Stenholm: *Foundations of Laser Spectroscopy*. Dover Publications, 2005.
- [256] J.T. Stewart, J.P. Gaebler und D.S. Jin, *Nature* **454** (2008), 744.
- [257] J. Stolze und D. Suter: *Quantum Computing, Revised and Enlarged: A Short Course from Theory to Experiment (Physics Textbook)*. Wiley-VCH, 2008.
- [258] H. Stoof, L. de Goey, B. Verhaar und W. Glöckle, *Physical Review B* **38** (1988), 11221.

- [259] A. Storozhenko, P. Schuck, T. Suzuki, H. Yabu und J. Dukelsky, *Physical Review A* **71** (2005).
- [260] N. Strohmaier, D. Greif, R. Jördens, L. Tarruell, H. Moritz und T. Esslinger, *Physical Review Letters* **104** (2010).
- [261] E.C.G. Stückelberg, *Helvetica Physica Acta* **5** (1932).
- [262] C. Sukumar und D. Brink, *Physical Review A* **56** (1997), 2451.
- [263] M. Szymaska, B. Simons und K. Burnett, *Physical Review Letters* **94** (2005).
- [264] E. Tiesinga, B. Verhaar und H. Stoof, *Physical Review A* **47** (1993), 4114.
- [265] B. Tolra, K. OHara, J. Huckans, W. Phillips, S. Rolston und J. Porto, *Physical Review Letters* **92** (2004).
- [266] D. Tong, K. Singh, L. Kwek und C. Oh, *Physical Review Letters* **95** (2005), 110407.
- [267] D. Tong, K. Singh, L. Kwek und C. Oh, *Physical Review Letters* **98** (2007).
- [268] S. Toshev, *Physics Letters B* **198** (1987), 551.
- [269] S. Trebst, U. Schollwöck, M. Troyer und P. Zoller, *Physical Review Letters* **96** (2006).
- [270] P. Treutlein, T. Steinmetz, Y. Colombe, B. Lev, P. Hommelhoff, J. Reichel, M. Greiner, O. Mandel, A. Widera, T. Rom, I. Bloch und T. Hänsch, *Fortschritte der Physik* **54** (2006), 702.
- [271] S. Trotzky, P. Cheinet, S. Fölling, M. Feld, U. Schnorrberger, A.M. Rey, A. Polkovnikov, E.A. Demler, M.D. Lukin und I. Bloch, *Science (New York, N.Y.)* **319** (2008), 295.
- [272] A.G. Truscott, K.E. Strecker, W.I. McAlexander, G.B. Partridge und R.G. Hulet, *Science (New York, N.Y.)* **291** (2001), 2570.
- [273] M. Vengalattore, S. Leslie, J. Guzman und D. Stamper-Kurn, *Physical Review Letters* **100** (2008), 170403.
- [274] G. Vidal, *Journal of Modern Optics* **47** (2000), 355.
- [275] G. Vidal, *Physical Review Letters* **91** (2003).
- [276] N. Vitanov, T. Halfmann, B. Shore und K. Bergmann, (2003).
- [277] N.V. Vitanov und S. Stenholm, *Physical Review A* **55** (1997), 2982.
- [278] G.H. Wannier, *Physics (Lond Island City, N. Y.)* **1** (1964).
- [279] G. Warner und A. Leggett, *Physical Review B* **71** (2005), 134514.

- [280] M. Weidenmüller und C. Zimmermann, Herausgeber. *Interactions in Ultracold Gases: From Atoms to Molecules*. Wiley-VCH, Weinheim, 2003.
- [281] A. Weller, J. Ronzheimer, C. Gross, J. Esteve, M. Oberthaler, D. Frantzeskakis, G. Theocharis und P. Kevrekidis, *Physical Review Letters* **101** (2008), 130401.
- [282] S. Wessel und M. Troyer, *Physical Review Letters* **95** (2005), 127205.
- [283] S. White, *Physical Review Letters* **69** (1992), 2863.
- [284] S. White, *Physical Review B* **48** (1993), 10345.
- [285] S. White und A. Feiguin, *Physical Review Letters* **93** (2004), 076401.
- [286] E.P. Wigner: *Group Theory and its Application to the Quantum Mechanics of Atomic Spectra*. ACADEMIC PRESS INC, 1959.
- [287] K. Winkler, G. Thalhammer, F. Lang, R. Grimm, J.H. Denschlag, A.J. Daley, A. Kantian, H.P. Büchler und P. Zoller, *Nature* **441** (2006), 853.
- [288] W.K. Wootters, *Phys. Rev. Lett.* **80** (1998), 2245.
- [289] L. Yatsenko, B. Shore, T. Halfmann, K. Bergmann und A. Vardi, *Physical Review A* **60** (1999), R4237.
- [290] W. Yi und L.M. Duan, *Physical Review Letters* **97** (2006), 120401.
- [291] K.C. Younge, B. Knuffman, S.E. Anderson und G. Raithel, *Physical Review Letters* **104** (2010), 173001.
- [292] C.H. Yuan, L.Q. Chen und W. Zhang, (2009), 7.
- [293] S. Yuan, M.I. Katsnelson und H. De Raedt, *Physical Review B* **77** (2008), 184301.
- [294] E. Yuzbashyan, B. Altshuler, V. Kuznetsov und V. Enolskii, *Physical Review B* **72** (2005).
- [295] E.A. Yuzbashyan, B.L. Altshuler, V.B. Kuznetsov und V.Z. Enolskii, *Journal of Physics A: Mathematical and General* **38** (2005), 7831.
- [296] N.C.H. Zachary: *Quantum Many-Body Systems in One Dimension (Series on Advances in Statistical Mechanics, Vol 12)*. World Scientific Publishing Company, 1996.
- [297] C. Zener, *Proceedings of the Royal Society of London. Series A, Containing Papers of a Mathematical and Physical Character* **137** Seite 696.
- [298] C. Zhang, V. Scarola und S. Das Sarma, *Physical Review A* **76** (2007), 023605.
- [299] R. Zhao, Y.O. Dudin, S.D. Jenkins, C.J. Campbell, D.N. Matsukevich, T.A.B. Kennedy und A. Kuzmich, *Nature Physics* **5** (2008), 100.

- [300] W.H. Zurek, (2003).
- [301] W. Zwerger, *Journal of Optics B: Quantum and Semiclassical Optics* **5** (2003), S9.
- [302] M.W. Zwierlein, A. Schirotzek, C.H. Schunck und W. Ketterle, *Science (New York, N.Y.)* **311** (2006), 492.

# Acknowledgments

A lot of people have contributed to this thesis to whom I am very grateful. Special thanks go to:

- Ulrich Schollwöck for the opportunity to work at his institute, introducing me to the field of numerical simulations and giving me the possibility to work on wonderful and interesting projects mostly together with experimentalists from the field of ultra cold quantum gases, sending me to several inspiring conferences and for his supervision, financial care and and funny comments,
- to my supervisor during the Landau-Zener project Giuliano Orso for the deep discussions about physics and life and to Yu-Ao and Stefan from the Bloch Group for their hospitality and the fruitful collaboration,
- my further collaborators Thomas Barthel, Thomas Konrad, Andreas Buchleitner, Markus Tiersch, Fernando de Melo, Adriano Aragao from and together with each of whom I learned a lot during our joint projects,
- my office mates Andreas Flesch, Andreas Holzner, Thomas Barthel (in Aachen) and Sebastian Smerat (in Munich) for the great time we had, office soccer, paper basketball, discussions on trivial and deep physics, women, politics and life in general,
- the rest of the group Adrian, David , Hai-Bo, Stefan, Stephan, Fabian, Alexei, Andre, Guillaume, Georg (Aachen), Tassilo, Georg, Simon, Robert, Ludwig (in Munich)
- the floor mates from Aachen Patrick (Gonzo), Karl, Jim, Frank, Severin, Jonas, Markus, Luuuucaaa, Hugo, Tanaa, Frank, Marteen, Martin, Natascha
- the Thursday evening physicists football team Karl, Dinesh, Viktor, Torge, Markus, Alex, Thomas, Peter, Klaus, Jevinth, Jim, Stephan, Mike, Tobi, Christian (Saunus), Moritz and many many more,
- the floor mates from Munich Wolfgang, Flo, Max, Max, Pablo, Arne
- Umut, Louis and Michael the most congenial (and untypical) Bavarians ever,
- the two wonderful secretaries Gaby (Aachen) and Cordula (Munich)

- the German Research Foundation (Deutsche Forschungsgemeinschaft) for substantial financial support
- to my best friends Aneta, Kasia, Izabela, Vice, Sascha, Umut, Louis, Michael, Daniele for the good moments in life out of the university!
- and most of all Sarah Gindner (for the unforgettable time in Aachen) and her lovely family, my brother, Sławomir and my, 4 years old, niece Mia and in particular to my mother Krystyna for their love, motivation, and unconditional support



# Curriculum vitae

*name* Christian Kasztelan  
*date of birth* 04/04/1979  
*place of birth* Gdańsk, Poland  
*nationality* German  
*adress* Physics Department  
Arnold Sommerfeld Center for Theoretical Physics  
Center for NanoScience  
Ludwig-Maximilians-Universität München  
Theresienstr. 37  
80333 München, Germany

## Education

04/2007 - 10/2010 Doktorarbeit (Ph.D. studies) with Prod. Dr. U. Schollwöck at the LMU München  
*“Strongly Interacting Quantum Systems out of Equilibrium  
Ultracold Quantum Gases and Magnetic Systems”*

07/2006 - 12/2006 Scientific internship in group of Prof. Dr. Juan Torres at the ICFO Barcelona  
*“Quantum Engineering of Light: Creating a Source of Entangled Photons”*

05/2005 - 06/2006 diploma thesis with Prof. Dr. J. Audretsch at the University of Konstanz  
*“Disentangling Action of Quantum Channels”*

10/2000 - 03/2005 studies of physics at the University of Konstanz and the La Sapienza Roma

07/1999 - 07/2000 civil service

06/1999 Abitur (high school diploma), Friedrich-Wöhler Gymnasium Singen am Hohentwiel

09/1986 - 06/1999 school education in Gdańsk (Poland) and Singen am Hohentwiel (Germany)

München, October 11th 2010